# AN X-RAY DIFFRACTION STUDY OF THE STRUCTURE OF FLUID ARGON

Thesis by

Paul G. Mikolaj

In Partial Fulfillment of the Requirements

For the Degree of

Doctor of Philosophy

California Institute of Technology

Pasadena, California

1965

(Submitted December 18, 1964)

# ACKNOWLEDGMENTS

I wish to express my sincere appreciation to Professor C. J. Pings for his helpful guidance and kind encouragement during the course of this investigation.

Special thanks go to Dr. W. I. Honeywell, who was responsible for the design and construction of the apparatus and who contributed greatly to the development of the experimental techniques.

During my graduate studies, I have been the recipient of scholarships and assistantships from the California Institute of Technology. I have also received fellowships from the National Science Foundation, the Woodrow Wilson Foundation, and the Union Carbide Corporation. The funds for this investigation were contributed by the Office of Naval Research and the Air Force Office of Scientific Research. I wish to express my appreciation for all of these gifts.

Finally, I wish to thank my family and especially my wife, Linda, for their sacrifice and continuous encouragement throughout the course of my education.

# ABSTRACT

Atomic radial distribution functions of fluid argon have been determined from experimental x-ray diffraction measurements at 13 different thermodynamic states. These states, forming a temperature-density grid in the critical region, include isotherms of -130°C, -125°C, -120°C, -110°C and isochores (in gm/cc) of 0.982, 0.910, 0.780, 0.536 (the critical density), and 0.280 (argon vapor).

Mo radiation, monochromated by a Zr filter and PHS set for 50% K$\alpha$ transmission, was used in a Debye-Scherrer type geometry and was detected with a NaI scintillation counter. A narrow incident beam was used to partially irradiate the argon sample which was confined in a cylindrical cell constructed from sintered beryllium powder. A calibration experiment, performed with a vitreous $SiO_2$ sample, established the validity of the experimental method and the data processing techniques.

The structural features in the x-ray diffraction patterns were found to depend predominantly on the bulk density of the argon sample and were relatively insensitive to the sample temperature. Except for the low density states, the intensity patterns showed three clearly defined peaks at $S_1 = 1.89\ \text{Å}^{-1}$, $S_2 = 3.56\ \text{Å}^{-1}$, and $S_3 = 5.6\ \text{Å}^{-1}$. The height of the main intensity peak was linear with the bulk sample density and the main peak broadened slightly with increasing temperature.

The radial atomic density functions, $4\pi r^2[\rho_a(r) - \bar{\rho}_a]$, had three maxima for the high density states and only a single well defined maximum for the vapor state. Their radial positions were relatively constant and were located at $r_1 = 3.91$ Å, $r_2 = 7.49$ Å, and $r_3 = 10.9$ Å. The height of these maxima was approximately linear with the bulk sample density and was independent of the sample temperature. The first coordination number showed a simple dependence on the argon density, varying from 6.0 atoms at the highest density to 2.1 atoms at the vapor state. Values of the radial electronic density functions are also reported.

The first maximum in the atomic radial distribution function, g(r), was found to be independent of both the temperature and the bulk sample density. The average height of this maximum was 1.97 and its average radial position was 3.83 Å. No abrupt changes or discontinuities were observed in g(r) as the critical state was approached. A subsidiary maximum, appearing at $r \approx 5.4$ Å, reported in the previous x-ray studies of argon is shown to be spurious. Tables are presented of the estimated g(r) values and also of the smooth x-ray intensity patterns.

# TABLE OF CONTENTS

# LIST OF TABLES

# LIST OF FIGURES

# NOMENCLATURE

## English Symbols

| | |
|---|---|
| A | absorption factor for an incident beam of uniform intensity |
| ACC | total absorption factor for scattering from the cell and self-absorption within the cell |
| ACSC | total absorption factor for scattering from the cell and absorption in the sample and the cell |
| ASSC | total absorption factor for scattering from the sample and absorption in the sample and the cell |
| a | absorption factor for a volume element; parameter in the intensity smoothing function |
| B | slope of the modification function; Breit-Dirac factor |
| B(T) | second virial coefficient |
| b | parameter in the intensity smoothing function |
| (C/N) | normalization constant |
| c | parameter in the intensity smoothing function |
| E | expected value of |
| F(Θ) | incoherent scattering correction factor |
| f(Θ), f(S) | atomic scattering factor |
| G(Θ) | incoherent scattering correction factor |
| g(r) | atomic radial distribution function |
| I(Θ), I(S) | scattered intensity |
| $I^o$ | incident intensity; average scattering power |

| | |
|---|---|
| $I_o$ | intensity of zero-angle scattering |
| $\Delta I^o$ | incident intensity of a composite beam segment |
| $\Delta I_s$ | confidence interval |
| i | index notation |
| i(S) | kernel of the Fourier integral |
| j | index notation |
| j(Θ), j(S) | scattered intensity function |
| k | index notation; constant |
| $\ell$ | optical path length |
| $\langle \ell \rangle$ | average optical path length |
| Mean | statistical mean of |
| N | number of counts; number of atoms |
| $\langle N \rangle$ | statistical mean number of counts |
| n | constant, characteristic of absorbing medium |
| P(0) | polarization factor |
| P(λ, v), P(ν) | normalized pulse amplitude distribution function |
| PAD | pulse amplitude distribution |
| PHS | pulse-height selector |
| Q | intensity scaling factor |
| R | intensity ratio |
| r | radial coordinate; intensity smoothing range |
| $r_o$ | location of intermolecular potential well |
| S | scattering parameter, $(4\pi/\lambda) \sin \Theta$ |

| | |
|---|---|
| $S_1, S_2, S_m$ | limits of the Fourier integral |
| $t_{PHS}$ | PHS transmission factor |
| $u(r)$ | intermolecular potential function |
| $V$ | volume |
| $Var$ | variance of |
| $v$ | voltage |
| $\bar{v}$ | average voltage |
| $\Delta v$ | volume element |
| $w$ | characteristic width of the PAD |
| $X$ | scattering geometry in $SiO_2$ experiment |
| $Y$ | scattering geometry in $SiO_2$ experiment |
| $Z$ | atomic number |

Greek Symbols

| | |
|---|---|
| $\alpha^{inc}$ | relative incoherent absorption factor |
| $\gamma$ | fraction of total radiation scattered coherently |
| $\epsilon$ | parameter in the intermolecular potential function |
| $\epsilon_p$ | relative probable error |
| $r$ | statistical random variable representing the number of counts |
| $\Theta$ | half of the total scattering angle |
| $\Lambda_s^d$ | fraction of the total optical path length through the sample due to diffracted radiation |

| | |
|---|---|
| $\lambda$ | radiation wavelength |
| $\mu$ | linear x-ray absorption coefficient |
| $\nu$ | normalized voltage |
| $\xi_s$ | statistical random variable representing the sample intensity |
| $\rho(r)$ | radial density |
| $\langle\rho(r)\rangle$ | average or estimated radial density |
| $\rho_o(r)$ | radial electron density within an isolated atom |
| $\overline{\rho}$ | average density |
| $\sigma$ | standard deviation of the Gaussian distribution; parameter in the intermolecular potential function |
| $\tau$ | counting time |
| $\phi(\Theta)$, $\phi(S)$ | intensity modification function |
| $\psi_{PHS}^{inc}$ | relative PHS transmission factor for incoherent scattering |

Subscripts

| | |
|---|---|
| a | atomic |
| b | bulk |
| c | cell; critical state |
| c+s | cell-plus-sample |
| c, c | scattering from the cell and self-absorption within the cell |
| c, sc | scattering from the cell and absorption in the sample and the cell |

| | |
|---|---|
| d | corrected for dispersion |
| e | electronic |
| f | beta filter |
| g | graphically determined |
| n | background noise |
| ref | reference angle |
| s | sample |
| s, sc | scattering from the sample and absorption in the sample and the cell |

Superscripts

| | |
|---|---|
| coh | coherent |
| d | diffracted radiation |
| E | experimental |
| i | incident radiation |
| inc | incoherent |
| obs | observed |
| smh | smooth |
| t | total |
| * | standard value |

# I. INTRODUCTION

Modern atomic theory depicts matter to be composed of various building blocks. Neutrons and electrons form atoms; atoms combine to form molecules; molecules may unite to give aggregates, etc. The manner in which these various combinations occur is manifested in the chemical and physical properties of the resultant product. Under this scheme, the three states of matter may be identified by their atomic structure, i.e., the internal arrangement of their atoms or molecules. The gaseous state is represented by large distances between neighboring atoms and a low degree of interaction between their force fields. This arrangement yields the familiar properties of a gas, e.g., a high degree of compressibility and low density. The solid state is characterized by a crystal lattice structure or a definite ordering of atoms within the solid. The interatomic distances are relatively short and there is a high degree of interaction between the atomic force fields. This type of atomic structure gives rise to a rigid material of relatively high density and low compressibility.

The liquid state of matter is more difficult to characterize because it includes a broader range of conditions. However, the relationship between the atomic structure and the physical properties of the gaseous and solid states may be used to deduce something about the nature of the atomic structure within liquids.

Near the freezing point, solids and liquids have comparable densities and, therefore, their interatomic distances and number of

nearest neighbors must be about the same. The low compressibility of liquids at this state suggests fairly strong atomic interactions, but the non-rigidity indicates that these interactions are not nearly as strong as in solids. As the temperature and pressure are increased toward (and past) the critical state, the liquid approaches and intermediate region and may be termed a "dense fluid." This intermediate state exhibits properties common to both the gaseous and the solid state, e.g., non-rigidity, high density, and moderate compressibility. In terms of atomic structure the interatomic distances are relatively short and there is a moderate degree of atomic interactions.

On the basis of this very qualitative picture, it is clear that one of the keys to understanding the physical behavior of matter lies in the determination of its atomic structure, i.e., the arrangement of the individual atoms within the macroscopic body of the material. In the case of liquids, knowledge of the atomic structure is especially important and interesting because of the broad range of conditions which comprise the liquid state. The purpose of this research program was to experimentally measure the atomic structure of a simple liquid. This investigation was performed in a systematic manner over a range of temperatures and pressures which include the gaseous, dense fluid, and liquid regions.

The method used to measure the atomic structure was an investigation of the interaction between a fluid sample and a beam of x rays. When an electromagnetic wave from a primary radiation

source is incident upon a sample, the electrons within the sample are raised to an excited energy state. These excited electrons then serve as sources for the emission of secondary radiation. The secondary radiation emitted from the sample is usually referred to as scattered radiation.

Several types of secondary radiation or scattering may be observed from the irradiated sample. When the scattered radiation has the same wavelength or energy as the incident radiation, it is termed coherent scattering. Because the wavelength is the same, coherent scattering gives rise to optical interference or diffraction effects which occur among waveforms from the various emitting electrons. Another type of secondary emission is incoherent scattering, for which the wavelength of the scattered ray is slightly greater than that of the incident ray. This wavelength difference is dependent upon the scattering angle. Incoherent scattering does not produce diffraction effects, but it does contribute to the total scattering observed from a system of electrons. Other types of secondary emission also occur which can contribute to the observed scattering; but by a suitable choice of experimental conditions they may be almost entirely eliminated and will not be discussed.

An x-ray diffraction pattern from a system of atoms is the result of optical interference of the coherently scattered radiation being emitted from the electrons of the atoms within the sample. Several modes of scattering may exist within a given system. The

collection of electrons into groups to form atoms gives rise to the diffraction pattern typical of a rarefied monatomic gas. In such a sample, the predominant interference effects are internal, i.e., they are due to the arrangement of electrons within the individual atoms. The interference caused by electrons of neighboring atoms contributes only slightly due to the low atomic density and low degree of atomic order within a gas. In the limiting case of an isolated atom, the entire diffracted intensity is due to this internal interference and is termed the atomic scattering factor, f. When a monatomic liquid is irradiated, an additional contribution to the interference pattern occurs. The interatomic distances are smaller, the atom density greater, and the degree of atomic order is higher. As a result, the external interference effects become significant, and form a large part of the total interference network.* Thus the experimentally observed diffraction pattern of a sample gives a qualitative picture of the atomic structure within that sample. Generally, the sharper the observed interference effects in the diffraction pattern, the greater is the degree of atomic order within the sample.

---

* Common to both these systems is the interference from the sample acting as a whole, and having the average electron density. The diffraction effect from such a system is termed the zero-angle scattering and has been demonstrated to be negligible for all practical purposes[1]. It is formally accounted for in the theory by subtracting it from the observed experimental scattering. Its presence will be neglected in all subsequent treatment.

In addition to the qualitative information conveyed by an x-ray diffraction pattern, there is also a certain amount of quantitative information which may be obtained regarding the internal structure of a fluid. The atoms in a fluid are in a continual state of motion governed by the interatomic forces acting between the individual atoms. Consider the average location of these atoms with respect to each other and let $\rho_a(r)$ be a spherically symmetrical, atomic density function. This function is selected such that $4\pi r^2 \rho_a(r)dr$ gives the average number of atoms in a spherical shell of radius $r$ and thickness $dr$ about any atom within the fluid. Now define an atomic radial distribution function as $g(r) = \rho_a(r)/\overline{\rho}_a$ where $\overline{\rho}_a$ is the average atomic density of the fluid. The function $g(r)$ represents the relative probability of finding two atoms separated by the distance $r$, averaged over time and over all possible configurations of the remaining atoms in the system.

The general features of the radial distribution function may be deduced by considering the behavior of atoms within the fluid. Since the atoms have a finite size, there is zero probability of two atoms occupying the same space and $g(r)$ is zero up to about one atomic diameter. There is a high probability of two particles being at a distance $r_o$ which is near the minimum of the potential curve describing their interaction. Because of the shell of atoms at $r_o$, there should be a minimum farther out. Depending upon the atomic structure and degree of order within the fluid, there may be other but

less pronounced maxima in $g(r)$ at higher values of $r$. Since there is no long range order in a fluid, $g(r)$ approaches unity at large values of $r$, i.e., there are no preferred interatomic separations and the local atomic density approaches the average density of the system. The atomic structure of a fluid may be more conveniently pictured through the atomic density function, $\rho_a(r) = g(r)\overline{\rho}_a$. The locations of the maxima in $\rho_a(r)$ furnish the mean interatomic distances in the fluid and the areas under the maxima of $4\pi r^2\rho_a(r)$ give an indication of the number of neighboring atoms at these various distances (usually referred to as coordination numbers).

The detailed manner in which the radial distribution function is computed from the x-ray diffraction pattern of a fluid has been widely discussed[1, 2, 3]. Recent reviews[4, 5] have presented the results of investigations for many liquids and have summarized the data treatment methods. In view of the extensive treatment in the literature, only the results will be presented here.

For a monatomic liquid, the intensity of coherently scattered radiation is related to the radial distribution function by the equation

$$\frac{I^{coh}(S)}{f^2(S)} = 1 + \int_0^\infty 4\pi r^2\overline{\rho}_a[g(r) - 1]\ \frac{\sin(Sr)}{Sr}\ dr, \qquad (1)$$

where

$$S = \frac{4\pi}{\lambda}\ \sin\Theta.$$

In this equation $I^{coh}(S)$ is the total time-averaged intensity of coherently scattered radiation from the fluid,* and $f(S)$ is the atomic scattering factor. The quantity $f^2(S)$ is the intensity which would be scattered coherently from an isolated atom. Both $I^{coh}(S)$ and $f^2(S)$ are expressed in units relative to the intensity which would be scattered by an isolated classical electron under identical conditions (usually referred to as electron units, eu). The quantity $S = (4\pi/\lambda) \sin \Theta$ is the scattering parameter, where $\lambda$ is the wavelength of the monochromatic radiation used, and $\Theta$ is half the scattering angle, i.e., half the angle defined by the direction of the incident beam and the direction of the observed scattered beam.

Eq. (1) may be formally solved by means of the Fourier integral theorem[1] to obtain an explicit expression for the radial distribution function. The transformed equation is

$$4\pi r^2 \overline{\rho}_a [g(r) - 1] = \frac{2r}{\pi} \int_0^\infty S\, i(S) \sin(Sr)\, dS , \qquad (2)$$

where

$$i(S) = \frac{I^{coh}(S)}{f^2(S)} - 1 .$$

* The formally correct term in Eq. (1) should be $[I^{coh}(S) - I_o(S)]$ where $I_o(S)$ is the zero-angle scattering previously discussed.

A rigorous application of this expression is not possible because it requires a complete knowledge of the intensity $I^{coh}(S)$, i. e., values of the intensity to $S = \infty$. In practice, the maximum value of $S$ which can be obtained experimentally depends on the wavelength of radiation used and is about 8 $\text{Å}^{-1}$ for CuK$\alpha$ and 17 $\text{Å}^{-1}$ for MoK$\alpha$ radiation. Experimental results have shown that the total coherent scattering from a monatomic liquid oscillates about and approaches the value of the intensity scattered from the isolated atoms as $S$ gets large, i. e., $I^{coh}(S) \rightarrow f^2(S)$. Under these conditions, the kernel of the integral in Eq. (2) approaches zero and the integral may be truncated at a value of $S$ where no further oscillations are observed. This required truncation of the Fourier integral results in an error curve superimposed on the radial distribution function. The effect of this truncation and the magnitude of the resulting error have been discussed by several authors[6, 7, 8].

The material selected for this investigation of liquid structure was argon. While other simple monatomic liquids were available, argon was selected for several reasons. Its liquid region is experimentally accessible over a broad range of temperatures and pressures and accurate thermodynamic properties are available over the experimental region of interest, thus permitting the correlation of atomic structure from this work with other physical properties. Also, high purity argon is readily available and can be purchased at a reasonable cost.

The atomic structure of liquid argon has been the subject of previous investigations by both x-ray and neutron diffraction techniques. The most extensive of these investigations is due to Eisenstein and Gingrich[9] who obtained the x-ray diffraction pattern of argon for twenty-six different conditions of pressure and temperature. The neutron diffraction study[10] was taken near the argon triple point.

In view of the attention this element has received, the need for further investigation might seem unnecessary. However, this is not the case. Of the twenty-six thermodynamic states investigated by Eisenstein and Gingrich, over half were in the low density gas phase region. Only six states were subjected to Fourier analysis to obtain atomic density functions and all of these were near the liquid-vapor coexistence curve. Also, these measurements were performed over twenty years ago without the refinements of modern experimental methods and computing techniques. In a recent study[11] performed at the argon triple point, Gingrich and Tompson indicated that improved techniques enabled them to determine the atomic structure at this state with more certainty than their earlier measurements. As a further reason for this investigation, evidence of errors in the atomic structure as reported by Eisenstein and Gingrich has been presented by Khan[12]. From theoretical considerations, Khan computed values of the radial distribution function and compared them with the experimental curves of Eisenstein and Gingrich. While the main features of $g(r)$ were in general agreement, the experimental curves exhibited

subsidiary maxima and minima which could not be produced from the theoretical model.

The desirability of systematically investigating the atomic structure over a wide range of thermodynamic states has been discussed earlier. The purpose of the present work was to undertake such a study. The systematic nature of this investigation was based to a large extent on measurements of the thermodynamic properties of argon by Levelt[13]. Using Levelt's volumetric measurements, a temperature-density grid was set up to span a range of thermodynamic states near the region of the argon critical state. This investigation was initiated by Honeywell[14] who measured the x-ray diffraction of liquid argon at three densities along the -130°C isotherm. The present study extends the range to cover eleven more thermodynamic states. In addition to these experimental measurements, the data from two states reported by Honeywell were reworked to give a total of thirteen states which are reported here.

A summary of the pressure, temperature, and density of these states is presented in Table 1 and the states are depicted graphically in Figure 1. Also shown on Figure 1 are some of the states measured by Eisenstein and Gingrich. Included in the present work are the results for temperatures of -130°C, -125°C, -120°C, and -110°C and bulk densities (in gm/cc) of 0.982, 0.910, 0.780, 0.536, and 0.280. Of special interest are measurements taken along the isochore of 0.536 gm/cc at temperatures of -110°C, -115°C, -120°C (the critical

temperature is -122.29°C) and along the -125°C isotherm at densities of 0.780 gm/cc (near the saturated liquid state) and 0.280 gm/cc (near the saturated vapor state).

# II. EXPERIMENTAL

## A. General

The experimental x-ray diffraction patterns were obtained by irradiating an argon sample contained in a cylindrical sample cell with a collimated beam of x rays and measuring the scattered intensity as a function of the scattering angle, $\theta$. The sample cell, similar in design to the one described by Paalman and Pings[15], was constructed from sintered beryllium powder and had an o. d. of 0.100 inches, an i. d. of 0.057 inches, and an irradiated length of about 0.40 inches. While the sample cell was believed to be cylindrical, it was found that the i. d. was not concentric with the o. d. by the amount of 0.005 inches. This nonconcentricity was discovered after the cell was installed and the experimental measurements had begun. Its effect is discussed in Section IV-C.

The sample cell was enclosed in a brass block containing coolant tubes and resistance heater wires. This entire assembly was contained in a cylindrical vacuum cryostat with a sheet of 0.0005 inch mylar serving as a window to transmit the incident and scattered x-ray beams. The cryogenic temperatures were obtained by cooling with cold nitrogen gas, and temperature control was effected by electrical heating to the desired control temperature. The temperature was measured with a platinum resistance thermometer placed within the sample cell and in direct contact with the argon sample. The

sample pressure was transmitted through a flexible stainless steel diaphragm to a hydraulic oil system and was measured with a Hart pressure balance. Pressure control was obtained through the use of a manually operated screw intensifier placed within the sample system. A detailed description of the apparatus design, performance characteristics, and operating procedure is given elsewhere[14, 16] and will not be presented here. The only modification made in the experimental equipment was to pack the grooves containing the electrical resistance heater wires with indium to increase the thermal response of the system.

Since the argon was confined in a sample cell, two separate experimental measurements were required; one being the scattered intensity from the empty cell alone, denoted by $I_c^E(\Theta)$, and the other being the intensity scattered from the assemblage consisting of the argon sample plus the sample cell denoted by $I_{c+s}^E(\Theta)$. The intensity was measured at incremental values of $\Theta$ over the angular range $1^o \leq \Theta \leq 60^o$ with $\Delta\Theta = 0.25^o$. Each scan (or series of measurements) consisted of 237 values of the experimental intensity, $I_c^E(\Theta)$ or $I_{c+s}^E(\Theta)$. The problem of combining these two intensities to determine the scattering which originates from the sample alone, $I_s(\Theta)$, is discussed in Section IV-A.

The empty cell scattering was measured at the two temperature extremes of $-125^oC$ and $-110^oC$. Four separate scans were made at each temperature. A statistical analysis of this data showed that there

was no significant difference between the diffraction patterns at these two temperatures. Also the effect of pressure on the sample cell diffraction pattern was assumed to be negligible. Under these conditions, the empty cell diffraction pattern was taken to be independent of temperature and pressure and the same set of values for $I_c^E(\Theta)$ was used for all the argon runs.

When measuring the scattering from the argon sample confined in the sample cell, an effort was made to obtain maximum control of the temperature and pressure, thereby minimizing uncertainties in the sample environment. To avoid any transient conditions, the apparatus was maintained under temperature control at least twelve hours prior to the introduction of argon into the cell. The apparatus was maintained at cryogenic temperatures for a duration of about 150 hours, during which time several argon scans were made. A single scan required about twelve hours and three separate scans were made at each thermodynamic state. These three scans were then averaged to obtain the experimental cell-plus-sample diffraction pattern, $I_{c+s}^E(\Theta)$. As previously mentioned, a thin sheet of mylar (0.0005 inches) served as a window on the vacuum cryostat to transmit the incident and scattered x-ray beams. To minimize the formation of ice on the cell surfaces resulting from diffusion of air through the mylar window, the apparatus was periodically warmed up and the condensible vapors were pumped out.

The argon used in the experiment was obtained from the Linde Rare Gas Department of Union Carbide and the maximum reported impurity was one part per million $H_2O$; traces of $O_2$, $N_2$, $CO_2$, and hydrocarbons (no $CH_4$) were also reported. At the conclusion of each scan, the argon was withdrawn from the sample cell and stored in a reservoir bomb. To prevent the accumulation of any contaminents, fresh argon was used for each thermodynamic state, i.e., every three scans.

The experimental control limits achieved in the measurement of the argon temperature and pressure are summarized in Table 1. These limits reflect both the uncertainties in the variables used to determine the sample environment and the limits in the actual control processes. For all eleven experimental runs, the temperature was maintained constant to within 0.02°C while the uncertainty in the absolute temperature measurement was 0.05°C. With the exception of Run 31, the maximum error in the pressure measurement was 0.6 psi. This figure represents an uncertainty in the absolute pressure of about 0.2 psi and control limits of better than 0.4 psi. The pressure control achieved on Run 31 was slightly worse than the rest because of the proximity of this state to the saturated liquid curve (see Figure 1). Also included in Table 1 is the maximum uncertainty in the sample density corresponding to the limits of the temperature and pressure measurements. These values were calculated from the compressibility data of Levelt[13]. As expected, the state showing the maximum

uncertainty in the density was the one nearest the critical state (Run 34; 0.536 ± 0.015 gm/cc). The uncertainty occurring in the remaining states depended strongly on the location of the state, but was better than 0.005 gm/cc in all cases.

## B. X-Ray Measurement

The radiation source used in this experiment was a Norelco x-ray generator with a molybdenum target having dimensions of 1.2 mm x 10.0 mm. The x-ray tube was operated at its maximum rated capacity of 55 kvp and 20 ma, and yielded a characteristic $K\alpha$ line with a wavelength of 0.711 Å. The scattered intensity was measured with a scintillation counter mounted on a Norelco wide-range goniometer. The Norelco goniometer had a vertical scattering plane, i.e., the vectors defining the nominal direction of the incident and scattered x-ray beams were in a vertical plane.

The optical conditions used in the experiment are depicted schematically in Figure 2 and are described below:

1. The take-off angle was $5.8^{\circ}$, giving virtually a line source of 0.12 mm x 10.0 mm.
2. The distances between the x-ray target, the goniometer axis, and the receiving slit were 6.98 inches and 5.63 inches, respectively.

3. The incident beam was defined by a divergence slit 0. 0062 inches in height and was placed between the x-ray target and the sample at a distance of 3. 35 inches from the target.

4. Collimation of the incident beam was obtained by using a vertical Soller slit assembly placed between the x-ray target and the divergence slit. These Soller slits were constructed from foil 0. 0025 inches thick and 1. 125 inches long and had a spacing of 0. 018 inches.

5. The receiving slit in front of the scintillation counter was 0. 112 inches in height. The scattered x-ray beam was collimated with a set of horizontal Soller slits constructed from foil 0. 0024 inches thick and 1. 31 inches long and had a spacing of 0. 005 inches.

The angular resolution of the diffractometer is given by the vertical and horizontal divergence of the detected radiation, $\Delta\Theta_V$ and $\Delta\Theta_H$, respectively. The maximum divergence is defined as the largest difference between the diffraction angle of any scattered ray from the irradiated sample (or sample cell) and the nominal scattering angle, $\Theta$. For the optical conditions used in this experiment, the total vertical divergence was $\Delta\Theta_V = \pm 0.375$ degrees and was independent of $\Theta$. The horizontal divergence was angular dependent and some of the values are given below[17].

| Nominal Scattering Angle $\Theta$ (degrees) | Maximum Horizontal Divergence $\Delta\Theta_h$ (degrees) |
|---|---|
| 1.50 | 1.40 |
| 2.50 | 1.02 |
| 5.00 | 1.07 |
| 10.00 | 0.30 |
| 30.00 | 0.08 |
| 60.00 | -0.01 |

Prior to the measurement of any x-ray diffraction patterns, the scattering geometry was precisely determined. The scattering geometry as used here refers to any geometric factors which affect the experimental intensity measurements. Such factors include the intensity distribution of the x-ray beams, the shape and size of the irradiated sample, and the location of the irradiated sample with respect to the goniometer axis. The primary consideration used in selecting the scattering geometry for this experiment was the desirability of maximizing the signal to noise ratio, i.e., obtaining the maximum amount of scattering from the argon sample relative to the scattering from the sample cell.

A relatively narrow incident beam was used so that the sample cell was only partially irradiated. This narrow incident beam, having a fairly large penumbra region, was positioned such that the upper edge of the umbra was roughly coincident with the upper edge of the cell interior. While this beam position did not yield a maximum ratio

of sample irradiated volume to cell irradiated volume, the additional consideration of corrections required for absorption losses in the relatively dense sample medium showed that this was an optimum geometry.

The dimensions and exact location of the sample cell were obtained in the following manner. With the divergence slit removed, and using a small (0.003 inches) receiving slit, the primary x-ray beam was scanned. This measurement yielded an "x-ray picture" of the sample cell cross section in a vertical plane perpendicular to the scattering plane. This "x-ray picture" clearly showed the high and the low absorption caused by the cell walls and the cell interior. The position of the cell in a horizontal plane perpendicular to the scattering plane was obtained by directing a narrow incident beam through the center of the cell interior. The scattered intensity was then measured over the angular range $5^{\circ} \leq 2\Theta \leq 150^{\circ}$ with a narrow receiving slit. Under these conditions, a minimum in the scattered intensity (apart from that caused by the polarization correction) was observed at an angular position of $2\Theta$ determined by a line through the goniometer axis and the axis of the cell interior. This minimum resulted from the fact that at this angular position, the incident and scattered x-ray beams intersected entirely within the cell interior. Once the location of the sample cell was established, the incident x-ray beam was positioned in the preselected position. With these measuring techniques, the following scattering geometry was determined (see Figure 3).

| | |
|---|---|
| cell outside diameter | 0. 100 inches (actual measurement) |
| cell inside diameter | 0. 057 ± 0. 001 inches |
| cell o. d. axis | 0. 028 ± 0. 001 inches below goniometer axis |
| cell i. d. axis | 0. 023 ± 0. 001 inches below goniometer center |
| incident beam centerline | 0. 0016 ± 0. 0002 inches below goniometer axis |
| height of beam umbra region | 0. 0082 ± 0. 0002 inches |
| height of beam penumbra region | 0. 0186 ± 0. 0002 inches |
| horizontal displacement of cell inside diameter | 0. 005 ± 0. 002 inches from goniometer axis toward x-ray target |

The height of the receiving slit was large enough to permit all scattered rays to enter the radiation detector. The intensity distribution of the scattered beam was calculated from the x-ray optical conditions given previously and is shown in Figure 3. The intensity distribution of the incident beam was calculated from the x-ray optics and agreed with the measured distribution within the experimental error.

Due to the thermal expansion of the sample cell supports within the vacuum cryostat, the location of the cell was dependent upon the operating temperature. However, within the precision of the experimental measurements, there was no detectable change in the cell location over the relatively small temperature range of -125°C to

$-110^{\circ}C$. The fact that the center of mass of the irradiated volume was slightly displaced from the goniometer axis necessitated the use of an angular correction factor. This angular correction in $\Theta$ (less than 0.03 degrees for all angles) was found to be considerably less than the total angular resolution and was therefore neglected.

The intensity of the scattered radiation was measured with a sodium iodide (thallium activated) scintillation counter. The output signal from the scintillation counter was fed through a high-gain linear amplifier (maximum gain = 50, 000) and a pulse-height selector (PHS). The output signal from the PHS was counted by an electronic scaler and timer. With these devices, the intensity was recorded as the total number of counts registered on the scaler, N, during a time interval, $\tau$.

Monochromatization of the x-ray beam was achieved by using an absorption filter in conjunction with the PHS[18]. A zirconium foil (0.0038 inches thick) mounted on the divergence slit reduced the intensity of the relatively strong $K\beta$ line by approximately 99% while the $K\alpha$ line was reduced by 65%. The PHS was operated with a symmetrical 50% transmission factor, i.e., 50% of the total intensity of $K\alpha$ wavelength was allowed to pass through the PHS and be counted by the scaler. The settings (or voltage window) of the PHS were determined at the beginning of each scan by measuring the pulse amplitude distribution of the $K\alpha$ radiation scattered from the (101) reflection of the beryllium sample cell. The voltage corresponding

to the maximum in the pulse amplitude distribution (the average $K\alpha$ voltage) was determined, and the voltage window which transmitted 50% of the total $K\alpha$ radiation was centered about this average $K\alpha$ voltage. The total amplification of the output signal from the scintillation counter was chosen to give an average $K\alpha$ pulse amplitude of about 50 volts. Under these conditions, the 50% transmission window was about 11.6 volts. (A further discussion on the use of the PHS is given in Section IV-D and Appendix 2.) An estimate of the spectrum of the incident x-ray beam after monochromatization is given in Figure 4. This spectrum was measured with a lithium fluoride crystal in place of the beryllium sample cell under the same conditions used in the experiment.

All experimental intensity measurements were scaled to the intensity at an arbitrary reference or check point. This check point was taken at $\Theta = 50$ degrees where the diffraction pattern of the empty beryllium cell was relatively flat, i.e., free from any pronounced diffraction peaks. The purpose of this reference measurement was to monitor the intensity of the incident x-ray beam, to check the stability of the electronic components associated with the x-ray detection, and to provide a scaling factor for the cell-plus-sample intensity. For each scan the check point intensity was measured at regular intervals approximately three hours apart; at the beginning and end, and three times during the scan. Each check point measurement consisted of ten consecutive 100-second counts. For the argon

runs, check point measurements were taken both from the empty cell and from the cell-plus-sample. These measurements, made at the beginning and end of each scan, were used to determine a scaling factor for normalizing the intensity of the cell-plus-sample to that of the empty cell. At the end of each scan, the check point intensities were statistically analyzed to determine if any systematic angular variation in the intensity pattern had occurred. Along with the measurement of the check point intensity, periodic measurements were made on the background noise level. This background noise, which was due to the associated electronic circuitry in the x-ray detection system, was relatively constant at about 0.08 counts/second.

The counting strategy employed in the experimental intensity measurement was dictated by the presence of the large number of prominent peaks in the empty cell diffraction pattern. To minimize the effect of any errors associated with intensity measurements on these peaks, a fine angular grid was used. In this manner, any suspicious data points in the regions of these peaks could be discarded while still leaving a sufficient number of data points to define the scattering curve. Experimental data points were taken in increments of $\Delta\Theta = 0.25$ degrees over the range $1^{\circ} \leq \Theta \leq 60^{\circ}$. The minimum angle ($\Theta$ = 1 degree) was limited by the presence of the primary x-ray beam and the maximum angle ($\Theta$ = 60 degrees) was arbitrarily selected. This angular grid resulted in 237 data points for each scan.

For reasons of experimental expediency, the large number of data points necessitated the use of fairly short counting times. As previously mentioned, the empty cell diffraction pattern was assumed to be independent of temperature and pressure. Four scans at each of the two temperature extremes were made on the empty cell with a fixed counting time during each scan of $\tau$ = 200 seconds. The resulting average empty cell diffraction pattern had an effective total counting time of $\tau$ = 1600 seconds for each of the 237 data points. For each of the eleven argon runs, three scans were made with a fixed counting time of $\tau$ = 100 seconds. The scans were then corrected for background noise, properly scaled to a common reference intensity and the results averaged for each thermodynamic state. Thus the argon runs had an effective total counting time of $\tau$ = 300 seconds for each data point.

The resulting experimental measurements of the empty cell and the cell-plus-argon-sample diffraction patterns are given in Table 2. The experimental data obtained by Honeywell[14] for Runs 22 and 23 are not listed here. As an illustration of the typical behavior of the diffraction patterns, the data for Run 40 (t = -125°C, $\overline{\rho}_b$ = 0.982 gm/cc) are plotted in Figure 5. The dashed lines in this figure show the magnitude of the beryllium diffraction peaks.

# III. CALIBRATION EXPERIMENT

Several aspects of this experiment may lead to the conjecture that the resulting x-ray diffraction patterns of the argon sample are inconclusive or are subject to large uncertainties. Probably the main cause for such concern lies in the fact that the diffraction pattern of the beryllium sample cell, with its large number of strong diffraction peaks, may completely or partially mask out the structural features of the confined sample. In addition to this, there is the previously mentioned problem of the nonconcentric sample cell, i.e., a cell having a nonuniform wall thickness. Based on the results obtained by Honeywell[14] and on an extensive series of experimental measurements and computations, a data processing technique was developed which was designed to overcome the problems associated with the presence of this high background scattering. In order to offer supporting evidence for the results of this experiment, the entire experiment was calibrated. The purpose of this calibration experiment was twofold:

1. To find out if the presence of large amounts of scattering from the sample cell interfered significantly with the determination of the scattering curve from the confined sample.
2. To establish the validity of the data processing techniques.

The calibration experiment consisted of measuring the diffraction pattern of a sample confined in a sample cell. After applying the various correction factors to the experimental data, the resulting intensity curve was compared to the intensity curve of the same unconfined sample. The beryllium sample cell in this experiment was not the same one used in the argon study. However, it was fabricated from the same material and had similar features, i. e., it was nonconcentric. The sample was a cylindrical specimen of vitreous $SiO_2$, accurately polished to give a snug fit with the cell interior. A vitreous $SiO_2$ sample was selected for three reasons:

1. The relative ease with which the diffraction pattern of the unconfined sample could be obtained.

2. Its x-ray diffraction pattern closely resembles that of a typical liquid.

3. Its linear absorption coefficient was in the same range as that of the argon samples.

Three separate experiments were performed; one with an unconfined sample and two with the $SiO_2$ sample confined in the beryllium cell.

Since this calibration was to serve as a test of the argon experiment, the experimental conditions were maintained as closely as possible to those described in the previous section. The beryllium cell used in the calibration test had an outside diameter of 0. 070 inches,

an inside diameter of 0. 037 inches, and the nonconcentricity (displacement of the i. d. axis from the o. d. axis) was 0. 005 $\pm$ 0. 001 inches. To determine the effect of the nonuniform wall thickness, two scattering geometries for the confined sample were used. These scattering geometries are shown in Figure 6. The geometry labeled "Cell Position-X" was similar to that of the argon experiment in that the minimum wall thickness was located above the goniometer axis. In the second experiment, labeled "Cell Position-Y," the sample cell was rotated $180^{\circ}$ so that the maximum wall thickness was above the goniometer axis. The sample cell was mounted directly on the goniometer and the axis of the outside diameter was coincident with the axis of the goniometer. In all three experiments the incident x-ray beam was positioned such that the upper edge of the umbra region roughly coincided with the upper edge of the $SiO_2$ sample. The x-ray optics were the same as those used in the argon experiment.

The counting strategy was again similar to that previously described for the argon experiment. The scattered intensity was measured in increments of $\Delta\Theta = 0.25^{\circ}$ over the angular range $1^{\circ} \leq \Theta \leq 60^{\circ}$. For the unconfined sample, two scans were made with a fixed counting time of 200 seconds each. For the two confined samples, three scans were made of both the empty cell and the cell-plus-sample with a counting time of 200 seconds for each scan. The background noise level was determined and all intensity measurements

were scaled to a check point reference intensity at $\Theta = 50$ degrees. Average intensities were then calculated and were used for all further computations.

A detailed description of the data reduction techniques is presented in Section IV. Following these methods, the experimental data were corrected for polarization, absorption, and incoherent scattering, and the empty sample cell scattering was subtracted to give the diffraction pattern of the $SiO_2$ sample. The resulting $SiO_2$ intensity data were statistically analyzed and any erroneous data points were discarded. The remaining data points were then smoothed by a least squares method to give the experimental scattering curve for the $SiO_2$ sample.

A comparison of the resulting curves was made by taking the ratio of the intensity of the unconfined sample to the intensity of the confined sample. If the presence of scattering from the sample cell does not affect the determination of the scattering curve for the sample, this ratio should yield a straight line with zero slope when plotted against $\Theta$ (or S). The results are shown in Figure 7. There are two significant features in this comparison:

1. For both of the scattering geometries, the ratio appears to be linear in $\Theta$ with a slope significantly different from zero.

2. Apart from this linear error, there is no systematic deviation in the scattering curves for the confined samples.

The linear behavior of the intensity ratios was determined by a least squares fit. Since there was no a priori reason for an error linear in $\Theta$, the correlation was also made with S as the independent variable. For both scattering geometries, the correlation against $\Theta$ gave a slightly lower standard deviation than the correlation against S. While this was not considered conclusive proof, it did suggest that $\Theta$ could reasonably be used as the correlating parameter. The results of this comparison showed that the $SiO_2$ scattering curve from geometry-X had a positive error (the intensity at the higher scattering angles was too high) while geometry-Y gave a negative error. The intensity ratio for both scattering geometries oscillated about the best linear fit through the data points. This oscillation appeared to be random and was presumed to be statistical in nature. There were no angular regions where it was apparent that the features of the sample scattering curve were significantly masked out by the scattering from the sample cell.

The results of this calibration experiment show that the scattering curves obtained for a confined sample may require a correction for distortion effects caused by the presence of the sample cell. To correct for this distortion, a linear modification function, $\phi(\Theta) = 1 + B\Theta$, was defined such that $\phi(\Theta) I_s(\Theta)$ gave the true (or undistorted) scattering curve for the confined sample. In the $SiO_2$ experiment, the least squares fit gave the slope of the modification function as -0.00319 for geometry-X and +0.00144 for geometry-Y.

This immediately suggests that the slope of $\phi(\Theta)$ is directly related to the position of the nonconcentric sample cell. However, as will be shown later, this is not necessarily true. In the argon runs, the sample cell was positioned with its minimum wall thickness above the goniometer axis, similar to that in geometry-X. As demonstrated in Figure 7, $\phi(0)$ had a negative slope for this $SiO_2$ experiment while all the argon experiments required a modification function with a positive slope. The corrected or modified scattering curves, $\phi(\Theta) I_s(\Theta)$, of the confined $SiO_2$ samples are plotted in Figures 8 and 9 for the geometries X and Y, respectively. Also shown on these figures is the unmodified scattering curve for the unconfined sample.

The conclusions resulting from this calibration experiment are summarized below.

1. The presence of scattering from the sample cell does not significantly mask out the features of the sample scattering curve.

2. The data reduction and smoothing techniques are satisfactory.

3. The scattering curves obtained from a confined sample may require a linear correction due to a distortion caused by the presence of the sample cell.

The possible causes of the distortion effect and a means of obtaining the required modification functions are discussed in Section IV-F and Appendix 4.

# IV. TREATMENT OF EXPERIMENTAL DIFFRACTION DATA

## A. General

The determination of the argon scattering curves from the experimental data involves the use of several correction terms. These corrections account for losses in the observed intensity due to absorption of the incident and scattered x-ray beams, polarization of the scattered beam, and losses in the observed incoherent scattering. The remainder of Section IV describes the detailed methods used in calculating and applying these correction factors. Since the experimental data were obtained in equal increments of the scattering angle, $\Theta$, all the data treatment computations were performed with $\Theta$ as the independent variable rather than the conventional scattering parameter, S. The conversion to S dependence was made during the Fourier transformation of the final intensity curves.

In order to obtain the scattered intensity originating from the confined sample, the scattering from the empty cell must be subtracted from the observed cell-plus-sample scattering. However, before this subtraction can be made, the observed experimental intensities, $I^E_{c+s}$ and $I^E_c$, must be corrected for absorption and polarization. Paalman and Pings[19] have discussed the application of the corrections to cylindrical samples and annular sample cells and their treatment will be followed here.

The scattering from the confined sample is related to the experimentally observed intensities by the equation

$$I_s(\Theta) = \frac{1/P(\Theta)}{F(\Theta)ASSC(\Theta)} \left[ I^E_{c+s}(\Theta) - \frac{ACSC(\Theta)}{ACC(\Theta)} I^E_c(\Theta) \right], \quad (3)$$

where $I_s(\Theta)$ is the total scattered intensity from the sample, i. e., the sum of the coherent and incoherent scattering. The factor $P(\Theta)$ corrects the observed intensities for polarization of the scattered x-ray beam. The polarization factor used in this experiment was $P(\Theta) = \frac{1}{2}[1 + \cos^2(2\Theta)]$. $F(\Theta)$ is a correction term arising from the fact that not all of the incoherently scattered radiation is actually detected. The evaluation of this incoherent scattering correction term is given in Section IV-D. The remaining terms in this equation are the absorption factors and are explained below.

1. ASSC(Θ), [sample absorption factor]; corrects the sample scattering for absorption in both the sample and the cell.
2. ACSC(Θ), [cell absorption factor]; corrects the cell scattering for absorption in both the sample and the cell.
3. ACC(Θ), [cell absorption factor]; corrects the empty cell scattering for self-absorption within the cell.

The scattering curve for the argon sample as obtained from Eq. (3) (see Figure 12) shows one fairly strong maximum followed by a number of other maxima or inflection points which are much less prominent. As discussed in Section I, the features of the scattered intensity are dependent upon the thermodynamic state of the argon sample. In order to show more clearly the effect of temperature and density of these scattering curves, the intensity data was normalized by the total independent argon scattering. Thus the experimental results are presented in terms of a scattering function, $j(\Theta)$, which is defined by the equation

$$j(\Theta) \equiv \frac{(C/N)\,\phi(\Theta)\,I_s(\Theta)}{f_d^2(\Theta) + I^{inc}(\Theta)} \quad . \tag{4}$$

$(C/N)$ is a normalization constant (per argon atom) to convert the intensity from the arbitrary units of counts/sec to electron units, and $\phi(\Theta)$ is the linear modification function (mentioned in Section III) used to correct the sample intensity for distortion effects caused by the sample cell.* In addition to sharpening the features of the scattering curve, $j(\Theta)$ also illustrates the behavior of the intensity kernel, $i(S)$, in the Fourier transform, Eq. (2). When the scattering function is expressed in terms of its S dependence, the relation between the two is

* The modification function is discussed in Section IV-F.

$$i(S) = [\,1/\gamma(S)\,]\,[\,j(S) - 1\,],$$

where

$$\gamma(S) = \frac{f_d^2(S)}{f_d^2(S) + I^{inc}(S)} \quad .$$

The quantity $\gamma(S)$ is a monotonically decreasing function and thus oscillations in $j(S)$ correspond to oscillations in the kernel of the Fourier integral.

In Eq. (4), $f_d$ is the dispersion corrected atomic scattering factor and $I^{inc}$ is the incoherent scattering factor. The values of f used in the computations were those determined by Berghuis[20]. The dispersion correction was applied using the formula

$$f_d^2 = (f + \Delta f')^2 + (\Delta f'')^2 \quad . \tag{5}$$

The real and imaginary parts used in the dispersion correction were $\Delta f' = 0.10$ and $\Delta f'' = 0.20$, respectively[21]. Values of $f_d^2$ in increments of $\Delta\Theta = 0.25^o$ were obtained by interpolation with a fifth-order polynomial fitted to the 18 data points of Berghuis. Incoherent scattering factors including exchange effects were not available for argon. Therefore, values were interpolated from those of $Ca^{++}$, $K^+$, and $Cl^-$, which did include the exchange effects[36]. This method of interpolation was used by Chipman and Jennings[21] and by Furumoto[22].

The latter compared similarly interpolated values for neon with calculated values and found the discrepancy to be of the order of one percent. A relativistic correction, the Breit-Dirac factor, must be applied to the incoherent scattering data. Since the scintillation counter used in the experiment was a quanta or photon detector, the incoherent scattering factors from the literature were divided by $B^2$ instead of the usual $B^3$ (Ref. 23) where $B$ is the Breit-Dirac factor. The data used to estimate the argon incoherent scattering factor were given only to $S = 13.8\ \text{Å}^{-1}$ and graphical extrapolation was used to extend the range to $S = 15.3\ \text{Å}^{-1}$. A fifth-order polynomial fitted to the data points was used to interpolate the intermediate values. Interpolated values of the atomic and incoherent scattering factors used in the computations are listed in Table 3.

## B. Preliminary Calculations

The experimental intensities in Eq. (3) are assumed to be measured relative to a common incident intensity, $I^o$. However, the experimental settings on the x-ray generator could not be reproduced with sufficient accuracy to give the same value of $I^o$ for all runs and it was necessary to scale the observed intensities, $I^{obs}$, to a common reference level. This was done for each scan by the equation

$$I^E = Q\left[I^{obs} - I_{noise}\right], \tag{6}$$

where $Q$ is an appropriate scaling factor and $I_{noise}$ is the average intensity of the background noise level during the scan.

With Eq. (6) the observed intensities were scaled to an arbitrary standard intensity of the empty cell scattering, $I_c^*$, at a reference angle of $\Theta = 50$ degrees. During each scan several measurements of the scattered intensity at the reference angle, $I_{ref}$, were taken. The average of these measurements was then used to compute the scaling factor. For the empty cell scans this scaling factor was $Q_c = I_c^*/(I_c)_{ref}$. Since the empty cell reference intensity $(I_c)_{ref}$ could not be measured during the argon runs, the determination of $Q_{c+s}$ required an additional measurement of the quantity $R_{ref} = (I_{c+s})_{ref}/(I_c)_{ref}$. This reference ratio was measured at the beginning and end of the argon scans. Several values of $(I_{c+s})_{ref}$ were measured during the scan and the average value was used to calculate the scaling factor by the equation $Q_{c+s} = R_{ref} I_c^*/(I_{c+s})_{ref}$. The standard reference intensity, $I_c^*$, was selected as 16.50 counts/sec and gave scale factors in the range 1.0 to 1.1.

Eq. (3) shows that the experimental intensities are subtracted and, therefore, the scale factors must be accurately determined if the calculated sample intensity is to be valid. Since all the intensity measurements were subject to statistical fluctuation, there was a corresponding possibility for error in $I_s$. The parameter in the scale factor which showed the largest uncertainty was the reference ratio, $R_{ref}$. The numerical value of this ratio may be shown to depend on

the number of irradiated argon atoms and on the absorption within the argon sample; both of which are related to the bulk sample density, $\overline{\rho}_b$. The measured values of $R_{ref}$ appeared to be linear with $\overline{\rho}_b$ and consequently a least squares line fitted to the data was used to determine the appropriate values for use in the scale factor $\Omega_{c+s}$. The measured values of $R_{ref}$ had an over all deviation from the least squares fit of about 0.2% and the maximum deviation of any one point was 2%.

To determine the effect of an incorrect value of $R_{ref}$ on the calculated sample intensity, a test case was computed for Run 40 ($t = -125^{\circ}C$, $\overline{\rho}_b = 0.982$ gm/cc). The results showed that a 1% error in $R_{ref}$ gave a linear error of 3% in the calculated $I_s$, i.e., the value of $I_s$ at $\Theta = 60^{\circ}$ varied by 3% when $R_{ref}$ was varied by 1%. Thus the previously mentioned linear error in the calculated intensity of the confined sample may be partially due to the use of an incorrect scale factor. However, the estimated error in the scale factor was not large enough to account for the total observed linear error.

## C. Absorption Factors

The process of subtracting the empty cell scattering from the cell-plus-sample intensity is intimately connected with the absorption of x rays in the cell and sample material. This problem has been discussed by Paalman and Pings[19] for the case of an annular sample

cell and cylindrical sample fully exposed to the incident x-ray beam. Kendig and Pings[24] have extended this analysis to the more general case of a partially irradiated cell and sample.

Both of these treatments utilize the symmetry of the cylindrical geometry to divide the sample and the cell into a number of annular rings. These rings are then subdivided to yield a set of approximately orthogonal volume elements. The irradiated volume, which is defined by the upper and lower edges of an incident beam of uniform intensity, is determined and absorption factors are computed for each element within the irradiated volume. These individual factors, which are based on path lengths measured from the center of the element, are then weighted with respect to the total irradiated volume to obtain the total absorption factors. Using the empty sample cell as an example, the experimentally observed intensity may be expressed as

$$I_c^E = I^o P\left[(1/V_c)\sum_j e^{-\mu(\ell_c)_j}\,\Delta(v_c)_j\right](N_c I_c) \qquad (7)$$

$$= I^o P A_{c,c}(N_c I_c)\,.$$

In this equation $V_c$ is the total irradiated volume of the cell, $N_c$ is the number of irradiated atoms, and $I_c$ is the intrinsic scattering power per atom of the cell material. The sum is taken over all volume elements, j, contained in the irradiated portion of the cell. The

linear absorption coefficient of the cell material is $\mu$ and $(\ell_c)_j$ is the total path length of incident and scattered rays through the cell for the volume element j. The quantity within the brackets of Eq. (7) is the empty cell absorption factor, $A_{c,c}$, for an incident beam of uniform intensity.

Since the present experiment utilizes the concept of a partially irradiated sample, the above method was employed to obtain the absorption factors. A computer program for the IBM 7094 written by A. P. Kendig was used to perform the computations.

A direct application of the treatment presented by Kendig and Pings could not be made because of two problems associated with the scattering geometry (see Figure 3). First, the computer program could not take into account the nonconcentricity of the sample cell and second, the intensity distribution of the incident beam was not uniform but was trapezoidal in shape. To correct for the nonuniform wall thickness, an effective outside diameter, concentric with the cell interior, was used. As shown by Eq. (7), the absorption factors are weighted or normalized with respect to the total irradiated volume. On this basis, an effective o. d. was determined which gave the same irradiated cell volume as the actual diameter. For the geometry previously described, the actual cell o. d. was 0.100 inches and the effective o. d. was determined as 0. 095 inches. As seen from Figure 3, the effective o. d. will give absorption factors which are slightly high because of the additional computed absorption occurring at the

top of the cell. An estimation of the magnitude of this effect showed it to be negligible due to the low linear absorption coefficient of beryllium. Additional evidence for this method of correcting the nonconcentricity is given by the results of the $SiO_2$ calibration experiment. Figure 6 shows the $SiO_2$ scattering geometries and the effective diameters employed in computing the absorption factors. For these cases, the nonconcentricity was even more pronounced than in the argon experiment.

Although the computer program had been written for the specific case of an incident beam with a uniform intensity distribution, it was readily adapted to provide absorption factors for the trapezoidal beam shape used in this experiment. An incident beam of arbitrary shape may be approximated to any desired degree of accuracy by decomposing the beam into several segments with each segment having a uniform intensity. The beam subdivision may be made to give either vertical or horizontal strips of different intensities as shown below.

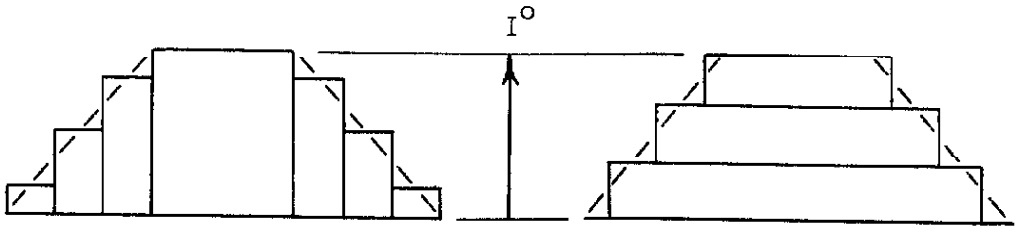


Vertical Subdivision Horizontal Subdivision

Absorption factors are computed for each strip and these individual factors are then appropriately weighted to give a composite beam absorption factor. For the present experiment, horizontal subdivision was used because the total beam width was relatively narrow. The incident beam was divided into five strips with each strip having the same relative intensity. This composite beam approximation is shown in Figure 6.

Again using the empty cell as an example, designate the absorption factor for strip k as $(A_{c,c})_k$. The relative intensity of beam k will be $\Delta I_k^o$ where $I^o = \sum_k \Delta I_k^o$ is the maximum intensity of the incident beam. The total experimentally observed intensity from all the beams is then obtained by summing Eq. (7) over k.

$$I_c^E = \sum_k (I_c^E)_k = \sum_k \Delta I_k^o \, (A_{c,c})_k \, (N_c)_k \, I_c \, . \tag{8}$$

This equation may be rearranged to give

$$I_c^E = I^o \left[ \sum_k \left( \frac{\Delta I_k^o}{I^o} \right) \frac{(N_c)_k}{(N_c)_t} \, (A_{c,c})_k \right] (N_c)_t \, I_c \, , \tag{9}$$

where $(N_c)_t$ is the total number of irradiated atoms. The quantity in the brackets of Eq. (9) is the empty cell composite beam absorption factor, ACC. With the assumption that the cell is homogeneous, the ratio $(N_c)_k/(N_c)_t$ is equal to the ratio of the respective irradiated

volumes. A similar analysis gives the absorption factors for the cell-plus-sample experiment. The resulting equations for the composite beam absorption factors used in Eq. (3) are given below:

$$ASSC(\Theta) = \sum_k \left(\frac{\Delta I_k^o}{I^o}\right) \frac{(V_s)_k}{(V_s)_t} \left[A_{s,sc}(\Theta)\right]_k ,$$

$$ACSC(\Theta) = \sum_k \left(\frac{\Delta I_k^o}{I^o}\right) \frac{(V_c)_k}{(V_c)_t} \left[A_{c,sc}(\Theta)\right]_k , \qquad (10)$$

$$ACC(\Theta) = \sum_k \left(\frac{\Delta I_k^o}{I^o}\right) \frac{(V_c)_k}{(V_c)_t} \left[A_{c,c}(\Theta)\right]_k .$$

Numerical values of the absorption factors were computed in increments of $\Delta\Theta = 2.5^\circ$ over the angular range $0^\circ \leq \Theta \leq 60^\circ$. The sample volume was divided into 15 annular rings. This division gave about 175 volume elements for the total irradiated portion of the sample and 260 elements for the cell. An interpolation program based on Aitkens method[25] was then used to secure the intermediate values. The values of the mass absorption coefficients used in the computations were 12.2 $cm^2/gm$ for argon[21] and 0.3 $cm^2/gm$ for beryllium[26]; the density of beryllium was taken as 1.82 gm/cc.

The composite beam absorption factors for the five argon densities used in this experiment are listed in Table 4. The values of $ASSC(\Theta)$ have been combined with the incoherent scattering correction factor, $F(\Theta)$, to provide coefficients compatible with the form of Eq. (3). These incoherent scattering corrections will be discussed in the following section.

## D. Incoherent Scattering Corrections

When experiments of the type used in this investigation are carried out at large values of S, the amount of incoherent scattering becomes appreciable both from the sample and the sample cell. Since the wavelength of incoherent scattering is angle dependent, corrections must be made for its effect on the absorption factors and for any variation in the amount of incoherent intensity which is transmitted through the pulse-height selector (PHS). The angular dependence of the incoherent wavelength is given by[27]

$$\Delta\lambda = \lambda^{inc} - \lambda^{coh} = 0.0243\,(1 - \cos 2\Theta)\,. \qquad (11)$$

Incoherently scattered radiation, because of its higher wavelength, is more strongly absorbed than coherently scattered radiation. The variation in the linear absorption coefficient may be approximated by the equation[28]

$$\mu^{inc} = \mu^{coh}\left[1 + \frac{\Delta\lambda}{\lambda^{coh}}\right]^{n} . \qquad (12)$$

The exponent n varies with the atomic number of the scatterer and the wavelength of the radiation but usually has a value between 2 and 3. Eq. (12) shows that this effect is more pronounced the lower the wavelength of the incident radiation. For example, at a scattering angle of $\Theta = 75^{o}$ for a material having $n = 3$, the ratio $\mu^{inc}/\mu^{coh}$ is 1.09 for copper radiation, 1.20 for molybdenum, and 1.26 for silver. Consequently, if the absorption correction for a material having an appreciable amount of incoherent scattering is computed on the basis of only coherently scattered radiation, the resulting calculated intensity will be too low. More important, this error in the calculated intensity will be angular dependent.

When a scintillation-type detector and PHS are used to measure the intensity of scattered radiation from a specimen having a significant amount of incoherent scattering, an additional angular dependent error may result. A beam of x rays incident upon the detector gives rise to voltage pulses which are amplified and counted. These voltage pulses have a pulse amplitude distribution (PAD) about an average voltage, $\overline{v}$, proportional to the energy of the incident radiation. The usual experimental procedure is to set a PHS window at $v = \overline{v} \pm \Delta v$, and count only those voltage pulses falling within the selected window. This constant voltage window defines a transmission factor, $t_{PHS}$

(defined in Appendix 2), giving that portion of the total intensity incident upon the detector which is transmitted through the PHS and into the counting circuit. The magnitude of $t_{PHS}$ is arbitrary, but in order to compare intensities at different scattering angles, it is essential that $t_{PHS}$ be the same for all values of $\Theta$. For coherently scattered radiation, $t_{PHS}^{coh}$ is constant. However, since $\lambda^{inc}$ is a function of the scattering angle, the incoherent PAD shifts, consequently; $t_{PHS}^{inc}$ is not constant. In effect, as the scanning angle increases, the incoherent PAD gradually moves through the constant PHS window with the result that the integrated area under the PAD between $v = \bar{v} \pm \Delta v$ is not constant. The magnitude of the variation in $t_{PHS}^{inc}$ depends on the size of the PHS window.

The effect of the incoherent scattering on the observed intensity for general experiments of the type described here may be evaluated in the following manner. For simplicity, the scattering from the empty sample cell will be considered, although the same analysis may be applied to the cell-plus-sample experiment. The total scattering in absolute units being emitted from the irradiated cell consists of two parts; the coherent scattering, $I_c^{coh}(\Theta)$, and the incoherent scattering, $I_c^{inc}(\Theta)$. Each mode of scattering has its own absorption factor, $ACC^{coh}(\Theta)$ and $ACC^{inc}(\Theta)$, respectively. If $(C/N)_c$ is a normalization constant that converts the absolute intensity from the empty cell to the experimental units of counts/sec, the total experimentally measured intensity will be

$$I_c^E(\Theta) = P(\Theta)\left[ t_{PHS}^{coh}(\Theta)\, ACC^{coh}(\Theta)\, (C/N)_c\, I_c^{coh}(\Theta) \right.$$

$$\left. + \; t_{PHS}^{inc}(\Theta)\, ACC^{inc}(\Theta)\, (C/N)_c\, I_c^{inc}(\Theta) \right]. \qquad (13)$$

This equation may be simplified by defining the following terms:

$$\psi_{PHS}^{inc}(\Theta) \equiv \frac{t_{PHS}^{inc}(\Theta)}{t_{PHS}^{coh}} \quad , \qquad (14)$$

$$\alpha_{c,c}^{inc}(\Theta) \equiv \frac{ACC^{inc}(\Theta)}{ACC^{coh}(\Theta)} \quad , \qquad (15)$$

$$\gamma_c(\Theta) \equiv \frac{I_c^{coh}(\Theta)}{I_c^{coh}(\Theta) + I_c^{inc}(\Theta)} \quad . \qquad (16)$$

The quantity $\psi_{PHS}^{inc}(0)$ is a relative PHS transmission factor for incoherent radiation and $\alpha_{c,c}^{inc}(\Theta)$ is a relative incoherent absorption factor. When Eqs. (14), (15), and (16) are substituted into Eq. (13) and $t_{PHS}^{coh}$ is combined with the normalization constant, $(C/N)_c$, the result is

$$I_c^E(\Theta) = P(\Theta) F_{c,c}(\Theta)\, ACC^{coh}(\Theta)[\, t_{PHS}^{coh}(C/N)_c\,][\, I_c^{coh}(\Theta) + I_c^{inc}(\Theta)\,] \, , \qquad (17)$$

where $F_{c,c}(\Theta)$ is the incoherent scattering correction factor for the empty cell intensity and is given by the equation

$$F_{c,c}(\Theta) = \gamma_c(\Theta) + [1 - \gamma_c(\Theta)]\, \psi^{inc}_{PHS}(\Theta)\, \alpha^{inc}_{c,c}(\Theta)\,. \qquad (18)$$

A similar analysis of the cell-plus-sample experiment shows that there is an incoherent scattering correction associated with each of the coherent absorption factors. These other two correction factors are

$$F_{c,sc}(\Theta) = \gamma_c(\Theta) + [1 - \gamma_c(\Theta)]\, \psi^{inc}_{PHS}(\Theta)\, \alpha^{inc}_{c,cs}(\Theta)\,, \qquad (19)$$

$$F_{s,sc}(\Theta) = \gamma_s(\Theta) + [1 - \gamma_s(\Theta)]\, \psi^{inc}_{PHS}(\Theta)\, \alpha^{inc}_{s,sc}(\Theta)\,, \qquad (20)$$

To simplify the final expression, let $F(\Theta) = F_{s,sc}(\Theta)$ and $G(\Theta) = F_{c,sc}(\Theta)/F_{c,c}(\Theta)$. The equation for the scattered intensity of the confined sample, in experimental units, is then given by

$$I_s(\Theta) = \frac{1/P(\Theta)}{F(\Theta)\,ASSC(\Theta)} \left[ I^E_{c+s}(\Theta) - G(\Theta)\, \frac{ACSC(\Theta)}{ACC(\Theta)}\, I^E_c(\Theta) \right], \qquad (21)$$

where $I_s(\Theta)$ is the sum of the coherent and incoherent scattered intensities. The absorption factors appearing here are those for coherently scattered radiation. Except for the presence of $G(\Theta)$, Eq. (21) is identical with Eq. (3).

The incoherent scattering corrections, as given by Eqs. (18), (19), and (20), may be extended to include effects other than those mentioned here. For example, if the filter used to reduce the intensity of the 3 peak of the spectrum were placed on the receiving slit rather than on the divergence slit, an additional term would be required to account for the variation in the absorption of $I^{inc}$ in the $\beta$ filter. For a $\beta$ filter having a thickness $\ell_f$ and a linear absorption coefficient $\mu_f$, this filter correction term would have the form $\exp[-(\mu_f^{inc} - \mu_f^{coh})\ell_f]$ where $\mu_f^{inc}$ is a function of $\Theta$.

The incoherent scattering correction factors derived in this section were expressed as functions related to the coherent absorption factors. This was done because the computer program described in the preceding section produced numerical values of absorption factors only for coherently scattered radiation. There were no means readily available for computing exact values of the incoherent absorption factors appearing in $F(\Theta)$ and $G(\Theta)$. Consequently these values had to be estimated. A detailed description of the method used in estimating the incoherent absorption factors is presented in Appendix 1. The equations used to calculate the variation in the incoherent PHS transmission factor, $\psi_{PHS}^{inc}(\Theta)$, are derived in Appendix 2.

In Eq. (21), $F(\Theta)$ represents the correction due to incoherent scattering from the sample and $G(\Theta) = F_{c,sc}(\Theta)/F_{c,c}(\Theta)$ is the corresponding correction for the sample cell. As seen from Eqs. (18)

and (19), $F_{c,sc}(\Theta)$ and $F_{c,c}(\Theta)$ are identical except for the incoherent absorption factors, $\alpha^{inc}(\Theta)$. For the test case described in Appendix I (which was typical of all the argon experiments) the maximum variation in $\alpha^{inc}_{s,sc}(\Theta)/\alpha^{inc}_{c,c}(\Theta)$ was less than 0.1%. Therefore, the correction for the incoherent scattering of the sample cell was negligible, i.e., $G(\Theta)$ was assumed to be unity for all the argon experiments, thus reducing Eq. (21) to Eq. (3).

The evaluation of the correction factor $F(\Theta)$ presupposes a knowledge of the sample scattering, $I_s(\Theta)$, because of the term $\gamma_s(\Theta)$ [see Eq. (16)]. Since $I_s^{coh}(\Theta)$ is actually unknown, Eq. (3) [or Eq. (21)] requires either an iterative type solution or the function $\gamma_s(\Theta)$ must be estimated. Since the coherently scattered radiation approaches the independent coherent scattering of the atom at large values of S, the assumption was made that the fraction of coherently scattered radiation could be approximated by the equation

$$\gamma_s(\Theta) \approx \frac{f_s^2(\Theta)}{f_s^2(\Theta) + I_s^{inc}(\Theta)} \quad . \tag{22}$$

In the high angle region ($\Theta > 20^o$) where the incoherent scattering correction is greatest, this assumption is valid (see Figure 12). The error introduced by this approximation at the low scattering angles is insignificant, since the effect of the incoherent scattering is almost negligible in this region.

Numerical values of the various terms appearing in the incoherent scattering correction factor, $F(\Theta)$, are listed in Table 5 for the five argon densities of this experiment. As expected, the maximum effect occurred at the highest scattering angles and became larger with increasing argon density.

At this point, special emphasis should be placed on the fact that, while for this experiment the incoherent scattering corrections were relatively small, these correction factors are strongly dependent upon the scattering geometry and in general cannot be neglected. The scattering geometry employed in this investigation represents, in many ways, an optimum for this type of experiment. The nature of this optimum is illustrated by examining the underlying reasons for neglecting the term $G(\Theta)$ in Eq. (21). At the higher values of S, the scattering from the beryllium cell is predominantly incoherent ($\gamma_c \approx 0.05$ at $S = 15\ \text{Å}^{-1}$; $\Theta = 60^\circ$). In view of Eqs. (11) and (12), a significant increase in the absorption of the scattered rays would be expected. For the case of a beryllium sample cell, $\mu_c^{coh}$ is low and the resulting variation in $(\mu_c^{inc} - \mu_c^{coh})$ is relatively small. Consequently, $\alpha_{c,c}^{inc}(O)$ does not differ appreciably from unity. However, this is not necessarily true for $\alpha_{c,sc}^{inc}(O)$. If the confined sample has a high density and the scattering geometry is such that a large portion of the cell scattering passes through the sample, $\alpha_{c,sc}^{inc}(\Theta)$ will differ greatly from unity. This effect can be minimized by using a scattering geometry such as that shown in Figure 3. For

this geometry, the amount of cell scattering which passes through the relatively dense sample medium is negligible except for the very high and the very low scattering angles. The low angle effect ($\Theta < 15^{\circ}$) is small because the relative amount of incoherent scattering is low and its wavelength does not differ greatly from that of coherently scattered radiation. The high angle effect can be avoided by ending the diffraction scans at $\Theta = 60^{\circ}$ to $75^{\circ}$. The effect of the incoherent scattering from the confined sample cannot be avoided, but again, the scattering geometry employed here minimizes the numerical value of the required correction factor.

## E. Data Smoothing

The intensity of scattered x rays from the confined argon sample was calculated from Eq. (3)*. Because of the statistical nature of the experimental intensity measurements, the computed values of $I_s$ showed a considerable amount of scatter. This scatter is evident in Figure 10 where the data for a typical experiment are plotted (Run 40, $t = -125^{\circ}C$, $\overline{\rho}_b = 0.982$ gm/cc). In addition to the statistical spread of the data, several points deviate markedly from the general behavior of the intensity curve. These data points, which were obviously in error, correspond to intensity measurements on the

* These calculations, as well as the smoothing calculations to be described, were performed on an IBM 7094 computer using a program written by R. H. Bigelow.

strong beryllium diffraction peaks. While these anomalous points could be immediately discarded, the statistical scatter in the remaining data was large enough to require smoothing before the intensity pattern could be subjected to Fourier analysis. In view of the statistical nature of the computed $I_s(\Theta)$ values, the smoothing process was designed to obtain the best statistical estimate of a smooth scattering curve.

The sample intensity data were smoothed by fitting a second-order polynomial in $\Theta$ to short segments of the scattering curve. This polynomial may be represented by the equation

$$\left[ I_s^{smh}(\Theta_i) \right]_r = (a_i)_r + (b_i)_r \Theta_i + (c_i)_r \Theta_i^2 . \qquad (23)$$

The coefficients $a_i$, $b_i$, and $c_i$ were evaluated by a least squares method over an angular smoothing range designated by the subscript r. As indicated by the subscript i in the above equation, a separate set of coefficients is applicable to each value of the scattering angle and the value of $I_s^{smh}$ corresponding to any given value of $\Theta_i$ depends on the smoothing range selected. This angular smoothing range is given by the expression

$$(\Theta_i - r\Delta\Theta) \leq \Theta \leq (\Theta_i + r\Delta\Theta)$$

where r is an integer and $\Delta\Theta$ is the angular spacing of the data points; for this experiment, the spacing was $\Delta\Theta = 0.25$ degrees.

Thus for each scattering angle, $\Theta_i$, the set of parameters $a_i$, $b_i$, and $c_i$ were determined by using $2r + 1$ values of the sample intensity, $I_s(\Theta)$.

Several smoothing ranges were used to determine the complete scattering curve for each argon run. These ranges were selected to include features that could be adequately represented by a second-order polynomial. In general, as the scattering angle increased and the intensity features became less prominent, a larger value of r was used. For the higher density argon samples, such as shown in Figure 10, the following smoothing ranges were found to be satisfactory.

| Approximate Angular Region | Smoothing Range |
|---|---|
| $1^\circ < \Theta < 7^\circ$ | $r = 0, \quad \Theta_i$ |
| $7^\circ < \Theta < 14^\circ$ | $r = 4, \quad \Theta_i \pm 1.0^\circ$ |
| $14^\circ < \Theta < 20^\circ$ | $r = 10, \quad \Theta_i \pm 2.5^\circ$ |
| $20^\circ < \Theta < 27^\circ$ | $r = 18, \quad \Theta_i \pm 4.5^\circ$ |
| $27^\circ < \Theta < 35^\circ$ | $r = 30, \quad \Theta_i \pm 7.5^\circ$ |
| $35^\circ < \Theta < 60^\circ$ | $r = 50, \quad \Theta_i \pm 12.5^\circ$ |

The transition between the various smoothing ranges was made by superimposing the smooth intensity curves resulting from each value of r. This superposition was made with the intensity function

$I_s^{smh}/(f^2 + I^{inc})$ rather than $I_s^{smh}$ since the former offered a more sensitive comparison of the intensity features; compare, for example, Figures 12 and 14. The junction points were then selected such that there were no discontinuities in the final $I_s^{smh}(\Theta)$ or its derivative.

Two separate smoothing computations were made for each argon run. The purpose of the first smoothing was to obtain a preliminary estimate of the scattering curve. This preliminary estimate of $I_s^{smh}(\Theta)$ was then used to statistically analyze the individual data points. In the preliminary smoothing, the obviously bad data points corresponding to measurements on the strong beryllium peaks were discarded. These points, 10-15 in number, were replaced by the estimated values obtained from a smooth curve drawn through the remaining data. The smoothing computations were then performed as described above.

To obtain the final estimate of the smooth scattering curve, a statistical analysis was made by computing a confidence interval about the preliminary estimate of $I_s^{smh}(\Theta)$ from the equation*

$$(\Delta I_s)_j = \frac{\pm k_j [1/P(\Theta)]}{F(\Theta)\,ASSC\,\sqrt{\tau_{c+s}}} \left[ I^E_{c+s} + \left(\frac{ACSC}{ACC}\right)^2 \left(\frac{\tau_{c+s}}{\tau_c}\right) I^E_c \right]^{\frac{1}{2}}. \tag{24}$$

* The derivation of this equation is presented in Appendix 3.

In the above expression, $k_j$ is a constant and the subscript j refers to the significance level of the computation. Eq. (24) may be interpreted in the following manner. For a sufficiently large number of observations of the statistical quantities $I^E_{c+s}$ and $I^E_c$ at any value of $\Theta$, j% of the computed values of $I_s$ will be in an interval $\pm \Delta I_s$ about the mean.

In any experiment, the true mean of $I_s(\Theta)$ is unknown because only a small number of measurements are generally made. In the present case, the best available estimate of the mean sample intensity was $[I_s^{smh}(\Theta)]_{prelim}$, since this curve was determined from a relatively large number of experimental observations. On this basis, the assumption was made that a confidence interval around $[I_s^{smh}(\Theta)]_{prelim}$ represented the relative probability of a deviation from the true mean sample intensity for any individual data point.

In this statistical analysis, a 90% confidence interval was used with the corresponding value of $k_j$ being 1.645. The counting intervals in Eq. (24) were $\tau_c$ = 1600 seconds (from eight 200-second scans) and $\tau_{c+s}$ = 300 seconds (from three 100-second scans). The confidence interval was computed with the background intensities, i.e., the intensity measurements on strong beryllium diffraction peaks were not used (see Figure 5). The width of $\Delta I_s$ differed for each argon run, but for any single run it was almost independent of $\Theta$. The average numerical values varied from about $\pm$ 2.2 counts/sec for

$\overline{\rho}_b$ = 0.982 gm/cc to about $\pm$ 1.4 counts/sec for $\overline{\rho}_b$ = 0.280 gm/cc. The preliminary estimate of the smooth intensity curve and a 90% confidence interval are plotted along with the experimental data points in Figure 10 for a typical argon run (Run 40, t = -125°C, $\overline{\rho}_b$ = 0.982 gm/cc).

The statistical analysis of the data was based on the assumption that any data points falling outside the 90% confidence interval had a very low probability of actually representing the true scattering curve and could therefore be rejected. This rejection was made because the inclusion of widely scattered points in the least squares smoothing computation unduly influenced the position of the resultant curve. As previously described, each data point was actually an average of three separate measurements. Therefore the points outside the interval were first examined to see if this deviation was caused by one of the individual values differing significantly from the other two. Large variations among the individual measurements could arise from either a gross statistical effect or a periodic malfunction in the x-ray counting equipment. Where these deviations were observed, the erroneous data point was rejected and a new average was computed from the remaining two. Following this preliminary adjustment of the data, all remaining points outside the confidence interval were discarded and replaced with corresponding values obtained from the preliminary smooth curve. With this complement of data points, the smoothing computations were repeated to obtain the final estimate of the smooth sample scattering curve.

The use of a 90% confidence interval implies that, on a statistical basis alone, about 10% of the total number of data points should fall outside the interval. The number actually observed was somewhat higher, being about 15-18%. Included in this observed number, however, were about 10 points (from a total of 237) corresponding to strong beryllium diffraction peaks. If these were discounted from the statistical analysis, the number of rejected points varied from 11% to 14%, which was reasonably close to the expected number.

## F. Normalization

The final estimates of the smooth scattering curves for the argon samples were in the arbitrary intensity units of counts/second. In order to obtain the radial distribution function by Fourier analysis, the atomic and incoherent scattering had to be subtracted from the measured intensity as shown by Eq. (2). Since this subtraction requires that all terms have the same units, the experimental scattering curves were normalized to obtain intensities expressed in the conventional electron units. The normalization was accomplished by multiplying the experimental intensities by a constant, (C/N).

If $I_s(S)$ denotes the S dependence of the experimental sample intensity, the kernel of the Fourier integral may be written [see Eq. (2)]

$$i(S) = \frac{(C/N)\, I_s(S) - I^{inc}(S) - f^2(S)}{f^2(S)} \qquad (25)$$

where $(C/N)\, I_s(S) - I^{inc}(S)$ represents the coherently scattered intensity. The normalization constant, $(C/N)$, in this equation can be determined by two methods. The first is a visual or graphical method, and is based on the fundamental assumption that the experimentally observed intensity converges to the total independent scattering at large values of the scattering angle. This procedure is best accomplished by plotting the intensity function $I_s/(f^2 + I^{inc})$ against $\Theta$ and observing its behavior at large scattering angles. This function should oscillate with diminishing amplitude about a horizontal line of magnitude $1/(C/N)$.

Where experimental data are not available at sufficiently large values of $\Theta$, or where the intensity measurements in this region are doubtful, an alternate procedure is useful. This method, developed by Krogh-Moe[29] and Norman[30], utilizes the complete intensity pattern instead of being limited to the intensity measurements at high angles as in the first method. The normalization constant is obtained by substituting Eq. (25) into Eq. (2) and taking the limit as the radial distance, r, approaches zero. The resultant expression is[1, 4]

$$(C/N) = \frac{\int_0^{S_m} S^2[f^2(S) + I^{inc}(S)]\,ds - 2\pi^2 Z \bar{\rho}_e}{\int_0^{S_m} S^2 I_s(S)\,dS}, \qquad (26)$$

where $Z$ is the atomic number and $\bar{\rho}_e$ is the average electron density of the sample. The numerical value of the normalization constant obtained from Eq. (26) will depend to some extent on the upper limit used in the integrals. However, on the basis of the previously mentioned assumption that $I_s(S)$ approaches the sum of $[f^2(S) + I^{inc}(S)]$ at large values of $S$, $(C/N)$ will converge to a constant value with increasing values of $S_m$. If the experimental intensity data are internally consistent, both methods should give the same normalization factor.

When these normalization methods were applied to the experimental argon data, the resultant values of $(C/N)$ were not constant, but were found to vary with the scattering angle. For both methods, $(C/N)$ increased with increasing $\Theta$ and moreover, at any given value of $\Theta$, the normalization constants from the two methods did not agree. This lack of internal consistency in the calculated intensity of the confined argon sample was alluded to in the discussion of the $SiO_2$ calibration experiment presented in Section III. The general behavior of the computed normalization constants indicated that the argon

intensities were too low at the higher scattering angles. This error in $I_s$, shown to be linear with $\Theta$ in Section III, was presumed to be primarily caused by a distortion effect due to the presence of scattering from the sample cell.

A plausible explanation for this distortion effect can be obtained by examining the nature of x-ray scattering and absorption in the sample cell. Eq. (13), used to calculate $I_s(\Theta)$, is based on a mathematical formality which allows the experimentally observed intensity to be written as a product of an average geometrical absorption correction and an intrinsic scattering power[19]. This formal representation is based on the physical assumption that the irradiated media are homogeneous and isotropic. For a confined fluid sample at equilibrium, this is a very reasonable assumption. However, for the case of a sample cell constructed from a crystalline powder (as in the present experiment), this assumption may not be valid.

Wilchinsky[31] has conducted a theoretical and experimental investigation on the diffraction of x rays from a crystalline powder in which the scattering power was modified by the powder coarseness and absorption unhomogeneities in the powder sample. An "ideal powder" was defined as having a crystal grain and particle size sufficiently small so that primary extinction effects were negligible. This "ideal powder" sample was also homogeneous with respect to applying the simple law of absorption of x rays. In this study, Wilchinsky related the intrinsic scattering power to the particle

diameter, the linear absorption coefficient, the degree of compaction of the powder, the crystal grain size, and the primary extinction coefficient. He showed, theoretically and experimentally, that these variables can cause the intrinsic scattering power of real powders to be significantly different from that of an "ideal powder."

Since the present experiment was conducted with a sample cell constructed from a sintered beryllium powder, the above mentioned effects could very well account for the observed error in the computed sample intensities. This is borne out by the results of a sample calculation presented in Appendix 4, and the $SiO_2$ calibration experiment discussed in Section III. The major defect in the analysis used to obtain the sample intensities lies in the assumption that the sample cell material is truly homogeneous, thereby allowing the absorption correction to be expressed as an over-all average geometric factor. However, due to practical considerations, this assumption was invoked since no means were available to ascertain the exact nature of these unhomogeneities. A correction factor was then applied to the data to account for the resulting errors.

The sample intensity data was corrected for the effect of cell unhomogeneities by multiplying $I_s(\Theta)$ by a linear modification function, $\phi(\Theta) = 1 + B\Theta$. The determination of the numerical values for this function was intimately related to the integral normalization process previously described. Assuming the validity of Eq. (26), the unknown function was obtained in terms of its S dependence by substituting

$\phi(S) I_s(S)$ for $I_s(S)$ into the denominator of this equation. The slope of the modification function was then determined as the value of B that resulted in a normalization constant, (C/N), independent of the upper integration limit. As a check on the internal consistency of the modified data, the resulting value of (C/N) from the integral method was compared to the value obtained by the visual method. In all cases, the agreement between the two was excellent.

The manner in which the function $\phi(\Theta)$ modified the smooth scattering curves for the argon samples is shown in Figure 11 for a typical run (Run 40, t = -125°C, $\overline{\rho}_b$ = 0.982 gm/cc). In this figure, the ratio of $\phi(\Theta) I_s(\Theta)$ to $[f^2(\Theta) + I^{inc}(\Theta)]$ is plotted against $\Theta$ for several values of the modification parameter, B. The unmodified scattering curve (B = 0) shows a definite downward slope indicating that the intensity at high angles is too low. In addition, the values of $(C/N)^{-1}$ obtained by the integral method (shown by the circles on the figure) do not agree with the graphical method and show a significant dependence on the upper integration limit. As the data are modified by increasing the value of B, the scattering curve becomes more horizontal and the agreement with the integral normalization constant improves. Finally, as the value of B is increased still further, the modification function begins to overcorrect the data. Thus the normalization integral of Eq. (26) serves to evaluate the modification function, $\phi(\Theta)$, as well as to establish the proper normalization constant, (C/N).

Numerical values of the integral normalization constant and the modification parameter, B, obtained by this method are given in Table 6 for all the argon runs of this experiment.

# V. DISCUSSION OF RESULTS

## A. Intensity Curves

Using the methods of data analysis described in the preceding section, x-ray scattering curves for argon were obtained at thirteen different thermodynamic states.* These states defined a temperature-density grid in the general region of the argon critical state. Included in this grid were the isotherms -130°C, -125°C, -120°C, and -110°C and isochores (in gm/cc) of 0.982, 0.910, 0.780, 0.536, and 0.280. The location of these states, along with the identifying run numbers, is shown on the argon compressibility diagram of Figure 1.

The conventional representation of the x-ray scattering curve is shown in Figure 12 for Run 40. In this figure the modified and normalized argon intensity, along with the total independent scattering of the argon atom, is plotted as a function of the scattering angle. As seen in a plot of this type, the general features of the intensity curve are not clearly shown in the high angular region. In order to distinctly illustrate the effects of temperature and density on the argon intensity curves, the data are presented in terms of the intensity function, j(S), defined in Eq. (4). The increased sensitivity in identifying the relative intensity features obtained by this representation is evident from a comparison of Figures 12 and 14.

---

* The experimental measurements for two of these states, Runs 22 and 23, were made by W. I. Honeywell (ref. 14).

The smooth argon intensity functions are plotted against the scattering parameter, S, in Figures 13 through 21. These plots are arranged to illustrate the effect of temperature and bulk density on the experimentally determined scattering curves. The density dependence of j(S) at constant temperature is shown in Figures 13 through 16 for the four previously mentioned isotherms. The effect of temperature is shown in Figures 17 through 21 for the five values of constant bulk density. In addition to the graphical presentation of the intensity data, the numerical values of j(S) used in the preparation of these plots are given in Table 7.

An error analysis of the smooth intensity curves was not attempted because of its complexity. However, the error in the smooth curves was believed to be somewhat lower than the corresponding error in a single intensity measurement, since the smoothing process involved the use of many individual data points. In addition to the statistical error, there was also some degree of uncertainty in the various correction terms applied to the data. The general nature of the experimental measurements indicated that the relative error in $I_s(\Theta)$ increased with the scattering angle and was greatest at the low density argon states.

A comparison of the accuracy among the various experimental runs can be made in terms of the probable relative error, $\epsilon_p$.

$$\epsilon_p = \frac{[\Delta I_s(\Theta)]_{50\%}}{I_s(\Theta)} \times 100 .$$

In this expression, the 50% confidence interval is computed from Eq. (24). For the high density argon runs, the value of $\epsilon_p$ was 1% at S = 4, 2% at S = 9, and 5% at S = 15. For the low density runs, the corresponding values were 2%, 4%, and 9%. In addition to the above mentioned sources of error, the presence of strong beryllium diffraction peaks also contributed to the over-all uncertainty in the final curves. The definition of the second maximum in j(S) was particularly troublesome in this respect. In general, however, this problem was minimized by the use of a fine angular grid in obtaining the experimental measurements. Under these conditions a sufficient number of "good" data points were available to suitably define the scattering curves.

The intensity functions shown in Figures 13 through 21 are plotted over the complete experimental range (to S = 15 $\text{Å}^{-1}$). The tails on these curves at high S values are extremely doubtful and are most likely due to experimental error. The maximum value of S for which the data are believed to be valid is marked with an arrowhead for each run. This value ranges from 9-10 $\text{Å}^{-1}$ for the high density runs to 7-8 $\text{Å}^{-1}$ for the low density runs. The region of uncertainty in the scattering functions is designated by the use of a dashed curve.

The general features of the argon intensity patterns are summarized in Table 8. The average locations of the observable maxima in $j(S)$ were found to be $S_1 = 1.89 \pm .01$ $\text{Å}^{-1}$, $S_2 = 3.56 \pm .06$ $\text{Å}^{-1}$, and $S_3 = 5.6 \pm .2$ $\text{Å}^{-1}$. The positions of these peaks showed no clear dependence on either the temperature or the bulk density of the argon sample. The most pronounced effect was a variation in the relative features of the main diffraction peak as shown in Figure 22. The height of the strong maximum in $j(S)$ was found to be approximately linear with the bulk density and was apparently independent of temperature. A least squares linear fit to the data points gave an intercept near unity. This condition would be expected as the bulk density approaches zero since the argon would then behave as a perfect gas and would show no external interference effects.

The temperature dependence of the intensity curves was less pronounced. The main effect seemed to be a slight broadening of the main diffraction peak as the temperature was increased. The characteristic width of the first maximum in $j(S)$, measured as $\Delta S$ in $\text{Å}^{-1}$ at $j(S) = 1$, is plotted against temperature in Figure 22. The numerical value of $\Delta S$ was found to be strongly dependent upon the normalization constant. The scatter of the data points in this plot reflects the uncertainty in the precise determination of (C/N).

The presence of low angle scattering was observed to some extent in all the experimental runs and was also reported in the earlier measurements of Eisenstein and Gingrich[9]. The general behavior of

this low angle scattering, including the position of the first minimum in j(S), is in good agreement with the experimental results of Thomas and Schmidt[32]. The observable features of the intensity pattern at these small angles, i. e., the first minimum in j(S) and the value of j(S) at the minimum angle of observation, were generally independent of temperature but showed a linear dependence on the bulk argon density.

The intensity curves in two regions of the argon liquid state are of special interest. The first of these, shown in Figure 14, is the change in the scattered intensity as the liquid-vapor coexistence curve is crossed along the $-125^{\circ}C$ isotherm. Run 31 of this figure corresponds very closely to the saturated liquid state and Run 32 to the saturated vapor state (see Figure 1). On crossing the phase boundary from the liquid side, there is a considerable decrease in the sharpness of the main intensity peak but a vestige of the second and third peaks still remains. There is also a significant increase in the amount of low angle scattering. The other region of interest is the argon critical state ($t_c = -122.29^{\circ}C$, $(\bar{\rho}_b)_c = 0.536$ gm/cc). Figure 15 shows the variation of the intensity function across the critical density, along the nearest experimental isotherm of $-120^{\circ}C$. Figure 20 shows the approach to the critical state along the critical isochore of 0.536 gm/cc. In both instances, there is no indication of an abrupt change or any discontinuities as the critical state is approached. This same observation was made by Eisenstein and Gingrich[9].

B. Atomic and Electronic Radial Densities

Information regarding the structure of the fluid argon samples was obtained by a Fourier inversion of the experimental x-ray scattering curves as discussed in Section I. This structural information may be presented either in terms of a radial density, $\rho(r)$, or a radial distribution function, $g(r)$. Although these functions are interrelated, the former tends to impart a better physical picture of the fluid structure, while the latter is more useful in a theoretical discussion of the liquid state.

The problems associated with a direct application of the Fourier analysis have been mentioned previously. The most obvious one is the lack of a complete knowledge of the intensity pattern, i.e., $I_s(S)$ over the range $0 \leq S \leq \infty$. In addition, the interpretation of the Fourier transform is hindered by the general presence of ripples caused by such factors as the inherent uncertainty in the normalization constant and possible errors in the experimental intensities. The effect of these experimental limitations on the resulting structural information has been discussed by many authors[1-8] and will not be presented here.

The radial atomic density, $\rho_a(r)$, is obtained from the experimental intensity data by writing Eq. (2) in the following form.

$$4\pi r^2[\rho_a(r) - \bar{\rho}_a] = \frac{2r}{\pi} \int_{S_1}^{S_2} S\, i(S) \sin(Sr)\, dS . \qquad (27)$$

In this expression the zero and infinite limits of Eq. (2) have been replaced by $S_1$ and $S_2$, corresponding to the minimum and maximum angular range over which the measured intensity data are believed to be valid. In terms of experimentally determined quantities, the intensity kernel of this integral is given by

$$i(S) = \frac{(C/N)\,\phi(S)\,I_s(S) - I^{inc}(S) - f_d^2(S)}{f_d^2(S)} \,. \qquad (28)$$

Eq. (27) is written in terms of the deviation of $\rho_a(r)$ from the average atomic density of the system. This type of representation is more useful in observing the effects of temperature and bulk argon density than the conventional displays of $4\pi r^2 \rho_a(r)$. In addition, any spurious peaks or ripples caused by experimental errors are clearly shown.

Although independently derived, an equation for the radial electronic density, $\rho_e(r)$, may be written in a similar form[1].

$$4\pi r^2[\,\rho_e(r) - \overline{\rho}_e - \rho_o(r)\,] = \frac{2r}{Z\pi} \int_{S_1}^{S_2} S\, i(S)\, f_d^2(S) \sin(Sr)\, dS \,. \qquad (29)$$

In this equation, $Z$ is the atomic number of the sample, $\overline{\rho}_e$ is the average electronic density of the system, and $\rho_o(r)$ is the radial electron density within the isolated reference atom. While the

electronic density does not yield any additional information concerning the fluid structure, it was proposed by Finbak[8] as a means of increasing the reliability of the Fourier transform. This is accomplished by including the term $f_d^2(S)$ within the integral and thus decreasing the relative importance of the intensity in the high S region where it is subject to the greatest errors. The general effect of this "damping factor" is to minimize the presence of ghost peaks and ripples superimposed on the density curves, while at the same time, decreasing the resolving power of the Fourier integral. The electron density may be viewed as a compromise which seeks to increase the detail in the transform by utilizing the data at large S, but to decrease the relative importance of this data in order to avoid creating false details. While the primary interest lies in the radial atomic densities, values of $\rho_e(r)$ were computed to provide a means for checking the consistency and reliability of the resulting data.

Because of physical limitations imposed by the nature of this experiment, three parameters of the Fourier integral in Eq. (27) are subject to uncertainty. These parameters are the integration limits, $S_1$ and $S_2$, and the normalization constant, (C/N), appearing in Eq. (28). Because of the presence of the primary x-ray beam, intensity measurements cannot be made in the immediate neighborhood of zero scattering angle. This problem is usually avoided by smoothly extrapolating the intensity to zero at $S = 0$ (ref. 33). However, in

the present experiment, there was a considerable amount of low angle scattering and this procedure was not realistic. Although Finbak[8] suggests an extrapolation to $j(S) = 1$ at $S = 0$, the experimental data indicated that $j(S)$ near $S = 0$ may be considerably greater than unity especially for the low density states. Since there was no readily apparent criteria for making an extrapolation to $S = 0$, the lower integration limit was taken as the minimum angle of observation; $\Theta = 1$ degree or $S_1 = 0.30$ $\text{Å}^{-1}$. The omission of this nonobservable low angle region was justified on the basis that the contribution of the intensity kernel, $S\,i(S)$, becomes quite small as $S$ approaches zero.

The maximum value of $S$ at which intensity measurements were taken was about 15 $\text{Å}^{-1}$. However, since the data in the high angular region were subject to large errors, this value for $S_2$ was not appropriate for use in Eq. (27). The usual procedure for obtaining the upper integration limit is to terminate the data at a value of $S$ beyond which no further oscillations in the intensity function, $j(S)$, are observed. However, this method presupposes a precise knowledge of the intensity curve in the sense that all the observed oscillations are taken to be real and the intensity measurements beyond the truncation limit are assumed to be unimportant. To avoid this rather arbitrary selection of the truncation limit, a more systematic, although somewhat pragmatic, method was used.

Rodriguez[34] has shown that the least biased estimate of the normalization constant is that value of (C/N) which makes j(S) equal to unity (or the intensity kernel i(S) = 0) at the truncation limit, i. e.,

$$(C/N) = \frac{f_d^2(S_2) + I^{inc}(S_2)}{\phi(S_2)\, I_s(S_2)} \qquad (30)$$

Since the numerical value of (C/N) was to some degree uncertain, this criteria provided a means of systematically varying the quantities $S_2$ and (C/N) to obtain the best estimate of the radial density function. While the previous method of evaluating the normalization constant described in Section IV-F provided a systematic means for comparing the intensity functions, these values of (C/N) were not necessarily the optimum for use in the Fourier integral. However, the numerical values of (C/N) which gave the best results in the Fourier transform were found to differ from the previous values by an average of less than 1% (see Tables 6 and 9).

For each argon run, about twenty separate Fourier inversions were made with a different combination of $S_2$ and (C/N) for each calculation.* The values of $S_2$ were varied from the maximum of 15 $\text{Å}^{-1}$ to a minimum that was well within the region of the large

* The calculations were done on the IBM 7094 computer using a program written by R. H. Bigelow. Increments of $\Delta r = 0.10$ Å were used.

oscillations in j(S). The corresponding variation in (C/N) as given by Eq. (30) was rather small in the high S range because of the small amplitude of the intensity oscillations. In the moderate S range where larger oscillations occurred, the variation in (C/N) was about 5%.

The resulting atomic density transforms for large values of S contained spurious ripples of small period and large amplitude, indicating that the intensity data in the high S region was in error. In general, the first peak in $\rho_a(r)$ was fairly well defined but the ripples were of such magnitude that the identity of the remaining peaks was difficult to discern. The corresponding electronic density transforms showed the same type of ripples but of considerably smaller amplitude and usually all the peaks were clearly distinguishable.

As the Fourier inversions were made with lower truncation limits, the amplitude of the ripples decreased somewhat but the general shape of the density function was still in doubt. As the value of $S_2$ was decreased, there appeared to be a particular region for each argon run where the majority of the ripples suddenly vanished. This value of S was then taken as the maximum for which the intensity data were believed to be reliable. A further decrease in $S_2$ generally tended to smooth out the ripples with no significant change occurring in the features of the density curves. However, as $S_2$ approached the region of large intensity oscillations in j(S), the maxima in the

density functions began to decrease and in some cases new ripples were introduced. Thus there appeared to be a range of $S_2$ values, generally in the region of the last observable oscillation of $j(S)$, that produced atomic density transforms differing only in the magnitude of the superimposed ripples.

In view of the uncertainties in the argon intensity patterns and the resulting lack of precision in determining $S_2$ and (C/N), no unique atomic density functions could be established. Instead, an inversion band was determined for each thermodynamic state based on the range of $S_2$ values used in the Fourier inversion integral. This inversion band was obtained by superimposing the atomic density functions resulting from several values of $S_2$ and drawing a smooth envelope about the ripples in these curves. The construction of this inversion band is shown in Figure 23 for a typical argon run (Run 40, $t = -125^{\circ}C$, $\overline{\rho}_b = 0.982$ gm/cc). The best estimate or average value of the atomic radial density function, denoted by $\langle \rho_a(r) \rangle$, available from the present intensity measurements was then taken as a smooth curve through the center of this band.

In order to show the relative magnitude of the ripples in the radial density functions, the Fourier transforms given by Eq. (27) and Eq. (29) were plotted against $r$ for a single combination of the parameters $S_2$ and (C/N). The value of $S_2$ used in these plots was different for each run and was selected to give the minimum amount

of ripples in the resulting curves. The numerical values of the normalization constants and truncation limits used to obtain these density functions are listed in Table 9. Also included in this table, under the heading of Atomic Radial Distribution Function, are the S ranges used to obtain the inversion band. The values of $\langle \rho_a(r) \rangle$ can be obtained from the estimated radial distribution function, g(r), discussed in the following section.

The radial atomic densities for the thirteen thermodynamic states of argon are shown in Figures 24 to 32. The plots of these density functions are arranged to illustrate their dependence on the temperature and bulk argon density in a manner similar to the representation of the intensity functions. The corresponding radial electronic densities are shown in Figures 33 to 41.

Examination of these two groups of figures shows that the ripples present in the atomic density curves become almost negligible in the electronic densities. However, both density functions show an appreciable amount of structure at subatomic distances where the expected behavior is indicated by the curves labeled $-4\pi r^2 \bar{\rho}$. The features in this region are certainly spurious and are presumed to be due to experimental errors. In general, the radial density curves show three maxima for the high density argon samples and vary more or less continuously until only a single well defined maximum remains for the argon vapor.

A comparison of the radial density functions among the various thermodynamic states indicated that the structural features were predominantly dependent upon the bulk density of the argon sample. This is demonstrated in Figure 42 where the relative heights of the maxima in the average atomic density function are plotted against the bulk sample density. Even though there was some uncertainty in these values, especially for the second and third maxima (see the width of the inversion band in Figure 23), there appeared to be a systematic dependence of the peak heights on the bulk sample density. This dependence, which was apparently independent of the sample temperature, is illustrated by the relative slope of the least squares line through the data points. The locations of the maxima were relatively constant and any clear dependence on the argon thermodynamic state was somewhat obscured by the width of the inversion band. However, the radial position of these peaks showed a slight tendency to increase as the temperature was raised and to decrease with increasing the sample density. The relative heights and the radial positions of these maxima are summarized in Table 10.

The number of nearest neighbors, also called the first coordination number, provides an additional means for characterizing the fluid structure. As discussed in Section I, the radial atomic density is defined in terms of the number of atoms contained in a spherical shell surrounding any reference atom in the system. The

fluid structure may be visualized as a succession of these shells, each having a larger radius and containing a correspondingly larger number of atoms. Because of the continual state of motion of the atoms within the fluid, the individual shells are not necessarily separated and distinct, but tend to overlap. The coordination numbers, or average number of atoms in each shell, are determined by evaluating the area under the corresponding peaks of the function $4\pi r^2 \rho_a(r)$.

For the thermodynamic states of the argon samples studied in this investigation, the first maximum in $4\pi r^2 \langle \rho_a(r) \rangle$ was only moderately well defined and the succeeding peaks appeared merely as inflection points. Therefore, only the first coordination number could be obtained with any degree of certainty. Because of the large amount of overlapping between the first and second shells, the required area was evaluated by symmetrizing the first peak in $4\pi r^2 \langle \rho_a(r) \rangle$ versus r. Since the inversion band produced an uncertainty in the exact location of this peak, the radius of symmetry was obtained through a correlation of the observed peak positions with the temperature and density of the argon samples. Using these partially smoothed values of the first peak positions, the number of nearest neighbors was obtained by doubling the area under the low r portion of the curves. Numerical values of the radius of symmetry and the first coordination number for each argon run are given in Table II.

The resulting values of the first coordination number as a function of the bulk argon density are plotted in Figure 43. The smooth curve through the data represents a least squares, second-order polynomial which was forced through the origin. This curve had a standard deviation of 0. 3 atoms and fitted the data points slightly better than a linear function. As indicated by the data, there was no apparent effect of temperature on the number of nearest neighboring atoms.

The presence of a small subsidiary maximum located between the first and second main peaks in $\rho_a(r)$ has been the subject of considerable discussion. The maximum was first reported by Eisenstein and Gingrich[9] and was also evident in the data obtained by Honeywell[14]. On the basis of a comprehensive analysis of several monatomic liquids, Finbak[8] concluded that this maximum was spurious and was caused by experimental errors in the intensity data. The validity of this peak was also questioned by Khan[12], as a result of his theoretical computations of the argon radial distribution function. The results of this investigation offer convincing evidence that this subsidiary maximum is indeed spurious. As previously indicated, the experimental data obtained by Honeywell for Runs 22 and 23 were reworked. On the basis of a correlation of the experimental intensity patterns with the argon density and temperature, Honeywell's data was slightly modified to bring it into agreement with the experimental

results of the present study. When this modified intensity data was analyzed by the previously described methods, the subsidiary peak, which was strongly evident in the original work, vanished almost completely. As illustrated in Figure 24, Run 22 shows no evidence of this peak and Run 23 has only a slight ripple. On the basis of the corrections made to Honeywell's data, the presence of this ghost peak was attributed to errors in the intensity data and improper normalization.

The eleven experimental runs of this investigation were almost completely devoid of this subsidiary peak with the exception of those states located at the argon critical density (see Figure 31). Because of the rather special nature of the critical state, the suggestion of such a maximum may be more than coincidental. However, this feature appeared to be more the result of a large ripple caused by errors in the intensity curves rather than an actual structural feature. This is borne out by the electronic density curves shown in Figure 40, where no trace of a ghost peak is evident.

## C. Atomic Radial Distribution Functions

As discussed in Section I, the atomic radial distribution function may be obtained by rearranging Eq. (27) to give

$$g(r) = \frac{\rho_a(r)}{\bar{\rho}_a} = 1 + \frac{1}{2\pi^2 r \bar{\rho}_a} \int_{S_1}^{S_2} S\, i(S) \sin(Sr) dS \qquad (31)$$

where the intensity kernel, i(S), is given by Eq. (28). On the basis of the experimental intensity measurements, the best estimate of g(r) was provided by the average atomic radial density function previously mentioned, i. e.,

$$g(r) = \frac{\langle \rho_a(r) \rangle}{\bar{\rho}_a} . \qquad (32)$$

The values of g(r) obtained from this expression are listed in Table 12 and are plotted in Figures 44 through 52. The corresponding values of $\langle \rho_a(r) \rangle$ may be computed from these tabulated values of g(r) by using Eq. (32).

The inversion band used in the computation of $\langle \rho_a(r) \rangle$ is shown on the plots of g(r) by the cross-hatched sections of the curves. A comparison of Figures 23 and 45 for Run 40 shows that, because of the different radial dependence, the uncertainties in the second and third maxima of the density curves are considerably diminished in g(r). The relatively wide inversion band for the states located at the critical density (shown in Figure 51) is the result of the large ripples in $\rho_a(r)$ previously mentioned (see Figure 31).

The experimental radial distribution functions exhibit one strong peak for all the argon states followed by a small second maximum with an amplitude depending upon the sample density. The general features of this main peak in $g(r)$ were the same for all thirteen runs. The average height of this maximum was 1.97 and its average radial position was 3.83 Å. Both measurements had a standard deviation of about 0.06 height units and Å, respectively. The radial position of this maximum compares very well with a value of 3.82 Å for the minimum in the Lennard-Jones 6-12 potential for argon[12]. The relatively constant value for the height of this main peak is consistent with the observed linear dependence of the first peak in $\langle \rho_a(r) \rangle$ on the sample density as shown in Figure 42.

The two low density argon states, Runs 32 and 36, offer a simple means of comparing the experimental values of $g(r)$ with a theoretically determined curve. For a dilute gas, the radial distribution function is related to the potential function, $u(r)$, describing the atomic interaction by the equation[35]

$$g(r) = e^{-u(r)/kT} . \tag{33}$$

This expression is valid for a gas whose equation of state is

$$\frac{PV}{RT} = 1 + \frac{B(T)}{V} \tag{34}$$

where B(T) is the second virial coefficient. The theoretical value of g(r) from Eq. (33) is shown in Figure 53 for a temperature of -110°C using the Lennard-Jones potential function

$$u(r) = 4\epsilon \left[ (\sigma/r)^{12} - (\sigma/r)^{6} \right] \qquad (35)$$

with the parameters[12]

$$\epsilon/k = 119.76^{\circ}K$$
$$\sigma = 3.405\ \text{Å} .$$

The theoretical curve for t = -125°C, which is not shown, has the same general features but possesses a slightly higher maximum. Also plotted in this figure are the experimental values for argon vapor at t = -110°C (Run 36) and t = -125°C (Run 32). A comparison of the curves in Figure 53 illustrates that there is still a significant amount of atomic ordering present in the argon vapor at these thermodynamic states. In addition, the slightly more pronounced second maximum in the experimental g(r) curve for t = -125°C indicates that this tendency toward atomic ordering is somewhat greater near the two-phase boundary (see Figure 1).

As a final item of interest, the experimental g(r) curves obtained from this laboratory are compared in Figure 54 with the earlier measurements of Eisenstein and Gingrich[9] (hereafter

referred to as E. G. ). As no attempt was made to duplicate these earlier measurements, this comparison was made between the closest thermodynamic states in both investigations. The relative locations of these states are shown in Figure 1 where the points labeled (5), (6), and (7) of E. G. are seen to correspond very nearly to Runs 22, 31, and 32 of the present study. The experimental curves due to E. G. were taken from the relatively large-scale plots of $g(r)$ in a paper by Khan[12]. These $g(r)$ values were computed by Khan from photographically enlarged curves of $4\pi r^2 \rho_a(r)$ taken from the original paper by E. G.

A comparison of these sets of curves shows that the previously mentioned ghost peak, which is strongly evident in curve 6 of E. G., is absent from the corresponding $g(r)$ of this study. In general, the $g(r)$ curves obtained by E. G. do not exhibit the continuity between thermodynamic states that has been consistently demonstrated by the results of the present investigation.

# VI. CONCLUSIONS

On the basis of the experimental results of this investigation, coupled with the methods used in the data analysis, the following conclusions have been reached.

1. The x-ray intensity patterns and the corresponding Fourier transforms of fluid argon exhibit structural features that vary smoothly and continuously with the thermodynamic state of the argon sample. Over the experimental range of the investigation, the height of the main intensity peak and the heights of maxima in $4\pi r^2[\rho_a(r) - \overline{\rho}_a]$ are related to the bulk density of the argon sample in a linear manner that is independent of the sample temperature. Within the experimental uncertainties, the first coordination number is also independent of temperature and varies in a simple manner with the sample density. The correlations leading to the above conclusion are discussed at greater length in Section V.

2. The small subsidiary peak in the radial atomic density reported by Eisenstein and Gingrich[9] is spurious. This ghost peak, appearing at about 5.4 Å, is believed to result from experimental errors in the x-ray scattering curve and improper normalization of the intensity data as discussed in Sections V-B and V-C.

3. If the incident and scattered x-ray beams are well collimated, the presence of strong diffraction peaks from a powder sample cell does not significantly interfere with the determination of the structural features in the intensity pattern of the confined sample. A necessary premise is the requirement that some reliable means, such as a statistical analysis, be available to reject any erroneous data points which result from intensity measurements on these diffraction peaks. The basis for this conclusion is discussed in Section III, Section IV-E, and Appendix 3.

4. If appreciable amounts of x-ray scattering are observed from a powder sample cell, the intensity pattern computed for the confined sample may require a correction for a distortion effect resulting from unhomogeneities within the powder cell. This possible distortion severely hinders the correct normalization of the sample intensity data and the subsequent Fourier analysis. The evidence leading to this conclusion is presented in Section III-B, Section IV-F, and Appendix 4.

5. For experiments involving the determination of x-ray diffraction patterns from samples confined in cylindrical sample cells, the scattering geometry employed in this investigation represents an optimum with respect to corrections required for the presence of

incoherent scattering. These corrections may become appreciable for dense samples at large scattering angles, and are minimized by using a narrow incident beam to partially irradiate the upper portion of the confined sample. The relation between the scattering geometry and the incoherent scattering corrections is discussed in Section IV-D and Appendix 1.

# APPENDIX 1

## ESTIMATION OF INCOHERENT ABSORPTION FACTORS

Consider a volume element j, lying either within the confined sample or the sample cell, being irradiated by a beam of x rays. Let $\mu$ and $\mu^{inc}$ be the linear absorption coefficient for coherent and incoherent radiation respectively. Designate the optical path length of the incident beam in the cell as $\ell_c^i$ and the sample as $\ell_s^i$. The incoherent scattering then leaves the volume element with a diffracted path length $\ell_s^d$ through the sample and $\ell_c^d$ through the cell. The incoherent absorption factor for this volume element is then

$$a_j^{inc} = \exp\left[ - \mu_c \ell_c^i - \mu_s \ell_s^i - \mu_c^{inc} \ell_c^d - \mu_s^{inc} \ell_s^d \right]_j \qquad (1\text{-}1)$$

The corresponding coherent absorption factor is simply obtained by setting $\mu_c^{inc} = \mu_c$ and $\mu_s^{inc} = \mu_s$.

If the volume element is contained in the sample, Eq. (1-1) gives $assc_j^{inc}$. For an element in the cell, the result is either $acsc_j^{inc}$ or $acc_j^{inc}$ where $\ell_s^i = \ell_s^d = 0$. The incoherent absorption factors for the entire sample or sample cell are obtained by summing Eq. (1-1) over the appropriate irradiated volume in the following manner.

$$ASSC^{inc} = (1/V_s) \sum_j assc_j^{inc} (\Delta v_s)_j \qquad (1\text{-}2a)$$

$$ACSC^{inc} = (1/V_c) \sum_j acsc_j^{inc} (\Delta v_c)_j \qquad (1\text{-}2b)$$

$$ACC^{inc} = (1/V_c) \sum_j acc_j^{inc} (\Delta v_c)_j \qquad (1\text{-}2c)$$

Eq. (1-2) was used to evaluate incoherent absorption factors for a test case having a scattering geometry similar to that described in II-B of the text. The conditions of this test case are listed in Table 1-1 below.

Table 1-1 Parameters for Test Case

| | |
|---|---|
| cell o. d. | 0. 100 inches |
| cell i. d. | 0. 056 inches |
| width of incident x-ray beam | 0. 012 inches |
| distance of beam center above cell center | 0. 018 inches |
| incident radiation wavelength | 0. 711 Å |
| mass absorption coefficient, argon | 12. 6 $cm^2/gm$ |
| mass absorption coefficient, beryllium | 0. 3 $cm^2/gm$ |
| argon density | 1. 00 gm/cc |
| beryllium density | 1. 82 gm/cc |
| number of volume elements in sample | 20 |
| number of volume elements in cell | 20 |

The linear absorption coefficients for incoherent radiation were calculated from Eqs. (11) and (12) of the text. The exponent in Eq. (12) was determined as 1. 40 for beryllium and 2. 86 for argon. The optical path lengths were measured from a large scale drawing of the scattering geometry. Since the relative effects of incoherent

scattering were desired, coherent absorption factors were also computed. The results of this test case, in terms of the relative incoherent absorption factor $\alpha^{inc}$ (see Eq. (15) of the text) are presented in Table 1-2 below.

Table 1-2 Relative Incoherent Absorption Factors

| $\Theta$ | $\alpha^{inc}_{c,c}(\Theta)$ | $\alpha^{inc}_{c,sc}(\Theta)$ | $\frac{\alpha^{inc}_{c,sc}(\Theta)}{\alpha^{inc}_{c,c}(\Theta)}$ | $\alpha^{inc}_{s,sc}(\Theta)$ |
|---|---|---|---|---|
| 5 | 1.000 | 1.000 | 1.000 | 1.000 |
| 15 | 1.000 | 0.999 | 0.999 | 0.993 |
| 25 | 1.000 | 0.999 | 0.999 | 0.988 |
| 35 | 0.999 | 0.999 | 1.000 | 0.982 |
| 45 | 0.999 | 0.999 | 1.000 | 0.976 |
| 55 | 0.998 | 0.998 | 1.000 | 0.968 |
| 65 | 0.997 | 0.997 | 1.000 | 0.957 |
| 75 | 0.996 | 0.996 | 1.000 | 0.941 |

The results of this test case show that, for the described scattering geometry, the only nonnegligible incoherent absorption factor is $ASSC^{inc}(\Theta)$.

The form of Eq. (1-1) was utilized to provide a means for estimating $ASSC^{inc}(\Theta)$ by introducing the concept of an over all average path length, $\langle \ell \rangle$. This approximation, as shown below, becomes exact if the various average path lengths can be accurately determined. The expressions for the absorption factors are

$$ASSC^{coh} = e^{-\mu_c[\langle \ell \rangle_c^i + \langle \ell \rangle_c^d]} \; e^{-\mu_s[\langle \ell \rangle_s^i + \langle \ell \rangle_s^d]} \tag{1-3}$$

$$ASSC^{inc} = e^{-[\mu_c \langle \ell \rangle_c^i + \mu_c^{inc} \langle \ell \rangle_c^d]} \; e^{-[\mu_s \langle \ell \rangle_s^i + \mu_s^{inc} \langle \ell \rangle_s^d]} \tag{1-4}$$

The linear absorption coefficients for incoherent radiation may be written as [ see Eq. (12) of the text]

$$\mu_c^{inc} = \mu_c + \Delta\mu_c \tag{1-5a}$$

$$\mu_s^{inc} = \mu_s + \Delta\mu_s \tag{1-5b}$$

When these values are substituted into Eq. (1-4), the result is

$$ASSC^{inc} = \left[ e^{-\mu_c[\langle \ell \rangle_c^i + \langle \ell \rangle_c^d]} \; e^{-\mu_s[\langle \ell \rangle_s^i + \langle \ell \rangle_s^d]} \right] e^{-\Delta\mu_s \langle \ell \rangle_s^d - \Delta\mu_c \langle \ell \rangle_c^d} \tag{1-6}$$

However, as seen from Eq. (1-3), the term in the brackets is just $ASSC^{coh}$. Therefore, the relative incoherent absorption factor may be calculated from the following equation.

$$\alpha_{s,sc}^{inc} = \frac{ASSC^{inc}}{ASSC^{coh}} = e^{-[\Delta\mu_s \langle \ell \rangle_s^d + \Delta\mu_c \langle \ell \rangle_c^d]} \tag{1-7}$$

The success of Eq. (1-7) in producing accurate values of $\alpha_{s,sc}^{inc}$ depends entirely upon the accuracy with which the average path lengths $\langle \ell \rangle_c^d$ and $\langle \ell \rangle_s^d$ can be determined.

The contribution of the term $\Delta\mu_c \langle \ell \rangle_c^d$ in Eq. (1-7) is small because of the relatively low absorption in the sample cell. Therefore, the average path length of the diffracted radiation in the cell was assumed constant and equal to the wall thickness of the cell, i. e., $\langle \ell \rangle_c^d \approx \frac{1}{2}$ [cell o. d. − cell i. d.].

The quantity $\langle \ell \rangle_s^d$, however, was not so readily obtained. Examination of Eqs. (1-3) and (1-4) shows that the path lengths should be dependent only on the scattering geometry, i. e., they should be the same for both coherently and incoherently scattered radiation. Since numerical values of the coherent absorption factors were readily available via a computer program, these values were used to determine the average path lengths in the argon sample. Eq. (1-3) shows that a plot of $\log_e(\mathrm{ASSC}^{coh})$ vs. $\mu_s$ should be linear with a slope equal to the negative of the <u>total</u> average path length, $\langle \ell \rangle_s^t = [\langle \ell \rangle_s^i + \langle \ell \rangle_s^d]$. For the geometric conditions of the test case described in Table 1-1, values of $\mathrm{ASSC}^{coh}$ were obtained from the computer program for several values of $\mu_s$. The range of $\mu_s$ was taken to correspond to the density range in the argon experiments. The computed values of $\log_e(\mathrm{ASSC}^{coh})$ were found to be linear with $\mu_s$, thus showing the validity of the original approximation. Values of the slope, $\langle \ell \rangle_s^t$, were obtained at several scattering angles by a least squares fit to the data points.

The final problem to be solved then, was what portion of $\langle \ell \rangle_s^t$ corresponded to the average path length of the diffracted radiation, $\langle \ell \rangle_s^d$. To accomplish this, the quantity $\Lambda_s^d$ was defined as the

fraction of the total path length in the sample which is due to the diffracted radiation. This quantity was estimated by constructing a large-scale drawing of the scattering geometry and dividing the irradiated sample volume into a number of equal volume elements. At several scattering angles, the incident and diffracted path lengths for each element were measured and an arithmetic average computed. These graphically determined path lengths are denoted by $\langle \ell_g \rangle_s^i$ and $\langle \ell_g \rangle_s^d$ respectively. The required path length $\langle \ell \rangle_s^d$ was then estimated by the equation

$$\langle \ell \rangle_s^d = \Lambda_s^d \langle \ell \rangle_s^t \approx \left[ \frac{\langle \ell_g \rangle_s^d}{\langle \ell_g \rangle_s^i + \langle \ell_g \rangle_s^d} \right] \langle \ell \rangle_s^t \qquad (1\text{-}8)$$

The various terms used in the computation of the relative incoherent absorption factor are listed in Table 1-3. The final estimated value is listed under the heading $[\alpha_{s,sc}^{inc}(\Theta)]_{est}$. For comparison, the hand calculated values, designated by the subscript calc are also tabulated. The maximum deviation between the two is seen to be 0.3%.

TABLE 1-3

RESULTS OF THE INCOHERENT ABSORPTION FACTOR ESTIMATION

| $\Theta$ deg | $\Delta\mu_s$ ($cm^{-1}$) | $\Delta\mu_c$ ($cm^{-1}$) | $(\Lambda_s^d)_{graph}$ | $\langle \ell \rangle_s^t$ (cm) | $\langle \ell \rangle_s^d$ (cm) | $[\alpha_{s,sc}^{inc}]_{est}$ | $[\alpha_{s,sc}^{inc}]_{calc}$ |
|---|---|---|---|---|---|---|---|
| 5 | 0.00 | 0.00 | 0.47 | 0.100 | 0.047 | 1.000 | 1.000 |
| 15 | 0.17 | 0.00 | 0.39 | 0.084 | 0.033 | 0.994 | 0.993 |
| 25 | 0.45 | 0.01 | 0.32 | 0.071 | 0.023 | 0.989 | 0.988 |
| 35 | 0.83 | 0.02 | 0.27 | 0.062 | 0.017 | 0.985 | 0.982 |
| 45 | 1.28 | 0.03 | 0.26 | 0.058 | 0.015 | 0.979 | 0.976 |
| 55 | 1.73 | 0.04 | 0.27 | 0.057 | 0.015 | 0.971 | 0.968 |
| 65 | 2.14 | 0.04 | 0.32 | 0.058 | 0.019 | 0.958 | 0.957 |
| 75 | 2.45 | 0.05 | 0.39 | 0.060 | 0.023 | 0.941 | 0.941 |

# APPENDIX 2

## EFFECT OF INCOHERENT SCATTERING ON THE PULSE-HEIGHT SELECTOR TRANSMISSION FACTOR

The relative intensity of voltage pulses in the range $v$ to $v + dv$ originating in a quanta counting radiation detector may be expressed in terms of a pulse amplitude distribution (PAD). Designate this distribution of pulse amplitudes for radiation of wavelength $\lambda$ as $P(\lambda, v)$ and impose the normalization restriction

$$\int_0^{v_m} P(\lambda, v)\, dv = 1 \qquad (2\text{-}1)$$

where $v_m$ is the maximum voltage that can be distinguished by the pulse-height selector (PHS). The distribution function, $P(\lambda, v)$, is characterized by two parameters; the mean of the distribution, $\overline{v}$, and the width of the distribution at half the maximum intensity, $w$. These parameters are related to the wavelength of the detected radiation in the following manner[18].

$$\overline{v} \propto 1/\lambda \qquad (2\text{-}2)$$

$$w \propto 1/\sqrt{\lambda} \qquad (2\text{-}3)$$

According to theory[18] and based on several experimental measurements, the PAD is well represented by a Gaussian type probability

function. The variance of the Gaussian distribution, $\sigma^2$, is related to the characteristic width of the PAD by the expression

$$\frac{1}{2} w = 1.1774 \sigma \tag{2-4}$$

The PAD may thus be expressed as an analytical function similar in form to that of the Gaussian distribution by the equation

$$P(\nu) = k e^{-\frac{1}{2}\nu^2} \tag{2-5}$$

where $k$ is a constant satisfying the restriction imposed by Eq. (2-1). The quantity $\nu$ is a normalized voltage and is given by

$$\nu = \nu(\lambda, v) = 2.355 \frac{(v - \bar{v})}{w} \tag{2-6}$$

Eq. (2-5) is not a true Gaussian probability function because of the normalization restruction given in Eq. (2-1). This restriction is based on the physical limitation that only those voltage pulses having an amplitude in the range $0 \leq v \leq v_m$ can be distinguished in the PHS circuit. For the conditions of this experiment, $v_m$ was 100 volts and the PAD was positioned such that its parameters were $\bar{v} \approx 50$ volts and $w \approx 20$ volts. From Eq. (2-6) these values correspond to $\nu \approx \pm 6.0$. If $P_{Gauss}(\nu)$ is the actual Gaussian function, the deviation of the PAD from true Gaussian behavior can be expressed as

$$\int_{-\infty}^{-6.0} P_{Gauss}(\nu)d\nu = \int_{6.0}^{\infty} P_{Gauss}(\nu)d\nu \approx 10^{-5}$$

Under these experimental conditions, the difference between the two functions is negligible and $P(\lambda, v)$ may be assumed equal to the Gaussian probability function. Thus the constant, k, in Eq. (2-5) becomes $1/\sqrt{2\pi}$ and the resulting normalized PAD is given by the equation

$$P(\nu) = (1/\sqrt{2\pi})\, e^{-\frac{1}{2}\nu^2} \tag{2-7}$$

The PHS transmission factors for coherent and incoherent radiation are then defined by the following functions.

$$t_{PHS}^{coh} \equiv \int_{v_1}^{v_2} P(\lambda^{coh}, v)dv \tag{2-8}$$

$$t_{PHS}^{inc} = \int_{v_1}^{v_2} P(\lambda^{inc}, v)dv \tag{2-9}$$

The integration limits $v_1$ and $v_2$ are the lower and upper limits of the PHS voltage window and remain constant during an experimental diffraction scan. The wavelength of coherently scattered radiation is

invariant during the experiment and therefore $t_{PHS}^{coh}$ is constant, i.e., independent of $\Theta$. The value of $\lambda^{inc}$, however, varies with the scattering angle (see Eq. (11) of the text) and consequently $t_{PHS}^{inc}$ is not constant. With the use of the equations given above, the variation in relative incoherent transmission factor, $\psi_{PHS}^{inc}(\Theta)$, (see Eq. (14) of the text) may be calculated by the expression

$$\psi_{PHS}^{inc}(\Theta) = [t_{PHS}^{coh}]^{-1} \int_{\nu_1^{inc}}^{\nu_2^{inc}} P(\nu)d\nu \qquad (2\text{-}10)$$

The computational procedures used to obtain numerical values of $\psi_{PHS}^{inc}(\Theta)$ are illustrated by the following sample calculation for a scattering angle of $\Theta$ = 75 degrees.

Several experimental measurements were made to obtain the PAD for coherently scattered Mo K$\alpha$ radiation using a NI scintillation counter. From these measurements, the PAD parameters were determined as $\bar{v}^{coh}$ = 47.0 volts and $w^{coh}$ = 19.7 volts. The wavelength of incoherent radiation at $\Theta$ = 75 degrees was calculated to be $\lambda^{inc} = 1.0637\,\lambda^{coh}$. From Eqs. (2-2) and (2-3), the corresponding parameters for the incoherent PAD were found to be $\bar{v}^{inc}$ = 44.19 volts and $w^{inc}$ = 19.10 volts. To suitably monochromate the incident x-ray beam in the argon diffraction experiments, a 50% PHS transmission factor was used. The voltage window corresponding

to this transmission factor was determined by setting $t_{PHS}^{coh} = 0.5$ in Eq. (2-8) and solving the resulting integral equation for the values of $v_1$ and $v_2$, i.e.,

$$t_{PHS}^{coh} = 0.5 = \frac{1}{\sqrt{2\pi}} \int_{\nu_1^{coh}}^{\nu_2^{coh}} e^{-\frac{1}{2}\nu^2} \, d\nu$$

where

$$\nu^{coh} = 2.355 \, \frac{(v - \overline{v}^{coh})}{w^{coh}}$$

With the aid of Gaussian probability tables, $\nu^{coh}$ was determined as $\pm$ 0.674 and the corresponding values of the PHS window were $v_1 = 41.36$ volts and $v_2 = 52.64$ volts.* Substitution of these window settings into Eq. (2-6) gave values for the incoherent normalized voltage of $\nu_1^{inc} = -0.349$ and $\nu_2^{inc} = 1.042$. The relative incoherent transmission factor was then calculated from Eq. (2-10).

$$\psi_{PHS}^{inc}(\Theta = 75^o) = \frac{1}{0.5\sqrt{2\pi}} \int_{-0.349}^{1.042} e^{-\frac{1}{2}\nu^2} \, d\nu$$

$$\psi_{PHS}^{inc}(\Theta = 75^o) = 0.9755$$

* For the same conditions, the experimentally determined values were 41.3 volts and 52.7 volts.

# APPENDIX 3

## STATISTICS OF X-RAY INTENSITY MEASUREMENTS

The determination of the scattered intensity from a confined sample requires the experimental measurement of three statistical quantities:

1. The number of scattered quanta detected from the empty cell, $N_c^E$, during a time interval, $\tau_c$.
2. The number of scattered quanta detected from the cell-plus-sample, $N_{c+s}^E$, during a time interval, $\tau_{c+s}$.
3. The number of counts corresponding to the background noise, $N_n$, accumulated during these time intervals.

From these measurements, the intensities or counting rates are determined, e.g., $I_c^E = (N_c^E - N_n)/\tau_c$. The intensity of x rays scattered from the confined sample is calculated from the expression (see Eq. (3) of the text)

$$I_s = (ABS)_1 [ I_{c+s}^E - (ABS)_2 \; I_c^E ] \tag{3-1}$$

where

$$(ABS)_1 = \frac{1/P(\Theta)}{F(\Theta)\,ASSC(\Theta)} \tag{3-2}$$

$$(ABS)_2 = \frac{ACSC(\Theta)}{ACC(\Theta)} \tag{3-3}$$

For any given set of experimental measurements, there is a definite statistical error or uncertainty, $\Delta I_s$, associated with the computed value of $I_s$. The following derivation will show the relationship between this uncertainty and the measured statistical quantities. In the analysis presented here, the assumption is made that the background noise, $N_n$, is negligible compared to the counting rates of the cell and sample. For conditions where this background noise is high or the counting rates are extremely low, the resulting expressions will not apply. However, the general analysis may readily be extended to include this effect.

The experimental measurements of $N_c^E$ or $N_{c+s}^E$ may be made with a single counting time, $\tau$, or a series of measurements may be taken each with a different value of $\tau$. In any event, all of these measurements contribute to the final accuracy with which $I_s$ is known. For any value of the scattering angle, $\Theta$, let the total number of counts accumulated from the empty cell be designated by the discrete random variable $\eta_c$ and from the cell-plus-sample by $\eta_{c+s}$. The total counting time or time of observation will be $\tau_c$ for the empty cell and $\tau_{c+s}$ for the cell-plus-sample. These quantities are the total values where more than one measurement has been made. The variables $\eta_c$ and $\eta_{c+s}$ are assumed to be independent random variables, with each having a Poisson distribution. The mean and variance of these distributions are designated by

$$\begin{aligned} \text{Mean}\,(\eta_c) \quad &= \text{Var}\,(\eta_c) \quad = \langle N_c \rangle \\ \text{Mean}\,(\eta_{c+s}) \;&= \text{Var}\,(\eta_{c+s}) \;= \langle N_{c+s} \rangle \end{aligned} \tag{3-4}$$

The variables of interest, however, are not the total number of counts but rather the counting rates or intensities, $\eta_c/\tau_c$ and $\eta_{c+s}/\tau_{c+s}$. Following the form of Eq. (3-1) a new random variable, $\xi_s$, is defined that corresponds to the intensity of the confined sample. This quantity is related to the experimental variables in the following manner.

$$\xi_s = (ABS)_1 \left[ \frac{\eta_{c+s}}{\tau_{c+s}} - (ABS)_2 \frac{\eta_c}{\tau_c} \right] \tag{3-5}$$

Because of the various parameters appearing in the above equation, $\xi_s$ will be a continuous random variable and its distribution or frequency function will be denoted by $f(\xi_s)$. The significant features of this distribution function, i.e., its mean and variance, may be conveniently computed by introducing the concept of an expected value. If $g(\xi_s)$ represents any function (or property) of $\xi_s$, the expected value of $g(\xi_s)$ is given by[37]

$$E\,\{g(\xi_s)\} = \int_{-\infty}^{\infty} g(\xi_s) f(\xi_s)\, d\xi_s \tag{3-6}$$

For discrete random variables, this integral would be replaced by a corresponding sum over all possible values of the variable. With this notation, the mean and variance of the distribution function are given by

$$\text{Mean}\,(\xi_s) = E\,\{\xi_s\} \tag{3-7}$$

$$\text{Var}\,(\xi_s) = E\,\{[\,\xi_s - \text{Mean}\,(\xi_s)]^2\} \tag{3-8}$$

Since $\xi_s$ is a linear combination of the independent random variables $\eta_c$ and $\eta_{c+s}$, substitution of Eq. (3-5) into Eqs. (3-7) and (3-8) yields the following expressions for the mean and variance of the distribution function, $f(\xi_s)$.

$$\text{Mean}\,(\xi_s) = (ABS)_1 \left[ \frac{\text{Mean}(\eta_{c+s})}{\tau_{c+s}} - (ABS)_2 \frac{\text{Mean}(\eta_c)}{\tau_c} \right] \tag{3-9}$$

$$\text{Var}\,(\xi_s) = (ABS)_1^2 \left[ \frac{\text{Var}(\eta_{c+s})}{(\tau_{c+s})^2} + (ABS)_2^2 \frac{\text{Var}(\eta_c)}{(\tau_c)^2} \right] \tag{3-10}$$

The mean and variance of the Poisson distributions for $\eta_c$ and $\eta_{c+s}$ are, in general, unknown quantities. For numerical computations, these parameters can be estimated by the experimental observations, i.e., $\langle N_c \rangle \approx N_c^E$ and $\langle N_{c+s} \rangle \approx N_{c+s}^E$. Let $I_s$

represent an estimate of the mean for the distribution $f(\xi_s)$. Using the above estimated values, Eq. (3-9) then reduces to Eq. (3-1) and the variance of $\xi_s$ may be estimated from the equation

$$\mathrm{Var}(\xi_s) = \frac{(\mathrm{ABS})_1^2}{\tau_{c+s}} \left[ I_{c+s}^E + (\mathrm{ABS})_2^2 \left( \frac{\tau_{c+s}}{\tau_c} \right) I_c^E \right] \qquad (3\text{-}11)$$

For the counting times used in this experiment, the values of the mean in the original Poisson distributions, $\langle N_c \rangle$ and $\langle N_{c+s} \rangle$, were all sufficiently large so that the distributions for $\eta_c$ and $\eta_{c+s}$ could be considered essentially Gaussian or normal. With this assumption, $\xi_s$ will also have a normal distribution since it is a linear combination of two independent, normally distributed random variables. The statistical uncertainty in the estimate of the confined sample scattering can then be represented by a confidence interval about the estimated mean, $I_s$. This confidence interval is given by the equation

$$(\Delta I_s)_j = \pm k_j \left[ \mathrm{Var}(\xi_s) \right]^{\frac{1}{2}} \qquad (3\text{-}12)$$

where $k_j$ is a constant and the subscript $j$ refers to the significance level. By substituting Eqs. (3-2), (3-3), and (3-11) into this expression, the confidence interval is given in terms of the experimental parameters by the equation

$$(\Delta I_s)_j = \frac{\pm k_j [1/P(\Theta)]}{F(\Theta)\,ASSC\sqrt{\tau_{c+s}}} \left[ I^E_{c+s} + \left(\frac{ACSC}{ACC}\right)^2 \left(\frac{\tau_{c+s}}{\tau_c}\right) I^E_c \right]^{\frac{1}{2}} \quad (3\text{-}13)$$

Some values of $k_j$ are listed below for various significance levels.[38]

| j | $k_j$ |
|---|---|
| 50 % | 0. 675 |
| 90 % | 1. 645 |
| 95 % | 1. 960 |
| 99 % | 2. 576 |

# APPENDIX 4

## EFFECT OF AN UNHOMOGENEOUS SAMPLE CELL ON THE SCATTERING FROM A CONFINED SAMPLE

Consider a hypothetical experiment having the following scattering geometry.

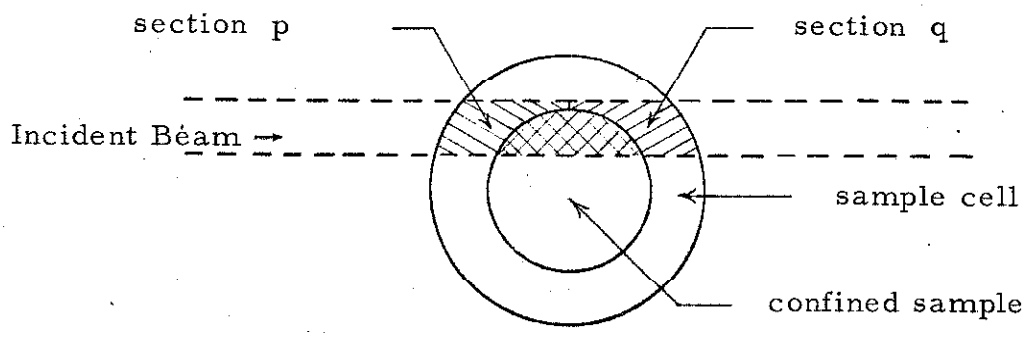


The irradiated portion of the sample cell is divided into two equal-volume sections, p and q. This sample cell is constructed from a material having an average intrinsic scattering power of $I_c^o(\Theta)$ and the experimentally observed scattering from this cell is $I_c^E(\Theta)$. The average geometric absorption factors for the two sections of the empty cell are $ACC^p(\Theta)$ and $ACC^q(\Theta)$. These absorption factors are normalized with respect to the total irradiated volume of the sample cell.

The object of the experiment is to calculate the intensity scattered from the confined sample, $I_s(\Theta)$, from the experimentally measured scattering of the cell-plus-sample, $I^E_{c+s}(\Theta)$. For the cell-plus-sample measurement, the absorption factors are $ASSC(\Theta)$ for the confined sample and $ACSC^p(\Theta)$ and $ACSC^q(\Theta)$ for the two sections of the sample cell.

If the polarization factor is omitted, the relation between the observed intensities and the intrinsic scattering power may be written[19]

$$I^E_c(\Theta) = \sum_{j=p,q} ACC^j(\Theta)\, I^j_c(\Theta) \tag{4-1}$$

$$I^E_{c+s}(\Theta) = ASSC(\Theta)\, I_s(\Theta) + \sum_{j=p,q} ACSC^j(\Theta)\, I^j_c(\Theta) \tag{4-2}$$

where $I^p_c(\Theta)$ and $I^q_c(\Theta)$ are the average intrinsic scattering powers for the two sections of the sample cell. Because of possible unhomogeneities, these values may or may not be equal to the average value of $I^o_c(\Theta)$. In the case of a sample cell constructed from an "ideal powder," the cell will be truly homogeneous and $I^p_c(\Theta) = I^q_c(\Theta) = I^o_c(\Theta)$. Under these conditions, Eqs. (4-1) and (4-2) may be combined to give the sample intensity directly in terms of the experimental

intensities as given by Eq. (3) of the text. However, if the sample cell is not homogeneous, Eq. (3) will give incorrect values for the calculated intensity of the confined sample.

The magnitude of this error may be estimated by a sample calculation. For a particular value of the scattering angle, $\Theta$, assume the following numerical values for the terms in Eqs. (4-1) and (4-2). These values are typical of the ones used in the argon experiments at high scattering angles.*

$$I_c^E = 20 \text{ counts/second}$$

$$I_{c+s}^E = 19 \text{ counts/second}$$

$$\text{ASSC} = 0.40$$

$$\left.\begin{aligned} \text{ACC}^p &= 0.34 \\ \text{ACC}^q &= 0.32 \end{aligned}\right\} (\text{ACC})^{\text{total}} = 0.66$$

$$\left.\begin{aligned} \text{ACSC}^p &= 0.34 \\ \text{ACSC}^q &= 0.11 \end{aligned}\right\} (\text{ACSC})^{\text{total}} = 0.45$$

With these parameters, the sample intensity, $I_s$, will be computed for a homogeneous sample cell and for two cases of an unhomogeneous cell having a 5% deviation in the average intrinsic scattering power.

---

* See Tables 2 and 4 of the text.

Case 1 Homogeneous Sample Cell

$$I_c^p = I_c^q = I_c^o$$

Eq. (4-1) gives $I_c^o = 30.30$ counts/sec

Eq. (4-2) gives $I_s = 13.40$ counts/sec

Case 2 Unhomogeneous Sample Cell

$$I_c^p = 0.95\, I_c^o;\ I_c^q = 1.05\, I_c^o$$

Eq. (4-1) gives $I_c^o = 30.35$ counts/sec

Eq. (4-2) gives $I_s = 14.23$ counts/sec

The assumption of a homogeneous cell leads to a value of $I_s$ that is too low by 5.8% (negative error)

Case 3 Unhomogeneous Sample Cell

$$I_c^p = 1.05\, I_c^o;\ I_c^q = 0.95\, I_c^o$$

Eq. (4-1) gives $I_c^o = 30.26$ counts/sec

Eq. (4-2) gives $I_s = 12.60$ counts/sec

The assumption of a homogeneous cell leads to a value of $I_s$ that is too high by 6.4% (positive error)

The results of this sample calculation show that an unhomogeneous sample cell can give rise to either a positive or negative error in the computed value of the sample intensity. Moreover, because the sample intensity decreases with increasing $\Theta$, this error will become more pronounced at the high scattering angles. Thus, within the experimental accuracy of the observations, this error may appear to be linear in $\Theta$.

Verification of these results is provided by the $SiO_2$ calibration experiment (see Section III of the text). In this experiment, the scattering geometry designated by cell position-X gave a positive error in the calculated $I_s(\Theta)$ indicating that Case 3 above was applicable. When the cell was rotated $180^o$ to obtain cell position-Y (similar to Case 2 above), a negative error in $I_s(\Theta)$ was observed.

## REFERENCES


1. H. H. Paalman and C. J. Pings, "Fourier Analysis of X-Ray Diffraction Data from Liquids," Rev. Mod. Phys., 35, 389 (1963).

2. N. S. Gingrich, "The Diffraction of X-Rays by Liquid Elements," Rev. Mod. Phys., 15, 90 (1943).

3. R. W. James, The Optical Principles of X-Rays (G. Bell and Sons, Ltd., London, 1958).

4. K. Furukawa, "The Radial Distribution Curves of Liquids by Diffraction Methods," Rept. Prog. Phys., 25, 395 (1962).

5. R. F. Kruh, "Diffraction Studies of the Structure of Liquids," Chem. Rev., 62, 319 (1962).

6. J. Waser and V. Shomaker, "The Fourier Inversion of Diffraction Data," Rev. Mod. Phys., 25, 671 (1953).

7. T. Sugawara, "On the Atomic Distribution Curves for Liquids, II. False Details in the Atomic Distribution Curves and their Discrimination," Sci. Repts., Research Inst. Tohoku Univ., 3A, 39 (1951).

8. C. Finbak, "The Structure of Liquids, I and II," Acta. Chem. Scand., 3, 1279, 1293 (1949).

9. A. Eisenstein and N. S. Gingrich, "The Diffraction of X-Rays by Argon in the Liquid, Vapor, and Critical Regions," Phys. Rev., 62, 261 (1942).

10. D. G. Henshaw, "Atomic Distribution in Liquid Argon by Neutron Diffraction and the Cross-Sections of $Ar^{36}$ and $Ar^{40}$," Phys. Rev., 105, 976 (1957).

11. N. S. Gingrich and C. W. Tompson, "Atomic Distribution in Liquid Argon Near the Triple Point," J. Chem. Phys., 36, 2398 (1962).

12. A. A. Khan, "Radial Distribution Functions of Fluid Argon," Phys. Rev., 134, No. 2A, A 367 (1964).

13. J. M. H. Levelt, "Measurements of the Compressibility of Argon in the Gaseous and Liquid Phase," doctoral thesis, Amsterdam (1958); this work also reported in A. Michels, J. M. Levelt and G. J. Wolkers, "Thermodynamic Properties of Argon at Temperatures between 0° and -140°C and at Densities up to 640 Amagats (Pressures up to 1050 atm.)," Physica, 24, 769 (1958).

14. W. I. Honeywell, "X-Ray Diffraction Studies of Dense Fluids," doctoral thesis, California Institute of Technology, Pasadena, California (1964).

15. H. H. Paalman and C. J. Pings, "Beryllium Sample Cell for the X-Ray Diffraction Study of Liquids," Rev. Sci. Instr., 33, 496 (1962).

16. W. I. Honeywell, C. M. Knobler, B. L. Smith and C. J. Pings, "Apparatus for the X-Ray Diffraction Studies of Confined Fluids," Rev. Sci. Instr., 35, 1216 (1964).

17. W. I. Honeywell, doctoral thesis, p. 175.

18. W. Parrish and T. R. Kohler, "Use of Counter Tubes in X-Ray Analysis," Rev. Sci. Instr., 27, 795 (1956).

19. H. H. Paalman and C. J. Pings, "Numerical Evaluation of X-Ray Absorption Factors for Cylindrical Samples and Annular Sample Cells," J. Appl. Phys., 33, 2635 (1962).

20. J. Berghuis et. al., "New Calculations of Atomic Scattering Factors," Acta. Cryst., 8, 478 (1955).

21. D. R. Chipman and L. D. Jennings, "Measurement of the Atomic Scattering Factor of Ne, Ar, Kr and Xe," Phys. Rev., 132, No. 2, 728 (1963).

22. H. W. Furumoto, "Diffraction of X-Rays by Liquids – Nitrogen, Oxygen and their Mixtures," doctoral thesis, Dept. of Physics, Ohio State University, (1963), p. 58.

23. C. B. Walker, "X-Ray Compton Scattering for Aluminum," Phys. Rev., 103, 558 (1956).

24. A. P. Kendig and C. J. Pings, "X-Ray Absorption Factors for Cylindrical Samples in Annular Sample Cells Exposed to Incident Beams of Limited Width," submitted for publication to J. Appl. Phys.

25. W. E. Milne, Numerical Calculus (Princeton University Press, 1949), p. 68.

26. B. D. Cullity, Elements of X-Ray Diffraction, (Addison-Wesley Pub. Co., Inc., Reading, Mass., 1956), p. 466.

27. ibid, p. 108.

28. ibid, p. 11.

29. J. Krogh-Moe, "A Method for Converting Experimental X-Ray Intensities to an Absolute Scale," Acta. Cryst., 9, 951 (1956).

30. N. Norman, "The Fourier Transform Method for Normalizing Intensities," Acta. Cryst., 10, 370 (1957).

31. Z. W. Wilchinsky, "Effect of Crystal Grain and Particle Size on X-Ray Power Diffracted from Powders," Acta. Cryst., 4, 1 (1951).

32. J. E. Thomas and P. W. Schmidt, "X-Ray Study of Critical Opalescence in Argon," J. Chem. Phys., 39, 2506 (1963).

33. K. Furukawa, op. cit., p. 406.

34. S. E. Rodriguez, "X-Ray Diffraction Studies of Stable and Supercooled Liquid Gallium," doctoral thesis, California Institute of Technology, Pasadena, California (1964), p. 83.

35. N. Davidson, "Statistical Mechanics," (McGraw-Hill Book Company, Inc., 1962), p. 475.

36. A. J. Freeman, "A Study of the Compton Scattering of X-Rays. II," Acta Cryst., 13, 190 (1960).

37. P. G. Hoel, Introduction to Mathematical Statistics, second edition, (John Wiley and Sons, New York, 1954), p. 196.

38. ibid, p. 320.

TABLE 1

SUMMARY OF ARGON THERMODYNAMIC STATES AND

UNCERTAINTY IN EXPERIMENTAL MEASUREMENT AND CONTROL

| Run No. | Temperature (°C) | Density (gm/cc) | Pressure (psia) |
|---|---|---|---|
| 22 | -130.00 | 0.910 | 586.60 |
| 23 | -130.00 | 0.982 | 964.53 |
| 30 | -125.00 ± 0.06 | 0.910 ± 0.001 | 965.51 ± 0.60 |
| 31 | -125.00 ± 0.07 | 0.780 ± 0.005 | 648.23 ± 1.02 |
| 32 | -125.00 ± 0.06 | 0.280 ± 0.003 | 624.74 ± 0.55 |
| 33 | -120.00 ± 0.06 | 0.780 ± 0.002 | 906.26 ± 0.45 |
| 34 | -120.00 ± 0.06 | 0.536 ± 0.015 | 774.76 ± 0.33 |
| 35 | -110.00 ± 0.07 | 0.536 ± 0.003 | 1058.22 ± 0.52 |
| 36 | -110.00 ± 0.06 | 0.280 ± 0.001 | 815.85 ± 0.38 |
| 37 | -115.00 ± 0.06 | 0.536 ± 0.003 | 915.75 ± 0.32 |
| 38 | -110.00 ± 0.06 | 0.780 ± 0.001 | 1445.98 ± 0.52 |
| 39 | -120.00 ± 0.06 | 0.910 ± 0.001 | 1350.46 ± 0.50 |
| 40 | -125.00 ± 0.06 | 0.982 ± 0.001 | 1438.29 ± 0.46 |

TABLE 2

SUMMARY OF THE EXPERIMENTAL ARGON DIFFRACTION DATA

$I_c^E$ = Average Intensity Scattered from the Evacuated Beryllium Cell (counts/sec)

$I_{c+s}^E$ = Average Intensity Scattered from the Beryllium Cell with the Confined Argon Sample (counts/sec)

Molybdenum Radiation; 55 kvp, 20 ma

Zr Foil; PHS with 50% K$\alpha$ Transmission

All Intensities Scaled to a Reference Value of 16.50 counts/sec for the Evacuated Cell at $\Theta$ = 50 Degrees

| | | $I^E_{C+S}$ | | | | | | | | | | |
|---|---|---|---|---|---|---|---|---|---|---|---|---|
| Run Number | | 30 | 31 | 32 | 33 | 34 | 35 | 36 | 37 | 38 | 39 | 40 |
| Temperature (°C) | | -125 | -125 | -125 | -120 | -120 | -110 | -110 | -115 | -110 | -120 | -125 |
| Pressure (psia) | | 965.51 | 648.23 | 624.74 | 906.26 | 774.76 | 1058.23 | 815.85 | 915.75 | 1445.98 | 1350.46 | 1438.29 |
| Density (gm/cc) | | 0.910 | 0.780 | 0.280 | 0.780 | 0.536 | 0.536 | 0.280 | 0.536 | 0.780 | 0.910 | 0.982 |
| $\Theta$ | $I^E_C$ | | | | | | | | | | | |
| 0. | | | | | | | | | | | | |
| 0.25 | | | | | | | | | | | | |
| 0.50 | | | | | | | | | | | | |
| 0.75 | | | | | | | | | | | | |
| 1.00 | 4.040 | 27.703 | 44.869 | 70.969 | 46.180 | 71.247 | 73.219 | 75.860 | 72.060 | 44.603 | 29.281 | 22.972 |
| 1.25 | 4.030 | 25.313 | 37.624 | 59.137 | 40.530 | 58.312 | 61.019 | 66.132 | 59.188 | 39.765 | 26.588 | 22.068 |
| 1.50 | 4.100 | 23.196 | 33.280 | 50.814 | 36.033 | 50.762 | 54.102 | 58.277 | 52.167 | 36.804 | 25.915 | 21.287 |
| 1.75 | 4.500 | 22.542 | 30.778 | 46.408 | 34.358 | 45.609 | 48.876 | 53.843 | 46.845 | 34.770 | 24.731 | 20.648 |
| 2.00 | 5.090 | 22.259 | 29.651 | 43.178 | 32.049 | 43.300 | 45.627 | 49.928 | 44.344 | 33.673 | 24.501 | 20.901 |
| 2.25 | 5.750 | 22.109 | 29.311 | 40.597 | 32.362 | 41.173 | 44.117 | 47.608 | 42.061 | 32.633 | 24.933 | 21.560 |
| 2.50 | 6.250 | 22.184 | 29.110 | 39.930 | 32.529 | 40.405 | 42.839 | 46.215 | 41.763 | 33.209 | 24.531 | 21.669 |
| 2.75 | 6.590 | 22.692 | 29.222 | 39.620 | 31.840 | 39.979 | 43.365 | 46.120 | 40.723 | 32.979 | 25.178 | 21.446 |
| 3.00 | 6.940 | 23.433 | 29.890 | 40.116 | 32.170 | 40.471 | 44.748 | 46.703 | 41.835 | 33.475 | 25.799 | 23.432 |
| 3.25 | 7.600 | 25.838 | 31.429 | 40.808 | 34.200 | 41.550 | 45.926 | 47.445 | 42.781 | 35.068 | 27.127 | 24.481 |
| 3.50 | 8.610 | 27.793 | 33.768 | 41.994 | 37.278 | 44.654 | 47.907 | 48.720 | 46.017 | 38.087 | 30.303 | 27.029 |
| 3.75 | 9.540 | 30.130 | 37.691 | 44.906 | 39.915 | 47.557 | 51.331 | 50.526 | 48.412 | 41.406 | 32.787 | 29.566 |
| 4.00 | 10.060 | 35.115 | 40.453 | 46.715 | 43.716 | 51.638 | 55.176 | 52.610 | 52.638 | 45.657 | 37.039 | 33.763 |
| 4.25 | 10.470 | 38.259 | 45.014 | 47.820 | 49.448 | 55.591 | 58.250 | 53.947 | 56.045 | 51.169 | 42.148 | 38.700 |
| 4.50 | 10.940 | 43.438 | 51.564 | 49.660 | 57.060 | 58.975 | 63.490 | 56.296 | 61.054 | 56.217 | 48.337 | 43.656 |
| 4.75 | 11.150 | 50.105 | 57.831 | 51.794 | 62.112 | 65.101 | 69.365 | 58.614 | 66.286 | 62.633 | 54.369 | 50.076 |
| 5.00 | 11.330 | 57.616 | 65.969 | 54.369 | 69.479 | 68.929 | 74.688 | 59.461 | 70.119 | 70.534 | 62.071 | 58.223 |
| 5.25 | 11.550 | 65.945 | 73.282 | 55.354 | 77.104 | 73.936 | 78.322 | 61.385 | 75.756 | 79.072 | 70.918 | 68.151 |
| 5.50 | 12.450 | 74.702 | 80.452 | 56.760 | 84.500 | 78.943 | 80.970 | 61.764 | 79.561 | 85.741 | 80.406 | 80.476 |
| 5.75 | 16.860 | 83.431 | 87.695 | 59.684 | 89.973 | 82.182 | 84.887 | 64.437 | 83.599 | 89.638 | 89.337 | 89.260 |
| 6.00 | 13.070 | 85.298 | 88.244 | 55.420 | 89.850 | 79.941 | 82.920 | 60.852 | 80.799 | 91.102 | 90.626 | 93.637 |
| 6.25 | 13.640 | 84.589 | 86.399 | 54.300 | 89.646 | 78.663 | 80.677 | 60.016 | 79.007 | 88.141 | 89.308 | 91.953 |
| 6.50 | 14.650 | 79.481 | 83.034 | 54.236 | 85.476 | 75.989 | 77.229 | 58.818 | 76.221 | 84.715 | 84.867 | 87.707 |
| 6.75 | 14.760 | 72.853 | 75.707 | 52.231 | 78.085 | 71.475 | 73.309 | 56.709 | 71.416 | 77.874 | 78.294 | 79.099 |
| 7.00 | 14.830 | 67.224 | 70.212 | 49.978 | 71.898 | 66.922 | 69.512 | 54.933 | 66.844 | 71.769 | 70.849 | 71.509 |
| 7.25 | 15.640 | 62.196 | 63.984 | 48.516 | 66.210 | 62.434 | 65.290 | 53.062 | 63.904 | 66.454 | 63.998 | 64.091 |
| 7.50 | 15.770 | 56.393 | 59.164 | 46.365 | 61.096 | 60.004 | 60.812 | 50.459 | 60.315 | 61.068 | 59.572 | 58.705 |
| 7.75 | 16.600 | 52.310 | 55.375 | 45.711 | 57.092 | 56.363 | 57.885 | 49.482 | 57.363 | 56.815 | 54.391 | 54.315 |
| 8.00 | 17.470 | 50.263 | 53.010 | 43.583 | 53.157 | 54.881 | 56.049 | 48.633 | 55.519 | 53.200 | 51.166 | 50.864 |
| 8.25 | 17.840 | 47.122 | 49.746 | 42.670 | 51.190 | 52.162 | 52.987 | 47.375 | 53.136 | 50.515 | 48.263 | 47.547 |
| 8.50 | 18.550 | 45.099 | 48.060 | 43.460 | 48.506 | 51.079 | 52.973 | 46.470 | 51.474 | 49.070 | 46.068 | 45.897 |
| 8.75 | 24.390 | 47.658 | 50.598 | 46.333 | 49.860 | 51.796 | 53.668 | 49.615 | 53.378 | 50.060 | 47.700 | 47.075 |
| 9.00 | 19.260 | 43.729 | 45.863 | 42.573 | 47.559 | 48.700 | 50.557 | 45.490 | 49.414 | 46.641 | 44.926 | 43.792 |
| 9.25 | 24.900 | 46.154 | 49.144 | 45.651 | 48.608 | 51.577 | 51.640 | 48.135 | 51.130 | 48.158 | 45.970 | 46.200 |
| 9.50 | 26.110 | 46.615 | 49.429 | 45.724 | 48.850 | 51.559 | 51.937 | 48.615 | 52.171 | 48.513 | 46.318 | 45.728 |
| 9.75 | 23.420 | 45.363 | 47.789 | 43.377 | 47.620 | 49.240 | 49.790 | 46.140 | 49.340 | 47.907 | 45.403 | 44.772 |

| | | $I^E_{C+S}$ | | | | | | | | | | |
|---|---|---|---|---|---|---|---|---|---|---|---|---|
| Run Number | | 30 | 31 | 32 | 33 | 34 | 35 | 36 | 37 | 38 | 39 | 40 |
| Temperature (°C) | | -125 | -125 | -125 | -120 | -120 | -110 | -110 | -115 | -110 | -120 | -125 |
| Pressure (psia) | | 965.51 | 648.23 | 624.74 | 906.26 | 774.76 | 1058.23 | 815.85 | 915.75 | 1445.98 | 1350.46 | 1438.29 |
| Density (gm/cc) | | 0.910 | 0.780 | 0.280 | 0.780 | 0.536 | 0.536 | 0.280 | 0.536 | 0.780 | 0.910 | 0.982 |
| $\theta$ | $I^E_C$ | | | | | | | | | | | |
| 10.00 | 27.430 | 47.352 | 49.299 | 46.139 | 49.440 | 50.871 | 52.294 | 49.070 | 51.731 | 48.448 | 47.560 | 47.100 |
| 10.25 | 105.230 | 88.723 | 84.171 | 105.255 | 78.215 | 96.179 | 98.951 | 110.726 | 98.247 | 84.708 | 79.621 | 80.949 |
| 10.50 | 28.390 | 49.066 | 50.451 | 45.870 | 50.379 | 51.504 | 52.531 | 47.880 | 51.823 | 50.582 | 48.270 | 47.980 |
| 10.75 | 25.210 | 47.147 | 48.575 | 43.016 | 48.260 | 49.620 | 50.498 | 45.740 | 49.120 | 47.669 | 47.314 | 47.141 |
| 11.00 | 28.930 | 49.182 | 50.740 | 46.115 | 51.164 | 52.591 | 52.119 | 48.695 | 53.087 | 50.900 | 49.950 | 49.362 |
| 11.25 | 55.600 | 64.638 | 69.514 | 75.865 | 65.789 | 80.403 | 69.871 | 72.756 | 72.400 | 63.114 | 63.666 | 66.890 |
| 11.50 | 115.910 | 98.753 | 95.637 | 100.421 | 90.779 | 103.756 | 95.546 | 100.831 | 97.784 | 84.589 | 87.774 | 91.191 |
| 11.75 | 358.820 | 225.411 | 287.821 | 330.193 | 208.592 | 271.034 | 247.544 | 320.583 | 255.355 | 194.200 | 201.878 | 163.390 |
| 12.00 | 46.100 | 61.406 | 61.020 | 58.986 | 60.781 | 61.720 | 63.331 | 61.356 | 64.696 | 59.460 | 60.475 | 61.459 |
| 12.25 | 37.700 | 53.032 | 53.982 | 50.805 | 52.772 | 53.707 | 53.942 | 51.890 | 53.929 | 51.690 | 51.990 | 52.187 |
| 12.50 | 36.460 | 49.865 | 51.396 | 47.796 | 49.751 | 52.880 | 52.054 | 49.309 | 53.120 | 49.245 | 49.580 | 51.043 |
| 12.75 | 35.610 | 49.854 | 50.630 | 47.540 | 49.599 | 50.764 | 50.869 | 49.220 | 52.034 | 48.427 | 48.550 | 49.427 |
| 13.00 | 32.750 | 46.636 | 48.182 | 44.907 | 46.729 | 48.907 | 47.982 | 45.654 | 48.873 | 46.483 | 46.135 | 47.469 |
| 13.25 | 31.840 | 45.110 | 45.830 | 43.407 | 45.020 | 46.557 | 46.924 | 45.043 | 46.708 | 44.900 | 44.472 | 45.361 |
| 13.50 | 30.470 | 45.050 | 44.530 | 41.510 | 44.149 | 45.200 | 45.080 | 43.303 | 45.265 | 43.190 | 42.968 | 43.243 |
| 13.75 | 29.920 | 42.612 | 43.260 | 39.819 | 42.586 | 43.061 | 44.290 | 42.030 | 43.884 | 41.910 | 40.858 | 41.557 |
| 14.00 | 28.330 | 41.007 | 42.287 | 38.872 | 40.779 | 43.090 | 42.140 | 40.315 | 42.259 | 40.520 | 40.160 | 40.245 |
| 14.25 | 27.380 | 39.750 | 40.046 | 37.747 | 40.414 | 41.380 | 41.700 | 39.450 | 41.628 | 39.895 | 39.047 | 39.200 |
| 14.50 | 26.480 | 38.893 | 39.195 | 37.200 | 38.933 | 39.886 | 40.816 | 37.813 | 40.275 | 38.820 | 37.783 | 38.594 |
| 14.75 | 26.520 | 37.795 | 39.466 | 36.306 | 38.657 | 39.180 | 40.123 | 38.181 | 40.250 | 36.500 | 37.362 | 37.898 |
| 15.00 | 26.480 | 37.524 | 38.467 | 36.226 | 38.770 | 39.997 | 40.410 | 37.810 | 40.055 | 38.726 | 37.600 | 37.424 |
| 15.25 | 31.410 | 40.920 | 40.349 | 40.020 | 40.784 | 43.201 | 42.064 | 41.626 | 42.102 | 40.712 | 39.613 | 40.540 |
| 15.50 | 93.120 | 78.140 | 79.485 | 91.975 | 76.670 | 88.137 | 81.432 | 87.902 | 82.645 | 72.006 | 73.069 | 74.392 |
| 15.75 | 26.790 | 37.380 | 38.394 | 35.500 | 37.852 | 38.420 | 39.369 | 37.320 | 38.727 | 37.300 | 37.300 | 36.812 |
| 16.00 | 25.590 | 36.138 | 37.730 | 34.006 | 36.212 | 38.340 | 38.422 | 36.045 | 38.700 | 37.003 | 36.417 | 36.208 |
| 16.25 | 24.910 | 36.016 | 36.900 | 34.284 | 36.500 | 38.261 | 41.440 | 35.649 | 37.560 | 36.284 | 35.937 | 35.920 |
| 16.50 | 26.160 | 36.849 | 37.338 | 34.560 | 37.165 | 38.560 | 38.220 | 36.370 | 37.960 | 36.958 | 36.994 | 36.681 |
| 16.75 | 26.670 | 37.142 | 37.681 | 35.254 | 37.790 | 38.365 | 38.353 | 36.785 | 37.962 | 37.412 | 36.492 | 36.828 |
| 17.00 | 24.450 | 36.134 | 35.532 | 33.150 | 36.665 | 36.177 | 36.774 | 34.370 | 36.126 | 34.697 | 34.932 | 35.279 |
| 17.25 | 24.370 | 34.752 | 35.570 | 33.186 | 35.968 | 35.879 | 36.837 | 33.918 | 35.985 | 35.580 | 35.019 | 35.073 |
| 17.50 | 24.830 | 35.065 | 36.040 | 32.652 | 35.711 | 36.010 | 37.086 | 34.317 | 36.329 | 35.678 | 35.313 | 35.156 |
| 17.75 | 27.430 | 36.934 | 37.727 | 35.330 | 36.774 | 37.273 | 37.863 | 35.741 | 37.580 | 37.187 | 36.823 | 36.864 |
| 18.00 | 59.620 | 57.475 | 56.141 | 62.910 | 56.016 | 57.521 | 60.136 | 65.124 | 59.484 | 55.058 | 53.998 | 52.108 |
| 18.25 | 35.650 | 42.335 | 42.179 | 41.590 | 40.740 | 42.199 | 43.920 | 41.798 | 43.360 | 42.177 | 40.515 | 41.265 |
| 18.50 | 25.220 | 34.046 | 35.203 | 32.340 | 35.140 | 34.759 | 35.629 | 33.545 | 35.090 | 34.995 | 34.370 | 34.940 |
| 18.75 | 24.780 | 34.236 | 34.713 | 32.155 | 36.257 | 35.147 | 36.235 | 33.471 | 35.300 | 34.370 | 33.380 | 34.810 |
| 19.00 | 24.770 | 33.340 | 34.400 | 31.825 | 34.700 | 34.448 | 34.920 | 33.036 | 34.920 | 33.960 | 33.528 | 34.220 |
| 19.25 | 24.810 | 33.983 | 35.001 | 32.053 | 33.821 | 34.597 | 34.476 | 33.182 | 34.578 | 33.703 | 33.617 | 33.880 |
| 19.50 | 24.700 | 32.578 | 33.786 | 31.040 | 33.352 | 33.549 | 34.094 | 33.570 | 33.752 | 33.838 | 32.800 | 33.020 |
| 19.75 | 26.270 | 33.434 | 34.601 | 32.590 | 34.281 | 34.568 | 35.355 | 33.407 | 35.110 | 34.080 | 33.680 | 34.070 |

| | | $I^E_{C+S}$ | | | | | | | | | | |
|---|---|---|---|---|---|---|---|---|---|---|---|---|
| Run Number | | 30 | 31 | 32 | 33 | 34 | 35 | 36 | 37 | 38 | 39 | 40 |
| Temperature (°C) | | -125 | -125 | -125 | -120 | -120 | -110 | -110 | -115 | -110 | -120 | -125 |
| Pressure (psia) | | 965.51 | 648.23 | 624.74 | 906.26 | 774.76 | 1058.23 | 815.85 | 915.75 | 1445.98 | 1350.46 | 1438.29 |
| Density (gm/cc) | | 0.910 | 0.780 | 0.280 | 0.780 | 0.536 | 0.536 | 0.280 | 0.536 | 0.780 | 0.910 | 0.982 |
| θ | $I^E_C$ | | | | | | | | | | | |
| 20.00 | 27.660 | 33.921 | 34.740 | 33.184 | 34.641 | 35.089 | 36.027 | 35.191 | 35.652 | 34.823 | 34.320 | 34.610 |
| 20.25 | 101.760 | 85.065 | 87.849 | 101.379 | 86.816 | 94.745 | 92.327 | 100.043 | 92.666 | 83.238 | 82.627 | 83.861 |
| 20.50 | 35.260 | 39.400 | 39.860 | 37.412 | 38.920 | 40.580 | 40.402 | 40.119 | 40.840 | 40.132 | 39.190 | 39.125 |
| 20.75 | 25.920 | 32.679 | 33.760 | 32.004 | 33.860 | 33.420 | 33.850 | 32.580 | 34.109 | 33.560 | 32.679 | 32.814 |
| 21.00 | 33.520 | 37.818 | 37.758 | 36.924 | 37.217 | 38.198 | 39.161 | 38.548 | 39.175 | 38.100 | 37.620 | 37.620 |
| 21.25 | 29.090 | 33.650 | 33.978 | 33.600 | 35.094 | 35.060 | 35.825 | 35.130 | 35.150 | 34.199 | 34.030 | 32.865 |
| 21.50 | 60.710 | 50.035 | 53.146 | 63.056 | 52.639 | 58.607 | 56.557 | 62.840 | 57.955 | 50.727 | 52.290 | 51.335 |
| 21.75 | 88.970 | 68.584 | 67.685 | 79.611 | 66.904 | 72.685 | 69.511 | 77.997 | 72.214 | 64.887 | 64.142 | 64.540 |
| 22.00 | 43.370 | 43.500 | 44.570 | 44.756 | 43.400 | 44.668 | 43.552 | 44.839 | 44.304 | 42.218 | 41.787 | 41.824 |
| 22.25 | 26.540 | 31.505 | 32.760 | 30.850 | 32.700 | 33.036 | 33.030 | 33.085 | 32.977 | 32.536 | 31.740 | 32.286 |
| 22.50 | 26.690 | 31.904 | 32.756 | 31.456 | 31.951 | 32.895 | 33.195 | 32.107 | 32.075 | 31.801 | 31.508 | 31.968 |
| 22.75 | 26.970 | 31.601 | 32.720 | 31.290 | 32.150 | 32.342 | 32.980 | 32.250 | 33.000 | 31.800 | 32.178 | 31.623 |
| 23.00 | 26.840 | 31.800 | 32.251 | 30.529 | 31.777 | 32.044 | 32.435 | 31.830 | 32.262 | 31.851 | 31.501 | 31.798 |
| 23.25 | 34.850 | 37.173 | 37.660 | 36.712 | 37.280 | 39.023 | 38.640 | 38.576 | 38.260 | 37.420 | 36.500 | 35.818 |
| 23.50 | 30.590 | 34.957 | 33.906 | 32.223 | 34.235 | 35.140 | 34.588 | 33.708 | 34.750 | 33.645 | 32.761 | 33.386 |
| 23.75 | 25.180 | 30.230 | 30.819 | 29.444 | 30.362 | 30.351 | 31.012 | 30.390 | 31.211 | 30.625 | 30.683 | 30.580 |
| 24.00 | 25.980 | 30.278 | 30.390 | 30.500 | 30.498 | 30.557 | 31.202 | 30.620 | 30.872 | 30.716 | 30.300 | 30.874 |
| 24.25 | 31.050 | 34.669 | 33.583 | 33.000 | 34.458 | 34.850 | 35.216 | 37.087 | 34.581 | 33.286 | 33.680 | 33.628 |
| 24.50 | 24.550 | 29.459 | 29.941 | 28.680 | 29.705 | 30.292 | 31.251 | 29.653 | 30.155 | 29.407 | 29.520 | 29.597 |
| 24.75 | 24.160 | 28.692 | 29.372 | 28.392 | 30.033 | 29.800 | 29.650 | 29.012 | 29.594 | 29.020 | 29.103 | 29.054 |
| 25.00 | 23.900 | 28.443 | 29.262 | 27.638 | 29.076 | 29.306 | 29.596 | 28.792 | 29.521 | 28.979 | 28.660 | 28.988 |
| 25.25 | 23.890 | 28.917 | 28.718 | 27.720 | 29.145 | 29.874 | 29.330 | 28.320 | 28.824 | 29.532 | 28.759 | 29.515 |
| 25.50 | 23.870 | 28.592 | 29.009 | 27.440 | 29.168 | 28.940 | 28.970 | 28.691 | 29.064 | 28.078 | 28.406 | 28.125 |
| 25.75 | 34.540 | 35.630 | 36.785 | 36.134 | 36.628 | 36.941 | 36.890 | 37.530 | 37.280 | 35.890 | 35.870 | 35.660 |
| 26.00 | 25.130 | 28.493 | 29.269 | 28.380 | 30.218 | 29.425 | 29.660 | 28.912 | 29.590 | 29.071 | 29.526 | 29.347 |
| 26.25 | 23.090 | 27.020 | 27.785 | 26.517 | 27.582 | 27.975 | 28.322 | 27.248 | 27.761 | 27.830 | 27.400 | 27.518 |
| 26.50 | 22.920 | 27.334 | 27.286 | 26.100 | 27.620 | 27.656 | 27.690 | 26.830 | 27.857 | 26.806 | 26.614 | 27.640 |
| 26.75 | 22.780 | 26.863 | 26.900 | 26.250 | 27.254 | 27.343 | 27.672 | 26.887 | 27.380 | 27.440 | 27.040 | 26.977 |
| 27.00 | 22.640 | 26.530 | 27.154 | 25.992 | 26.969 | 27.418 | 27.540 | 26.887 | 26.877 | 26.904 | 26.673 | 26.933 |
| 27.25 | 22.780 | 26.105 | 26.820 | 25.685 | 26.590 | 27.659 | 27.119 | 26.892 | 27.370 | 26.834 | 26.685 | 26.443 |
| 27.50 | 22.870 | 26.292 | 25.855 | 26.090 | 26.836 | 26.794 | 27.497 | 26.625 | 26.831 | 26.720 | 25.993 | 26.336 |
| 27.75 | 36.870 | 36.270 | 35.390 | 33.740 | 34.636 | 35.794 | 35.381 | 36.889 | 35.965 | 36.056 | 34.399 | 34.996 |
| 28.00 | 25.520 | 27.900 | 27.416 | 27.002 | 28.291 | 28.430 | 29.007 | 28.440 | 28.927 | 28.161 | 27.942 | 28.051 |
| 28.25 | 24.870 | 27.228 | 27.998 | 27.520 | 27.365 | 28.115 | 28.021 | 28.127 | 28.200 | 27.631 | 27.131 | 27.423 |
| 28.50 | 23.660 | 26.384 | 27.130 | 25.890 | 26.817 | 26.321 | 27.320 | 27.034 | 27.560 | 26.151 | 26.720 | 26.416 |
| 28.75 | 22.750 | 24.825 | 25.765 | 24.729 | 25.967 | 25.971 | 25.816 | 25.700 | 26.142 | 26.004 | 25.371 | 26.000 |
| 29.00 | 38.300 | 36.300 | 36.502 | 38.430 | 34.517 | 36.372 | 36.613 | 38.199 | 36.636 | 35.790 | 35.521 | 35.819 |
| 29.25 | 24.620 | 26.773 | 26.931 | 26.688 | 26.941 | 27.974 | 28.053 | 27.680 | 27.740 | 27.226 | 27.067 | 26.983 |
| 29.50 | 21.660 | 24.764 | 25.335 | 24.308 | 25.314 | 25.122 | 25.047 | 24.688 | 24.370 | 25.176 | 24.802 | 25.277 |
| 29.75 | 21.550 | 24.533 | 24.686 | 24.310 | 24.850 | 25.091 | 24.880 | 25.376 | 25.338 | 24.678 | 24.973 | 24.368 |

| | | $I^E_{C+S}$ | | | | | | | | | | |
|---|---|---|---|---|---|---|---|---|---|---|---|---|
| Run Number | | 30 | 31 | 32 | 33 | 34 | 35 | 36 | 37 | 38 | 39 | 40 |
| Temperature (°C) | | -125 | -125 | -125 | -120 | -120 | -110 | -110 | -115 | -110 | -120 | -125 |
| Pressure (psia) | | 965.51 | 648.23 | 624.74 | 906.26 | 774.76 | 1058.23 | 815.85 | 915.75 | 1445.98 | 1350.46 | 1438.29 |
| Density (gm/cc) | | 0.910 | 0.780 | 0.280 | 0.780 | 0.536 | 0.536 | 0.280 | 0.536 | 0.780 | 0.910 | 0.982 |
| $\theta$ | $I^E_C$ | | | | | | | | | | | |
| 30.00 | 21.890 | 24.694 | 24.663 | 24.295 | 24.950 | 24.833 | 25.679 | 24.747 | 25.270 | 25.335 | 24.620 | 25.064 |
| 30.25 | 33.370 | 32.544 | 32.031 | 32.747 | 31.369 | 32.946 | 31.361 | 32.500 | 33.840 | 31.138 | 32.260 | 31.554 |
| 30.50 | 23.280 | 25.361 | 25.677 | 25.439 | 25.386 | 26.000 | 26.110 | 25.540 | 26.148 | 25.930 | 24.903 | 24.960 |
| 30.75 | 21.300 | 24.224 | 24.319 | 23.666 | 23.995 | 24.670 | 24.100 | 23.633 | 24.424 | 24.780 | 23.920 | 23.680 |
| 31.00 | 23.550 | 24.805 | 25.467 | 24.395 | 24.905 | 24.942 | 25.720 | 24.724 | 26.009 | 24.920 | 25.383 | 25.839 |
| 31.25 | 20.940 | 23.295 | 23.772 | 22.820 | 23.531 | 23.657 | 23.765 | 23.229 | 23.748 | 23.491 | 23.210 | 23.170 |
| 31.50 | 20.820 | 23.143 | 23.621 | 22.760 | 23.267 | 23.351 | 23.915 | 23.480 | 24.209 | 23.200 | 22.950 | 23.276 |
| 31.75 | 32.860 | 30.738 | 32.848 | 33.330 | 32.441 | 33.280 | 33.040 | 33.750 | 32.915 | 31.690 | 31.740 | 31.252 |
| 32.00 | 24.990 | 26.030 | 27.675 | 26.520 | 27.420 | 28.004 | 28.293 | 27.400 | 26.820 | 26.911 | 26.907 | 27.007 |
| 32.25 | 23.200 | 24.320 | 24.477 | 24.176 | 23.691 | 24.675 | 24.880 | 24.435 | 24.920 | 25.278 | 23.980 | 24.110 |
| 32.50 | 25.370 | 25.614 | 25.318 | 25.950 | 25.097 | 26.800 | 25.967 | 25.555 | 26.061 | 24.727 | 24.895 | 25.227 |
| 32.75 | 21.590 | 23.210 | 23.576 | 23.300 | 23.105 | 21.820 | 24.097 | 23.477 | 23.598 | 23.230 | 22.442 | 23.510 |
| 33.00 | 19.750 | 21.964 | 22.360 | 21.237 | 21.620 | 22.469 | 22.587 | 22.220 | 22.440 | 22.324 | 21.340 | 22.468 |
| 33.25 | 19.670 | 21.598 | 21.940 | 21.227 | 22.129 | 22.187 | 22.209 | 21.978 | 21.776 | 22.174 | 21.921 | 21.582 |
| 33.50 | 19.720 | 21.234 | 21.720 | 21.386 | 22.140 | 21.982 | 22.019 | 22.000 | 21.655 | 21.847 | 21.340 | 21.317 |
| 33.75 | 19.550 | 21.173 | 21.590 | 21.031 | 21.868 | 22.324 | 21.659 | 22.099 | 21.739 | 21.633 | 21.265 | 21.345 |
| 34.00 | 28.980 | 27.544 | 28.650 | 29.455 | 28.270 | 28.916 | 27.824 | 29.500 | 27.967 | 27.900 | 26.614 | 27.420 |
| 34.25 | 23.920 | 24.935 | 24.577 | 24.626 | 24.500 | 24.371 | 25.300 | 25.808 | 24.702 | 24.848 | 24.330 | 24.969 |
| 34.50 | 18.960 | 20.490 | 20.661 | 20.514 | 20.920 | 21.171 | 20.930 | 21.290 | 21.169 | 21.388 | 20.860 | 20.814 |
| 34.75 | 19.100 | 20.476 | 20.870 | 20.689 | 21.070 | 21.170 | 21.320 | 21.021 | 21.355 | 20.950 | 20.652 | 20.604 |
| 35.00 | 22.870 | 23.359 | 23.749 | 24.597 | 23.380 | 23.750 | 23.417 | 23.904 | 23.839 | 23.240 | 23.174 | 23.164 |
| 35.25 | 20.180 | 21.387 | 21.598 | 21.361 | 21.279 | 21.765 | 22.057 | 21.979 | 22.070 | 21.343 | 21.374 | 21.391 |
| 35.50 | 18.160 | 19.653 | 20.169 | 19.620 | 20.101 | 20.360 | 20.068 | 20.418 | 20.259 | 19.900 | 19.904 | 19.952 |
| 35.75 | 18.210 | 19.622 | 20.266 | 19.350 | 19.611 | 20.031 | 20.086 | 19.887 | 20.317 | 20.113 | 19.560 | 19.998 |
| 36.00 | 18.200 | 19.270 | 20.127 | 19.363 | 19.974 | 19.891 | 20.110 | 19.488 | 19.894 | 19.976 | 19.198 | 19.592 |
| 36.25 | 18.250 | 19.598 | 19.903 | 19.873 | 19.760 | 19.935 | 19.760 | 19.919 | 20.373 | 19.796 | 19.290 | 19.756 |
| 36.50 | 18.840 | 19.780 | 20.057 | 20.096 | 20.510 | 20.392 | 20.472 | 20.390 | 20.862 | 19.820 | 20.013 | 19.726 |
| 36.75 | 18.380 | 19.286 | 19.746 | 19.136 | 19.920 | 20.032 | 19.581 | 20.320 | 19.719 | 19.623 | 19.324 | 19.934 |
| 37.00 | 17.800 | 19.290 | 19.259 | 19.050 | 19.180 | 19.361 | 19.519 | 19.383 | 19.860 | 19.015 | 19.150 | 18.990 |
| 37.25 | 17.730 | 18.660 | 18.800 | 19.110 | 20.338 | 19.088 | 19.563 | 19.167 | 19.631 | 18.974 | 18.911 | 18.737 |
| 37.50 | 17.930 | 19.247 | 19.333 | 19.222 | 19.846 | 19.382 | 18.775 | 19.446 | 19.397 | 19.240 | 19.080 | 18.575 |
| 37.75 | 19.050 | 19.596 | 19.903 | 19.740 | 20.220 | 20.030 | 20.126 | 20.320 | 19.789 | 19.938 | 19.920 | 20.183 |
| 38.00 | 18.390 | 18.718 | 19.760 | 19.530 | 19.513 | 19.717 | 19.719 | 19.716 | 19.525 | 20.304 | 19.080 | 19.350 |
| 38.25 | 19.210 | 19.878 | 20.172 | 20.012 | 19.773 | 19.998 | 19.649 | 19.632 | 20.030 | 19.809 | 19.346 | 19.410 |
| 38.50 | 18.350 | 19.010 | 19.559 | 19.320 | 19.528 | 19.171 | 19.471 | 19.440 | 19.573 | 19.382 | 18.937 | 19.313 |
| 38.75 | 17.310 | 18.051 | 18.995 | 18.160 | 18.262 | 18.408 | 18.517 | 18.331 | 18.732 | 19.036 | 17.978 | 18.046 |
| 39.00 | 17.040 | 18.134 | 18.135 | 17.740 | 17.766 | 17.940 | 18.832 | 18.060 | 18.316 | 18.242 | 17.945 | 18.094 |
| 39.25 | 16.940 | 17.850 | 17.791 | 17.920 | 18.286 | 17.945 | 18.035 | 18.431 | 18.443 | 17.818 | 18.019 | 17.623 |
| 39.50 | 16.810 | 17.479 | 17.833 | 18.253 | 18.199 | 18.300 | 17.938 | 17.835 | 17.874 | 18.559 | 17.911 | 17.986 |
| 39.75 | 16.860 | 17.780 | 18.220 | 17.643 | 17.850 | 18.323 | 17.981 | 18.182 | 17.810 | 17.455 | 17.440 | 17.201 |

| | | $I^E_{C+S}$ | | | | | | | | | | |
|---|---|---|---|---|---|---|---|---|---|---|---|---|
| Run Number | | 30 | 31 | 32 | 33 | 34 | 35 | 36 | 37 | 38 | 39 | 40 |
| Temperature (°C) | | -125 | -125 | -125 | -120 | -120 | -110 | -110 | -115 | -110 | -120 | -125 |
| Pressure (psia) | | 965.51 | 648.23 | 624.74 | 906.26 | 774.76 | 1058.23 | 815.85 | 915.75 | 1445.98 | 1350.46 | 1438.29 |
| Density (gm/cc) | | 0.910 | 0.780 | 0.280 | 0.780 | 0.536 | 0.536 | 0.280 | 0.536 | 0.780 | 0.910 | 0.982 |
| θ | $I^E_C$ | | | | | | | | | | | |
| 40.00 | 16.700 | 17.335 | 17.817 | 17.588 | 17.958 | 17.663 | 18.035 | 17.811 | 17.913 | 17.802 | 17.990 | 17.721 |
| 40.25 | 17.240 | 17.460 | 18.018 | 18.784 | 17.890 | 18.020 | 17.877 | 18.099 | 18.485 | 17.720 | 17.882 | 17.445 |
| 40.50 | 17.120 | 17.641 | 18.093 | 17.850 | 17.785 | 18.145 | 17.503 | 18.557 | 18.046 | 18.034 | 17.855 | 17.356 |
| 40.75 | 19.290 | 18.428 | 19.293 | 19.818 | 19.392 | 20.009 | 19.820 | 19.709 | 19.006 | 19.309 | 19.231 | 19.083 |
| 41.00 | 17.780 | 18.004 | 18.355 | 18.578 | 17.993 | 18.478 | 19.047 | 18.617 | 18.654 | 18.596 | 18.119 | 17.980 |
| 41.25 | 16.870 | 17.066 | 17.917 | 17.460 | 17.650 | 18.106 | 17.827 | 18.042 | 17.644 | 17.237 | 17.134 | 17.520 |
| 41.50 | 16.500 | 16.918 | 17.474 | 17.197 | 17.604 | 17.680 | 17.476 | 17.394 | 17.305 | 17.013 | 17.033 | 17.116 |
| 41.75 | 16.910 | 17.266 | 17.438 | 17.410 | 17.553 | 17.768 | 17.500 | 18.103 | 17.865 | 17.351 | 17.205 | 17.194 |
| 42.00 | 19.040 | 18.487 | 18.820 | 19.440 | 18.923 | 19.429 | 19.126 | 19.745 | 19.126 | 18.816 | 18.554 | 19.517 |
| 42.25 | 17.770 | 17.712 | 17.970 | 18.210 | 18.166 | 18.249 | 18.070 | 18.651 | 18.692 | 17.890 | 17.699 | 17.935 |
| 42.50 | 17.480 | 17.535 | 17.400 | 17.930 | 17.322 | 18.047 | 18.006 | 18.501 | 18.162 | 17.909 | 17.960 | 17.674 |
| 42.75 | 16.540 | 16.782 | 16.857 | 16.820 | 17.036 | 17.019 | 17.201 | 17.146 | 17.387 | 16.880 | 16.680 | 17.278 |
| 43.00 | 16.340 | 16.621 | 16.974 | 16.475 | 17.220 | 17.157 | 17.575 | 17.107 | 16.825 | 16.991 | 16.796 | 17.373 |
| 43.25 | 19.260 | 18.762 | 18.776 | 19.644 | 18.676 | 19.320 | 19.093 | 19.106 | 19.225 | 18.840 | 18.424 | 18.643 |
| 43.50 | 16.940 | 16.814 | 17.032 | 17.268 | 17.212 | 17.288 | 17.496 | 17.580 | 17.160 | 17.329 | 16.632 | 17.005 |
| 43.75 | 16.290 | 16.196 | 16.709 | 17.160 | 16.948 | 16.670 | 16.819 | 16.781 | 17.055 | 16.410 | 16.606 | 16.620 |
| 44.00 | 16.440 | 16.423 | 16.809 | 17.281 | 16.900 | 16.680 | 16.993 | 17.155 | 17.052 | 16.786 | 16.424 | 16.855 |
| 44.25 | 16.070 | 16.230 | 17.156 | 17.226 | 16.360 | 16.917 | 16.636 | 17.107 | 17.062 | 17.328 | 16.528 | 16.782 |
| 44.50 | 16.140 | 16.047 | 16.990 | 16.620 | 16.520 | 16.862 | 16.671 | 16.766 | 16.533 | 16.312 | 17.030 | 16.136 |
| 44.75 | 15.990 | 16.212 | 16.610 | 16.750 | 16.200 | 16.322 | 16.842 | 16.890 | 16.860 | 16.400 | 15.977 | 16.220 |
| 45.00 | 16.010 | 16.150 | 16.524 | 16.490 | 16.260 | 16.661 | 16.739 | 17.240 | 16.240 | 16.260 | 16.207 | 16.136 |
| 45.25 | 16.810 | 16.551 | 16.810 | 17.680 | 16.427 | 16.870 | 17.472 | 17.550 | 17.260 | 16.928 | 16.803 | 16.593 |
| 45.50 | 16.460 | 16.428 | 16.507 | 17.196 | 16.532 | 16.982 | 16.693 | 16.844 | 16.591 | 16.265 | 16.416 | 15.757 |
| 45.75 | 17.460 | 17.050 | 17.500 | 17.864 | 17.401 | 17.517 | 17.534 | 17.584 | 17.958 | 17.417 | 17.283 | 17.216 |
| 46.00 | 16.870 | 17.809 | 16.784 | 17.068 | 16.551 | 17.240 | 17.196 | 17.340 | 17.072 | 16.880 | 16.304 | 16.509 |
| 46.25 | 16.390 | 16.321 | 16.220 | 16.800 | 15.642 | 16.779 | 16.700 | 16.471 | 16.609 | 16.436 | 16.060 | 15.880 |
| 46.50 | 16.270 | 15.863 | 16.431 | 16.192 | 16.366 | 16.453 | 16.151 | 16.181 | 16.821 | 16.450 | 16.200 | 15.746 |
| 46.75 | 16.280 | 15.760 | 16.569 | 16.540 | 15.566 | 15.744 | 16.340 | 16.222 | 16.520 | 16.311 | 15.739 | 16.381 |
| 47.00 | 15.990 | 16.321 | 16.148 | 16.828 | 15.810 | 16.540 | 16.248 | 16.570 | 16.190 | 16.340 | 15.471 | 16.014 |
| 47.25 | 16.100 | 15.692 | 16.320 | 16.360 | 16.299 | 16.436 | 15.734 | 16.761 | 16.300 | 15.912 | 16.208 | 15.800 |
| 47.50 | 16.780 | 16.637 | 16.384 | 16.984 | 16.314 | 16.660 | 16.980 | 17.300 | 16.898 | 16.625 | 16.170 | 16.482 |
| 47.75 | 16.780 | 16.263 | 16.024 | 16.904 | 16.110 | 16.407 | 16.395 | 16.836 | 16.234 | 16.480 | 16.011 | 16.159 |
| 48.00 | 16.180 | 16.394 | 16.006 | 16.010 | 15.822 | 16.458 | 16.620 | 16.622 | 16.300 | 15.674 | 15.349 | 16.010 |
| 48.25 | 15.940 | 15.985 | 16.240 | 16.804 | 16.240 | 16.390 | 16.223 | 16.576 | 16.280 | 15.755 | 15.860 | 15.629 |
| 48.50 | 16.130 | 16.414 | 16.510 | 16.450 | 16.171 | 16.540 | 16.275 | 15.936 | 16.160 | 16.313 | 16.063 | 16.036 |
| 48.75 | 16.160 | 16.292 | 15.461 | 16.412 | 15.914 | 16.370 | 16.010 | 16.731 | 16.427 | 15.990 | 15.580 | 15.936 |
| 49.00 | 16.100 | 15.978 | 15.825 | 16.720 | 16.263 | 16.549 | 16.913 | 16.758 | 16.036 | 15.916 | 16.155 | 15.930 |
| 49.25 | 16.710 | 16.162 | 16.180 | 16.500 | 16.046 | 16.762 | 16.849 | 16.770 | 16.657 | 16.525 | 16.152 | 16.290 |
| 49.50 | 16.760 | 16.450 | 16.367 | 17.341 | 16.512 | 17.039 | 16.205 | 17.260 | 17.026 | 16.394 | 16.320 | 16.387 |
| 49.75 | 16.560 | 16.176 | 15.701 | 16.592 | 16.540 | 16.614 | 16.917 | 16.100 | 16.376 | 16.701 | 15.710 | 16.186 |

| | | $I^E_{C+S}$ | | | | | | | | | | |
|---|---|---|---|---|---|---|---|---|---|---|---|---|
| Run Number | | 30 | 31 | 32 | 33 | 34 | 35 | 36 | 37 | 38 | 39 | 40 |
| Temperature (°C) | | -125 | -125 | -125 | -120 | -120 | -110 | -110 | -115 | -110 | -120 | -125 |
| Pressure (psia) | | 965.51 | 648.23 | 624.74 | 906.26 | 774.76 | 1058.23 | 815.85 | 915.75 | 1445.98 | 1350.46 | 1438.29 |
| Density (gm/cc) | | 0.910 | 0.780 | 0.280 | 0.780 | 0.536 | 0.536 | 0.280 | 0.536 | 0.780 | 0.910 | 0.982 |
| $\Theta$ | $I^E_C$ | | | | | | | | | | | |
| 50.00 | 16.380 | 15.917 | 16.075 | 16.676 | 16.075 | 15.368 | 16.368 | 16.676 | 16.369 | 16.074 | 15.918 | 15.830 |
| 50.25 | 16.330 | 16.001 | 15.940 | 16.520 | 16.123 | 15.144 | 16.353 | 17.009 | 16.391 | 15.970 | 15.758 | 15.602 |
| 50.50 | 16.520 | 15.997 | 15.839 | 16.523 | 16.235 | 15.346 | 16.543 | 16.840 | 16.588 | 16.100 | 16.304 | 15.835 |
| 50.75 | 16.570 | 16.033 | 16.190 | 16.328 | 16.000 | 15.922 | 16.266 | 17.224 | 16.259 | 16.310 | 16.167 | 15.980 |
| 51.00 | 16.750 | 16.234 | 16.160 | 16.525 | 16.240 | 15.791 | 16.742 | 16.940 | 16.694 | 16.486 | 16.327 | 16.381 |
| 51.25 | 17.440 | 16.778 | 16.792 | 17.864 | 17.150 | 17.460 | 17.361 | 17.373 | 17.219 | 17.040 | 17.142 | 16.940 |
| 51.50 | 16.910 | 16.241 | 16.440 | 16.382 | 16.346 | 15.767 | 16.571 | 16.900 | 16.190 | 15.609 | 15.833 | 16.158 |
| 51.75 | 17.200 | 16.482 | 16.738 | 16.779 | 16.737 | 15.573 | 17.009 | 16.903 | 16.438 | 16.055 | 16.287 | 15.874 |
| 52.00 | 17.650 | 16.967 | 17.100 | 17.028 | 16.603 | 16.942 | 16.995 | 17.680 | 17.150 | 16.858 | 16.509 | 17.090 |
| 52.25 | 17.100 | 16.304 | 16.360 | 16.870 | 16.459 | 16.676 | 16.620 | 16.825 | 16.649 | 16.762 | 16.130 | 16.110 |
| 52.50 | 16.980 | 16.403 | 16.446 | 17.170 | 16.568 | 16.888 | 17.190 | 17.200 | 16.938 | 16.988 | 16.670 | 16.448 |
| 52.75 | 16.900 | 16.270 | 16.197 | 16.800 | 16.372 | 16.339 | 16.655 | 17.556 | 16.752 | 16.411 | 16.123 | 16.150 |
| 53.00 | 17.020 | 16.772 | 16.515 | 16.889 | 16.319 | 16.813 | 16.992 | 16.940 | 16.712 | 16.800 | 16.186 | 16.470 |
| 53.25 | 17.960 | 16.756 | 17.040 | 17.750 | 17.162 | 17.362 | 17.496 | 18.469 | 17.320 | 17.212 | 16.844 | 16.893 |
| 53.50 | 17.190 | 16.433 | 16.375 | 16.933 | 16.636 | 16.745 | 17.744 | 17.157 | 17.011 | 16.640 | 15.963 | 16.280 |
| 53.75 | 18.010 | 16.760 | 16.567 | 17.699 | 17.145 | 17.912 | 17.445 | 17.756 | 17.201 | 17.230 | 16.558 | 16.665 |
| 54.00 | 17.280 | 16.145 | 16.940 | 17.170 | 16.331 | 16.857 | 17.120 | 16.914 | 17.260 | 16.372 | 16.400 | 16.353 |
| 54.25 | 17.770 | 16.600 | 16.767 | 17.570 | 16.875 | 18.100 | 17.377 | 18.049 | 17.562 | 16.716 | 16.948 | 17.033 |
| 54.50 | 18.460 | 17.649 | 17.736 | 18.318 | 17.200 | 17.775 | 17.867 | 18.690 | 18.120 | 17.690 | 17.420 | 17.100 |
| 54.75 | 17.750 | 16.355 | 16.950 | 17.570 | 16.880 | 17.482 | 17.352 | 17.844 | 17.198 | 16.920 | 17.160 | 16.916 |
| 55.00 | 18.290 | 17.160 | 17.439 | 18.070 | 17.393 | 17.852 | 18.100 | 18.466 | 18.290 | 17.820 | 16.282 | 17.194 |
| 55.25 | 18.100 | 16.890 | 17.323 | 17.995 | 17.288 | 17.979 | 17.768 | 18.026 | 17.432 | 17.550 | 16.915 | 16.921 |
| 55.50 | 18.040 | 17.008 | 16.969 | 17.444 | 17.100 | 17.280 | 17.401 | 17.937 | 17.341 | 16.449 | 17.320 | 16.626 |
| 55.75 | 18.090 | 16.946 | 17.020 | 18.052 | 17.080 | 17.980 | 17.579 | 17.998 | 17.670 | 17.155 | 17.060 | 17.011 |
| 56.00 | 18.140 | 16.783 | 17.250 | 18.259 | 17.205 | 17.893 | 17.988 | 17.760 | 17.391 | 16.980 | 17.000 | 16.760 |
| 56.25 | 18.170 | 17.005 | 17.330 | 18.031 | 17.373 | 17.528 | 17.513 | 18.060 | 17.172 | 17.680 | 16.669 | 17.055 |
| 56.50 | 18.160 | 17.161 | 17.360 | 18.589 | 17.493 | 17.926 | 17.820 | 18.677 | 18.053 | 17.550 | 16.840 | 16.777 |
| 56.75 | 19.260 | 17.670 | 18.323 | 18.702 | 18.134 | 17.854 | 18.493 | 19.267 | 18.381 | 17.355 | 17.454 | 17.710 |
| 57.00 | 18.940 | 17.463 | 17.688 | 19.024 | 17.648 | 18.133 | 18.099 | 18.957 | 18.214 | 17.900 | 17.650 | 17.840 |
| 57.25 | 19.190 | 17.748 | 18.154 | 19.681 | 17.930 | 18.248 | 18.796 | 19.409 | 18.247 | 18.420 | 17.651 | 17.910 |
| 57.50 | 18.900 | 17.369 | 17.760 | 18.300 | 17.885 | 18.228 | 18.438 | 18.777 | 18.425 | 17.780 | 17.520 | 17.520 |
| 57.75 | 19.750 | 17.849 | 18.600 | 18.850 | 18.126 | 19.243 | 18.902 | 20.007 | 18.223 | 18.440 | 19.980 | 18.330 |
| 58.00 | 18.910 | 17.904 | 17.700 | 18.470 | 17.893 | 18.530 | 17.940 | 18.779 | 18.074 | 17.899 | 17.460 | 17.380 |
| 58.25 | 20.080 | 18.411 | 18.589 | 19.420 | 18.570 | 19.443 | 18.680 | 20.002 | 19.405 | 19.160 | 17.986 | 18.091 |
| 58.50 | 19.250 | 17.516 | 18.020 | 19.020 | 18.062 | 18.414 | 18.970 | 19.437 | 18.392 | 17.081 | 17.811 | 17.729 |
| 58.75 | 19.350 | 17.630 | 18.220 | 19.605 | 18.403 | 18.699 | 19.350 | 19.625 | 18.648 | 17.911 | 17.930 | 17.874 |
| 59.00 | 19.330 | 18.175 | 18.429 | 18.980 | 18.194 | 18.494 | 18.756 | 19.213 | 18.469 | 18.320 | 18.064 | 18.280 |
| 59.25 | 20.120 | 18.560 | 19.100 | 19.480 | 18.707 | 19.157 | 19.007 | 20.417 | 19.404 | 18.756 | 18.186 | 18.390 |
| 59.50 | 19.440 | 17.945 | 18.540 | 18.850 | 17.749 | 18.708 | 18.773 | 19.177 | 18.997 | 17.977 | 17.810 | 17.874 |
| 59.75 | 19.910 | 18.135 | 18.082 | 19.430 | 18.810 | 19.357 | 19.701 | 20.014 | 19.219 | 18.320 | 18.450 | 18.270 |
| 60.00 | 19.840 | 18.464 | 18.480 | 19.460 | 18.111 | 18.831 | 18.821 | 19.336 | 19.156 | 18.760 | 18.417 | 18.430 |

TABLE 3

ATOMIC AND INCOHERENT SCATTERING FACTORS FOR ARGON

| $\Theta^*$ | S | $f_d^2$ | $(1/B^2)I^{inc}$ |
|---|---|---|---|
| 0.0 | 0.000 | 327.646 | 0.000 |
| 1.0 | 0.308 | 323.856 | 0.226 |
| 2.0 | 0.617 | 311.776 | 0.691 |
| 3.0 | 0.925 | 293.403 | 1.315 |
| 4.0 | 1.233 | 270.811 | 2.032 |
| 5.0 | 1.541 | 245.966 | 2.792 |
| 6.0 | 1.848 | 220.592 | 3.556 |
| 7.0 | 2.155 | 196.050 | 4.296 |
| 8.0 | 2.461 | 173.458 | 4.992 |
| 9.0 | 2.766 | 153.547 | 5.634 |
| 10.0 | 3.070 | 136.392 | 6.217 |
| 12.0 | 3.676 | 109.530 | 7.217 |
| 14.0 | 4.278 | 90.526 | 8.047 |
| 16.0 | 4.874 | 77.368 | 8.727 |
| 18.0 | 5.464 | 68.052 | 9.287 |
| 20.0 | 6.048 | 61.095 | 9.754 |
| 22.5 | 6.767 | 54.404 | 10.247 |
| 25.0 | 7.473 | 48.965 | 10.670 |
| 27.5 | 8.165 | 44.186 | 11.044 |
| 30.0 | 8.841 | 39.828 | 11.379 |
| 35.0 | 10.142 | 32.160 | 11.948 |
| 40.0 | 11.366 | 25.883 | 12.391 |
| 45.0 | 12.503 | 20.814 | 12.700 |
| 50.0 | 13.545 | 16.949 | 12.950 |
| 55.0 | 14.484 | 14.066 | 13.174 |
| 60.0 | 15.313 | 11.944 | 13.377 |

* $\Theta$ values for molybdenum K$\alpha$ radiation

TABLE 4

TOTAL COMPOSITE BEAM ABSORPTION FACTORS

(Includes correction for incoherent scattering)

Argon sample density = 0.982 gm/cc

| Θ | F(Θ) · ASSC(Θ) | ACC(Θ) | ACSC(Θ) |
|---|---|---|---|
| 0.0 | 0.22328 | 0.64573 | 0.25000 |
| 2.5 | 0.23588 | 0.64397 | 0.28718 |
| 5.0 | 0.24854 | 0.64228 | 0.32944 |
| 7.5 | 0.26112 | 0.64113 | 0.36975 |
| 10.0 | 0.27344 | 0.64085 | 0.40199 |
| 12.5 | 0.28536 | 0.64150 | 0.42352 |
| 15.0 | 0.29665 | 0.64288 | 0.43443 |
| 17.5 | 0.30715 | 0.64452 | 0.44180 |
| 20.0 | 0.31671 | 0.64627 | 0.44671 |
| 22.5 | 0.32519 | 0.64806 | 0.44937 |
| 25.0 | 0.33254 | 0.64976 | 0.45143 |
| 30.0 | 0.34380 | 0.65263 | 0.45442 |
| 35.0 | 0.35104 | 0.65458 | 0.46556 |
| 40.0 | 0.35511 | 0.65564 | 0.45792 |
| 45.0 | 0.35665 | 0.65599 | 0.45870 |
| 50.0 | 0.35589 | 0.65569 | 0.45906 |
| 55.0 | 0.35289 | 0.65470 | 0.45902 |
| 60.0 | 0.34744 | 0.65284 | 0.45858 |

TABLE 4 (continued)

TOTAL COMPOSITE BEAM ABSORPTION FACTORS

(Includes correction for incoherent scattering)

Argon sample density = 0.910 gm/cc

| Θ | F(Θ) · ASSC(Θ) | ACC(Θ) | ACSC(Θ) |
|---|---|---|---|
| 0.0 | 0.24261 | 0.64573 | 0.26638 |
| 2.5 | 0.25522 | 0.64397 | 0.30240 |
| 5.0 | 0.26784 | 0.64228 | 0.34304 |
| 7.5 | 0.28032 | 0.64113 | 0.38160 |
| 10.0 | 0.29249 | 0.64085 | 0.41233 |
| 12.5 | 0.30422 | 0.64150 | 0.43279 |
| 15.0 | 0.31528 | 0.64288 | 0.44322 |
| 17.5 | 0.32554 | 0.64452 | 0.45027 |
| 20.0 | 0.33485 | 0.64627 | 0.45500 |
| 22.5 | 0.34311 | 0.64806 | 0.45760 |
| 25.0 | 0.35022 | 0.64976 | 0.45964 |
| 30.0 | 0.36113 | 0.65263 | 0.46262 |
| 35.0 | 0.36807 | 0.65458 | 0.46476 |
| 40.0 | 0.37196 | 0.65564 | 0.46610 |
| 45.0 | 0.37336 | 0.65599 | 0.46687 |
| 50.0 | 0.37247 | 0.65569 | 0.46720 |
| 55.0 | 0.36939 | 0.65470 | 0.46713 |
| 60.0 | 0.36389 | 0.65284 | 0.46662 |

TABLE 4 (continued)

TOTAL COMPOSITE BEAM ABSORPTION FACTORS

(Includes correction for incoherent scattering)

Argon sample density = 0.780 gm/cc

| Θ | F(Θ) · ASSC(Θ) | ACC(Θ) | ACSC(Θ) |
|---|---|---|---|
| 0.0 | 0.28216 | 0.64573 | 0.29952 |
| 2.5 | 0.29460 | 0.64397 | 0.33303 |
| 5.0 | 0.30695 | 0.64228 | 0.37030 |
| 7.5 | 0.31907 | 0.64113 | 0.40532 |
| 10.0 | 0.33083 | 0.64085 | 0.43306 |
| 12.5 | 0.34202 | 0.64150 | 0.45144 |
| 15.0 | 0.35256 | 0,64288 | 0.46093 |
| 17.5 | 0.36223 | 0.64452 | 0.46737 |
| 20.0 | 0.37097 | 0.64627 | 0.47175 |
| 22.5 | 0.37868 | 0.64806 | 0.47425 |
| 25.0 | 0.38532 | 0.64976 | 0.47625 |
| 30.0 | 0.39540 | 0.65263 | 0.47922 |
| 35.0 | 0.40178 | 0.65458 | 0.48134 |
| 40.0 | 0.40531 | 0.65564 | 0.48267 |
| 45.0 | 0.40645 | 0.65599 | 0.48340 |
| 50.0 | 0.40539 | 0.65569 | 0.48368 |
| 55.0 | 0.40212 | 0.65470 | 0.48352 |
| 60.0 | 0.39652 | 0.65284 | 0.48291 |

TABLE 4 (continued)

TOTAL COMPOSITE BEAM ABSORPTION FACTORS

(Includes correction for incoherent scattering)

Argon sample density = 0.536 gm/cc

| Θ | F(Θ) · ASSC(Θ) | ACC(Θ) | ACSC(Θ) |
|---|---|---|---|
| 0.0 | 0.37599 | 0.64573 | 0.37655 |
| 2.5 | 0.38715 | 0.64347 | 0.40346 |
| 5.0 | 0.39808 | 0.64228 | 0.43255 |
| 7.5 | 0.40867 | 0.64113 | 0.45942 |
| 10.0 | 0.41878 | 0.64085 | 0.48046 |
| 12.5 | 0.42831 | 0.64150 | 0.49436 |
| 15.0 | 0.43714 | 0.64288 | 0.50181 |
| 17.5 | 0.44520 | 0.64452 | 0.50699 |
| 20.0 | 0.45239 | 0.64627 | 0.51063 |
| 22.5 | 0.45865 | 0.64806 | 0.51295 |
| 25.0 | 0.46400 | 0.64976 | 0.51486 |
| 30.0 | 0.47212 | 0.65263 | 0.51781 |
| 35.0 | 0.47718 | 0.65458 | 0.51990 |
| 40.0 | 0.47987 | 0.65564 | 0.52116 |
| 45.0 | 0.48044 | 0.65600 | 0.52181 |
| 50.0 | 0.47908 | 0.65569 | 0.52196 |
| 55.0 | 0.47569 | 0.65470 | 0.52163 |
| 60.0 | 0.47013 | 0.65284 | 0.52074 |

TABLE 4 (continued)

TOTAL COMPOSITE BEAM ABSORPTION FACTORS

(Includes correction for incoherent scattering)

Argon sample density = 0.280 gm/cc

| $\Theta$ | $F(\Theta) \cdot ASSC(\Theta)$ | $ACC(\Theta)$ | $ACSC(\Theta)$ |
|---|---|---|---|
| 0.0 | 0.51058 | 0.64573 | 0.48430 |
| 2.5 | 0.51835 | 0.64397 | 0.50059 |
| 5.0 | 0.52585 | 0.64228 | 0.51769 |
| 7.5 | 0.53301 | 0.64113 | 0.53325 |
| 10.0 | 0.53976 | 0.64085 | 0.54543 |
| 12.5 | 0.54604 | 0.64150 | 0.55368 |
| 15.0 | 0.55181 | 0.64288 | 0.55854 |
| 17.5 | 0.55701 | 0.64452 | 0.56216 |
| 20.0 | 0.56162 | 0.64627 | 0.56496 |
| 22.5 | 0.56564 | 0.64806 | 0.56705 |
| 25.0 | 0.56907 | 0.64976 | 0.56886 |
| 30.0 | 0.57430 | 0.65263 | 0.57178 |
| 35.0 | 0.57753 | 0.65458 | 0.57381 |
| 40.0 | 0.57910 | 0.65564 | 0.57500 |
| 45.0 | 0.57915 | 0.65600 | 0.57553 |
| 50.0 | 0.57758 | 0.65569 | 0.57550 |
| 55.0 | 0.57450 | 0.65470 | 0.57490 |
| 60.0 | 0.56958 | 0.65284 | 0.57363 |

TABLE 5

CORRECTION FACTORS FOR ARGON INCOHERENT SCATTERING

| Θ (deg) | $\gamma_s(\Theta)$ | $\psi^{inc}_{PHS}(\Theta)$ | Argon density 0.982 gm/cc | | Argon density 0.910 gm/cc | | Argon density 0.780 gm/cc | | Argon density 0.536 gm/cc | | Argon density 0.280 gm/cc | |
|---|---|---|---|---|---|---|---|---|---|---|---|---|
| | | | $\alpha^{inc}_{s,sc}(\Theta)$ | F(Θ) | $\alpha^{inc}_{s,sc}(\Theta)$ | F(Θ) | $\alpha^{inc}_{s,sc}(\Theta)$ | F(Θ) | $\alpha^{inc}_{s,sc}(\Theta)$ | F(Θ) | $\alpha^{inc}_{s,sc}(\Theta)$ | F(Θ) |
| 0 | 1.0000 | 1.0000 | 1.0000 | 1.0000 | 1.0000 | 1.0000 | 1.0000 | 1.0000 | 1.0000 | 1.0000 | 1.0000 | 1.0000 |
| 5 | 0.9888 | 1.0000 | 0.9988 | 1.0000 | 0.9989 | 1.0000 | 0.9991 | 1.0000 | 0.9994 | 1.0000 | 0.9996 | 1.0000 |
| 10 | 0.9564 | 1.0010 | 0.9974 | 0.9999 | 0.9976 | 0.9999 | 0.9980 | 1.0000 | 0.9986 | 1.0000 | 0.9992 | 1.0000 |
| 15 | 0.9084 | 1.0017 | 0.9959 | 0.9998 | 0.9962 | 0.9998 | 0.9968 | 0.9999 | 0.9977 | 1.0000 | 0.9987 | 1.0000 |
| 20 | 0.8623 | 1.0026 | 0.9942 | 0.9996 | 0.9946 | 0.9996 | 0.9954 | 0.9997 | 0.9968 | 1.0000 | 0.9981 | 1.0000 |
| 25 | 0.8211 | 1.0033 | 0.9925 | 0.9992 | 0.9930 | 0.9993 | 0.9940 | 0.9995 | 0.9957 | 0.9998 | 0.9975 | 1.0000 |
| 30 | 0.7778 | 1.0035 | 0.9908 | 0.9987 | 0.9914 | 0.9989 | 0.9926 | 0.9991 | 0.9946 | 0.9996 | 0.9969 | 1.0000 |
| 35 | 0.7291 | 1.0028 | 0.9889 | 0.9978 | 0.9897 | 0.9980 | 0.9910 | 0.9983 | 0.9935 | 0.9990 | 0.9962 | 0.9997 |
| 40 | 0.6763 | 1.0015 | 0.9868 | 0.9962 | 0.9877 | 0.9965 | 0.9893 | 0.9970 | 0.9922 | 0.9980 | 0.9955 | 0.9990 |
| 45 | 0.6211 | 0.9993 | 0.9843 | 0.9938 | 0.9854 | 0.9942 | 0.9873 | 0.9949 | 0.9908 | 0.9962 | 0.9946 | 0.9977 |
| 50 | 0.5669 | 0.9960 | 0.9815 | 0.9903 | 0.9827 | 0.9908 | 0.9849 | 0.9918 | 0.9892 | 0.9936 | 0.9936 | 0.9955 |
| 55 | 0.5164 | 0.9921 | 0.9782 | 0.9857 | 0.9796 | 0.9864 | 0.9822 | 0.9876 | 0.9872 | 0.9900 | 0.9924 | 0.9926 |
| 60 | 0.4717 | 0.9878 | 0.9734 | 0.9797 | 0.9753 | 0.9807 | 0.9786 | 0.9824 | 0.9845 | 0.9855 | 0.9908 | 0.9887 |

TABLE 6

INTENSITY NORMALIZATION AND MODIFICATION VALUES

$$[I_s(\Theta)]_{eu} = (C/N)(1 + B\Theta) I_s(\Theta)$$

| Run No. | C/N (eu/cps) | B ($deg^{-1}$) |
|---|---|---|
| 22 | 0.905 | 0.0028 |
| 23 | 0.873 | 0.0039 |
| 30 | 1.186 | 0.0029 |
| 31 | 1.292 | 0.0037 |
| 32 | 2.790 | 0.0106 |
| 33 | 1.336 | 0.0028 |
| 34 | 1.643 | 0.0065 |
| 35 | 1.575 | 0.0078 |
| 36 | 2.538 | 0.0100 |
| 37 | 1.627 | 0.0067 |
| 38 | 1.330 | 0.0031 |
| 39 | 1.195 | 0.0026 |
| 40 | 1.096 | 0.0023 |

TABLE 7

SUMMARY OF THE SMOOTH ARGON INTENSITY FUNCTIONS

$$j(S) = \frac{(C/N)\,\phi(S)\,I_s(S)}{f_d^2(S) + I^{inc}(S)}$$

| | j (S) | | | | | | | | | | | | |
|---|---|---|---|---|---|---|---|---|---|---|---|---|---|
| Run Number | 22 | 23 | 30 | 31 | 32 | 33 | 34 | 35 | 36 | 37 | 38 | 39 | 40 |
| Temperature (°C) | -130 | -130 | -125 | -125 | -125 | -120 | -120 | -110 | -110 | -115 | -110 | -120 | -125 |
| Pressure (psia) | 586.60 | 964.53 | 965.51 | 648.23 | 624.74 | 906.26 | 774.76 | 1058.23 | 815.85 | 915.75 | 1445.98 | 1350.46 | 1438.29 |
| Density (gm/cc) | 0.910 | 0.982 | 0.910 | 0.780 | 0.280 | 0.780 | 0.536 | 0.536 | 0.280 | 0.536 | 0.780 | 0.910 | 0.982 |
| $S(\mathring{A}^{-1})$ | | | | | | | | | | | | | |
| 0.31 | 0.379 | 0.293 | 0.385 | 0.598 | 1.151 | 0.637 | 0.924 | 0.912 | 1.121 | 0.926 | 0.612 | 0.411 | 0.317 |
| 0.39 | 0.339 | 0.271 | 0.350 | 0.499 | 0.958 | 0.557 | 0.754 | 0.759 | 0.979 | 0.759 | 0.544 | 0.372 | 0.304 |
| 0.46 | 0.311 | 0.262 | 0.319 | 0.440 | 0.823 | 0.494 | 0.656 | 0.674 | 0.865 | 0.669 | 0.503 | 0.362 | 0.292 |
| 0.54 | 0.299 | 0.254 | 0.308 | 0.404 | 0.750 | 0.470 | 0.588 | 0.608 | 0.799 | 0.599 | 0.474 | 0.344 | 0.281 |
| 0.62 | 0.298 | 0.256 | 0.302 | 0.387 | 0.694 | 0.435 | 0.557 | 0.566 | 0.739 | 0.566 | 0.457 | 0.338 | 0.283 |
| 0.69 | 0.292 | 0.264 | 0.297 | 0.381 | 0.649 | 0.432 | 0.524 | 0.547 | 0.701 | 0.534 | 0.445 | 0.338 | 0.286 |
| 0.77 | 0.296 | 0.265 | 0.297 | 0.378 | 0.637 | 0.431 | 0.516 | 0.533 | 0.687 | 0.525 | 0.443 | 0.339 | 0.293 |
| 0.85 | 0.304 | 0.265 | 0.306 | 0.381 | 0.636 | 0.435 | 0.517 | 0.545 | 0.686 | 0.527 | 0.448 | 0.346 | 0.304 |
| 0.93 | 0.324 | 0.294 | 0.318 | 0.393 | 0.646 | 0.452 | 0.528 | 0.570 | 0.700 | 0.540 | 0.463 | 0.361 | 0.319 |
| 1.00 | 0.346 | 0.313 | 0.355 | 0.417 | 0.671 | 0.474 | 0.553 | 0.590 | 0.722 | 0.566 | 0.490 | 0.384 | 0.340 |
| 1.08 | 0.373 | 0.342 | 0.384 | 0.451 | 0.703 | 0.511 | 0.591 | 0.620 | 0.752 | 0.603 | 0.529 | 0.427 | 0.373 |
| 1.16 | 0.429 | 0.391 | 0.421 | 0.512 | 0.742 | 0.567 | 0.644 | 0.675 | 0.786 | 0.654 | 0.588 | 0.473 | 0.421 |
| 1.23 | 0.496 | 0.459 | 0.507 | 0.560 | 0.786 | 0.645 | 0.707 | 0.742 | 0.827 | 0.716 | 0.663 | 0.546 | 0.485 |
| 1.31 | 0.575 | 0.524 | 0.566 | 0.642 | 0.837 | 0.739 | 0.784 | 0.801 | 0.877 | 0.795 | 0.754 | 0.637 | 0.568 |
| 1.39 | 0.676 | 0.645 | 0.663 | 0.759 | 0.894 | 0.853 | 0.869 | 0.898 | 0.931 | 0.880 | 0.863 | 0.746 | 0.670 |
| 1.46 | 0.782 | 0.784 | 0.793 | 0.880 | 0.952 | 0.989 | 0.965 | 1.013 | 0.989 | 0.980 | 0.997 | 0.881 | 0.800 |
| 1.54 | 0.939 | 0.919 | 0.945 | 1.040 | 1.015 | 1.140 | 1.070 | 1.125 | 1.045 | 1.085 | 1.150 | 1.039 | 0.964 |
| 1.62 | 1.121 | 1.113 | 1.119 | 1.192 | 1.075 | 1.298 | 1.173 | 1.214 | 1.093 | 1.188 | 1.300 | 1.220 | 1.157 |
| 1.70 | 1.308 | 1.311 | 1.303 | 1.342 | 1.120 | 1.458 | 1.266 | 1.281 | 1.178 | 1.276 | 1.448 | 1.421 | 1.408 |
| 1.77 | 1.449 | 1.523 | 1.457 | 1.462 | 1.143 | 1.548 | 1.332 | 1.332 | 1.152 | 1.340 | 1.560 | 1.583 | 1.565 |
| 1.85 | 1.530 | 1.605 | 1.572 | 1.552 | 1.151 | 1.649 | 1.373 | 1.380 | 1.165 | 1.377 | 1.623 | 1.689 | 1.730 |
| 1.93 | 1.527 | 1.612 | 1.589 | 1.549 | 1.150 | 1.660 | 1.375 | 1.369 | 1.162 | 1.372 | 1.626 | 1.697 | 1.731 |
| 2.00 | 1.482 | 1.519 | 1.509 | 1.508 | 1.139 | 1.603 | 1.347 | 1.326 | 1.156 | 1.340 | 1.583 | 1.633 | 1.673 |
| 2.08 | 1.349 | 1.416 | 1.402 | 1.394 | 1.123 | 1.484 | 1.299 | 1.283 | 1.142 | 1.290 | 1.507 | 1.529 | 1.528 |
| 2.16 | 1.253 | 1.279 | 1.311 | 1.312 | 1.098 | 1.386 | 1.235 | 1.239 | 1.115 | 1.230 | 1.395 | 1.400 | 1.398 |
| 2.23 | 1.157 | 1.158 | 1.219 | 1.199 | 1.071 | 1.283 | 1.169 | 1.174 | 1.086 | 1.170 | 1.293 | 1.267 | 1.254 |
| 2.31 | 1.059 | 1.080 | 1.111 | 1.120 | 1.034 | 1.196 | 1.111 | 1.118 | 1.059 | 1.118 | 1.193 | 1.193 | 1.159 |
| 2.38 | 0.988 | 1.002 | 1.029 | 1.054 | 1.000 | 1.117 | 1.064 | 1.065 | 1.034 | 1.076 | 1.112 | 1.091 | 1.068 |
| 2.46 | 0.932 | 0.946 | 0.977 | 0.993 | 0.975 | 1.051 | 1.029 | 1.016 | 1.012 | 1.040 | 1.045 | 1.019 | 0.995 |
| 2.54 | 0.895 | 0.907 | 0.927 | 0.953 | 0.954 | 0.995 | 0.995 | 0.981 | 0.996 | 1.004 | 0.991 | 0.964 | 0.942 |
| 2.61 | 0.876 | 0.879 | 0.899 | 0.921 | 0.942 | 0.952 | 0.956 | 0.952 | 0.981 | 0.975 | 0.950 | 0.915 | 0.902 |
| 2.69 | 0.858 | 0.865 | 0.881 | 0.903 | 0.937 | 0.923 | 0.936 | 0.928 | 0.964 | 0.951 | 0.922 | 0.888 | 0.880 |
| 2.77 | 0.854 | 0.867 | 0.869 | 0.894 | 0.943 | 0.908 | 0.921 | 0.914 | 0.952 | 0.936 | 0.906 | 0.869 | 0.867 |
| 2.84 | 0.857 | 0.871 | 0.877 | 0.903 | 0.947 | 0.906 | 0.924 | 0.915 | 0.950 | 0.932 | 0.899 | 0.869 | 0.867 |
| 2.92 | 0.870 | 0.881 | 0.890 | 0.912 | 0.951 | 0.921 | 0.931 | 0.924 | 0.958 | 0.937 | 0.904 | 0.883 | 0.874 |
| 2.99 | 0.895 | 0.895 | 0.906 | 0.925 | 0.962 | 0.942 | 0.953 | 0.939 | 0.966 | 0.946 | 0.924 | 0.906 | 0.889 |
| 3.07 | 0.927 | 0.919 | 0.930 | 0.942 | 0.969 | 0.964 | 0.963 | 0.958 | 0.974 | 0.958 | 0.951 | 0.932 | 0.905 |
| 3.15 | 0.964 | 0.952 | 0.963 | 0.963 | 0.977 | 0.987 | 0.979 | 0.980 | 0.980 | 0.974 | 0.976 | 0.961 | 0.936 |
| 3.22 | 1.000 | 0.992 | 0.993 | 0.985 | 0.986 | 1.013 | 1.002 | 1.000 | 0.987 | 0.989 | 1.004 | 0.994 | 0.972 |
| 3.30 | 1.034 | 1.022 | 1.019 | 1.010 | 0.994 | 1.035 | 1.026 | 1.014 | 0.996 | 1.007 | 1.029 | 1.023 | 1.003 |

| | j (S) | | | | | | | | | | | | |
|---|---|---|---|---|---|---|---|---|---|---|---|---|---|
| Run Number | 22 | 23 | 30 | 31 | 32 | 33 | 34 | 35 | 36 | 37 | 38 | 39 | 40 |
| Temperature (°C) | -130 | -130 | -125 | -125 | -125 | -120 | -120 | -110 | -110 | -115 | -110 | -120 | -125 |
| Pressure (psia) | 586.60 | 964.53 | 965.51 | 648.23 | 624.74 | 906.26 | 774.76 | 1058.23 | 815.85 | 915.75 | 1445.98 | 1350.46 | 1438.29 |
| Density (gm/cc) | 0.910 | 0.982 | 0.910 | 0.780 | 0.280 | 0.780 | 0.536 | 0.536 | 0.280 | 0.536 | 0.780 | 0.910 | 0.982 |
| $S(\text{Å}^{o-1})$ | | | | | | | | | | | | | |
| 3.37 | 1.061 | 1.052 | 1.045 | 1.041 | 1.001 | 1.060 | 1.056 | 1.032 | 1.001 | 1.024 | 1.049 | 1.055 | 1.039 |
| 3.45 | 1.080 | 1.074 | 1.059 | 1.061 | 1.009 | 1.070 | 1.065 | 1.039 | 1.006 | 1.037 | 1.064 | 1.077 | 1.069 |
| 3.53 | 1.089 | 1.087 | 1.066 | 1.074 | 1.013 | 1.073 | 1.073 | 1.039 | 1.007 | 1.046 | 1.067 | 1.083 | 1.090 |
| 3.60 | 1.090 | 1.095 | 1.072 | 1.075 | 1.014 | 1.064 | 1.064 | 1.023 | 1.005 | 1.050 | 1.057 | 1.073 | 1.093 |
| 3.68 | 1.087 | 1.095 | 1.071 | 1.071 | 1.014 | 1.043 | 1.041 | 1.006 | 0.999 | 1.046 | 1.031 | 1.054 | 1.090 |
| 3.75 | 1.076 | 1.082 | 1.065 | 1.053 | 1.008 | 1.025 | 1.023 | 0.990 | 0.994 | 1.042 | 1.019 | 1.033 | 1.072 |
| 3.83 | 1.059 | 1.061 | 1.054 | 1.039 | 1.004 | 1.007 | 1.012 | 0.981 | 0.987 | 1.033 | 1.005 | 1.014 | 1.056 |
| 3.90 | 1.040 | 1.038 | 1.037 | 1.019 | 0.998 | 0.989 | 0.994 | 0.969 | 0.984 | 1.021 | 0.988 | 0.998 | 1.039 |
| 3.98 | 1.021 | 1.018 | 1.023 | 1.007 | 0.992 | 0.979 | 0.984 | 0.959 | 0.980 | 1.011 | 0.972 | 0.987 | 1.020 |
| 4.05 | 1.003 | 0.988 | 1.006 | 0.992 | 0.981 | 0.971 | 0.978 | 0.950 | 0.974 | 0.995 | 0.959 | 0.974 | 1.006 |
| 4.13 | 0.991 | 0.969 | 0.997 | 0.982 | 0.975 | 0.961 | 0.972 | 0.947 | 0.970 | 0.980 | 0.945 | 0.966 | 0.986 |
| 4.20 | 0.983 | 0.960 | 0.983 | 0.971 | 0.969 | 0.954 | 0.964 | 0.944 | 0.968 | 0.967 | 0.935 | 0.952 | 0.964 |
| 4.28 | 0.976 | 0.957 | 0.979 | 0.963 | 0.962 | 0.951 | 0.961 | 0.945 | 0.966 | 0.959 | 0.929 | 0.942 | 0.945 |
| 4.35 | 0.971 | 0.957 | 0.969 | 0.957 | 0.959 | 0.950 | 0.960 | 0.947 | 0.966 | 0.956 | 0.928 | 0.936 | 0.941 |
| 4.43 | 0.966 | 0.959 | 0.961 | 0.953 | 0.955 | 0.949 | 0.961 | 0.954 | 0.962 | 0.957 | 0.931 | 0.935 | 0.937 |
| 4.50 | 0.964 | 0.959 | 0.957 | 0.953 | 0.958 | 0.952 | 0.964 | 0.961 | 0.963 | 0.959 | 0.937 | 0.936 | 0.934 |
| 4.58 | 0.967 | 0.959 | 0.958 | 0.954 | 0.959 | 0.955 | 0.965 | 0.967 | 0.967 | 0.963 | 0.940 | 0.940 | 0.931 |
| 4.73 | 0.982 | 0.966 | 0.964 | 0.960 | 0.970 | 0.967 | 0.975 | 0.981 | 0.974 | 0.968 | 0.952 | 0.949 | 0.936 |
| 4.87 | 0.998 | 0.977 | 0.974 | 0.975 | 0.980 | 0.981 | 0.986 | 0.995 | 0.986 | 0.979 | 0.967 | 0.967 | 0.956 |
| 5.02 | 1.016 | 0.988 | 0.993 | 0.992 | 0.992 | 0.996 | 0.997 | 1.006 | 0.989 | 0.991 | 0.984 | 0.983 | 0.977 |
| 5.17 | 1.030 | 0.999 | 1.012 | 1.009 | 1.001 | 1.009 | 1.009 | 1.012 | 0.994 | 1.007 | 0.998 | 0.999 | 0.997 |
| 5.32 | 1.037 | 1.010 | 1.027 | 1.020 | 1.008 | 1.019 | 1.015 | 1.018 | 0.999 | 1.015 | 1.010 | 1.013 | 1.020 |
| 5.46 | 1.037 | 1.014 | 1.029 | 1.025 | 1.014 | 1.024 | 1.018 | 1.022 | 1.002 | 1.019 | 1.016 | 1.022 | 1.032 |
| 5.61 | 1.033 | 1.016 | 1.023 | 1.021 | 1.018 | 1.028 | 1.017 | 1.020 | 1.006 | 1.021 | 1.021 | 1.025 | 1.030 |
| 5.76 | 1.019 | 1.012 | 1.012 | 1.015 | 1.017 | 1.026 | 1.009 | 1.020 | 1.009 | 1.022 | 1.024 | 1.023 | 1.024 |
| 5.90 | 1.010 | 1.001 | 1.004 | 1.009 | 1.012 | 1.022 | 1.005 | 1.016 | 1.015 | 1.014 | 1.021 | 1.013 | 1.016 |
| 6.05 | 0.998 | 0.990 | 0.997 | 1.004 | 1.009 | 1.014 | 0.994 | 1.011 | 1.011 | 1.008 | 1.012 | 1.006 | 1.005 |
| 6.19 | 0.991 | 0.984 | 0.989 | 0.997 | 1.008 | 1.004 | 0.988 | 1.006 | 1.011 | 1.000 | 1.007 | 0.998 | 0.996 |
| 6.34 | 0.984 | 0.982 | 0.981 | 0.989 | 1.006 | 0.993 | 0.982 | 1.002 | 1.012 | 0.991 | 0.999 | 0.989 | 0.988 |
| 6.48 | 0.981 | 0.983 | 0.977 | 0.984 | 1.006 | 0.987 | 0.979 | 0.996 | 1.013 | 0.988 | 0.991 | 0.983 | 0.982 |
| 6.62 | 0.980 | 0.988 | 0.976 | 0.982 | 1.005 | 0.979 | 0.978 | 0.990 | 1.011 | 0.982 | 0.985 | 0.979 | 0.981 |
| 6.77 | 0.979 | 0.993 | 0.982 | 0.983 | 1.006 | 0.977 | 0.977 | 0.987 | 1.009 | 0.978 | 0.980 | 0.978 | 0.981 |
| 6.91 | 0.982 | 0.997 | 0.988 | 0.988 | 1.007 | 0.979 | 0.978 | 0.984 | 1.007 | 0.977 | 0.978 | 0.980 | 0.985 |
| 7.05 | 0.984 | 1.005 | 0.994 | 0.993 | 1.007 | 0.982 | 0.982 | 0.986 | 1.007 | 0.975 | 0.977 | 0.985 | 0.990 |
| 7.19 | 0.989 | 1.006 | 0.998 | 0.997 | 1.009 | 0.986 | 0.986 | 0.989 | 1.006 | 0.975 | 0.977 | 0.989 | 0.993 |
| 7.33 | 0.992 | 1.004 | 1.001 | 0.999 | 1.015 | 0.993 | 0.991 | 0.989 | 1.005 | 0.979 | 0.977 | 0.993 | 0.999 |
| 7.47 | 0.995 | 1.001 | 1.007 | 1.001 | 1.011 | 0.997 | 0.998 | 0.993 | 1.002 | 0.981 | 0.979 | 0.998 | 1.004 |
| 7.61 | 0.998 | 0.996 | 1.009 | 1.003 | 1.009 | 1.000 | 1.000 | 0.996 | 1.000 | 0.988 | 0.981 | 1.004 | 1.005 |
| 7.75 | 1.001 | 0.992 | 1.006 | 0.999 | 1.009 | 1.004 | 1.002 | 1.000 | 1.000 | 0.993 | 0.985 | 1.008 | 1.008 |
| 7.89 | 1.002 | 0.992 | 1.001 | 1.000 | 1.010 | 1.006 | 1.005 | 1.003 | 1.001 | 0.996 | 0.992 | 1.010 | 1.007 |

| | j (S) | | | | | | | | | | | | |
|---|---|---|---|---|---|---|---|---|---|---|---|---|---|
| Run Number | 22 | 23 | 30 | 31 | 32 | 33 | 34 | 35 | 36 | 37 | 38 | 39 | 40 |
| Temperature (°C) | -130 | -130 | -125 | -125 | -125 | -120 | -120 | -110 | -110 | -115 | -110 | -120 | -125 |
| Pressure (psia) | 586.60 | 964.53 | 965.51 | 648.23 | 624.74 | 906.26 | 774.76 | 1058.23 | 815.85 | 915.75 | 1445.98 | 1350.46 | 1438.29 |
| Density (gm/cc) | 0.910 | 0.982 | 0.910 | 0.780 | 0.280 | 0.780 | 0.536 | 0.536 | 0.280 | 0.536 | 0.780 | 0.910 | 0.982 |
| $S(\mathring{A}^{o-1})$ | | | | | | | | | | | | | |
| 8.03 | 1.000 | 0.994 | 0.998 | 0.999 | 1.009 | 1.007 | 1.004 | 1.003 | 1.001 | 1.002 | 0.997 | 1.011 | 1.006 |
| 8.17 | 0.999 | 0.994 | 0.996 | 0.995 | 1.006 | 1.005 | 1.008 | 1.005 | 0.999 | 1.007 | 0.999 | 1.013 | 1.006 |
| 8.30 | 1.000 | 0.997 | 0.992 | 0.991 | 1.003 | 1.002 | 1.003 | 1.005 | 0.999 | 1.011 | 0.999 | 1.011 | 1.001 |
| 8.44 | 0.999 | 0.996 | 0.995 | 0.990 | 1.002 | 0.996 | 1.006 | 1.000 | 0.998 | 1.010 | 0.998 | 1.007 | 1.001 |
| 8.57 | 1.000 | 0.998 | 0.995 | 0.989 | 0.998 | 0.993 | 1.005 | 1.001 | 0.998 | 1.011 | 1.000 | 1.004 | 1.000 |
| 8.71 | 0.998 | 1.000 | 0.999 | 0.989 | 0.997 | 0.994 | 1.005 | 1.002 | 0.999 | 1.006 | 1.004 | 0.999 | 0.999 |
| 8.84 | 1.000 | 1.003 | 0.999 | 0.990 | 0.995 | 0.991 | 1.007 | 1.001 | 0.999 | 1.002 | 1.008 | 0.995 | 0.999 |
| 8.97 | 0.997 | 1.002 | 0.998 | 0.993 | 0.996 | 0.990 | 1.005 | 1.003 | 0.999 | 1.006 | 1.007 | 0.993 | 0.997 |
| 9.11 | 0.998 | 1.002 | 1.001 | 0.995 | 0.996 | 0.993 | 1.006 | 1.001 | 1.000 | 1.005 | 1.007 | 0.993 | 0.996 |
| 9.24 | 0.998 | 1.003 | 0.999 | 0.998 | 0.996 | 0.996 | 1.004 | 1.001 | 1.003 | 1.004 | 1.007 | 0.995 | 0.995 |
| 9.37 | 0.996 | 1.005 | 1.003 | 1.000 | 0.999 | 0.996 | 1.001 | 0.998 | 1.004 | 0.999 | 1.007 | 0.995 | 0.995 |
| 9.50 | 0.997 | 1.005 | 1.001 | 1.001 | 0.998 | 0.999 | 1.002 | 0.998 | 1.004 | 1.000 | 1.009 | 0.994 | 0.994 |
| 9.63 | 0.996 | 1.007 | 1.000 | 1.002 | 0.998 | 0.999 | 1.003 | 1.000 | 1.005 | 0.999 | 1.009 | 0.994 | 0.996 |
| 9.76 | 0.996 | 1.005 | 0.999 | 1.003 | 1.000 | 0.997 | 1.003 | 0.998 | 1.008 | 1.002 | 1.007 | 0.993 | 0.996 |
| 9.89 | 1.002 | 1.004 | 1.000 | 1.004 | 0.998 | 0.997 | 1.002 | 0.996 | 1.009 | 1.002 | 1.007 | 0.995 | 0.996 |
| 10.02 | 1.002 | 1.003 | 1.000 | 1.003 | 1.000 | 0.996 | 1.002 | 0.998 | 1.013 | 1.003 | 1.007 | 0.997 | 0.998 |
| 10.14 | 1.002 | 1.000 | 0.999 | 1.002 | 0.998 | 0.999 | 1.001 | 1.000 | 1.013 | 1.004 | 1.008 | 1.000 | 0.998 |
| 10.39 | 1.002 | 1.000 | 1.000 | 1.002 | 1.000 | 1.006 | 0.999 | 1.002 | 1.009 | 1.003 | 1.005 | 1.001 | 0.998 |
| 10.64 | 1.002 | 1.001 | 1.000 | 1.001 | 1.001 | 1.005 | 0.993 | 1.002 | 1.008 | 1.000 | 1.003 | 1.002 | 0.998 |
| 10.89 | 1.002 | 1.000 | 0.998 | 1.003 | 1.001 | 1.004 | 0.997 | 0.999 | 1.005 | 1.000 | 1.003 | 1.002 | 1.000 |
| 11.13 | 1.002 | 1.001 | 0.994 | 1.006 | 1.003 | 1.005 | 0.996 | 0.999 | 1.003 | 0.999 | 1.000 | 1.004 | 1.001 |
| 11.37 | 1.000 | 0.998 | 0.995 | 1.005 | 1.007 | 1.006 | 1.001 | 1.000 | 1.007 | 1.001 | 1.000 | 1.004 | 1.001 |
| 11.60 | 0.999 | 0.999 | 0.995 | 1.005 | 1.006 | 1.005 | 1.001 | 1.002 | 1.001 | 0.999 | 0.996 | 1.006 | 1.005 |
| 11.83 | 0.999 | 1.000 | 0.997 | 1.004 | 1.000 | 1.003 | 1.000 | 1.004 | 1.001 | 0.998 | 0.997 | 1.001 | 1.001 |
| 12.06 | 0.999 | 1.000 | 1.000 | 1.003 | 0.998 | 1.002 | 0.999 | 1.008 | 0.996 | 1.000 | 0.996 | 1.003 | 1.001 |
| 12.28 | 0.999 | 0.998 | 1.002 | 1.001 | 0.998 | 0.998 | 1.000 | 1.006 | 0.991 | 1.001 | 0.996 | 0.997 | 1.003 |
| 12.50 | 1.001 | 0.998 | 1.004 | 1.000 | 0.999 | 0.997 | 1.001 | 1.007 | 0.984 | 0.999 | 0.995 | 1.001 | 1.004 |
| 12.72 | 1.001 | 0.999 | 1.007 | 1.002 | 0.992 | 0.992 | 1.001 | 1.002 | 0.979 | 0.996 | 0.997 | 1.001 | 1.005 |
| 12.93 | 1.001 | 0.999 | 1.004 | 0.999 | 0.983 | 0.989 | 1.002 | 1.002 | 0.978 | 0.990 | 0.999 | 1.000 | 1.004 |
| 13.14 | 1.000 | 1.000 | 1.003 | 0.996 | 0.976 | 0.985 | 1.002 | 0.997 | 0.981 | 0.986 | 1.000 | 1.001 | 1.004 |
| 13.35 | 1.000 | 1.000 | 1.001 | 0.995 | 0.971 | 0.981 | 1.001 | 1.001 | 0.982 | 0.983 | 0.999 | 1.002 | 1.002 |
| 13.55 | 1.001 | 1.000 | 0.999 | 0.994 | 0.965 | 0.978 | 1.000 | 0.993 | 0.983 | 0.981 | 0.998 | 1.000 | 1.001 |
| 13.74 | 1.002 | 1.000 | 0.997 | 0.993 | 0.960 | 0.974 | 0.998 | 0.996 | 0.985 | 0.979 | 0.996 | 0.998 | 1.000 |
| 13.93 | 1.003 | 1.000 | 0.995 | 0.992 | 0.954 | 0.971 | 0.997 | 0.990 | 0.989 | 0.978 | 0.995 | 0.996 | 0.999 |
| 14.12 | 1.005 | 1.000 | 0.992 | 0.992 | 0.949 | 0.969 | 0.996 | 0.993 | 0.995 | 0.977 | 0.994 | 0.994 | 0.997 |
| 14.31 | 1.008 | 1.001 | 0.990 | 0.992 | 0.945 | 0.966 | 0.995 | 0.992 | 1.002 | 0.978 | 0.992 | 0.992 | 0.997 |
| 14.48 | 1.012 | 1.002 | 0.988 | 0.994 | 0.941 | 0.964 | 0.994 | 0.992 | 1.011 | 0.979 | 0.992 | 0.990 | 0.996 |
| 14.66 | 1.017 | 1.004 | 0.985 | 0.995 | 0.937 | 0.963 | 0.993 | 0.992 | 1.022 | 0.981 | 0.991 | 0.989 | 0.996 |
| 14.83 | 1.023 | 1.007 | 0.983 | 0.998 | 0.935 | 0.962 | 0.993 | 0.993 | 1.036 | 0.984 | 0.991 | 0.988 | 0.996 |
| 15.00 | 1.026 | 1.010 | 0.982 | 1.002 | 0.934 | 0.963 | 0.994 | 0.995 | 1.052 | 0.988 | 0.991 | 0.987 | 0.997 |

TABLE 8

GENERAL FEATURES OF THE ARGON INTENSITY PATTERNS

| Run No. | Location of Peaks S ($\AA^{-1}$) | | | Main Peak | |
|---|---|---|---|---|---|
| | First | Second | Third | Height j (S) | Width $\Delta S$ ($\AA^{-1}$) |
| 22 | 1.90 | 3.60 | 5.4 | 1.54 | 0.82 |
| 23 | 1.87 | 3.62 | 5.6 | 1.62 | 0.82 |
| 30 | 1.89 | 3.61 | 5.5 | 1.58 | 0.86 |
| 31 | 1.89 | 3.58 | 5.5 | 1.56 | 0.94 |
| 32 | 1.89 | 3.61 | - | 1.15 | 0.88 |
| 33 | 1.89 | 3.50 | 5.6 | 1.66 | 1.06 |
| 34 | 1.88 | 3.50 | 5.5 | 1.38 | 1.02 |
| 35 | 1.89 | 3.47 | 5.7 | 1.38 | 1.06 |
| 36 | 1.90 | 3.52 | - | 1.17 | 1.04 |
| 37 | 1.88 | 3.62 | 5.7 | 1.38 | 1.06 |
| 38 | 1.90 | 3.50 | 5.8 | 1.63 | 1.07 |
| 39 | 1.90 | 3.52 | 5.7 | 1.70 | 0.96 |
| 40 | 1.90 | 3.61 | 5.6 | 1.73 | 0.91 |
| AVG. | $1.89 \pm .01$ | $3.56 \pm .06$ | $5.6 \pm .2$ | | |

TABLE 9

NORMALIZATION CONSTANTS AND TRUNCATION LIMITS USED IN THE FOURIER INVERSION

| Run No. | Atomic and Electronic Radial Density | | Atomic Radial Distribution Function |
|---|---|---|---|
| | C/N (cps/eu) | S ($A^{o-1}$) | S range ($A^{o-1}$) |
| 22 | 0.907 | 7.64 | 7.6 - 9.2 |
| 23 | 0.879 | 7.85 | 6.8 - 10.2 |
| 30 | 1.179 | 7.78 | 7.2 - 8.9 |
| 31 | 1.288 | 9.86 | 8.9 - 10.8 |
| 32 | 2.740 | 5.71 | 4.2 - 6.8 |
| 33 | 1.331 | 7.78 | 7.5 - 9.7 |
| 34 | 1.682 | 6.81 | 6.2 - 8.3 |
| 35 | 1.600 | 6.94 | 6.5 - 8.3 |
| 36 | 2.533 | 5.50 | 5.5 - 7.2 |
| 37 | 1.663 | 6.81 | 6.8 - 8.9 |
| 38 | 1.350 | 7.78 | 7.6 - 8.9 |
| 39 | 1.195 | 7.57 | 7.4 - 8.8 |
| 40 | 1.097 | 8.87 | 8.1 - 10.1 |

TABLE 10

GENERAL FEATURES OF THE ATOMIC DENSITY FUNCTION $4\pi r^2[\langle \rho_a(r) \rangle - \bar{\rho}_a]$

| Run | First Maximum | | Second Maximum | | Third Maximum | |
|---|---|---|---|---|---|---|
| | Position Å | Height atoms/Å | Position Å | Height atoms/Å | Position Å | Height atoms/Å |
| 22 | 3.90 | 2.36 | 7.48 | 0.88 | 11.1 | 0.33 |
| 23 | 3.86 | 2.57 | 7.35 | 1.12 | 10.9 | 0.45 |
| 30 | 3.85 | 2.35 | 7.40 | 0.80 | 11.0 | 0.33 |
| 31 | 3.88 | 2.03 | 7.42 | 0.75 | 10.9 | 0.28 |
| 32 | 3.90 | 0.85 | - | - | - | - |
| 33 | 4.00 | 2.05 | 7.45 | 0.57 | 10.8 | 0.25 |
| 34 | 3.90 | 1.57 | 7.55 | 0.30 | - | - |
| 35 | 4.04 | 1.50 | 7.75 | 0.23 | - | - |
| 36 | 3.96 | 0.78 | - | - | - | - |
| 37 | 3.87 | 1.50 | 7.65 | 0.25 | - | - |
| 38 | 4.00 | 2.15 | 7.45 | 0.55 | 10.8 | 0.20 |
| 39 | 3.90 | 2.45 | 7.52 | 0.87 | 10.9 | 0.42 |
| 40 | 3.80 | 2.72 | 7.35 | 1.13 | 10.9 | 0.43 |
| Average | 3.91 | | 7.49 | | 10.9 | |

TABLE 11

FIRST COORDINATION NUMBERS

| Run Number | Temp. (°C) | Density (gm/cc) | Radius of Symmetry (Å) | First Coordination Number (atoms) |
|---|---|---|---|---|
| 32 | -125 | 0.280 | 4.01 | 1.9 |
| 36 | -110 | 0.280 | 4.08 | 2.1 |
| 34 | -120 | 0.536 | 4.02 | 3.6 |
| 37 | -115 | 0.536 | 4.04 | 3.7 |
| 35 | -110 | 0.536 | 4.06 | 3.9 |
| 31 | -125 | 0.780 | 3.99 | 5.1 |
| 33 | -120 | 0.780 | 4.01 | 5.7 |
| 38 | -110 | 0.780 | 4.05 | 5.6 |
| 22 | -130 | 0.910 | 3.96 | 5.5 |
| 30 | -125 | 0.910 | 3.98 | 5.3 |
| 39 | -120 | 0.910 | 4.00 | 6.1 |
| 23 | -130 | 0.982 | 3.95 | 5.7 |
| 40 | -125 | 0.982 | 3.97 | 6.0 |

# TABLE 12

## ESTIMATES OF THE ARGON RADIAL DISTRIBUTION FUNCTIONS

| | g (r) | | | | | | | | | | | | |
|---|---|---|---|---|---|---|---|---|---|---|---|---|---|
| Run Number | 22 | 23 | 30 | 31 | 32 | 33 | 34 | 35 | 36 | 37 | 38 | 39 | 40 |
| Temperature (°C) | -130 | -130 | -125 | -125 | -125 | -120 | -120 | -110 | -110 | -115 | -110 | -120 | -125 |
| Pressure (psia) | 586.60 | 964.53 | 965.51 | 648.23 | 624.74 | 906.26 | 774.76 | 1058.23 | 815.85 | 915.75 | 1445.98 | 1350.46 | 1438.29 |
| Density (gm/cc) | 0.910 | 0.982 | 0.910 | 0.780 | 0.280 | 0.780 | 0.536 | 0.536 | 0.280 | 0.536 | 0.780 | 0.910 | 0.982 |
| r (Å) | | | | | | | | | | | | | |
| 3.00 | -0.028 | 0.130 | 0.068 | -0.140 | -0.118 | -0.181 | -0.084 | -0.008 | 0.101 | -0.126 | -0.088 | -0.109 | -0.124 |
| 3.10 | 0.138 | 0.264 | 0.186 | 0.051 | 0.119 | 0.103 | 0.126 | 0.206 | 0.364 | 0.171 | 0.209 | 0.186 | 0.135 |
| 3.20 | 0.445 | 0.489 | 0.488 | 0.419 | 0.430 | 0.521 | 0.410 | 0.482 | 0.624 | 0.533 | 0.538 | 0.564 | 0.539 |
| 3.30 | 0.804 | 0.791 | 0.868 | 0.876 | 0.784 | 0.938 | 0.810 | 0.787 | 0.914 | 0.956 | 0.922 | 0.965 | 0.976 |
| 3.40 | 1.160 | 1.127 | 1.276 | 1.321 | 1.203 | 1.336 | 1.175 | 1.080 | 1.146 | 1.334 | 1.263 | 1.326 | 1.383 |
| 3.50 | 1.472 | 1.438 | 1.614 | 1.661 | 1.498 | 1.592 | 1.473 | 1.331 | 1.430 | 1.630 | 1.537 | 1.590 | 1.712 |
| 3.60 | 1.716 | 1.714 | 1.854 | 1.865 | 1.827 | 1.752 | 1.738 | 1.551 | 1.646 | 1.850 | 1.729 | 1.805 | 1.917 |
| 3.70 | 1.854 | 1.890 | 1.943 | 1.949 | 2.016 | 1.862 | 1.941 | 1.726 | 1.838 | 1.948 | 1.862 | 1.910 | 2.020 |
| 3.80 | 1.914 | 1.948 | 1.946 | 1.941 | 2.100 | 1.889 | 2.017 | 1.856 | 1.944 | 1.987 | 1.936 | 1.952 | 2.004 |
| 3.90 | 1.903 | 1.909 | 1.868 | 1.892 | 2.081 | 1.899 | 2.012 | 1.914 | 1.958 | 1.952 | 1.954 | 1.943 | 1.918 |
| 4.00 | 1.836 | 1.817 | 1.756 | 1.844 | 1.987 | 1.875 | 1.938 | 1.916 | 1.916 | 1.868 | 1.907 | 1.896 | 1.808 |
| 4.10 | 1.722 | 1.685 | 1.636 | 1.744 | 1.877 | 1.822 | 1.815 | 1.864 | 1.838 | 1.723 | 1.844 | 1.782 | 1.673 |
| 4.20 | 1.606 | 1.561 | 1.524 | 1.640 | 1.740 | 1.737 | 1.672 | 1.766 | 1.725 | 1.594 | 1.728 | 1.656 | 1.544 |
| 4.30 | 1.464 | 1.446 | 1.414 | 1.511 | 1.609 | 1.611 | 1.538 | 1.626 | 1.580 | 1.457 | 1.638 | 1.532 | 1.418 |
| 4.40 | 1.332 | 1.344 | 1.311 | 1.383 | 1.495 | 1.480 | 1.416 | 1.474 | 1.418 | 1.319 | 1.436 | 1.398 | 1.296 |
| 4.50 | 1.207 | 1.256 | 1.211 | 1.264 | 1.348 | 1.342 | 1.301 | 1.334 | 1.292 | 1.226 | 1.309 | 1.280 | 1.194 |
| 4.60 | 1.113 | 1.174 | 1.139 | 1.159 | 1.248 | 1.204 | 1.196 | 1.203 | 1.196 | 1.144 | 1.160 | 1.164 | 1.106 |
| 4.70 | 1.042 | 1.088 | 1.068 | 1.076 | 1.166 | 1.084 | 1.098 | 1.114 | 1.128 | 1.088 | 1.046 | 1.066 | 1.028 |
| 4.80 | 0.986 | 1.013 | 1.006 | 0.999 | 1.106 | 0.978 | 1.031 | 1.042 | 1.074 | 1.038 | 0.956 | 0.982 | 0.968 |
| 4.90 | 0.947 | 0.956 | 0.958 | 0.952 | 1.063 | 0.909 | 0.986 | 0.992 | 1.035 | 1.004 | 0.909 | 0.918 | 0.919 |
| 5.00 | 0.917 | 0.910 | 0.922 | 0.919 | 1.030 | 0.872 | 0.954 | 0.956 | 1.012 | 0.984 | 0.881 | 0.872 | 0.884 |
| 5.20 | 0.884 | 0.866 | 0.866 | 0.875 | 0.986 | 0.841 | 0.918 | 0.928 | 0.986 | 0.946 | 0.850 | 0.834 | 0.840 |
| 5.40 | 0.870 | 0.851 | 0.841 | 0.860 | 0.964 | 0.837 | 0.909 | 0.917 | 0.981 | 0.932 | 0.847 | 0.830 | 0.826 |
| 5.60 | 0.875 | 0.850 | 0.842 | 0.864 | 0.961 | 0.855 | 0.912 | 0.914 | 0.979 | 0.928 | 0.863 | 0.841 | 0.834 |
| 5.80 | 0.886 | 0.864 | 0.866 | 0.876 | 0.966 | 0.877 | 0.922 | 0.922 | 0.980 | 0.932 | 0.887 | 0.860 | 0.848 |
| 6.00 | 0.902 | 0.878 | 0.897 | 0.896 | 0.979 | 0.903 | 0.944 | 0.936 | 0.984 | 0.944 | 0.910 | 0.892 | 0.872 |
| 6.20 | 0.925 | 0.902 | 0.938 | 0.923 | 0.992 | 0.938 | 0.962 | 0.952 | 0.988 | 0.952 | 0.946 | 0.924 | 0.904 |
| 6.40 | 0.956 | 0.934 | 0.972 | 0.956 | 1.002 | 0.967 | 0.982 | 0.967 | 0.991 | 0.968 | 0.977 | 0.962 | 0.942 |
| 6.60 | 0.990 | 0.976 | 1.008 | 0.992 | 1.017 | 1.000 | 1.004 | 0.984 | 0.994 | 0.990 | 1.008 | 0.996 | 0.986 |
| 6.80 | 1.028 | 1.036 | 1.040 | 1.028 | 1.022 | 1.027 | 1.024 | 1.001 | 0.998 | 1.012 | 1.033 | 1.033 | 1.032 |

TABLE 12 (continued)

ESTIMATES OF THE ARGON RADIAL DISTRIBUTION FUNCTIONS

| | g (r) | | | | | | | | | | | | |
|---|---|---|---|---|---|---|---|---|---|---|---|---|---|
| Run Number | 22 | 23 | 30 | 31 | 32 | 33 | 34 | 35 | 36 | 37 | 38 | 39 | 40 |
| Temperature (°C) | -130 | -130 | -125 | -125 | -125 | -120 | -120 | -110 | -110 | -115 | -110 | -120 | -125 |
| Pressure (psia) | 586.60 | 964.53 | 965.51 | 648.23 | 624.74 | 906.26 | 774.76 | 1058.23 | 815.85 | 915.75 | 1445.98 | 1350.46 | 1438.29 |
| Density (gm/cc) | 0.910 | 0.982 | 0.910 | 0.780 | 0.280 | 0.780 | 0.536 | 0.536 | 0.280 | 0.536 | 0.780 | 0.910 | 0.982 |
| r (Å) | | | | | | | | | | | | | |
| 7.00 | 1.030 | 1.082 | 1.068 | 1.062 | 1.025 | 1.050 | 1.038 | 1.012 | 1.008 | 1.030 | 1.050 | 1.060 | 1.078 |
| 7.20 | 1.080 | 1.110 | 1.086 | 1.088 | 1.025 | 1.064 | 1.044 | 1.026 | 1.012 | 1.041 | 1.062 | 1.077 | 1.108 |
| 7.40 | 1.093 | 1.110 | 1.088 | 1.092 | 1.024 | 1.069 | 1.048 | 1.034 | 1.014 | 1.044 | 1.066 | 1.086 | 1.110 |
| 7.60 | 1.084 | 1.093 | 1.078 | 1.080 | 1.021 | 1.065 | 1.048 | 1.036 | 1.016 | 1.042 | 1.061 | 1.088 | 1.088 |
| 7.80 | 1.066 | 1.066 | 1.058 | 1.058 | 1.019 | 1.054 | 1.042 | 1.036 | 1.017 | 1.039 | 1.051 | 1.072 | 1.060 |
| 8.00 | 1.044 | 1.038 | 1.038 | 1.037 | 1.014 | 1.036 | 1.033 | 1.030 | 1.018 | 1.034 | 1.038 | 1.049 | 1.036 |
| 8.25 | 1.018 | 1.012 | 1.016 | 1.015 | 1.013 | 1.010 | 1.018 | 1.020 | 1.016 | 1.022 | 1.016 | 1.018 | 1.006 |
| 8.50 | 1.000 | 0.996 | 0.998 | 0.998 | 1.010 | 0.997 | 1.007 | 1.012 | 1.013 | 1.012 | 0.998 | 0.990 | 0.982 |
| 8.75 | 0.984 | 0.986 | 0.984 | 0.987 | 1.006 | 0.987 | 1.000 | 1.006 | 1.011 | 1.002 | 0.988 | 0.975 | 0.970 |
| 9.00 | 0.979 | 0.981 | 0.980 | 0.985 | 1.004 | 0.984 | 0.995 | 1.002 | 1.009 | 0.994 | 0.984 | 0.976 | 0.968 |
| 9.25 | 0.980 | 0.981 | 0.988 | 0.987 | 1.000 | 0.987 | 0.994 | 1.001 | 1.007 | 0.990 | 0.987 | 0.981 | 0.973 |
| 9.50 | 0.986 | 0.985 | 0.988 | 0.992 | 0.999 | 0.992 | 0.998 | 1.000 | 1.004 | 0.992 | 0.994 | 0.989 | 0.983 |
| 9.75 | 0.994 | 0.994 | 0.997 | 0.997 | 0.996 | 0.999 | 0.998 | 1.000 | 1.002 | 0.994 | 1.002 | 0.998 | 0.993 |
| 10.00 | 1.002 | 1.005 | 1.004 | 1.003 | 0.993 | 1.005 | 1.000 | 1.000 | 1.000 | 0.998 | 1.008 | 1.007 | 1.003 |
| 10.25 | 1.008 | 1.014 | 1.010 | 1.009 | | 1.010 | | | | | 1.010 | 1.014 | 1.012 |
| 10.50 | 1.015 | 1.019 | 1.014 | 1.013 | | 1.013 | | | | | 1.010 | 1.018 | 1.017 |
| 10.75 | 1.017 | 1.020 | 1.017 | 1.016 | | 1.015 | | | | | 1.010 | 1.021 | 1.019 |
| 11.00 | 1.016 | 1.020 | 1.016 | 1.015 | | 1.015 | | | | | 1.008 | 1.020 | 1.018 |
| 11.25 | 1.014 | 1.016 | 1.014 | 1.011 | | 1.011 | | | | | 1.006 | 1.016 | 1.014 |
| 11.50 | 1.011 | 1.011 | 1.012 | 1.007 | | 1.005 | | | | | 1.004 | 1.011 | 1.009 |
| 11.75 | 1.008 | 1.006 | 1.007 | 1.002 | | 1.000 | | | | | 1.002 | 1.004 | 1.002 |
| 12.00 | 1.004 | 1.000 | 1.002 | 0.997 | | 0.997 | | | | | 1.000 | 0.999 | 0.996 |
| 12.25 | 1.000 | 0.996 | 0.999 | | | | | | | | | 0.996 | 0.994 |
| 12.50 | 0.998 | 0.996 | 0.996 | | | | | | | | | 0.994 | 0.994 |
| 12.75 | 0.996 | 0.996 | 0.995 | | | | | | | | | 0.995 | 0.994 |
| 13.00 | 0.997 | 0.998 | 0.996 | | | | | | | | | 0.996 | 0.995 |
| 13.25 | 0.998 | 1.000 | 0.998 | | | | | | | | | 0.998 | 0.997 |
| 13.50 | 1.000 | 1.001 | 1.000 | | | | | | | | | 0.998 | 0.998 |
| 13.75 | 1.000 | 1.001 | 1.001 | | | | | | | | | 0.999 | 1.000 |
| 14.00 | 1.000 | 1.001 | 1.002 | | | | | | | | | 1.000 | 1.002 |

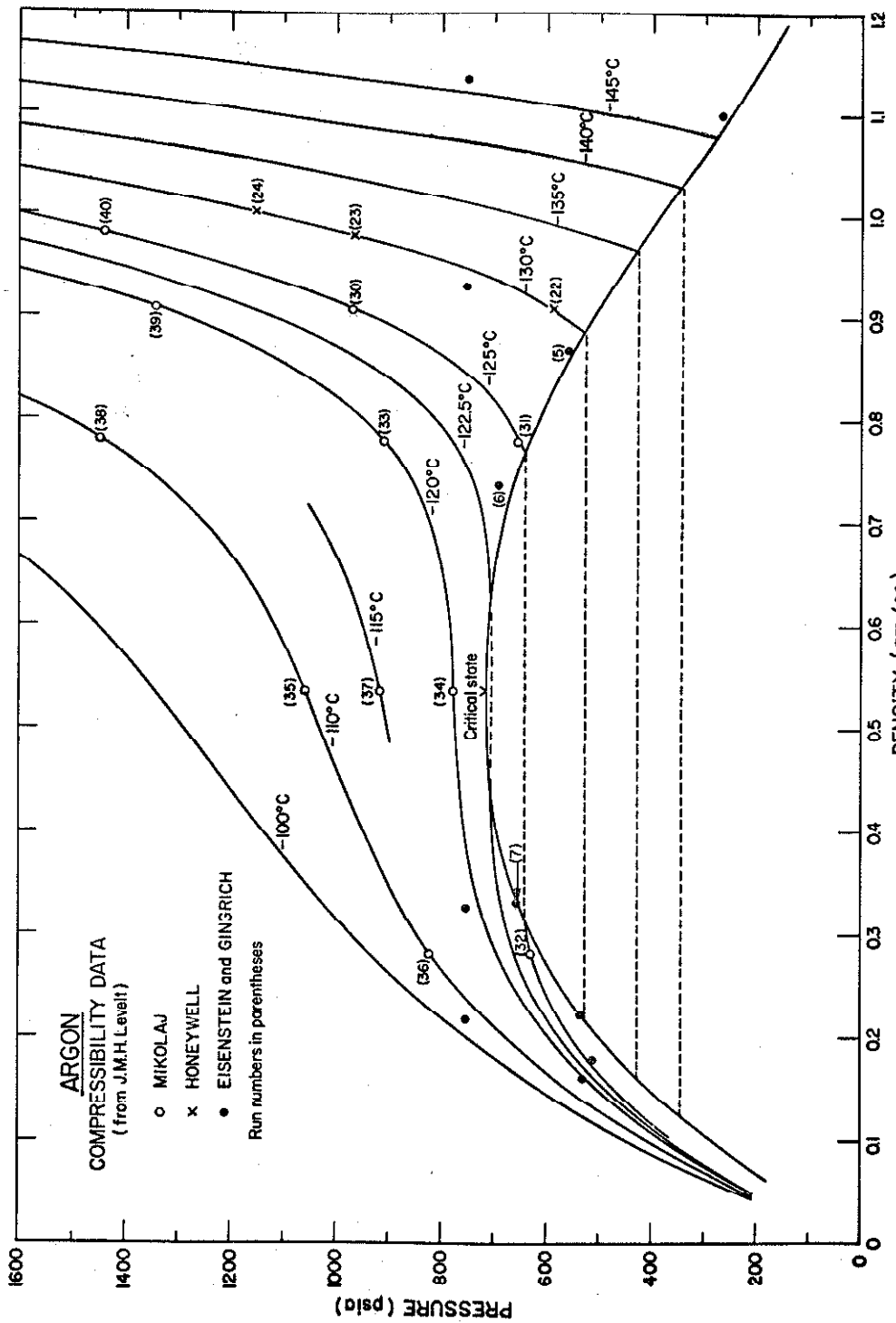


Figure 1. Argon Compressibility Diagram Showing Locations of the Experimental States

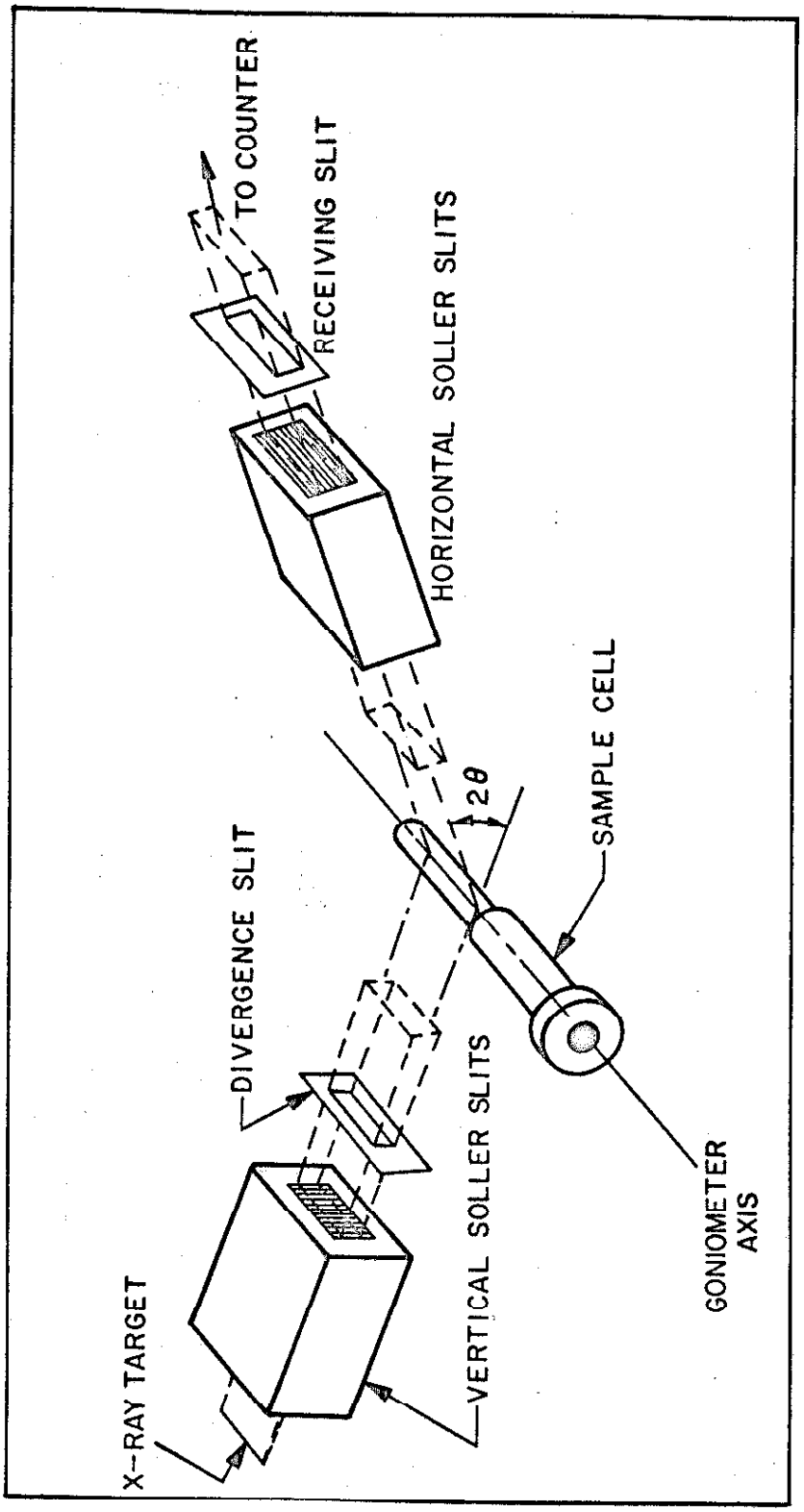


Figure 2. Pictorial Illustration of the X-Ray Optical System

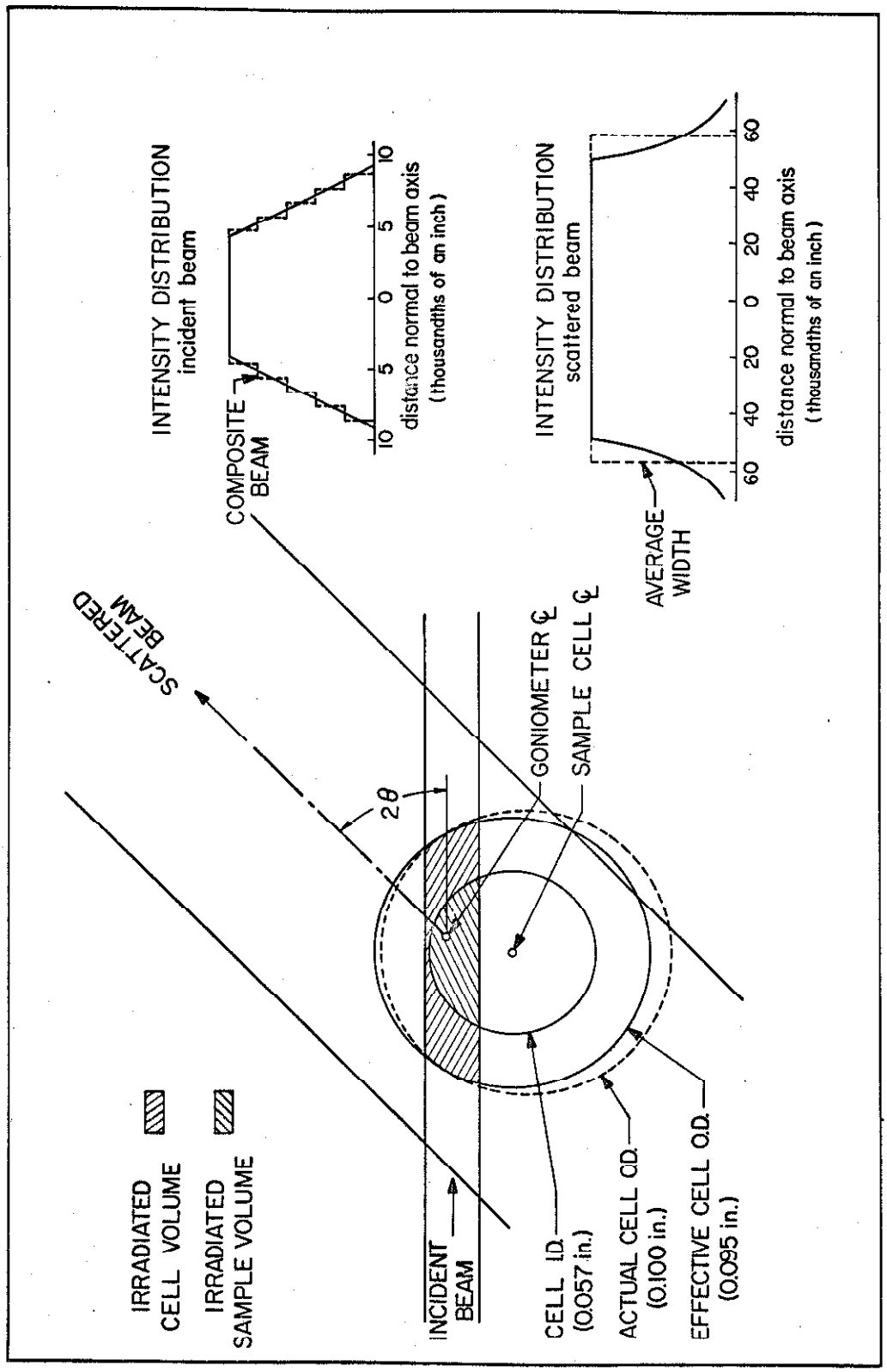


Figure 3. Scattering Geometry used in the Argon Experiments

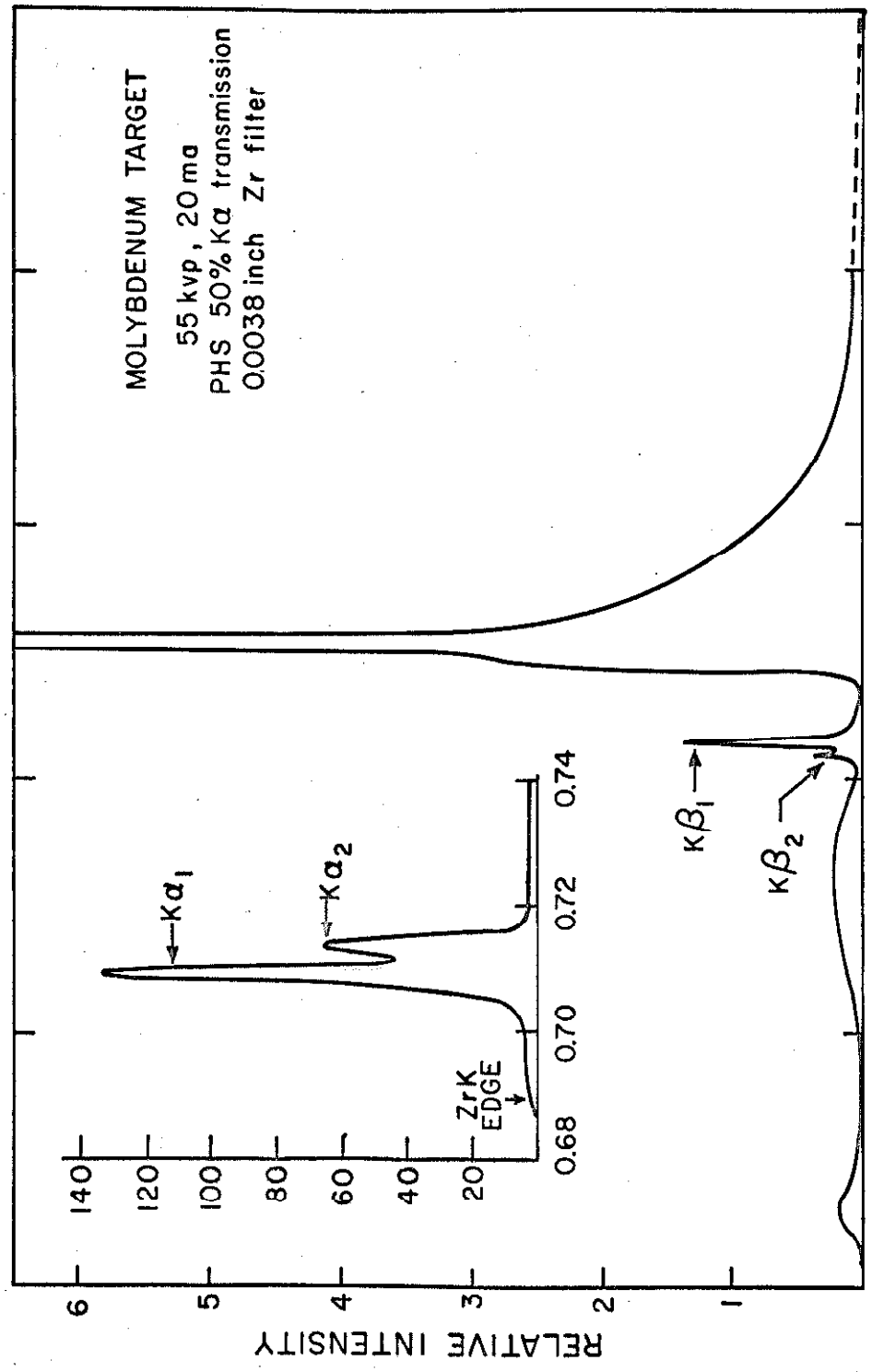


Figure 4. Estimated Spectrum of the Incident X-Ray Beam after Monochromatization

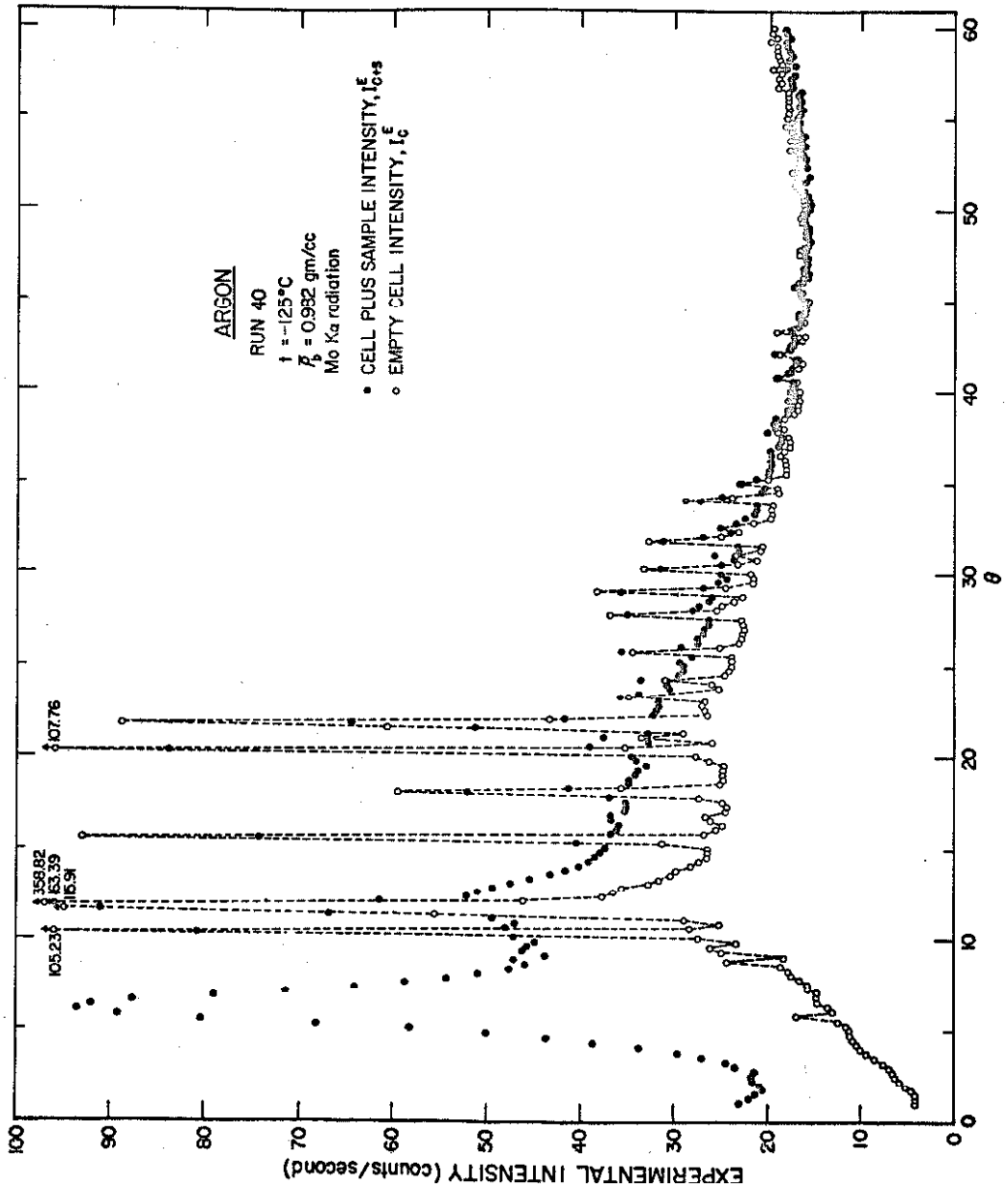


Figure 5. Experimental Intensity Data for a Typical Argon Run

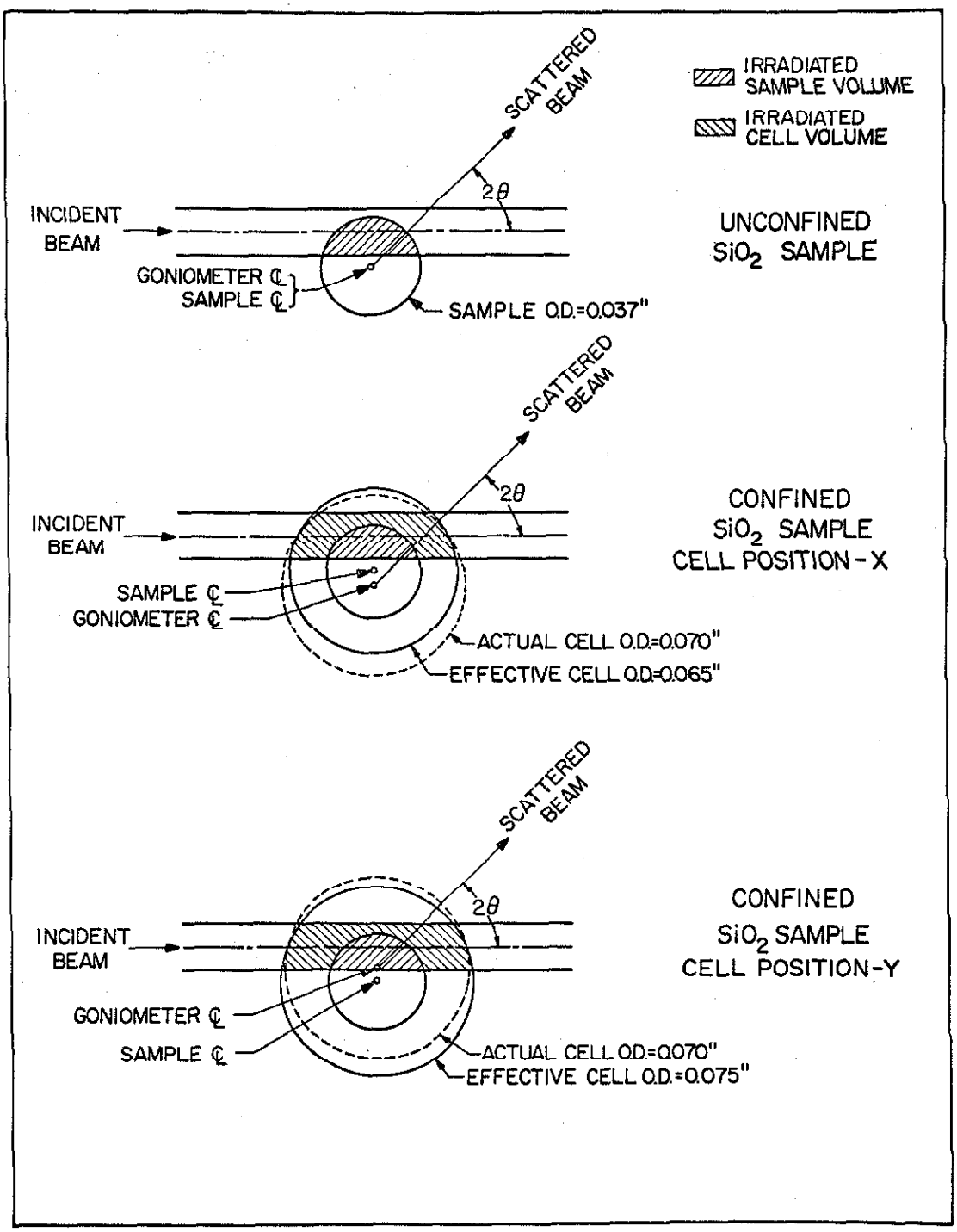


Figure 6. Scattering Geometries used in the $SiO_2$ Calibration Experiment

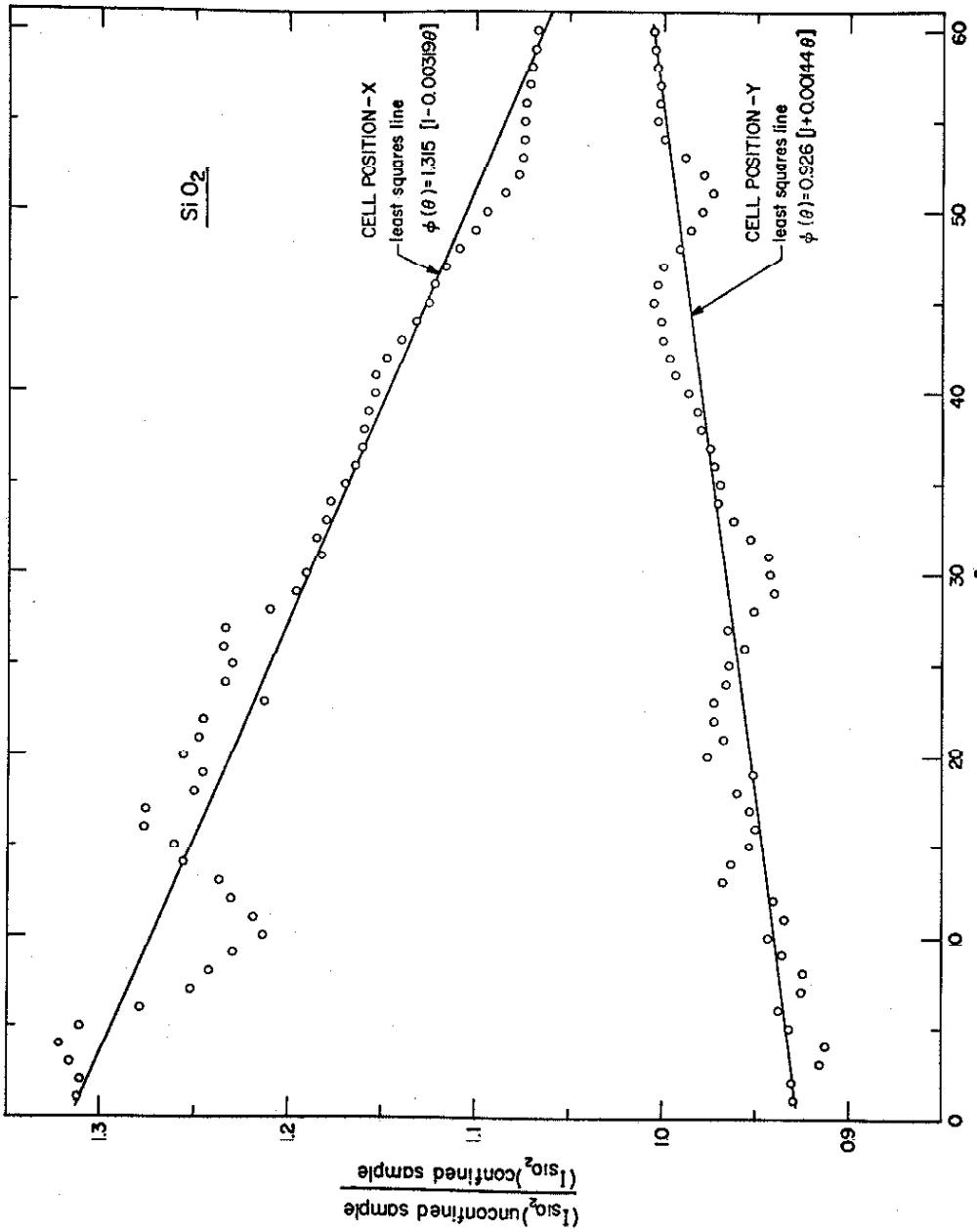


Figure 7. Ratio of the Scattering Curves in the $SiO_2$ Calibration Experiment

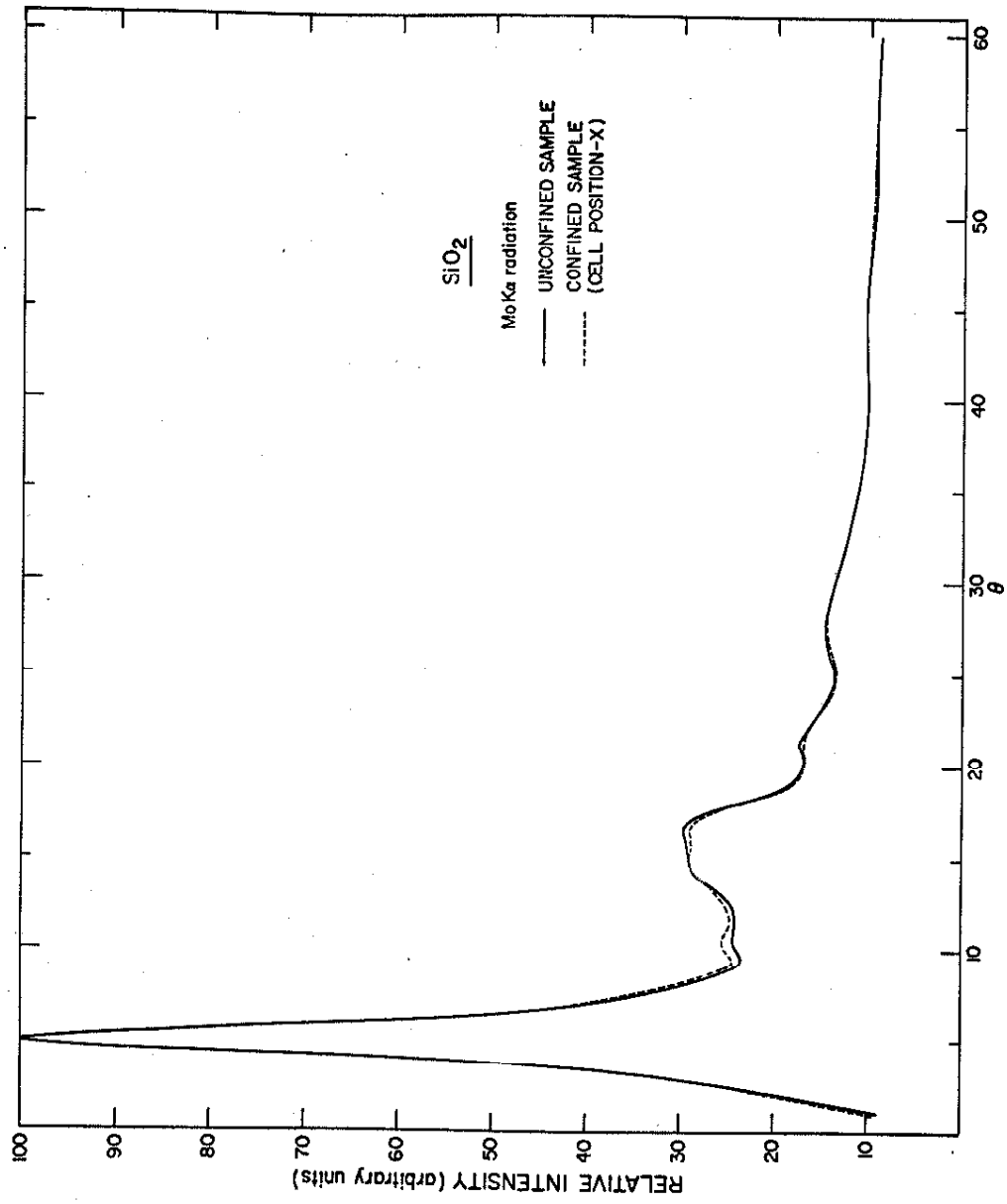


Figure 8. $SiO_2$ Scattering Curve for Cell Position-X

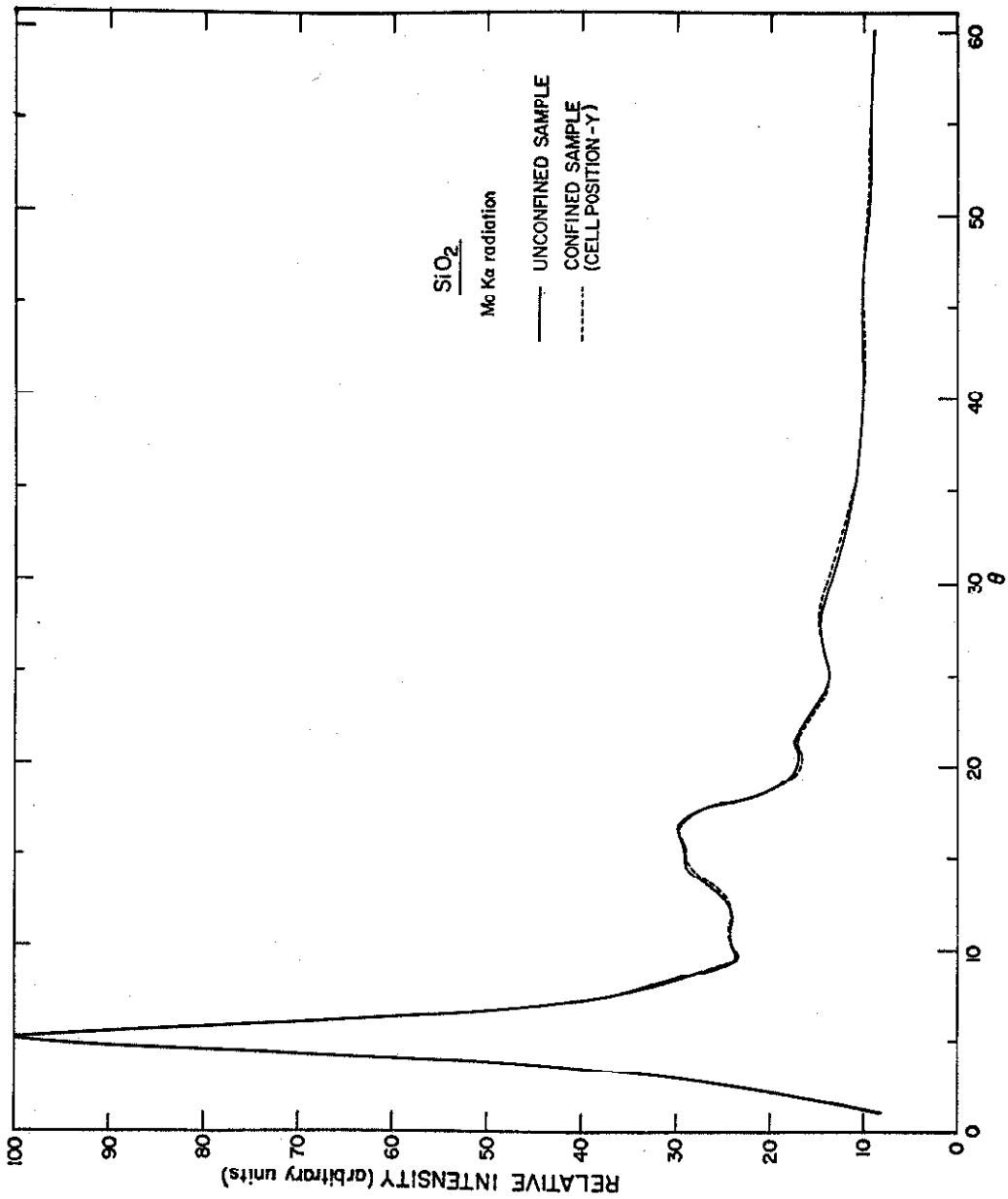


Figure 9. $SiO_2$ Scattering Curve for Cell Position-Y

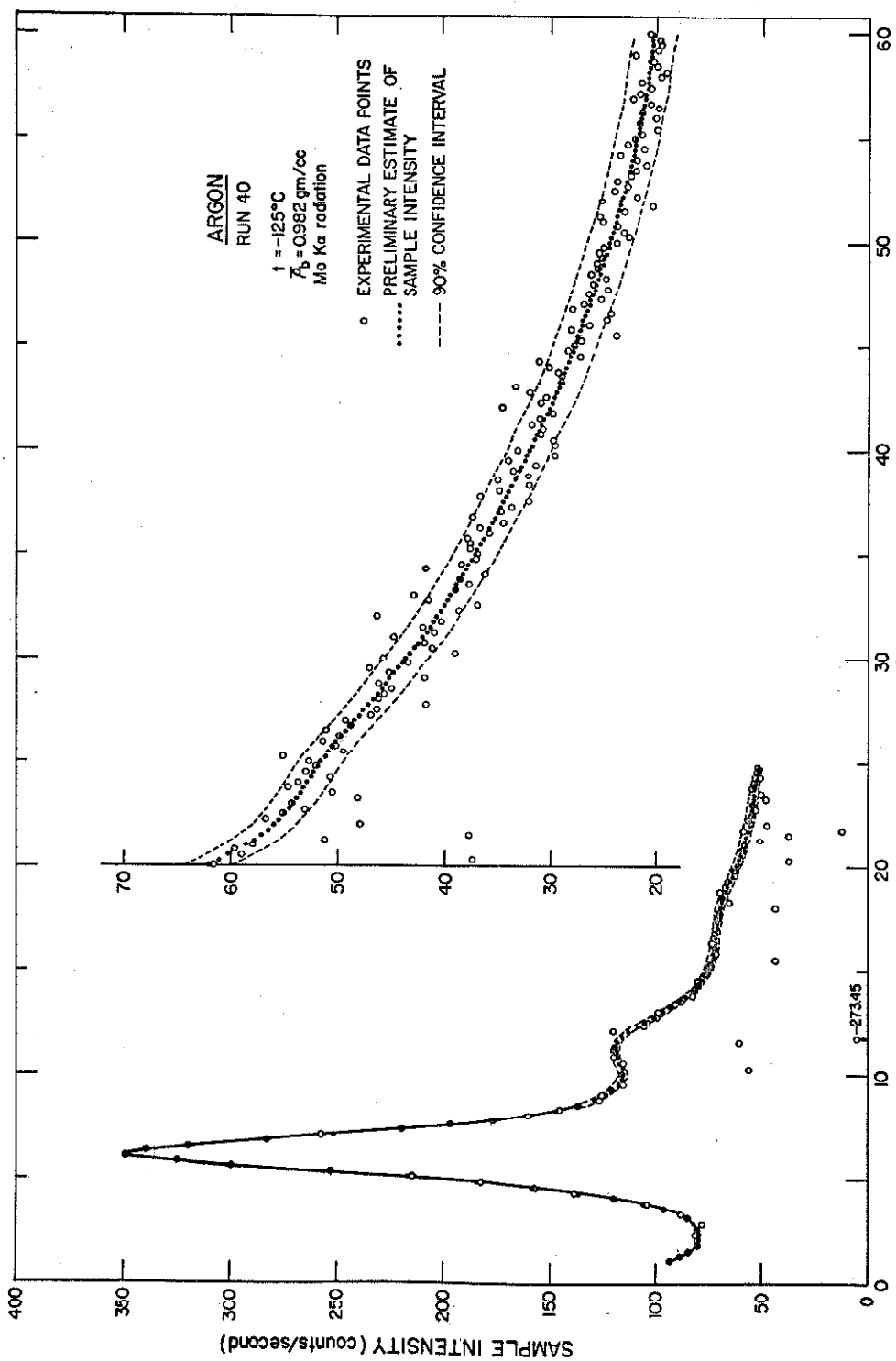


Figure 10. Argon Scattering Curve with the 90% Confidence Interval for a Typical Run

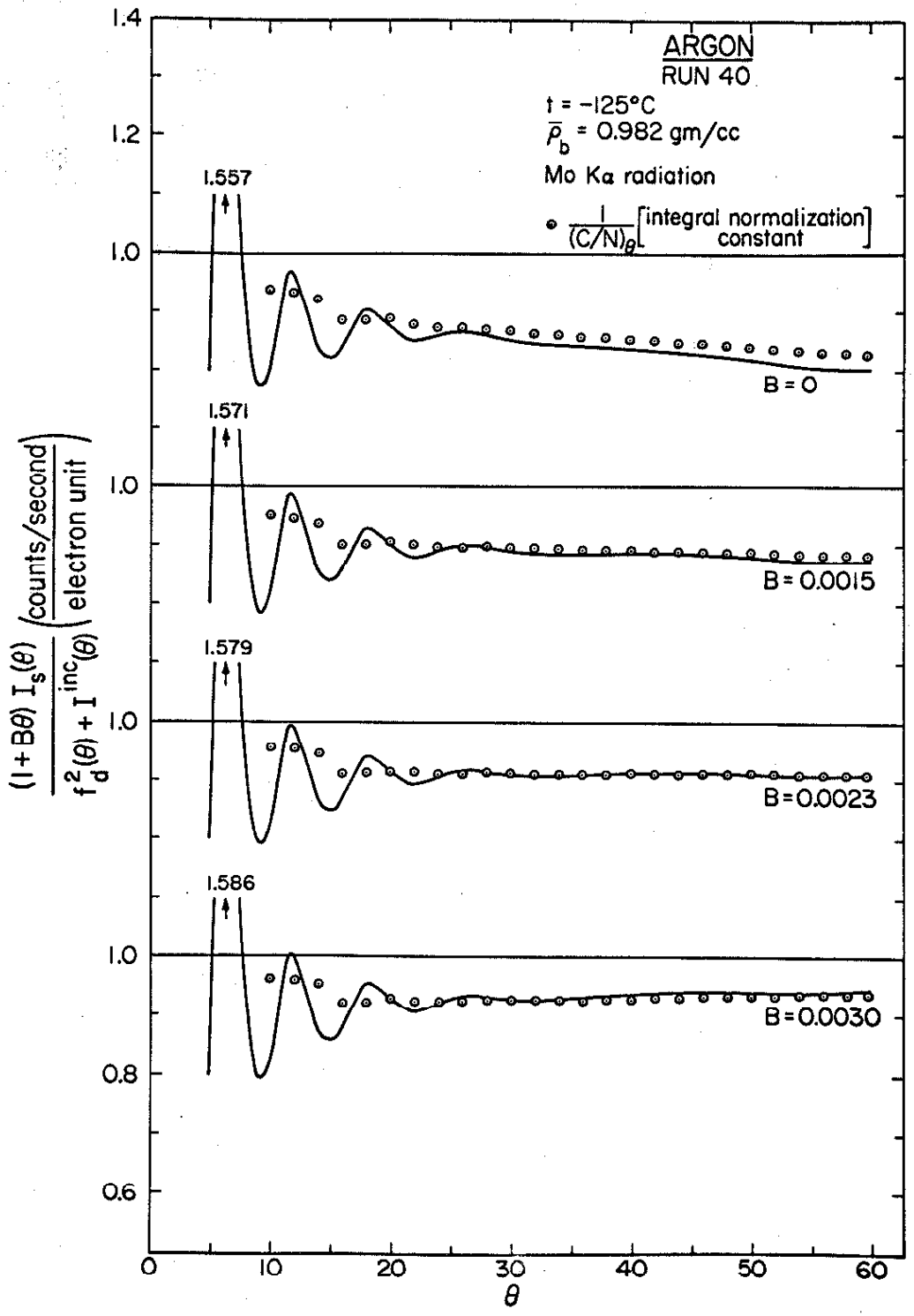


Figure 11. Effect of the Modification Function, $\phi(\Theta) = 1 + B\Theta$, on the Argon Intensity Pattern

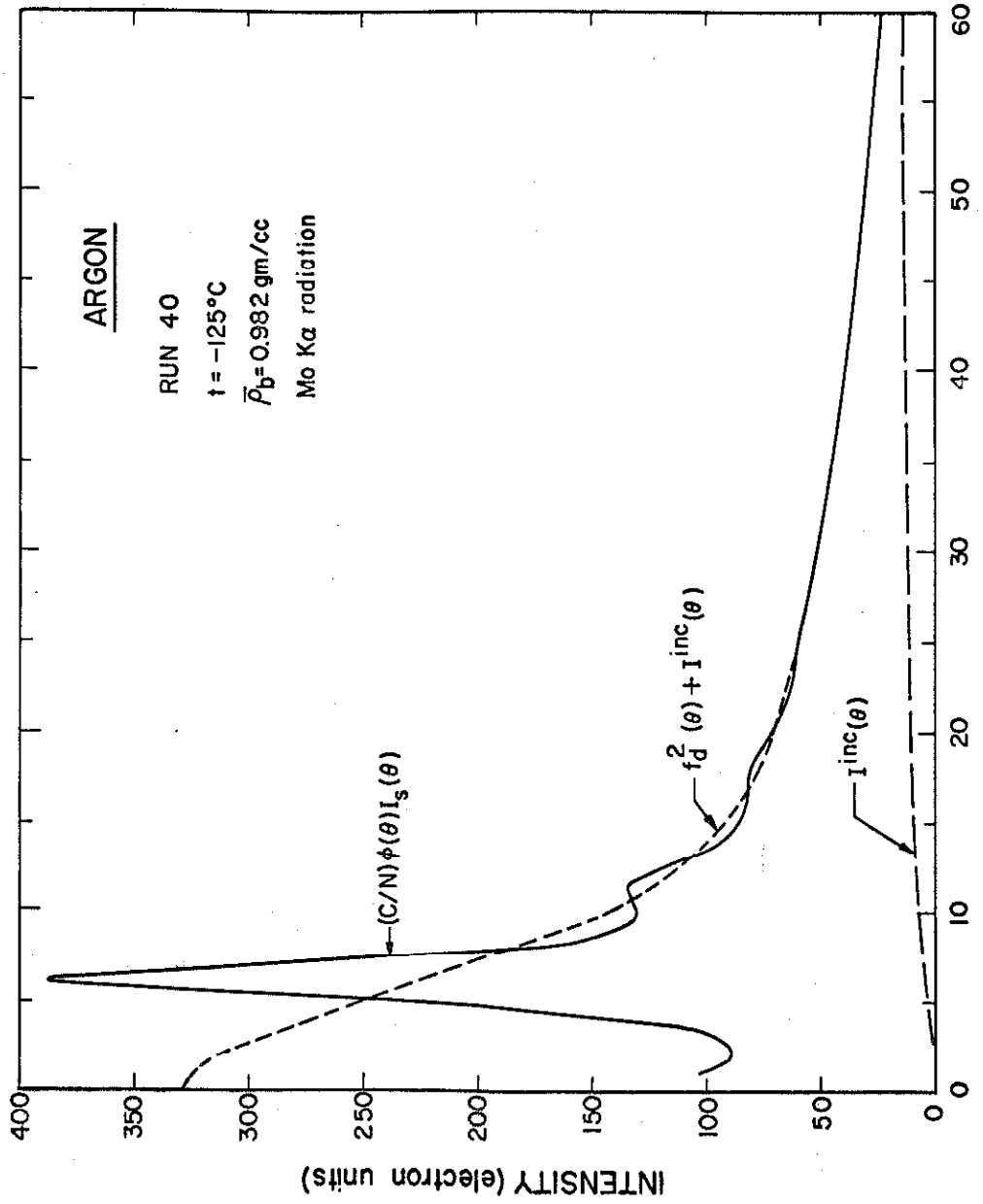


Figure 12. The Fully Corrected and Normalized Scattering Curve for a Typical Argon Run

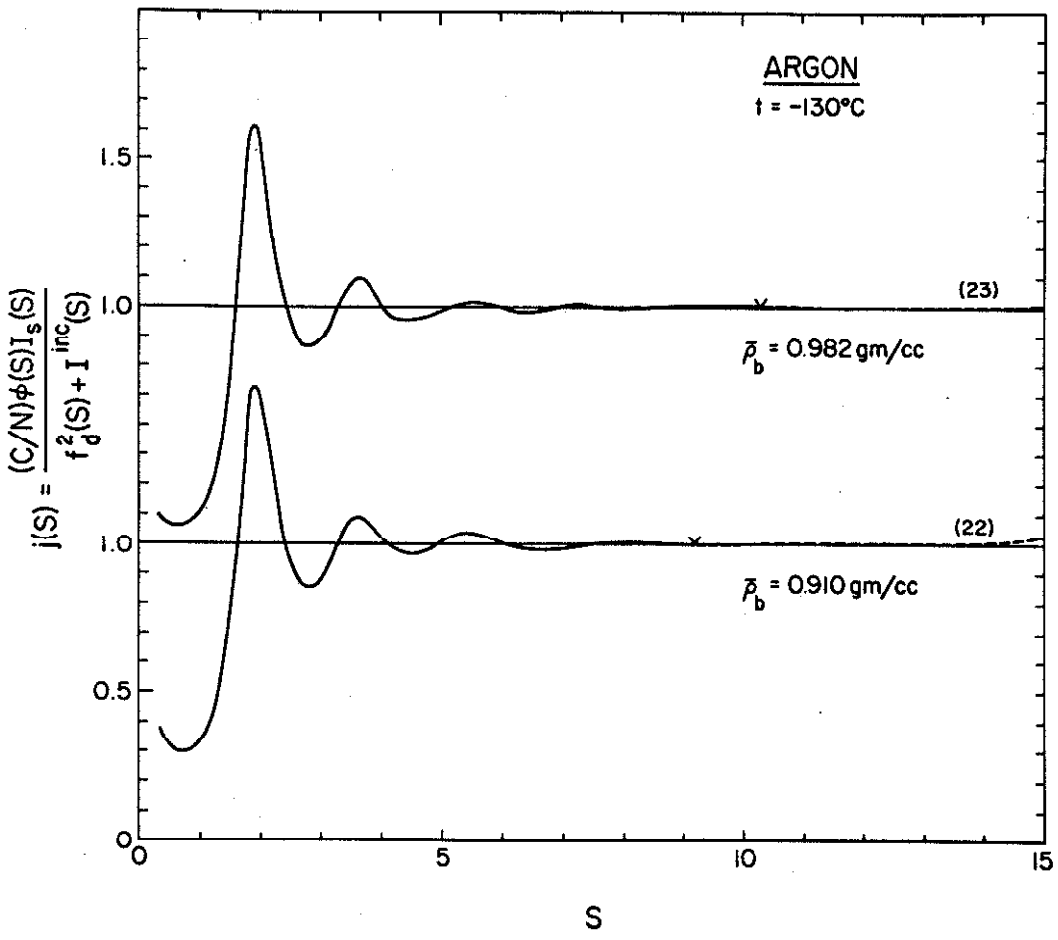


Figure 13. The Argon Intensity Function, j(S), at t = -130°C

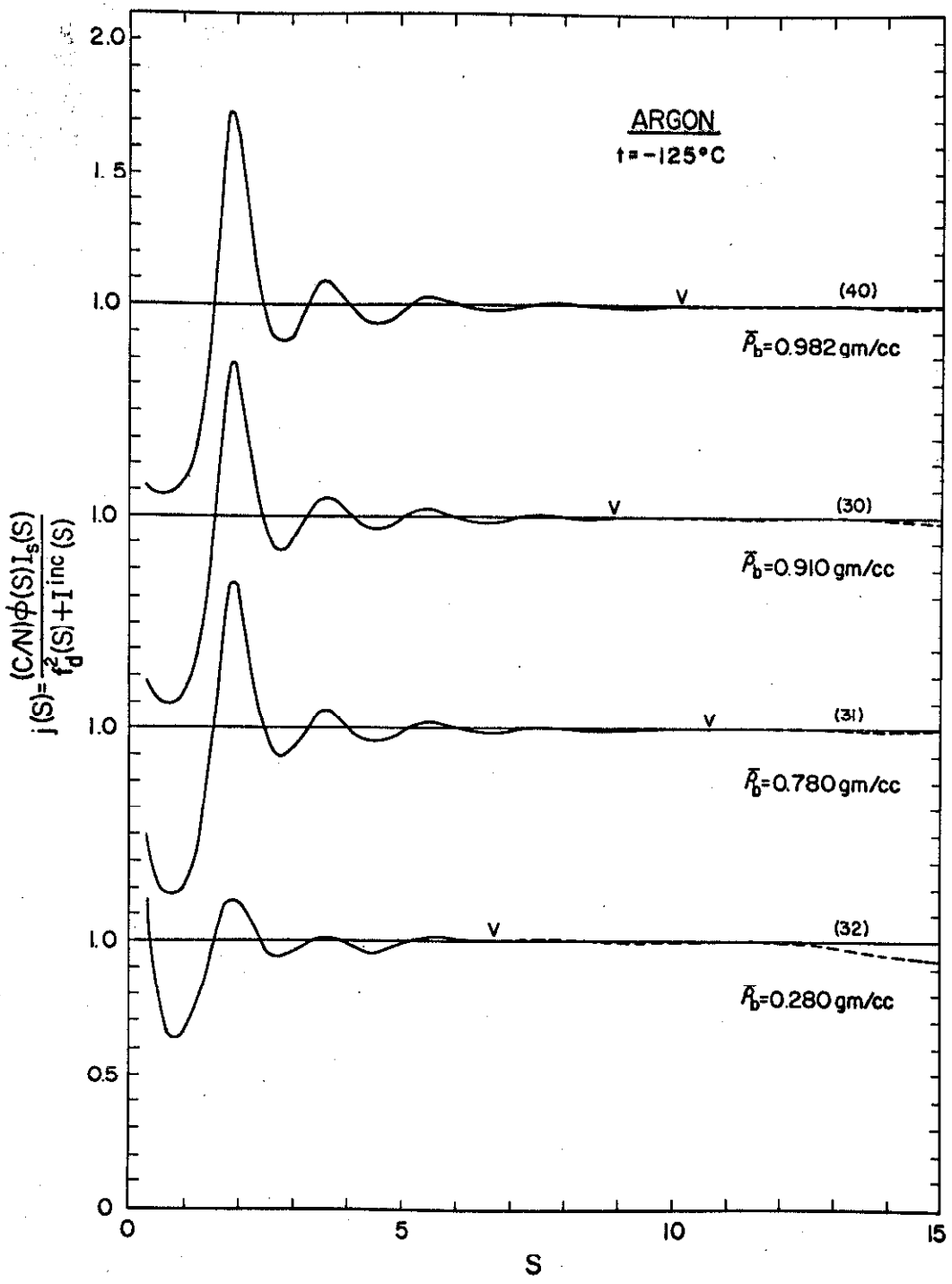


Figure 14. The Argon Intensity Function, j(S), at t = -125°C

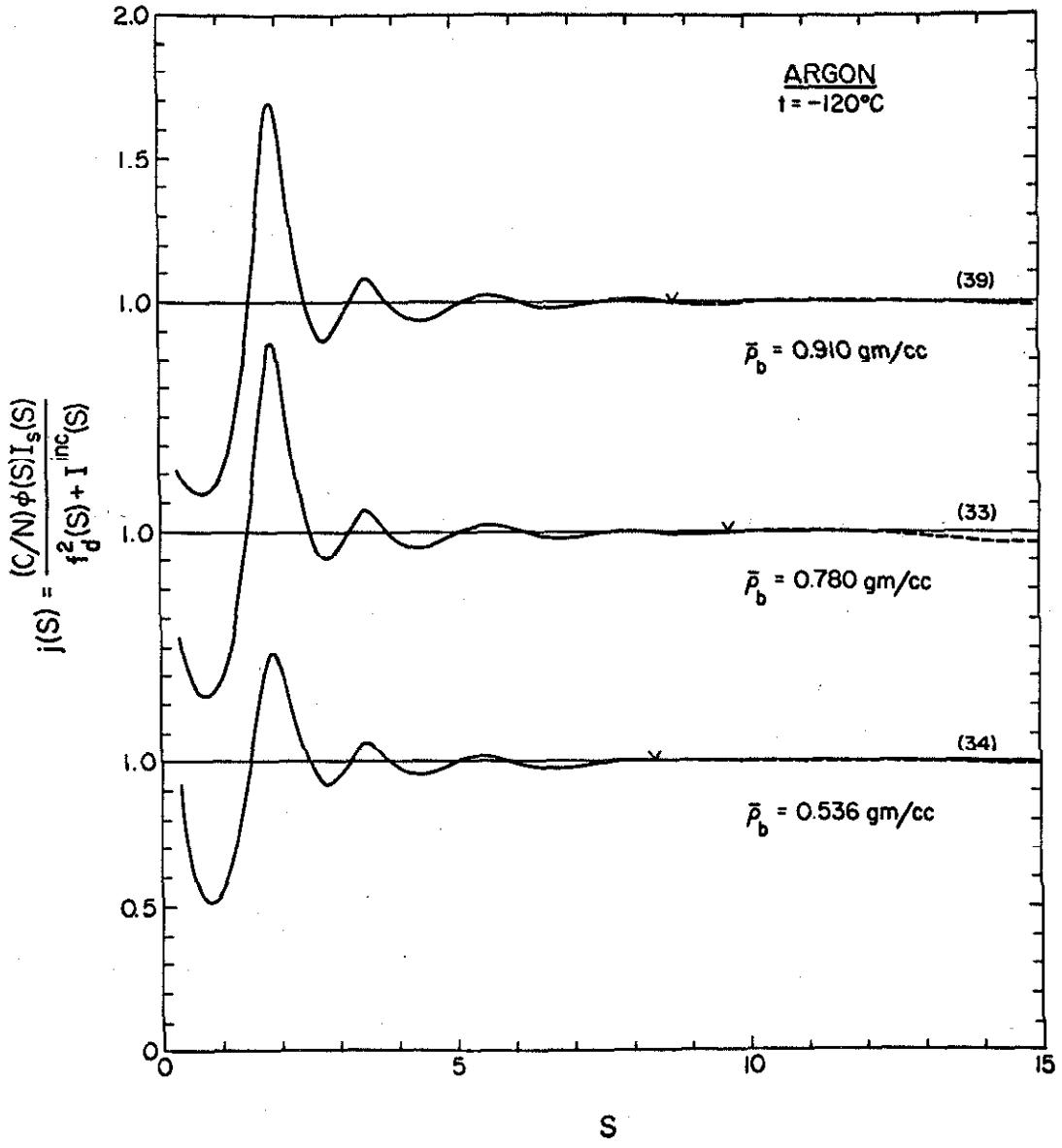


Figure 15. The Argon Intensity Function, j(S), at t = -120°C

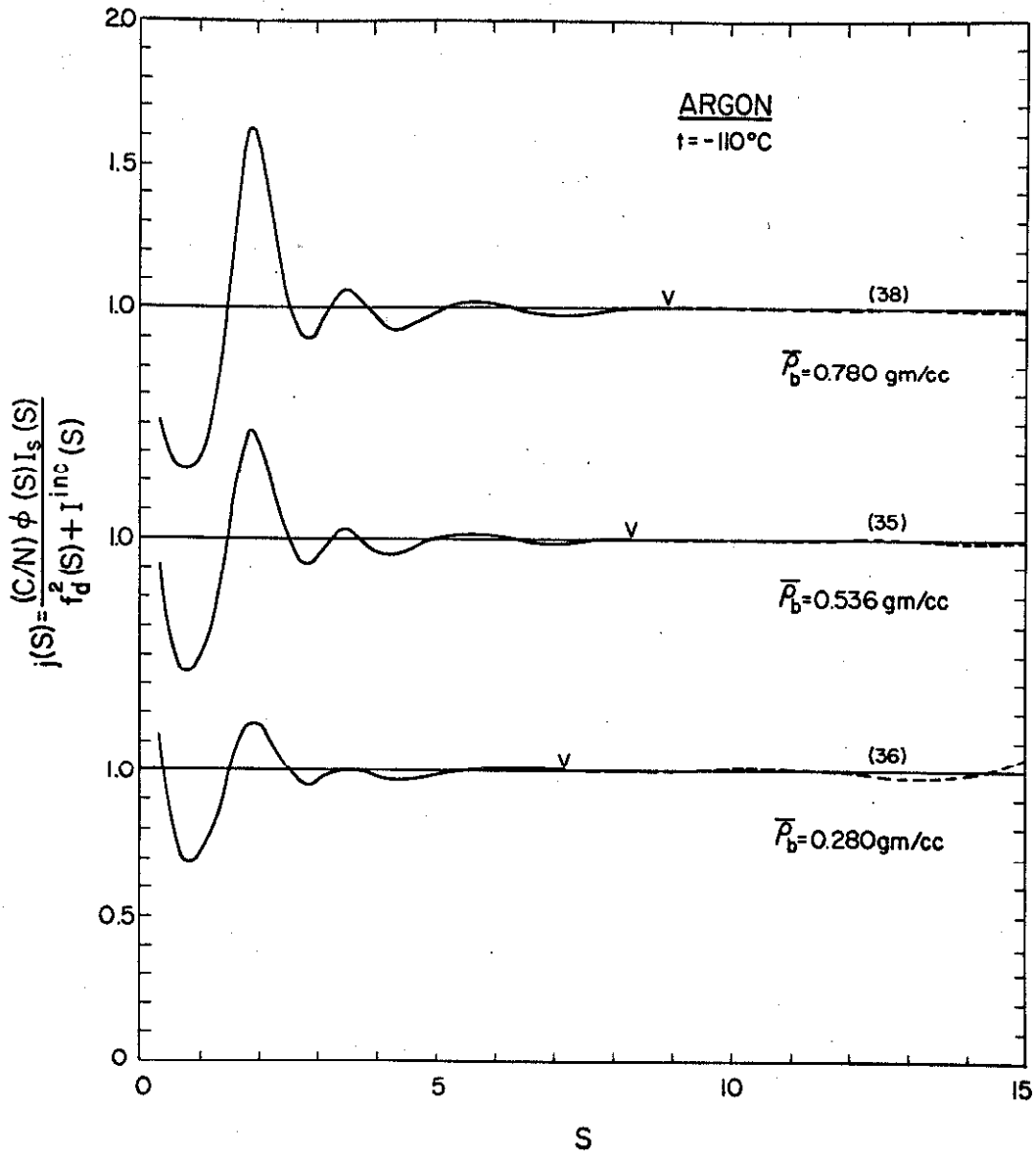


Figure 16. The Argon Intensity Function, j(S), at t = -110°C

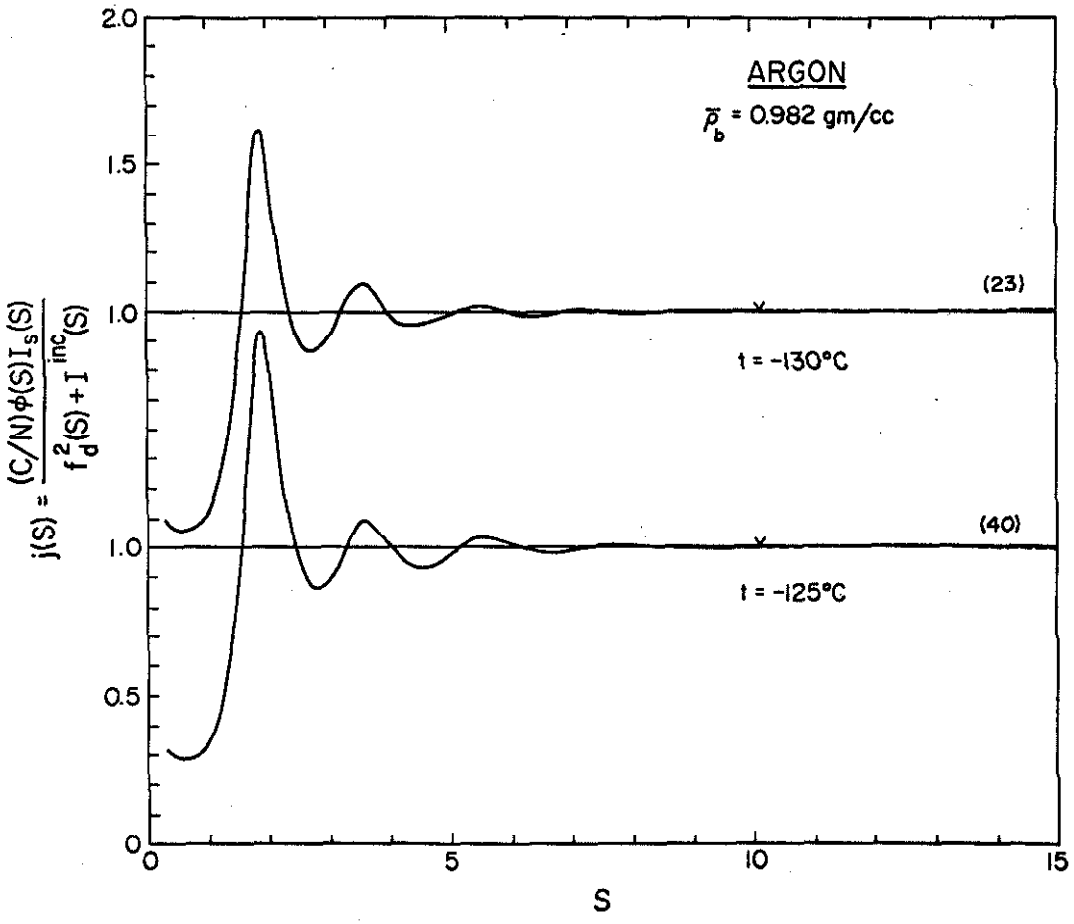


Figure 17. The Argon Intensity Function, j(S), at a Bulk Density of 0.982 gm/cc

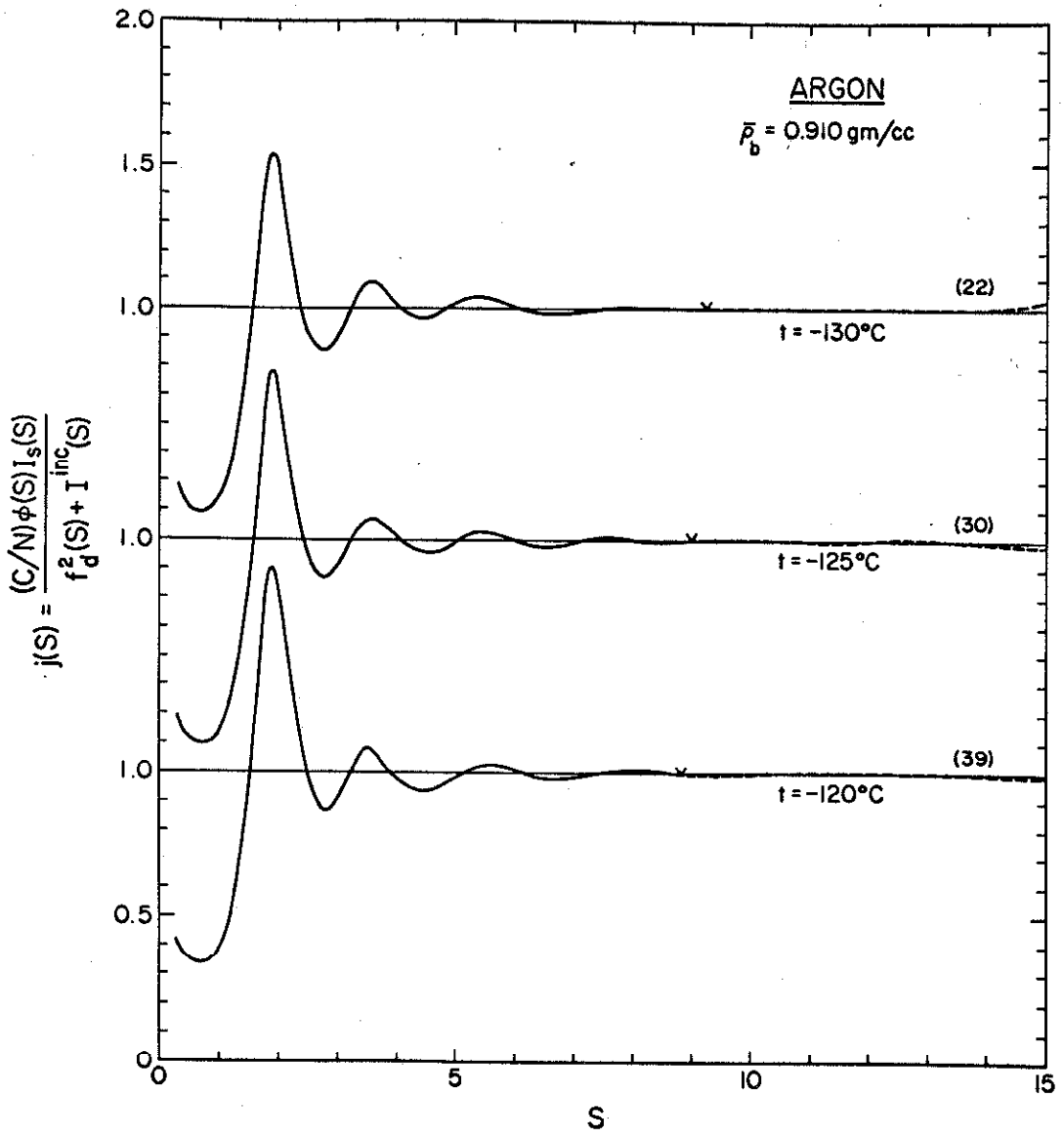


Figure 18. The Argon Intensity Function, j(S), at a Bulk Density of 0.910 gm/cc

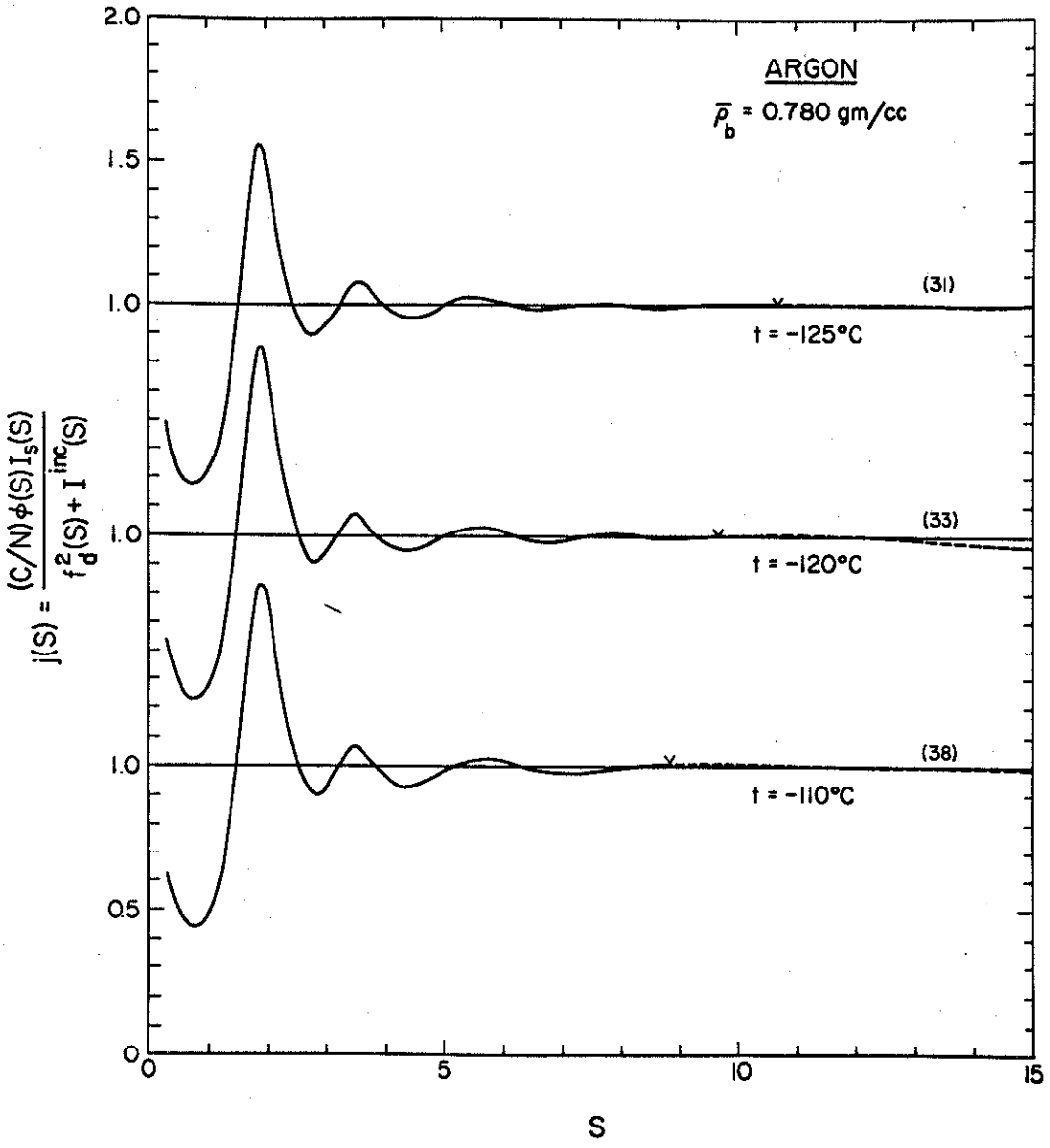


Figure 19. The Argon Intensity Function, j(S), at a Bulk Density of 0.780 gm/cc

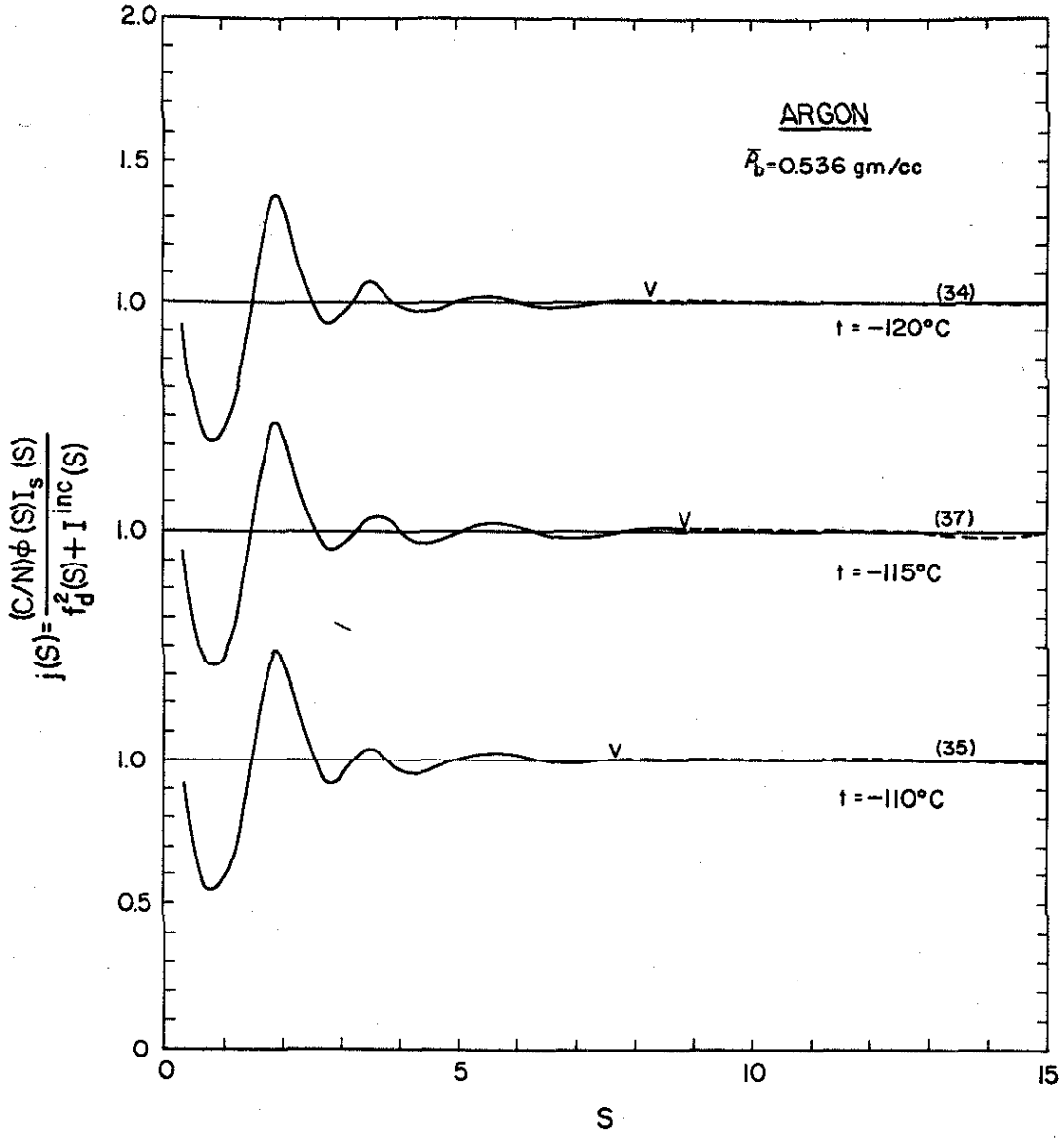


Figure 20. The Argon Intensity Function, j(S), at a Bulk Density of 0.536 gm/cc

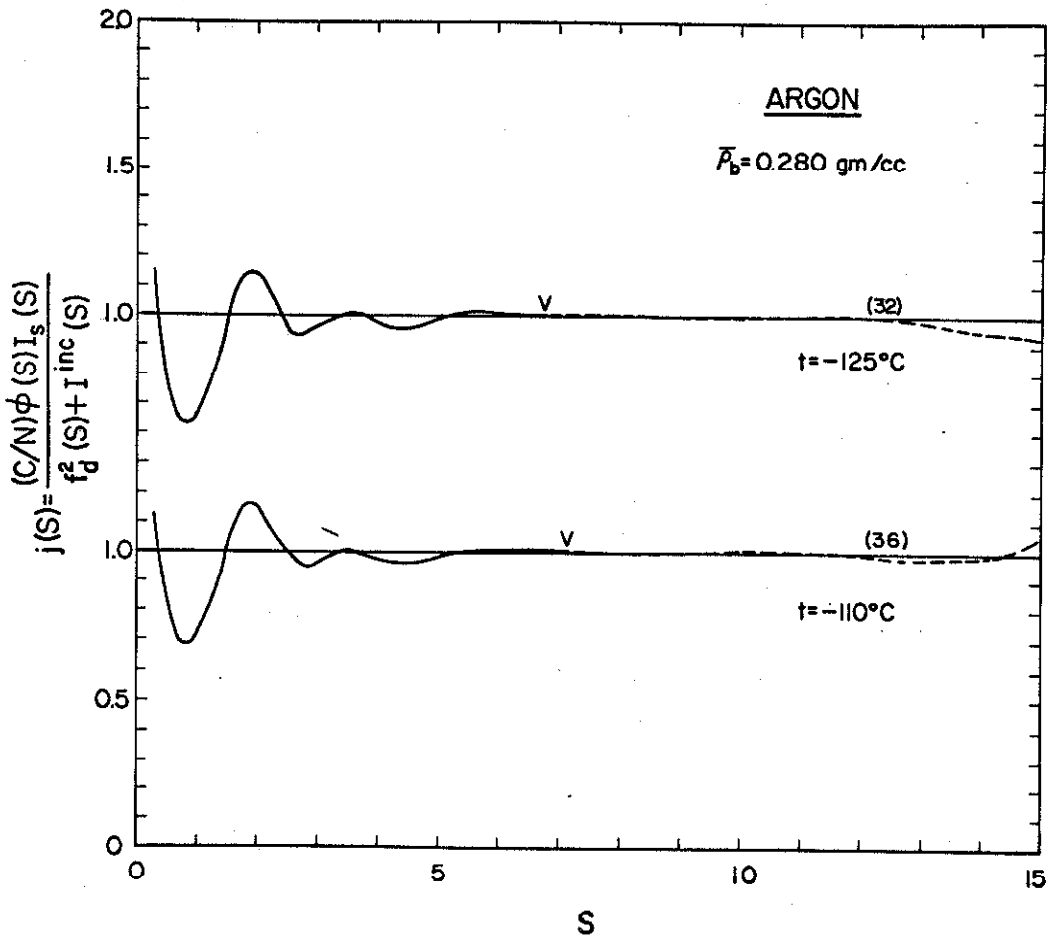


Figure 21. The Argon Intensity Function, j(S), at a Bulk Density of 0.280 gm/cc

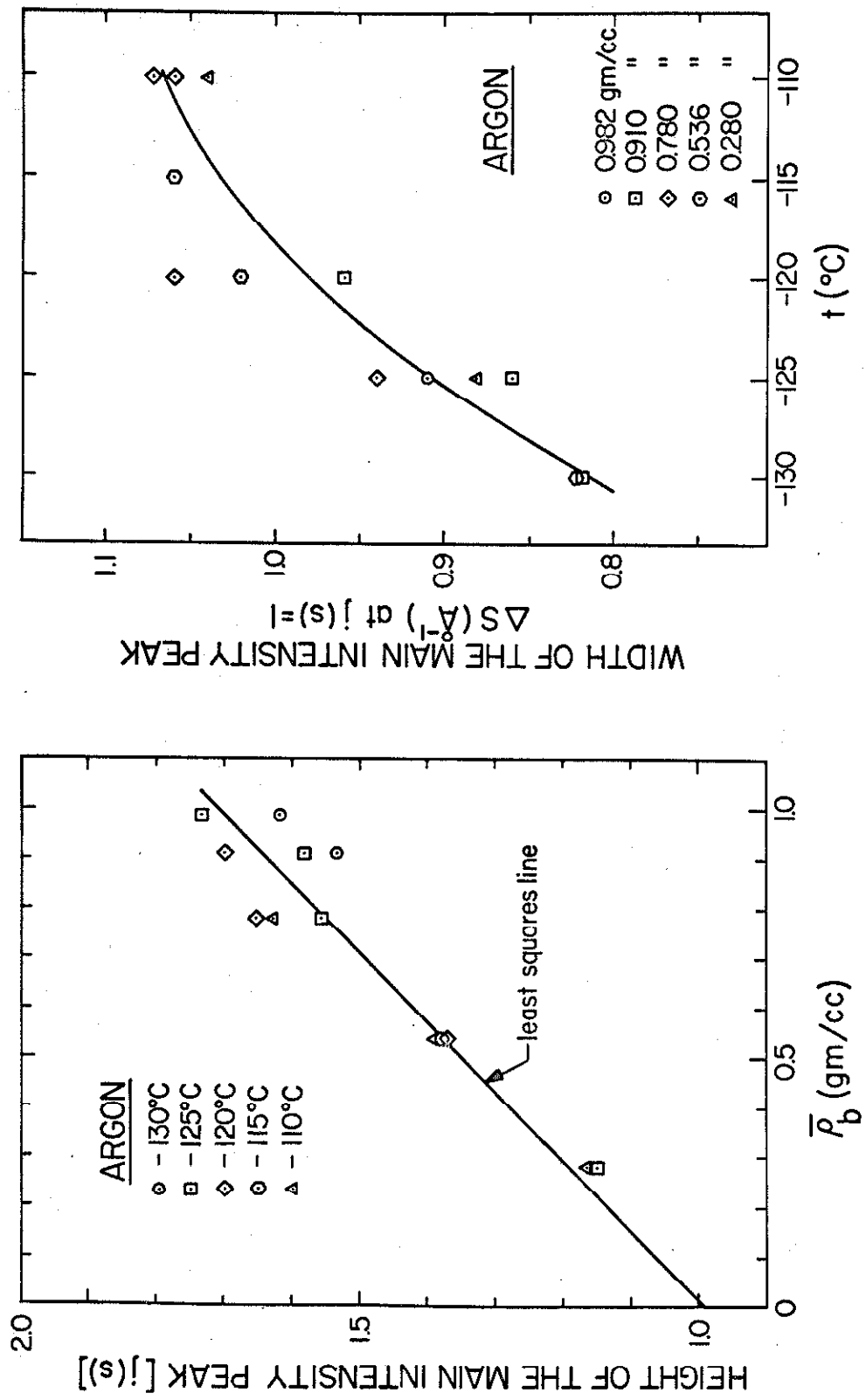


Figure 22. The Effect of Temperature and Bulk Density on the Main Peak in the Argon Intensity Function, j(S)

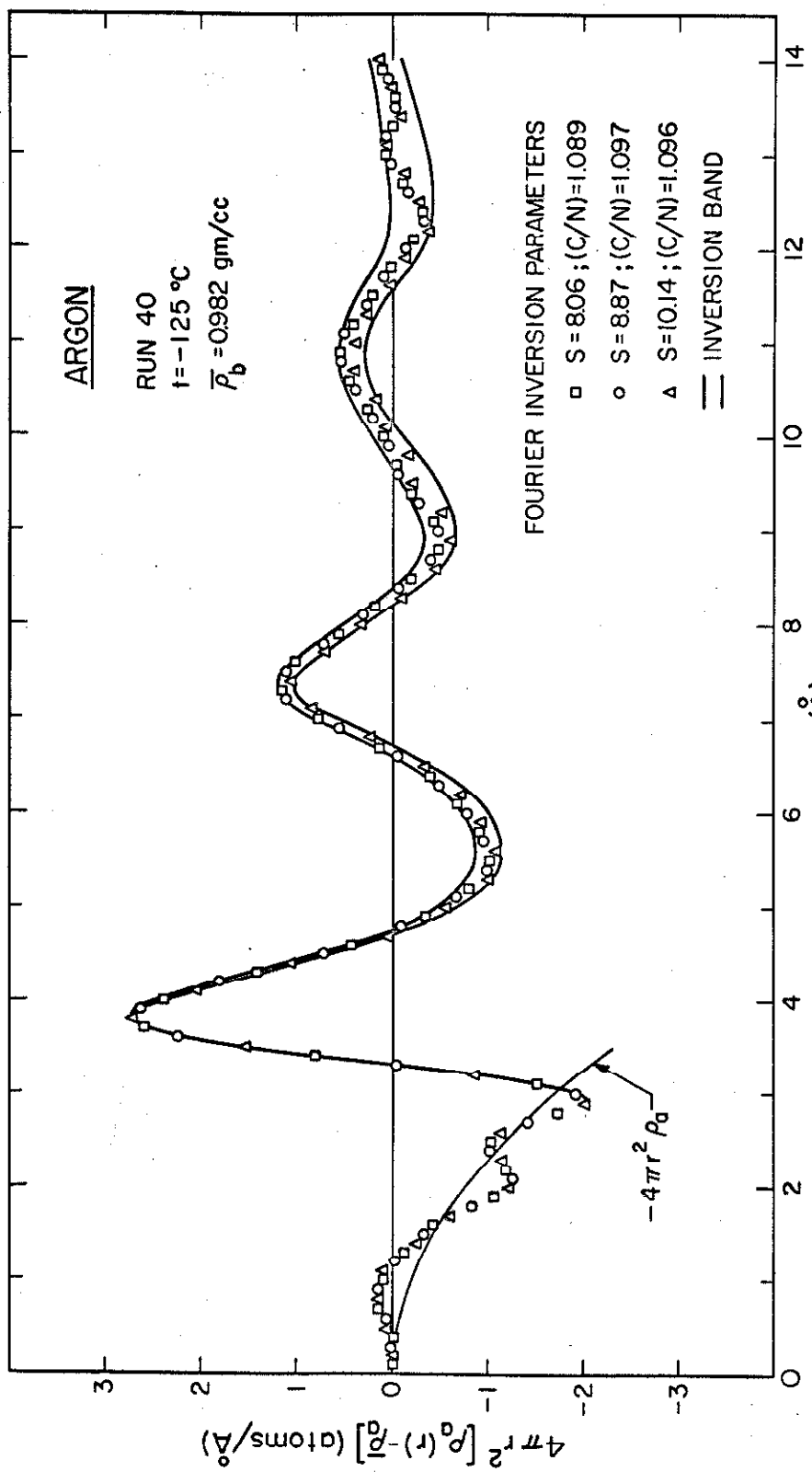


Figure 23. Superposition of Radial Atomic Density Functions and the Inversion Band for a Typical Argon Run

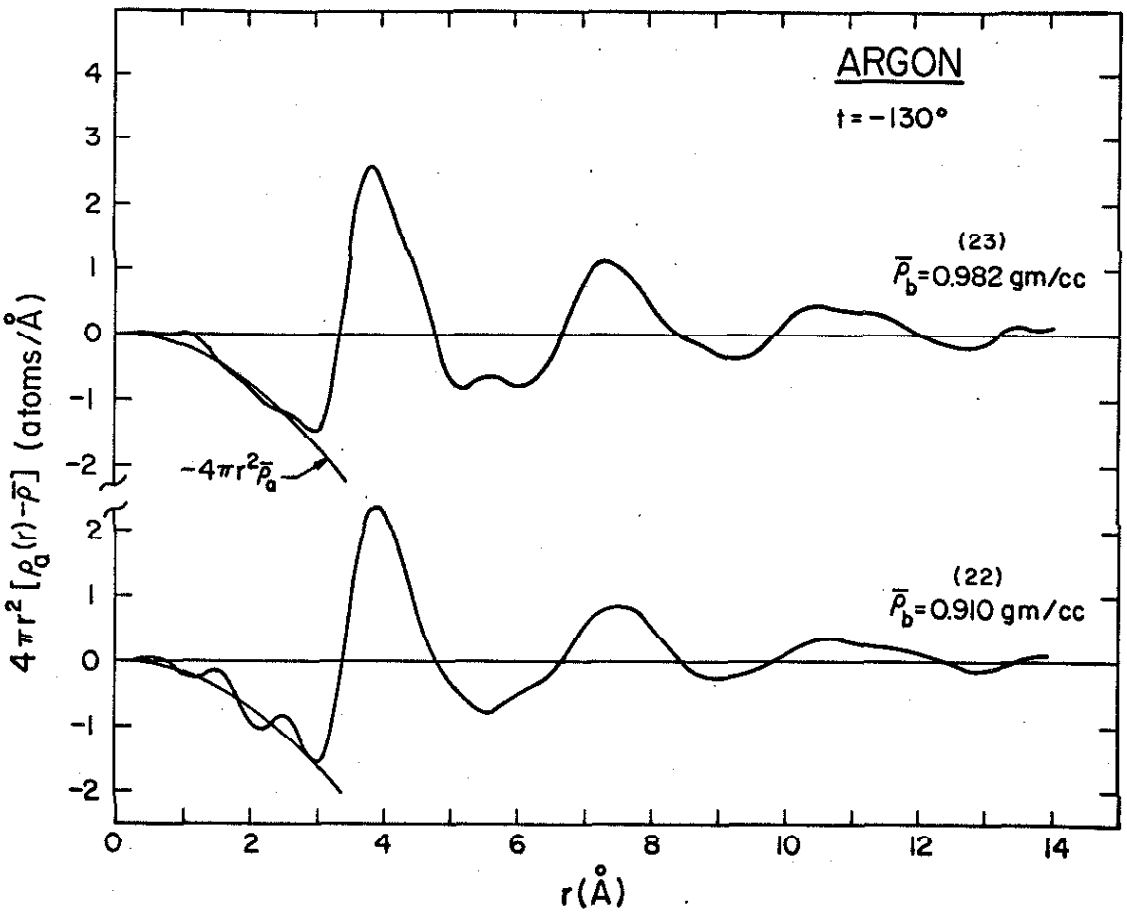


Figure 24. The Radial Atomic Density Function of Argon at t = -130°C

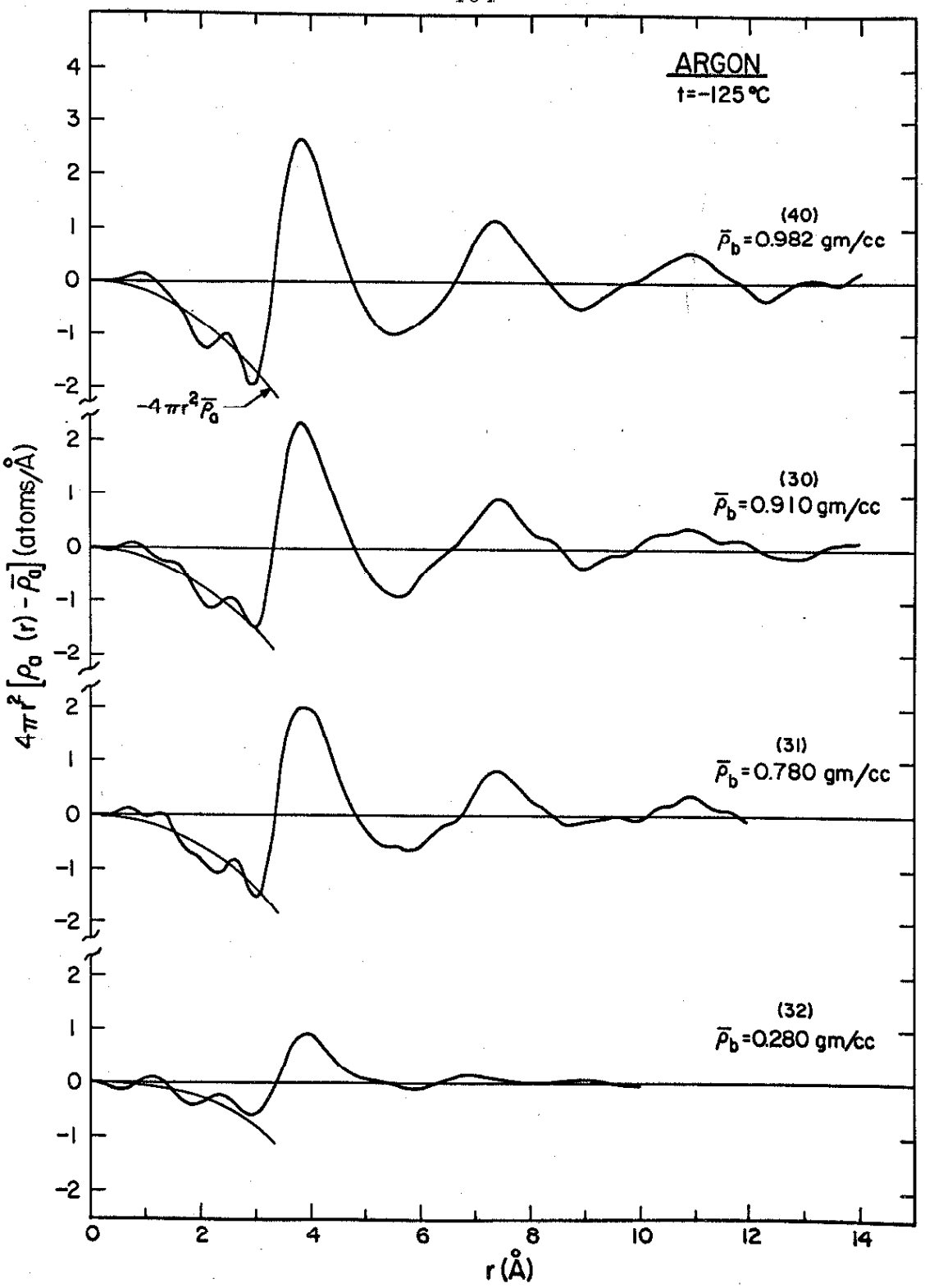


Figure 25. The Radial Atomic Density Function of Argon at t = -125°C

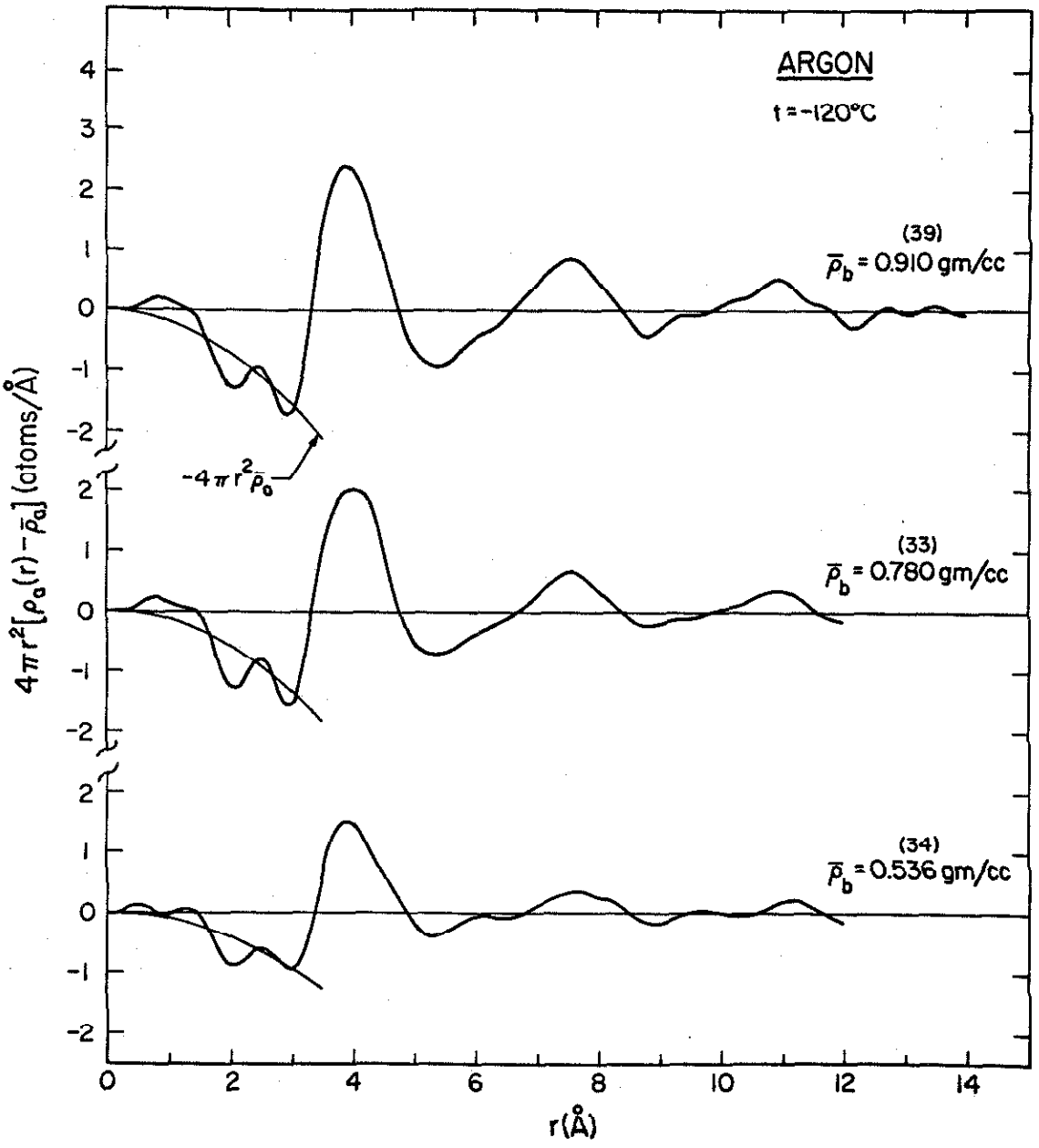


Figure 26. The Radial Atomic Density Function of Argon at t = -120°C

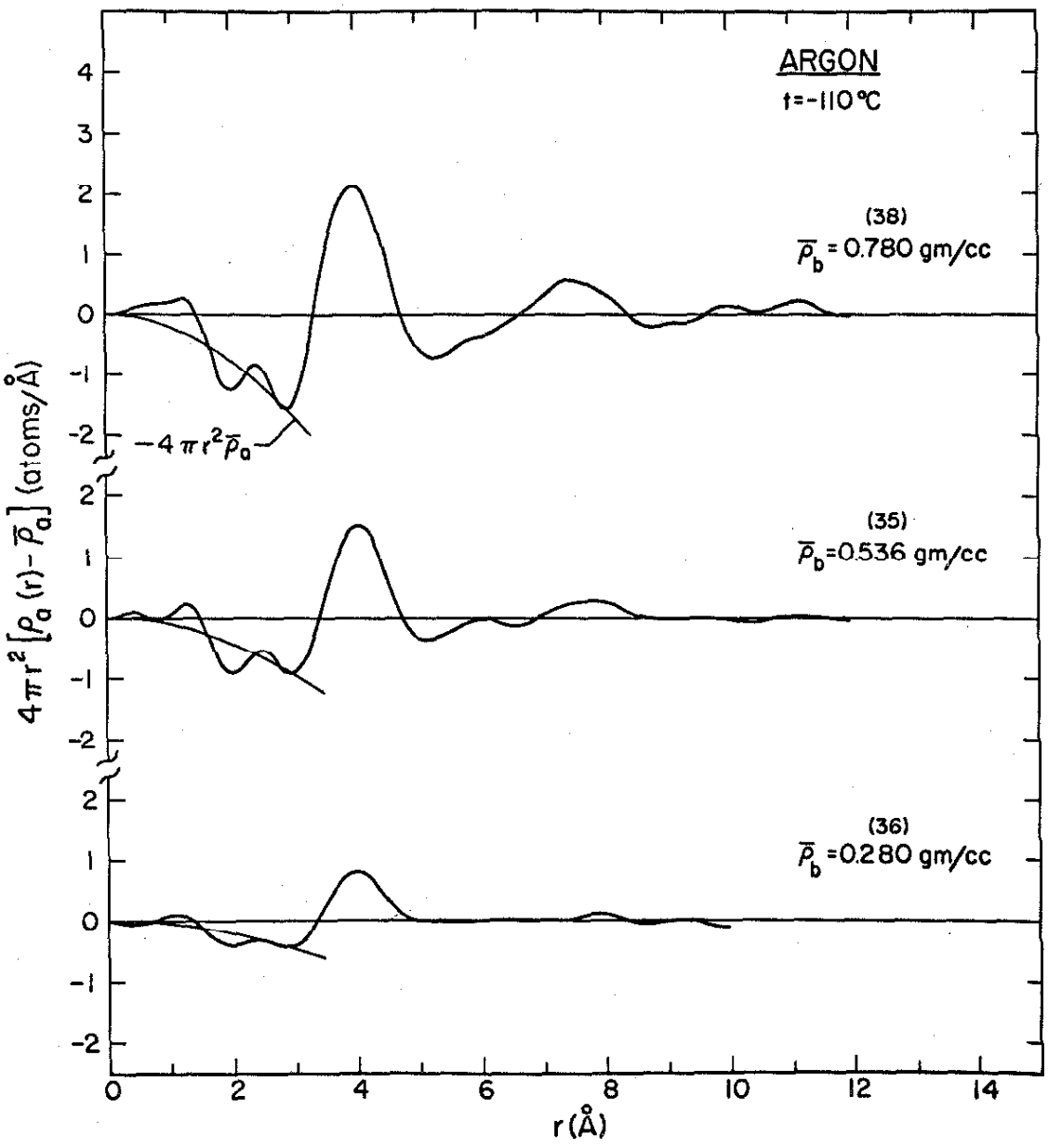


Figure 27. The Radial Atomic Density Function of Argon at t = -110°C

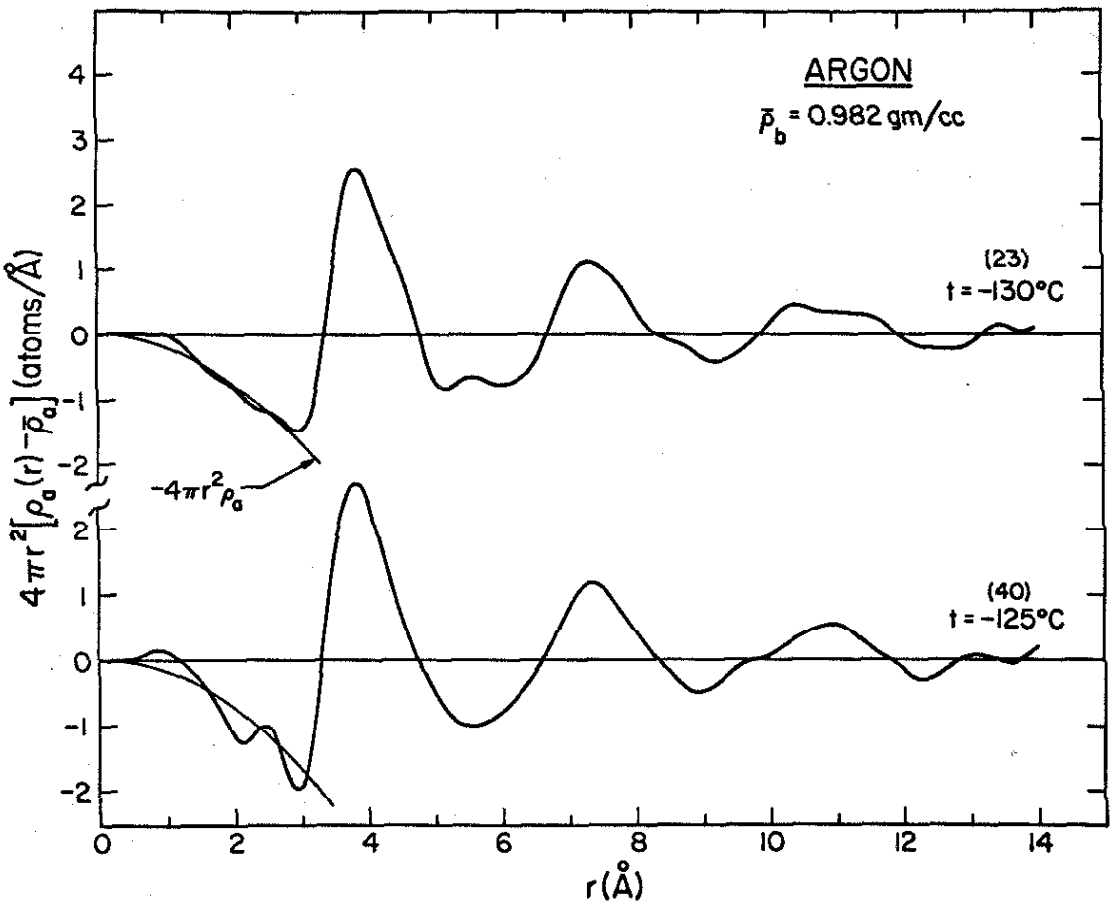


Figure 28. The Radial Atomic Density Function of Argon at a Bulk Density of 0.982 gm/cc

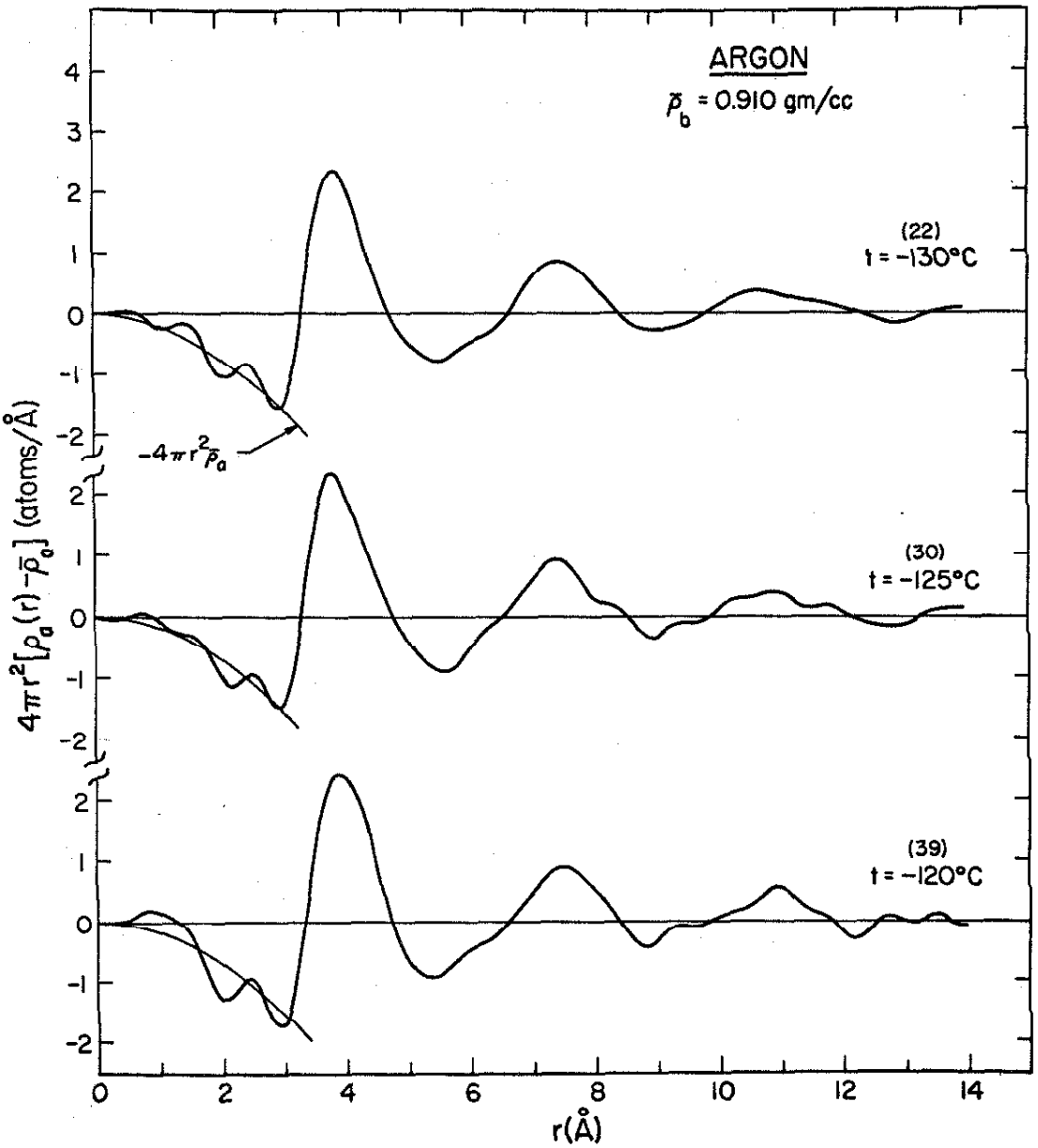


Figure 29. The Radial Atomic Density Function of Argon at a Bulk Density of 0.910 gm/cc

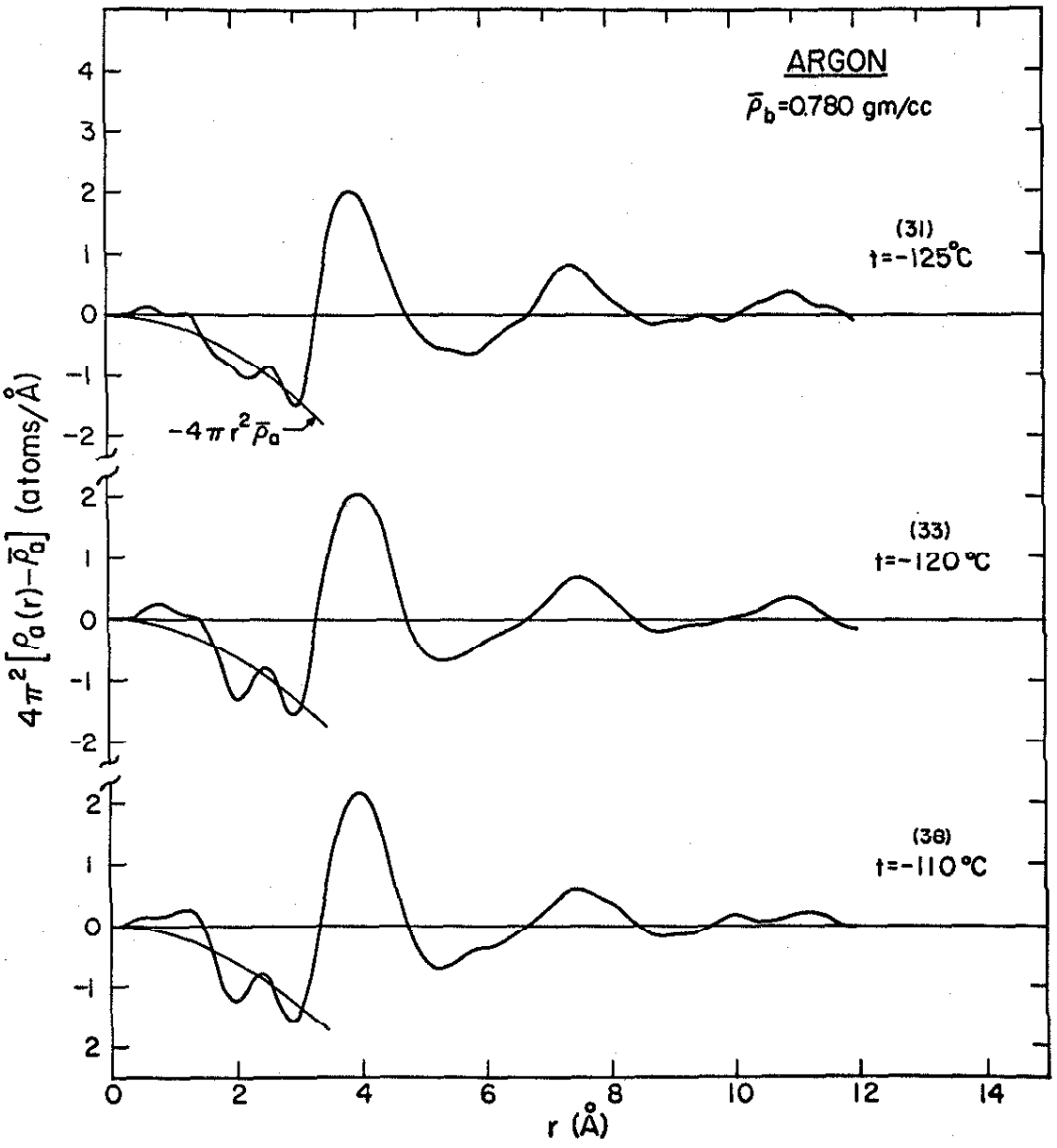


Figure 30. The Radial Atomic Density Function of Argon at a Bulk Density of 0. 780 gm/cc

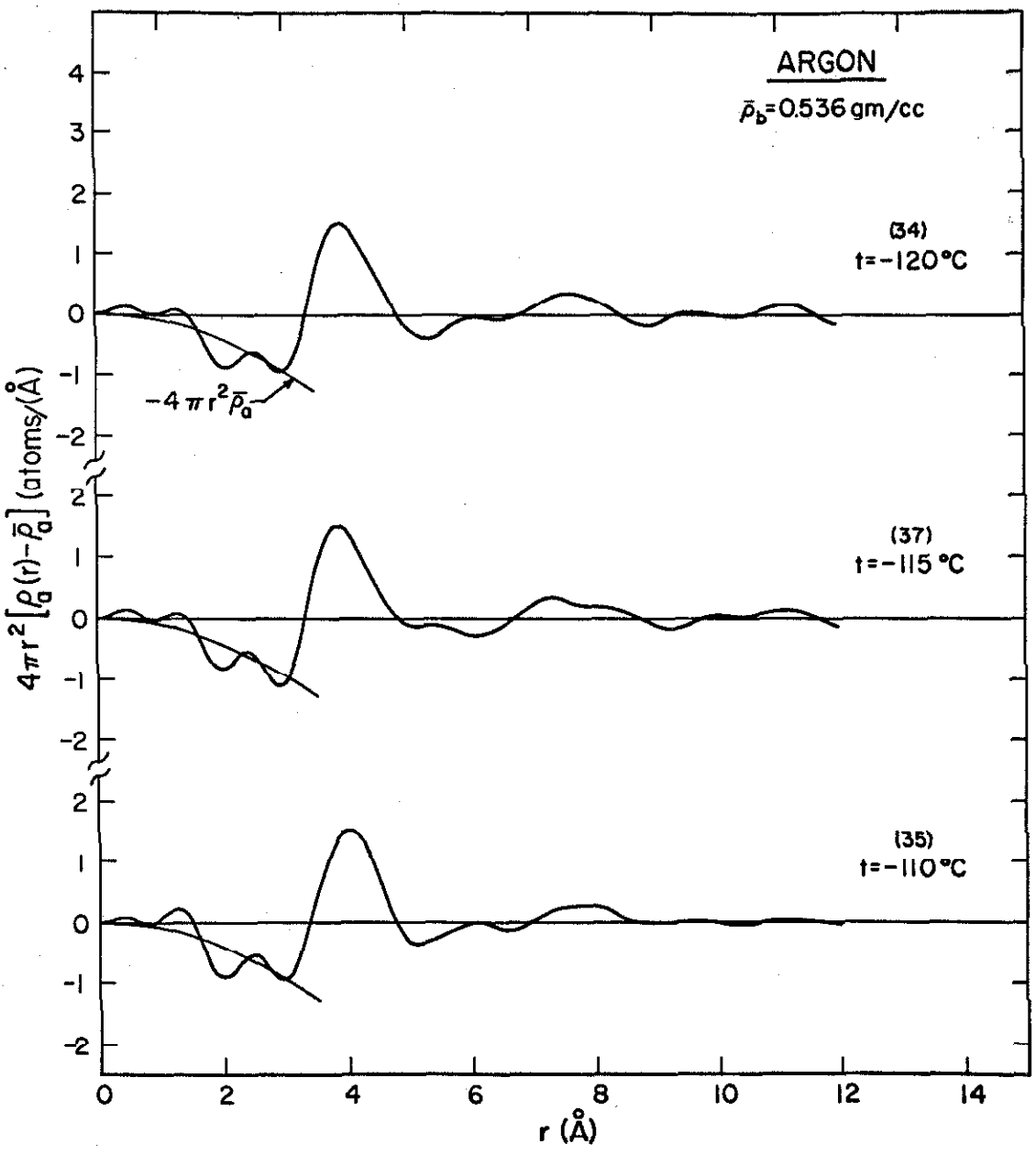


Figure 31. The Radial Atomic Density Function of Argon at a Bulk Density of 0.536 gm/cc

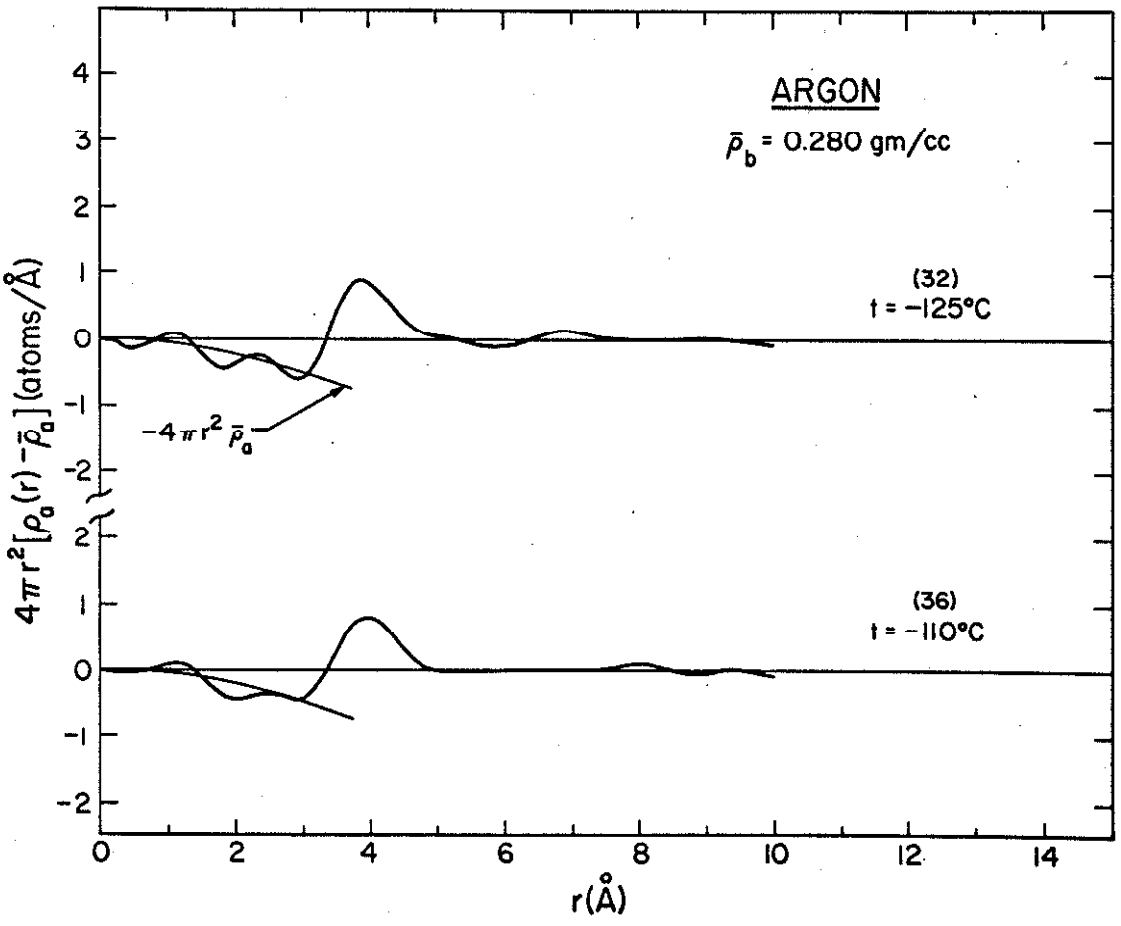


Figure 32. The Radial Atomic Density Function of Argon at a Bulk Density of 0.280 gm/cc

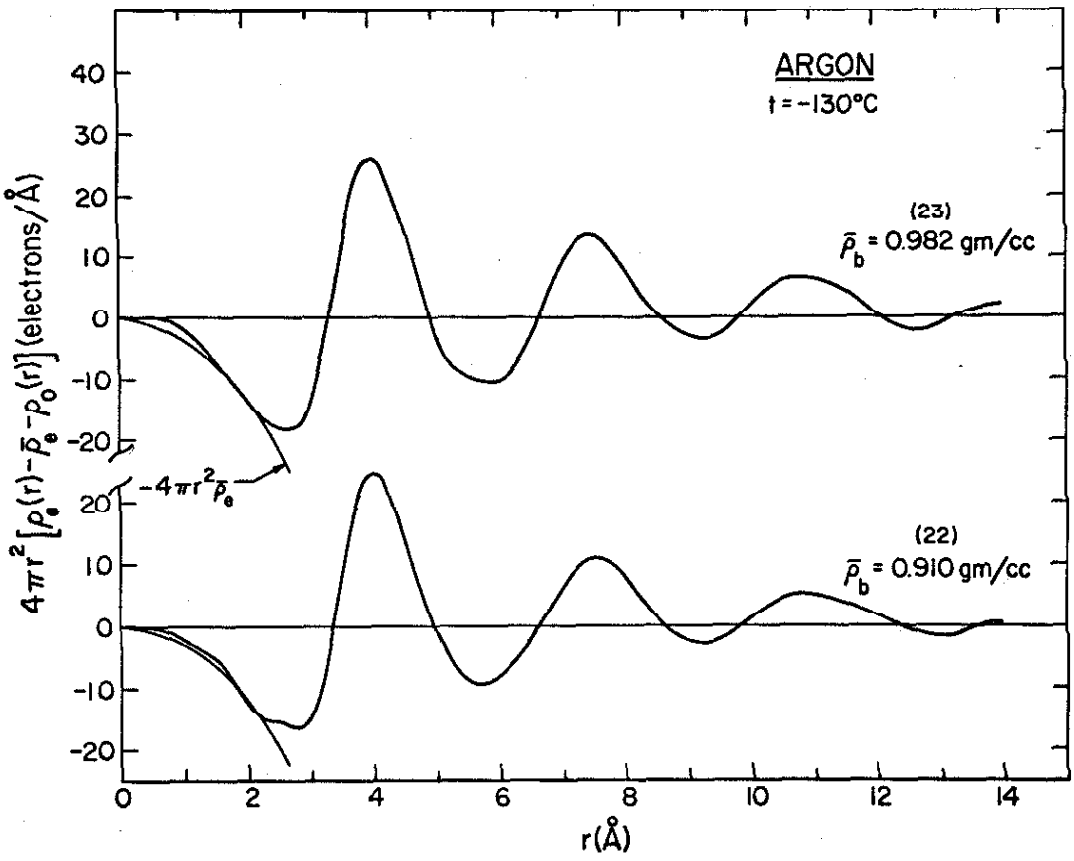


Figure 33. The Radial Electronic Density Function of Argon at t = -130°C

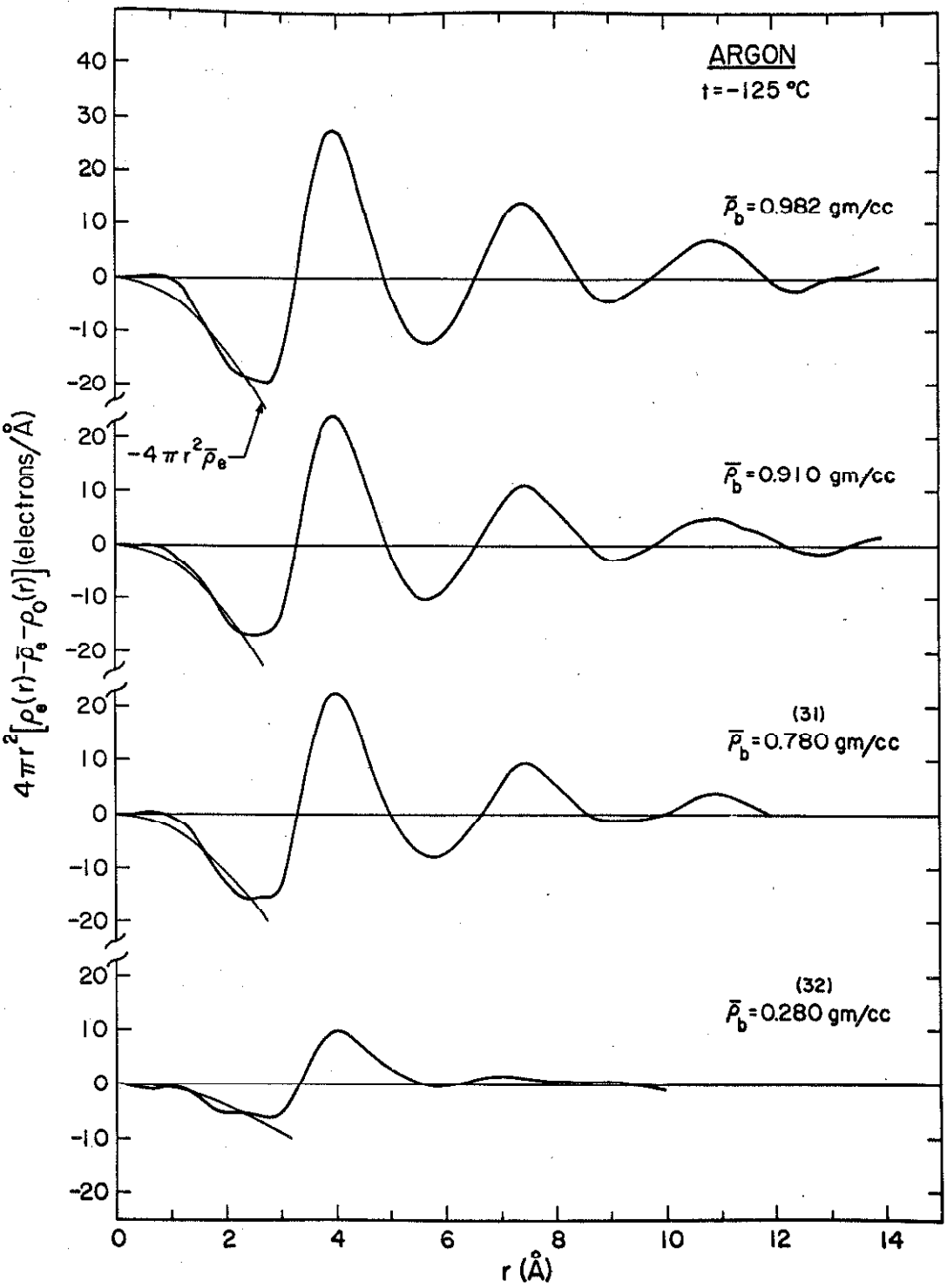


Figure 34. The Radial Electronic Density Function of Argon at t = -125°C

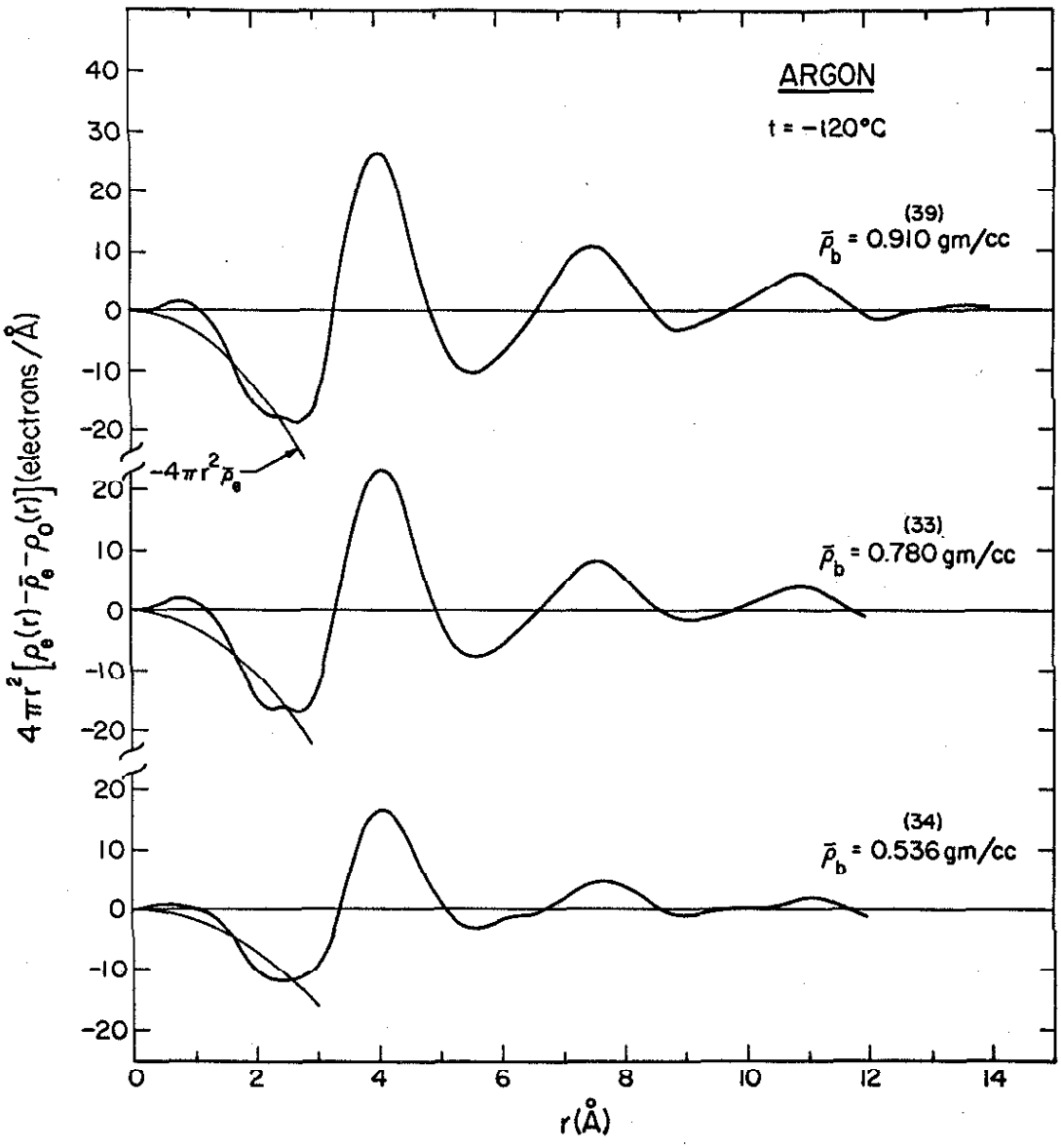


Figure 35. The Radial Electronic Density Function of Argon at t = -120°C

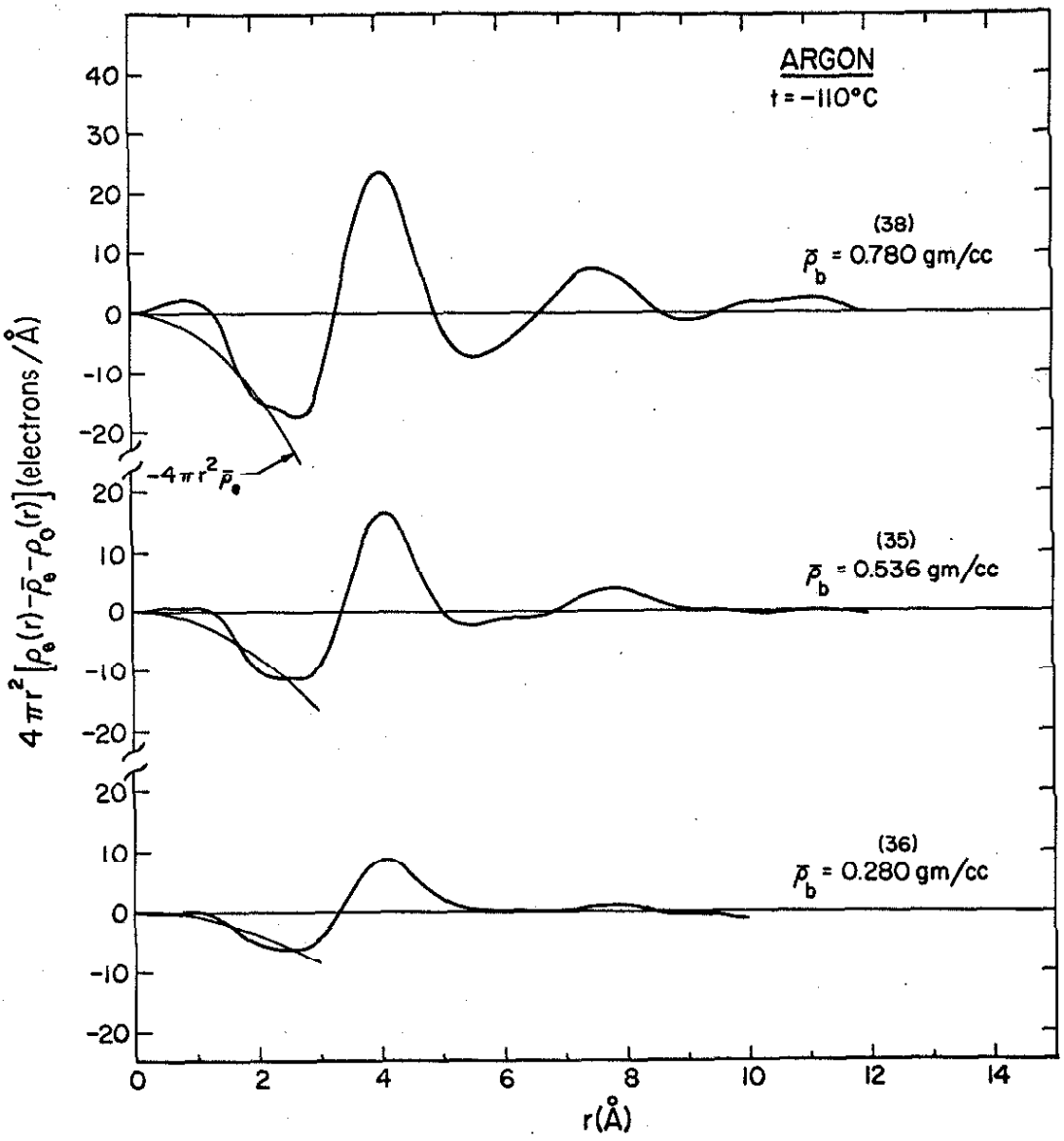


Figure 36. The Radial Electronic Density Function of Argon at t = -110°C

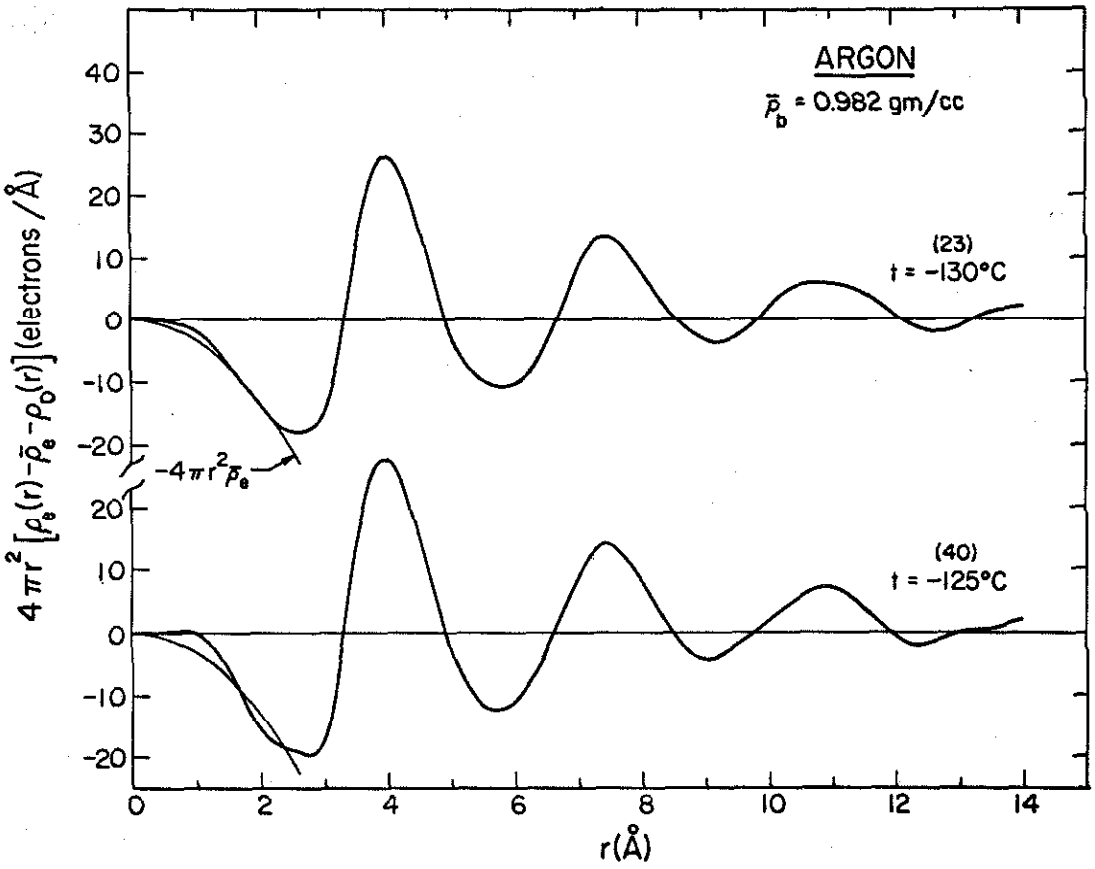


Figure 37. The Radial Electronic Density Function of Argon at a Bulk Density of 0.982 gm/cc

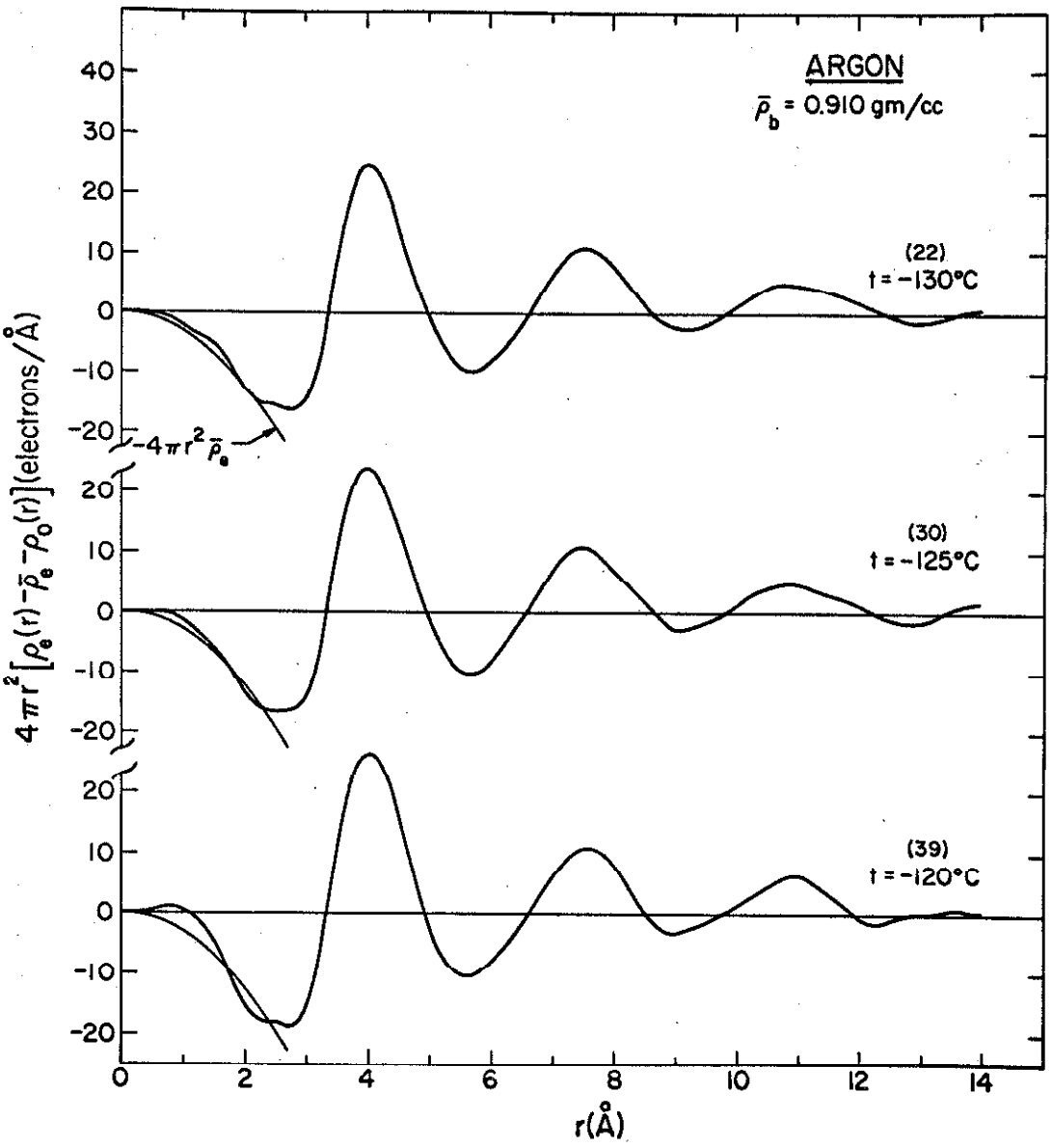


Figure 38. The Radial Electronic Density Function of Argon at a Bulk Density of 0.910 gm/cc

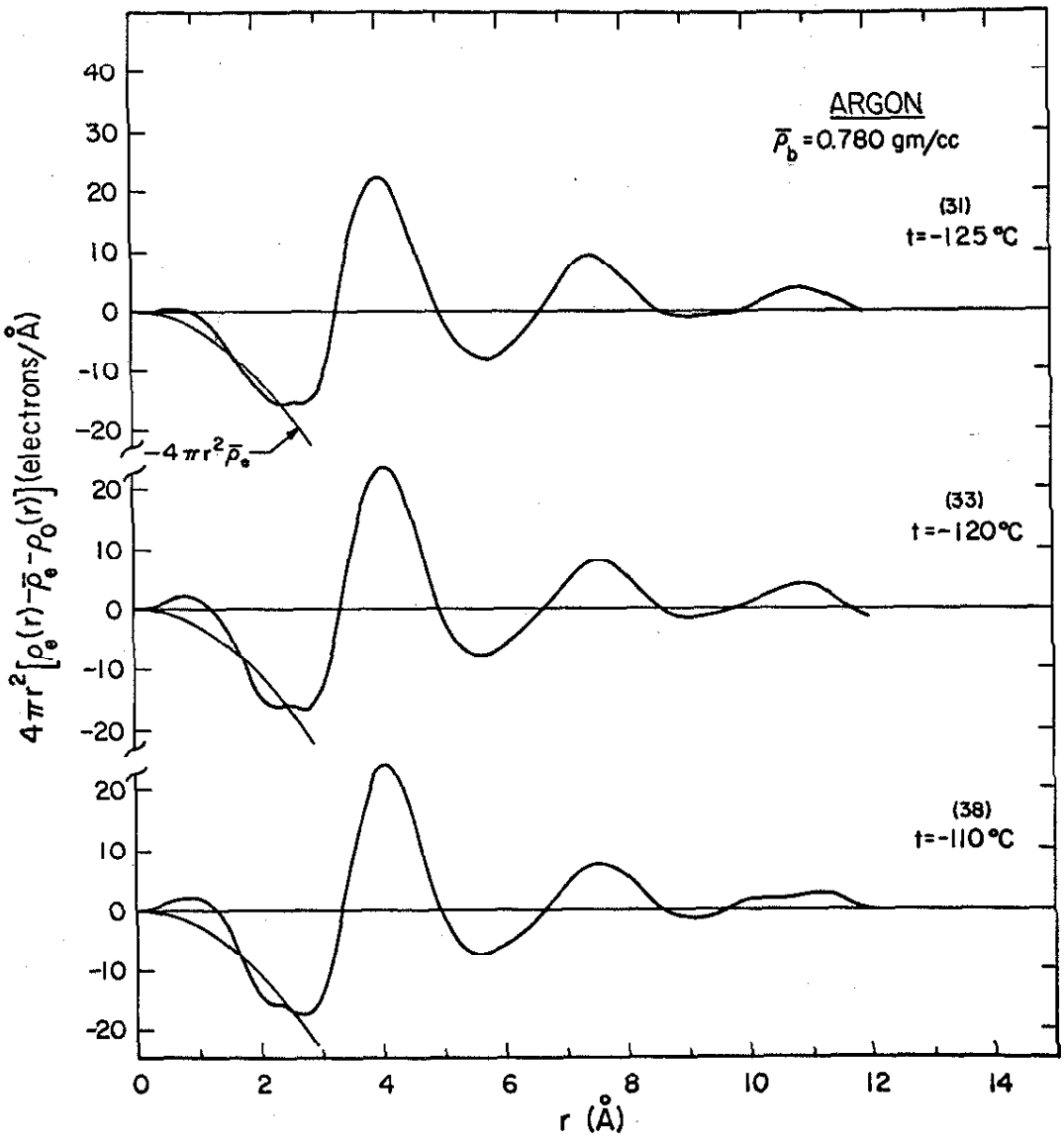


Figure 39. The Radial Electronic Density Function of Argon at a Bulk Density of 0.780 gm/cc

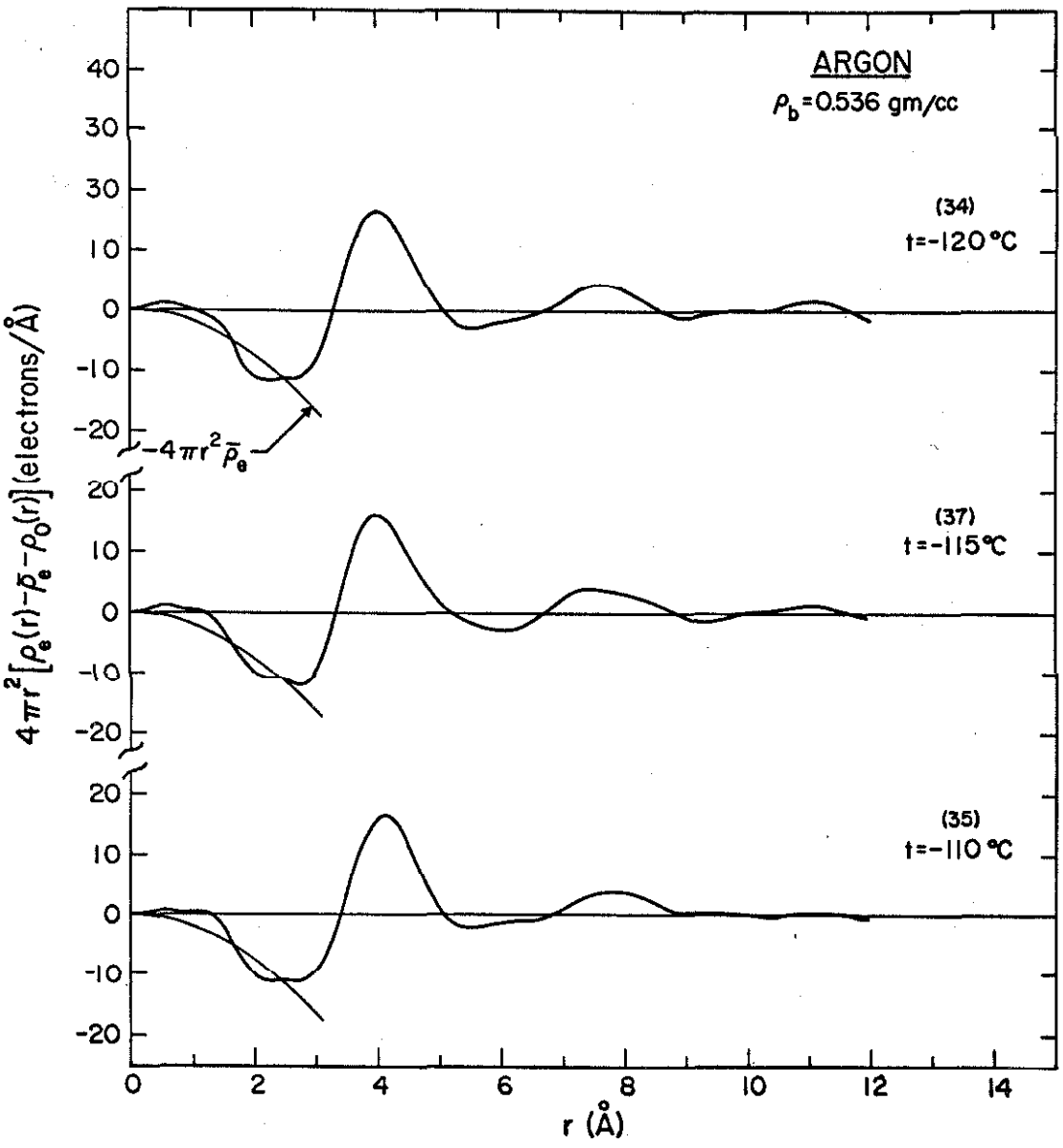


Figure 40. The Radial Electronic Density Function of Argon at a Bulk Density of 0.536 gm/cc

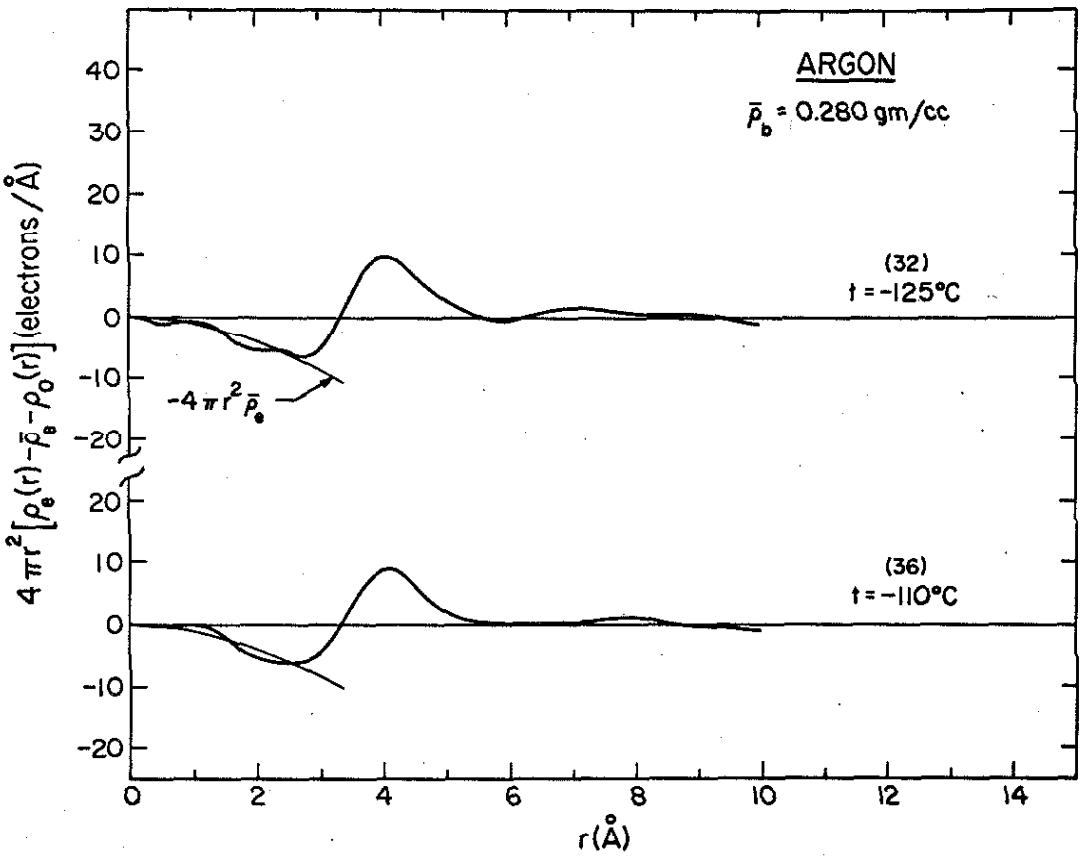


Figure 41. The Radial Electronic Density Function of Argon at a Bulk Density of 0.280 gm/cc

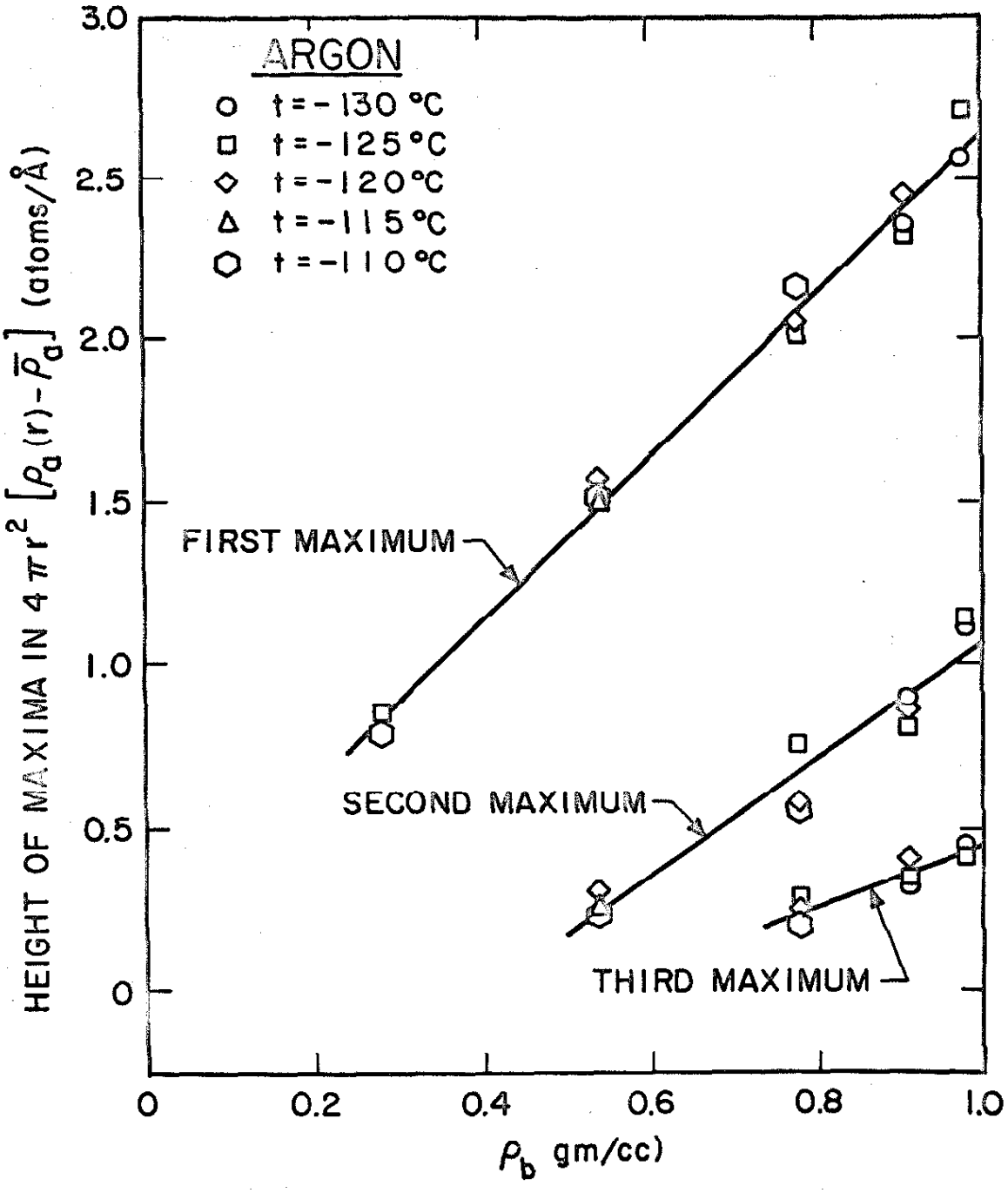


Figure 42. The Effect of Bulk Density on the Height of Maxima in the Radial Atomic Density Function of Argon

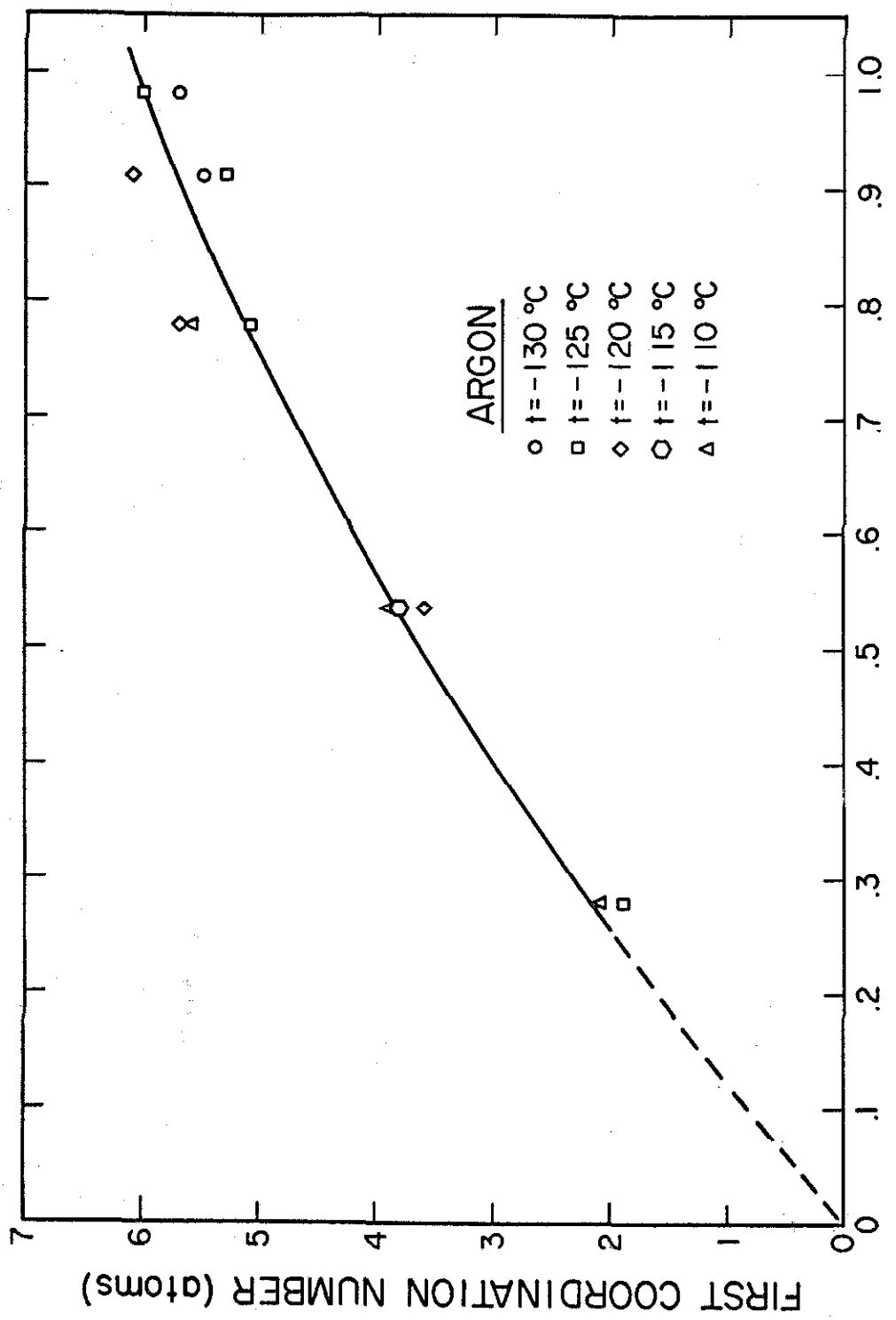


Figure 43. The Effect of Bulk Density on the First Coordination Number of Fluid Argon

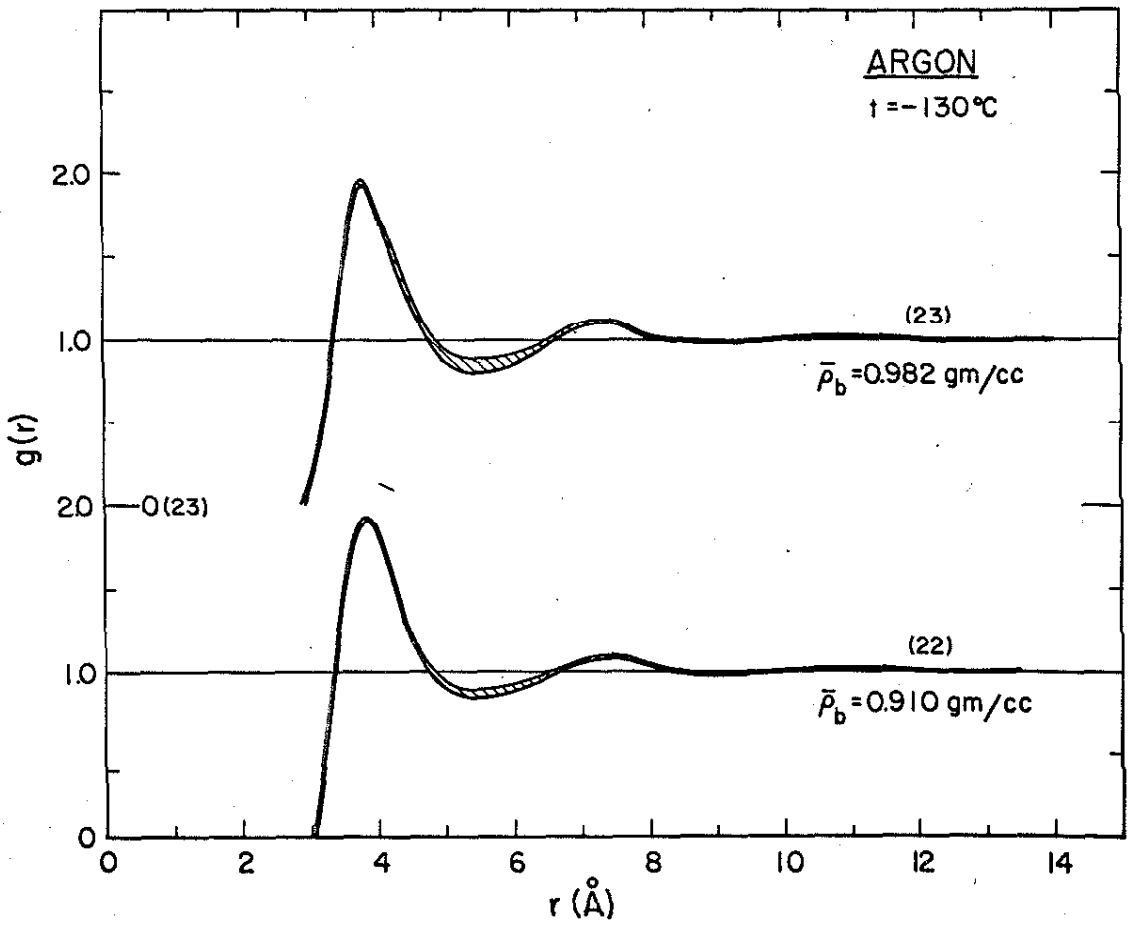


Figure 44. The Estimated Radial Distribution Function of Argon at t = -130°C

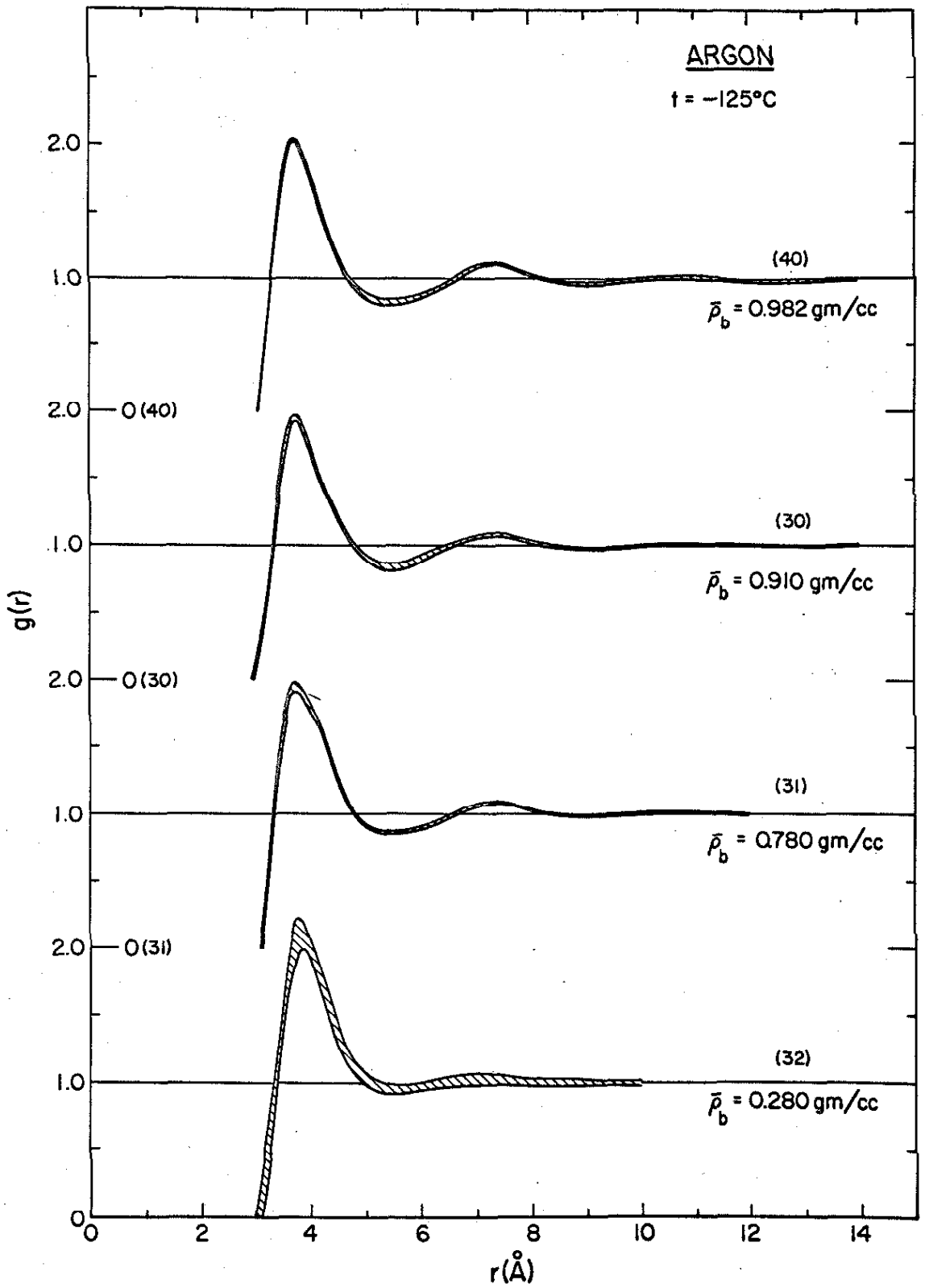


Figure 45. The Estimated Radial Distribution Function of Argon at t = -125°C

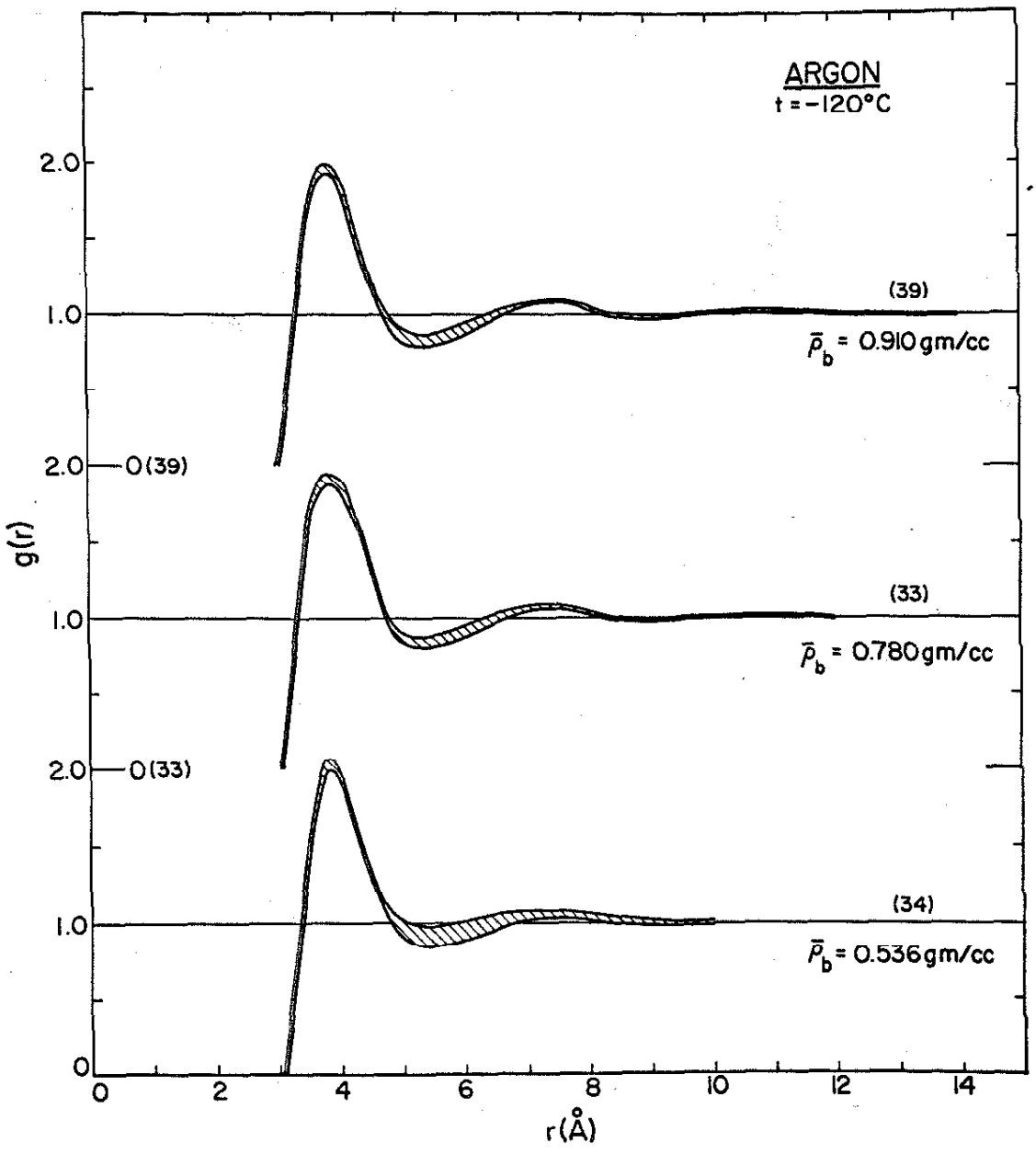


Figure 46. The Estimated Radial Distribution Function of Argon at t = -120°C

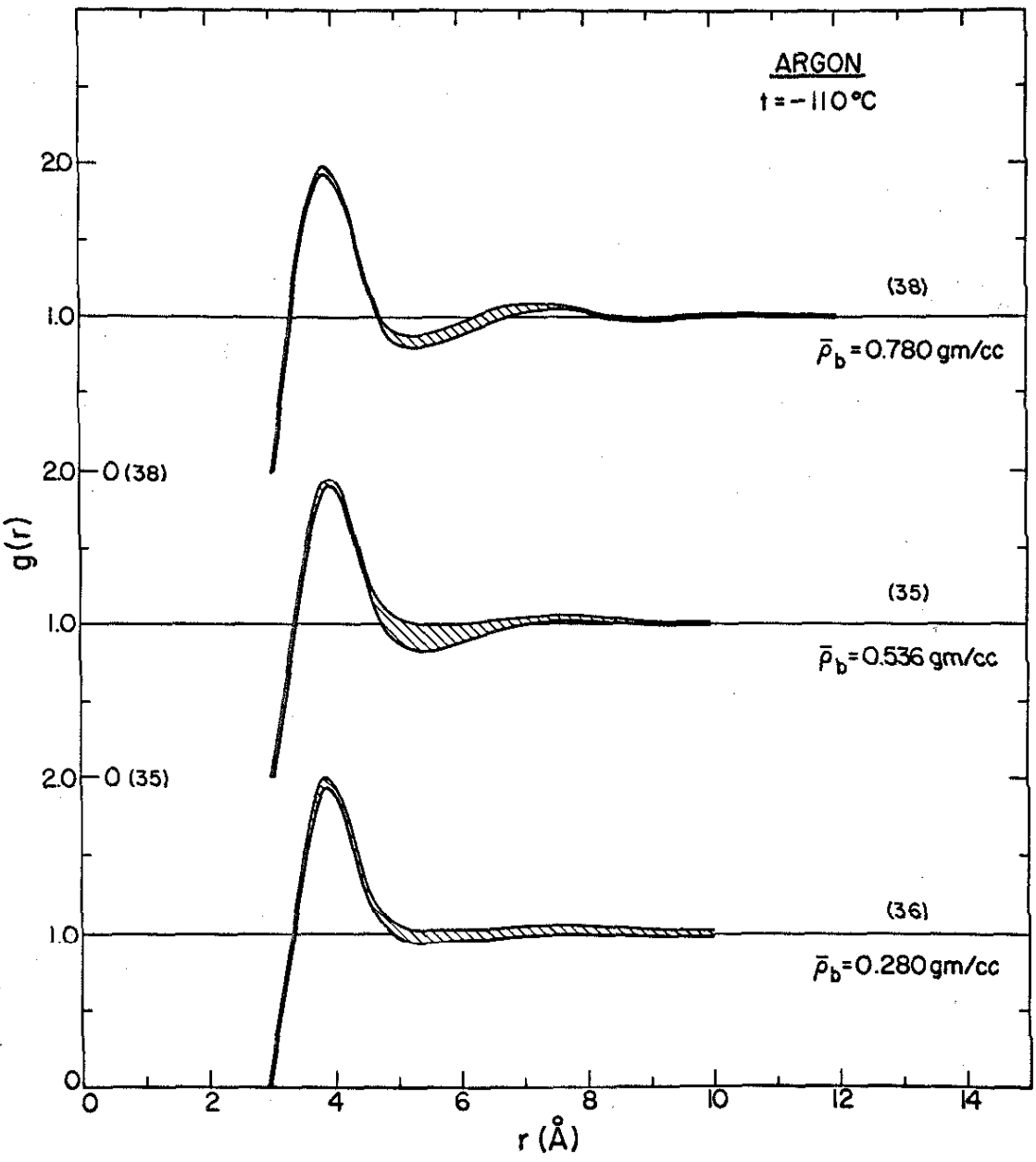


Figure 47. The Estimated Radial Distribution Function of Argon at t = -110°C

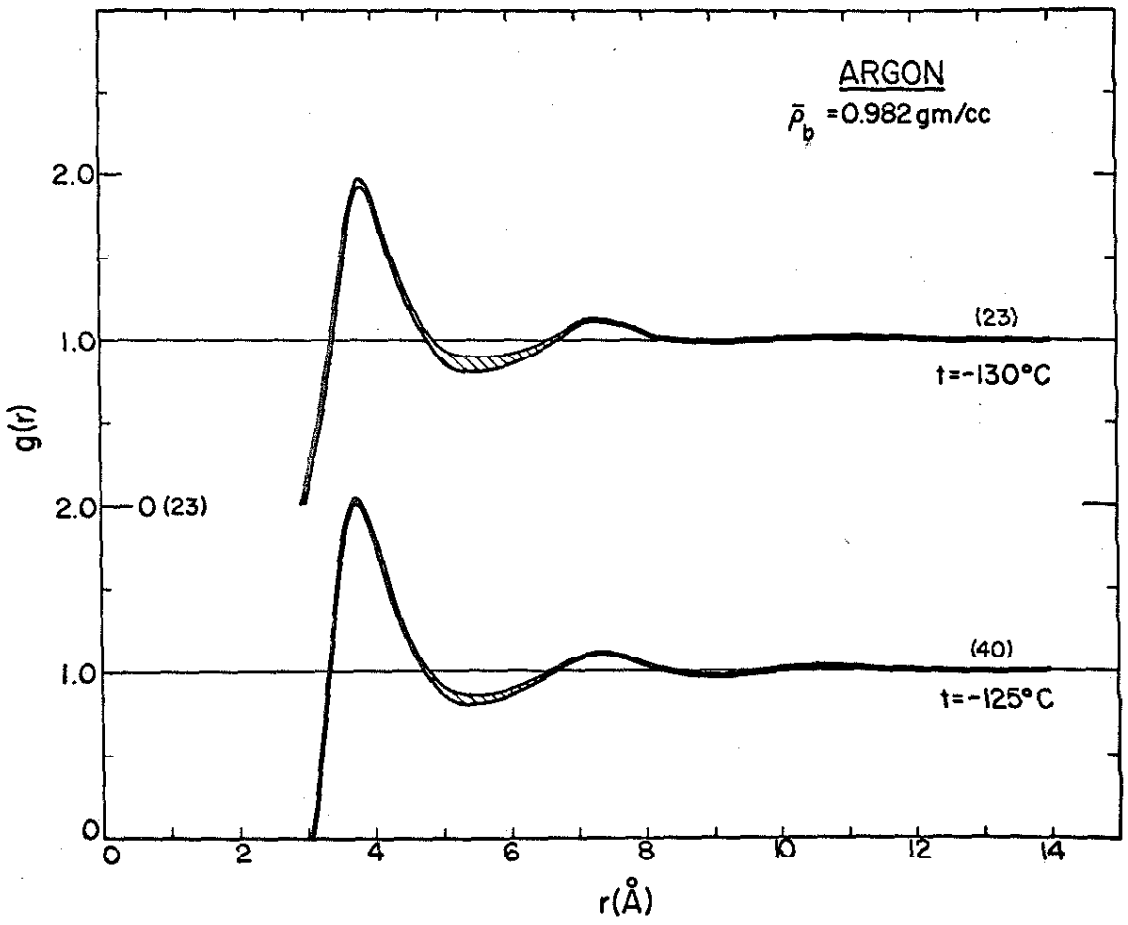


Figure 48. The Estimated Radial Distribution Function of Argon at a Bulk Density of 0.982 gm/cc

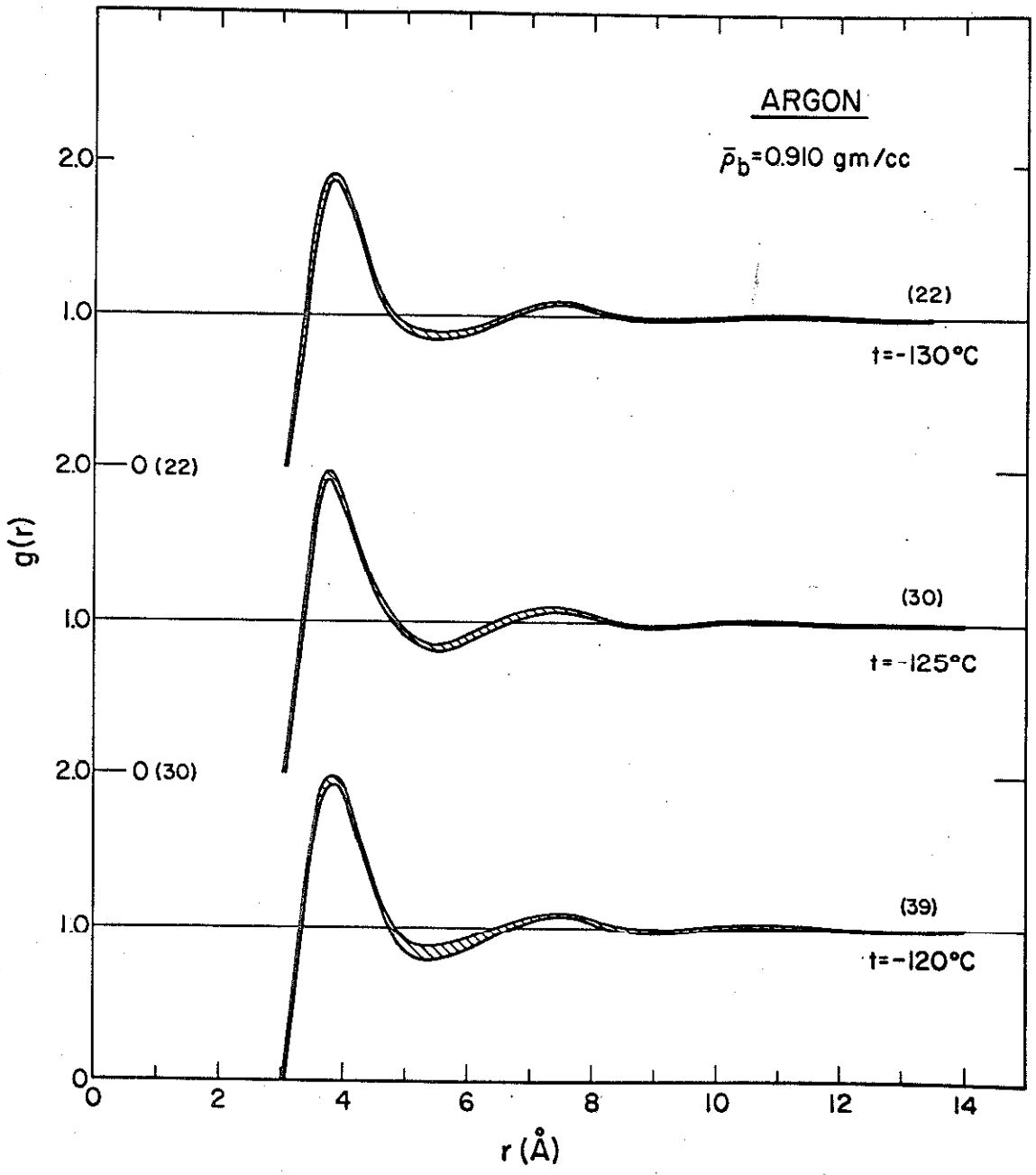


Figure 49. The Estimated Radial Distribution Function of Argon at a Bulk Density of 0.910 gm/cc

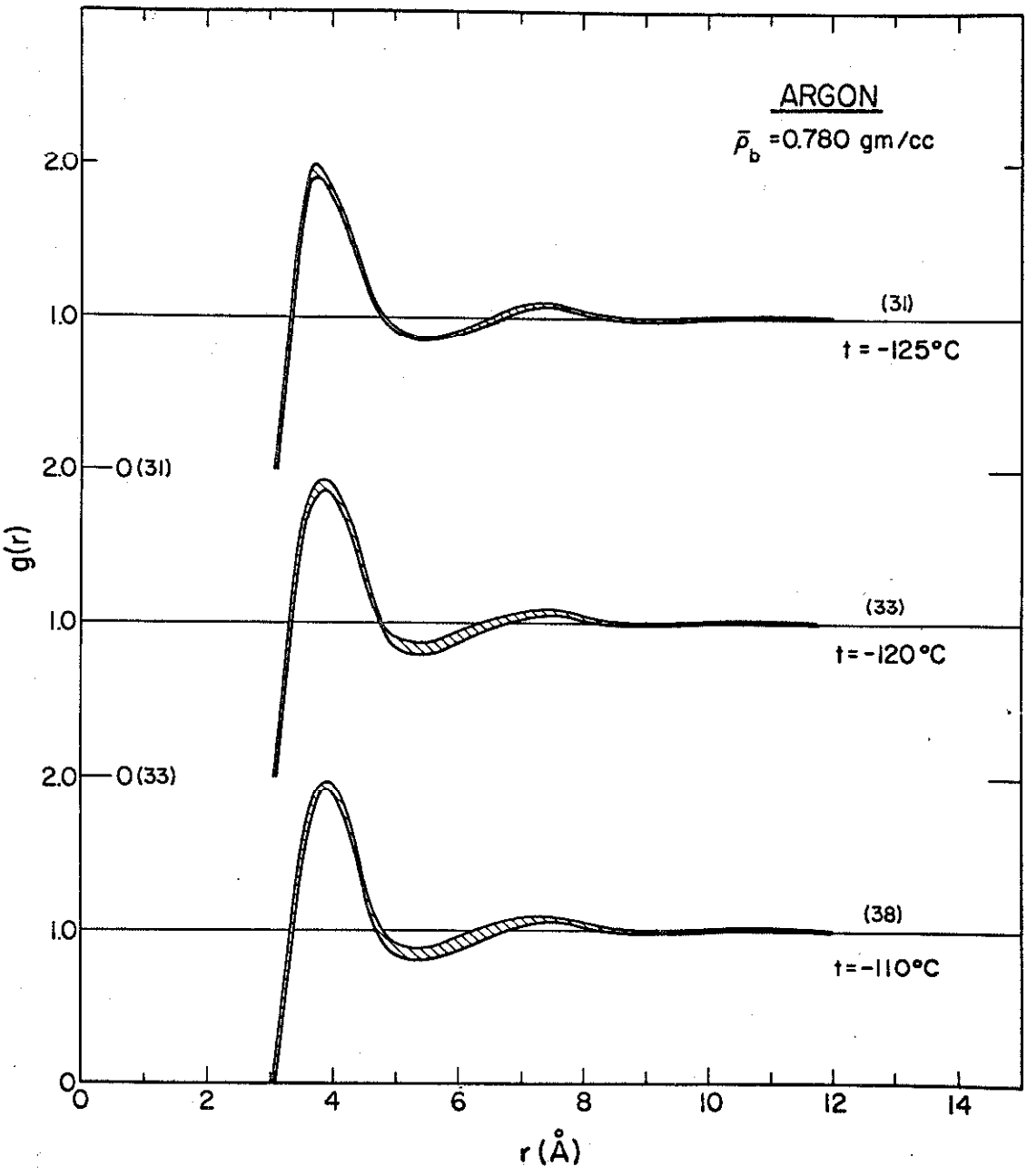


Figure 50. The Estimated Radial Distribution Function of Argon at a Bulk Density of 0.780 gm/cc

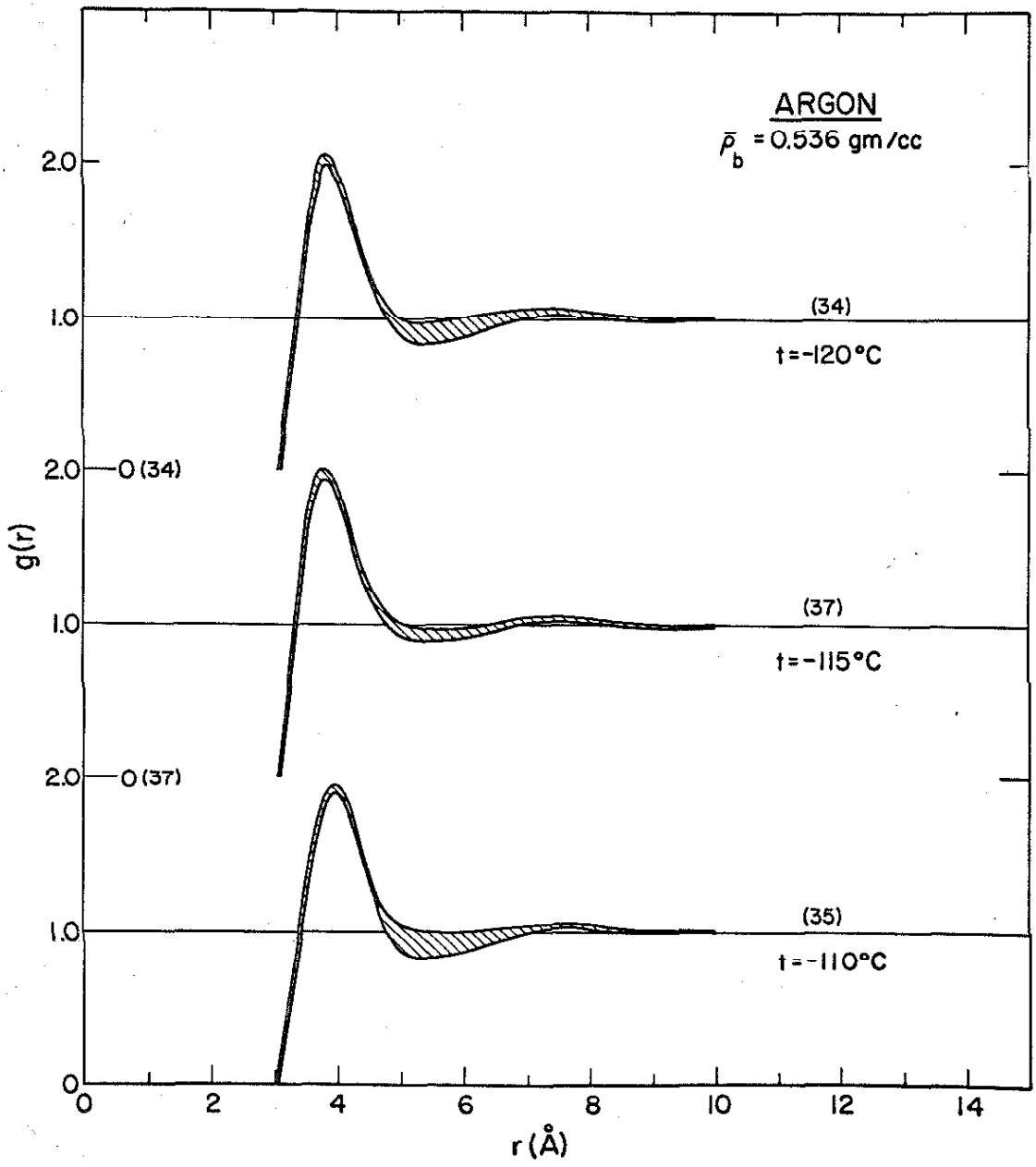


Figure 51. The Estimated Radial Distribution Function of Argon at a Bulk Density of 0.536 gm/cc

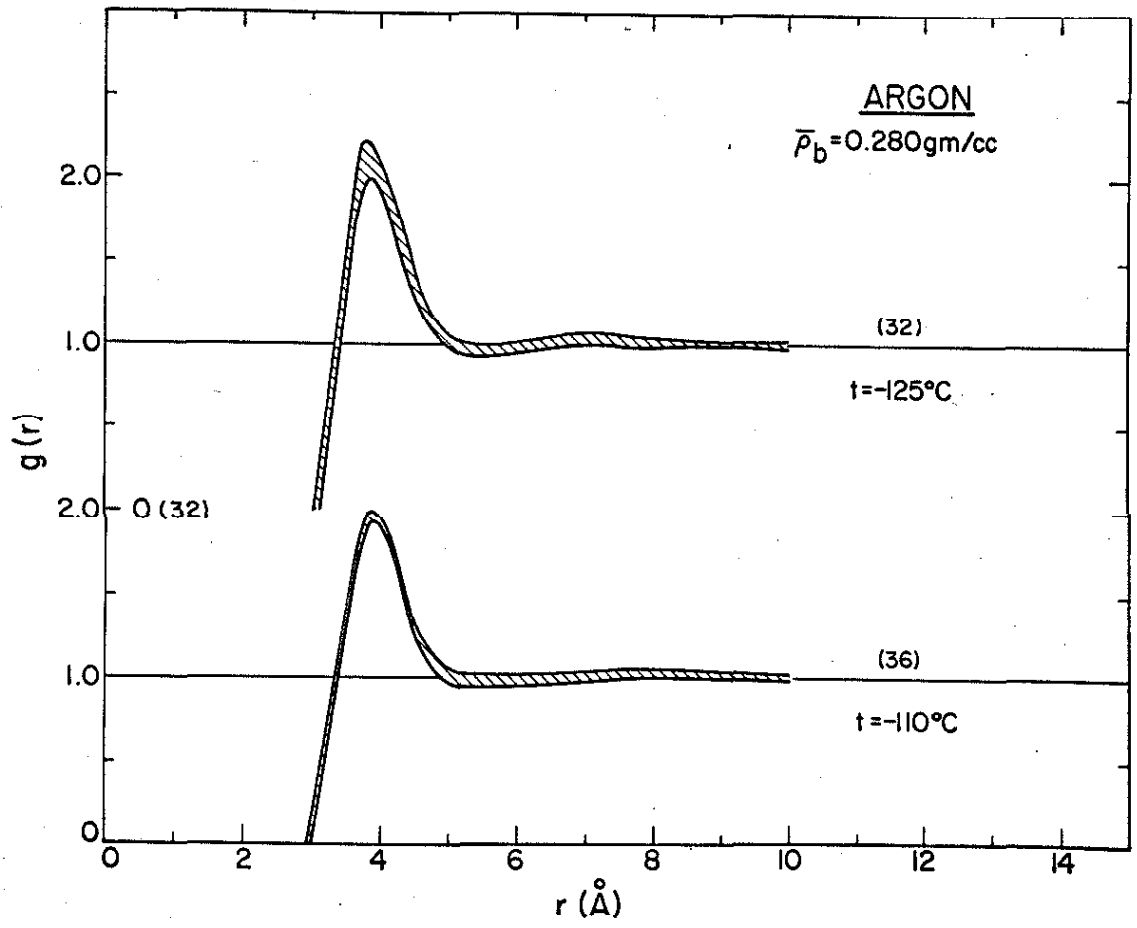


Figure 52. The Estimated Radial Distribution Function of Argon at a Bulk Density of 0.280 gm/cc

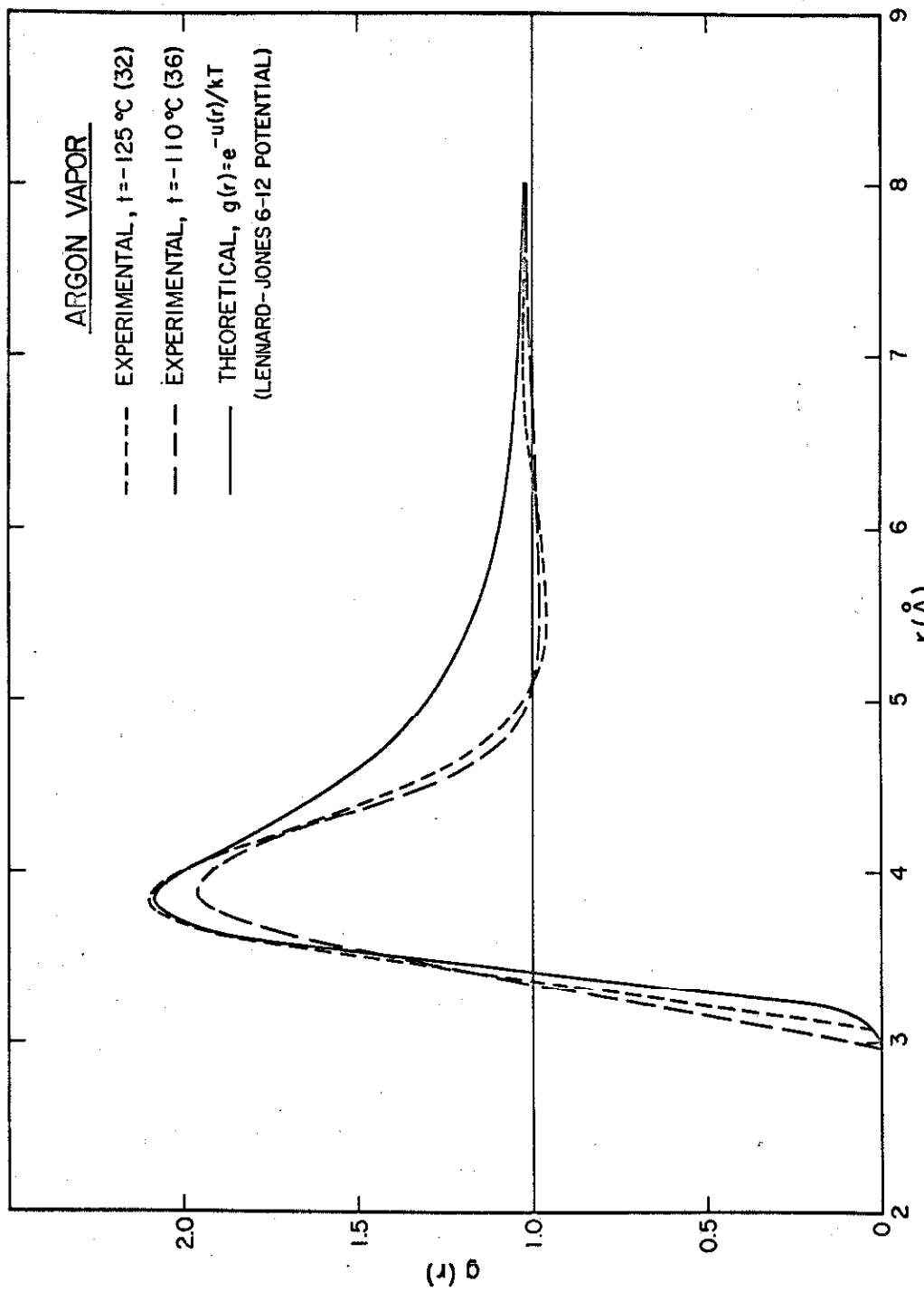


Figure 53. Radial Distribution Functions of Argon Vapor
(The theoretical curve is for t = -110°C.)

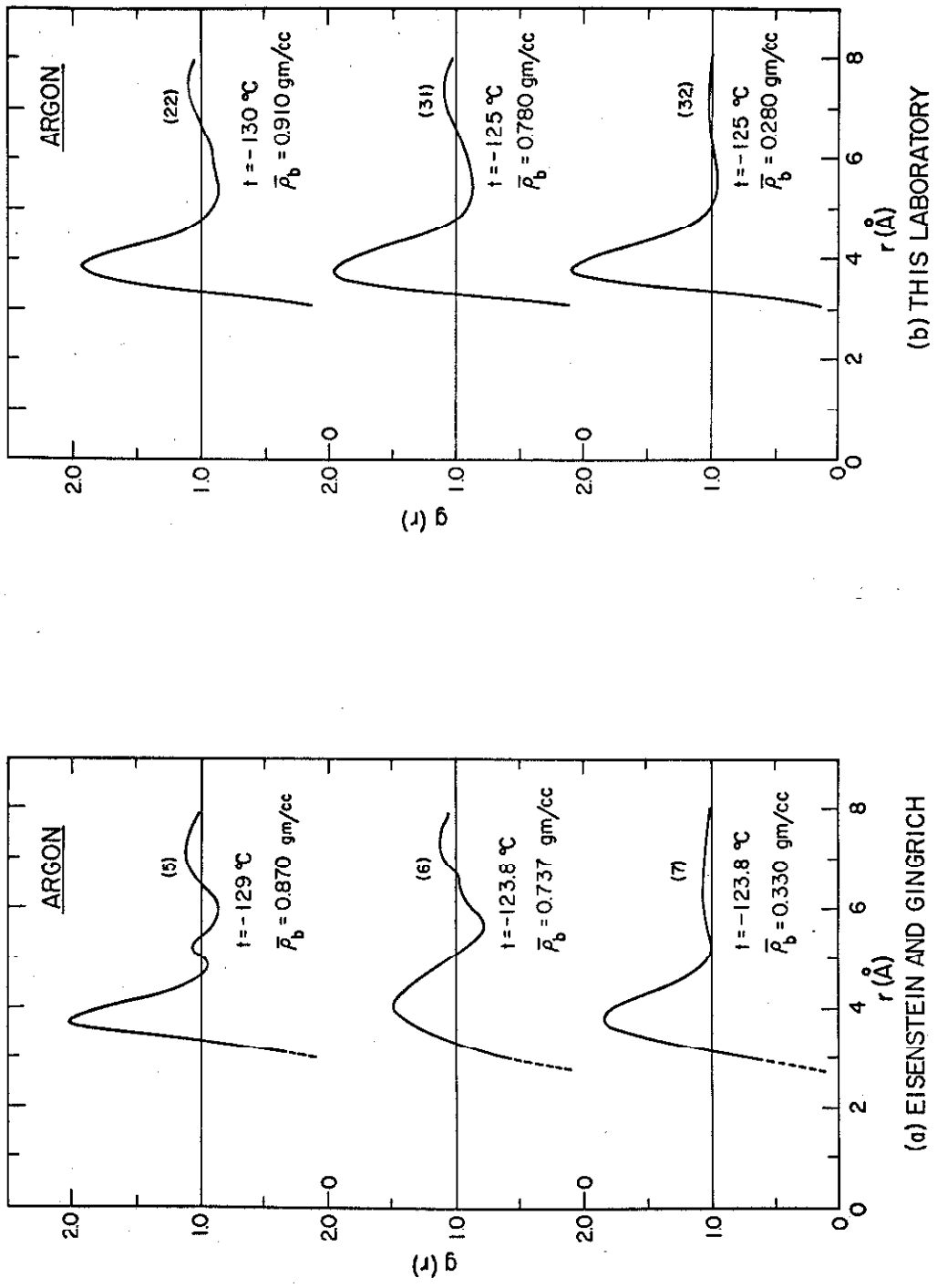


Figure 54. A Comparison of Radial Distribution Functions

# PROPOSITION I

Under certain conditions, the use of Newtonian flow equations leads to a simple expression which may be used to predict the existence of laminar or turbulent flow of a non-Newtonian fluid.

---

Many non-Newtonian fluids follow the empirical "power-law" rheology where the shear stress is related to the shear rate by the equation

$$\tau = K\left(-\frac{du}{dr}\right)^n \qquad (1)$$

The exponent $n$ is the flow behavior index and has the following range of values:

| | |
|---|---|
| pseudoplastic | $n < 1$ |
| dilatant | $n > 1$ |
| Newtonian | $n = 1, \quad K = \eta$ |

Metzner and Reed[1] have defined a generalized Reynolds number applicable to non-Newtonian fluids which is useful in predicting the end of the stable laminar flow region. For the case of a non-Newtonian fluid following the power law model over the range of shear rates of interest, the generalized Reynolds number takes the form

$$Re' = \frac{D_o^n \, U^{2-n} \rho}{8^{n-1} K'} \tag{2}$$

where

$$K' = 8^{-n} \left( \frac{6n + 2}{n} \right)^n K \tag{3}$$

As is often the case, the flow is steady and uniform and the available experimental information is the pressure drop or wall shear. Therefore, in order to calculate the Reynolds number, the bulk velocity must first be determined by the equations

$$U = \frac{n D_o^{(n+1)/n}}{6n + 2} \left[ \frac{1}{4K} \left( - \frac{dP}{dx} \right) \right]^{1/n} \tag{4}$$

$$\left( - \frac{dP}{dx} \right) = \frac{4\tau_o}{D_o} \tag{5}$$

As shown by the preceding equations, the determination of a Reynolds number for a non-Newtonian fluid involves rather lengthy and tedious calculations. Nebeker[2] has proposed a simplification of these calculations by considering the case of a Newtonian fluid flowing at the same bulk velocity. He uses a conventional Reynolds number employing an apparent viscosity and suggests that knowledge of K and n are not necessary in this calculation. This is obviously not

true if only the pressure gradient is known and in any case, the data necessary to calculate the apparent viscosity are also the data required for the determination of K and n.

As proposed here, a more useful concept is that of a Newtonian fluid flowing under the same pressure gradient. This method utilizes the Newtonian flow equations and presents a much simpler method for gaining information as to the existence of laminar or turbulent flow. By introducing an apparent viscosity, $\eta^*$, the following modified Reynolds number is defined

$$Re^* = \frac{D_o U^* \rho}{\eta^*} \tag{6}$$

$$\eta^* \equiv \tau_o \Big/ \left(-\frac{du}{dr}\right)_o \tag{7}$$

The subscript o refers to conditions at the wall. The velocity $U^*$ is obtained from the usual Newtonian discharge equation

$$U^* = \frac{D_o^2}{32\,\eta^*}\left(-\frac{dP}{dx}\right) \tag{8}$$

By expressing the apparent viscosity and velocity in terms of the wall shear, the modified Reynolds number becomes

$$Re^* = \frac{D_o^2 \rho}{8\tau_o}\left(\frac{\tau_o}{K}\right)^{2/n} \tag{9}$$

By substituting Eqs. (3), (4), and (5) into Eq. (2), the conventional non-Newtonian Reynolds number takes the form

$$Re' = \frac{2D_o^2 \rho \tau_o^{(2-n)/n}}{(3+1/n)^2 K^{2/n}} = \left(\frac{4}{3+1/n}\right)^2 Re^* \qquad (10)$$

From Eq. (10), it follows immediately that

$$Re' < Re^* \text{ for } n < 1 \quad \text{(pseudoplastic)}$$

$$Re' > Re^* \text{ for } n > 1 \quad \text{(dilatant)}$$

As proposed here, the more simple modified Reynolds number is useful in predicting the existence of laminar flow. If the calculated $Re^*$ for a pseudoplastic is less than the maximum for stable laminar flow, the fluid is definitely in the laminar region. If $Re^*$ for a dilatant is greater than this maximum, then the fluid cannot be in laminar flow.

The concept of a Newtonian fluid flowing under the same pressure gradient is also very useful when the available information is the bulk velocity, U. By substituting $(-dP/dx)$ from Eq. (8) into Eq. (4), the following simple equation results.

$$U = \left(\frac{4}{3+1/n}\right) U^* \qquad (11)$$

Thus $U^*$ may easily be calculated and used directly in the modified Reynolds number.

References

1. Metzner, A. B., and Reed, J. C., A. I. Ch. E. Journal, 1, 434 (1955).

2. Nebeker, E. B., Research Report, Chemical Engineering Laboratory, California Institute of Technology, July, 1961.

## PROPOSITION II

The limitations on the use of the two suffix ternary van Laar equations can be removed by proper consideration of the imposed symmetry restriction.

---

The two equations most commonly employed to predict activity coefficients in ternary liquid systems are the three suffix Margules equation and the two suffix van Laar equation. Although both equations utilize the constants from the three separate binary pairs, the Margules equation contains an additional constant which must be determined from ternary experimental data. The ternary van Laar equation, as presented by Wohl[1], requires only the six binary constants, but its use is limited by a symmetry restriction. The Wohl equation is valid only for those ternary systems whose binary van Laar constants obey the equation

$$\frac{A_{3-2}}{A_{2-3}} = \frac{A_{3-1}}{A_{1-3}} \frac{A_{1-2}}{A_{2-1}} \tag{1}$$

where the subscripts refer to the appropriate binary pair. When applied to systems for which Eq. (1) does not hold, the Wohl equation assumes an arbitrary nature because of the manner in which the binary constants are introduced.

The method used by Wohl to extend the binary van Laar equations to an N component system was based on the following expression for the excess free energy of mixing

$$\frac{\Delta F^e}{RT} = \sum_j^N \sum_i x_i q_i x_j q_j 2a_{ij} \Big/ \sum_j^N x_j q_j , \qquad j > i \tag{2}$$

In this equation, $q_i$, $q_j$, and $a_{ij}$ are arbitrary constants and $x_i$ and $x_j$ are the mole fractions of components i and j in the liquid phase. The activity coefficient, $\gamma$, for component k is then obtained from this equation by the relation

$$\log_e \gamma_k = \frac{\partial}{\partial n_k} \left[ \left( \sum_i^N n_i \right) \left( \frac{\Delta F^e}{RT} \right) \right]_{T,\, n_i \neq n_k} \tag{3}$$

where $n_i$ is the number of moles of component i. In applying Eq. (2) to a binary system of components i and j, the van Laar constants are defined by the equations

$$\begin{aligned} A_{i-j} &= 2a_{ij}q_i \\ A_{j-i} &= 2a_{ij}q_j \end{aligned} \tag{4}$$

When Eq. (2) is applied to a ternary system, the symmetry restriction of Eq. (1) follows immediately from Eq. (4) for the binary constants.

To avoid this inherent symmetry restriction, the following expression for the excess free energy of an N component system is proposed.

$$\frac{\Delta F^e}{RT} = \sum_j^N \sum_i x_i a_{ij} x_j a_{ji} \Big/ \sum_j^N \sum_i (x_i a_{ij} + x_j a_{ji}), \quad j > i \qquad (5)$$

where $a_{ij}$ and $a_{ji}$ are arbitrary constants. This expression in conjunction with Eq. (3) will yield an equation for the activity coefficients in terms of the constants $a_{ij}$ and $a_{ji}$. These arbitrary constants can then be related to the binary van Laar constants by the limiting conditions.

$$\lim_{\substack{x_i \to 0 \\ x_j \to 1}} (\log \gamma_i) = A_{i-j}, \quad \text{all } i \text{ and } j, \quad i \neq j \qquad (6)$$

For the case of a ternary system, after substitution of Eq. (5) into Eq. (3) and identification of the resulting constants by means of Eq. (6), the following result is obtained

$$\log \gamma_1 = \frac{x_2^2 (A_{2-1}^2/A_{1-2}) + x_3^2 (A_{3-1}^2/A_{1-3}) + x_2 x_3 B_1}{[x_1 + x_2(A_{2-1}/A_{1-2}) + x_3(A_{3-1}/A_{1-3})]^2} \qquad (7)$$

$$B_1 = (A_{2-1}A_{3-1}/A_{1-3}) + (A_{3-1}A_{2-1}/A_{1-2}) - (\alpha_1 \text{ or } \beta_1) \qquad (8)$$

where

$$\alpha_1 = A_{3\text{-}2}A_{2\text{-}1}/A_{1\text{-}2} \qquad \beta_1 = A_{2\text{-}3}A_{3\text{-}1}/A_{1\text{-}3}$$

Similar equations can be written for $\gamma_2$ and $\gamma_3$ by changing the subscripts in Eqs. (7) and (8) according to the scheme

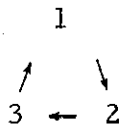


The constants $\alpha$ and $\beta$ in Eq. (8) represent the arbitrary nature of the ternary van Laar equation because these constants will normally vary over the range $\frac{1}{2} < \frac{\alpha}{\beta} < 2$. For a symmetric system, $\alpha = \beta$, and when $\alpha$ is used, Eq. (7) is identical with the Wohl equation. However, for unsymmetric systems, Eq. (7) becomes arbitrary since there is no a priori reason for selecting either $\alpha$ or $\beta$ to describe the entire ternary system.

As herein proposed, Eq. (7) has been derived to fit the limiting concentration ranges and will yield consistent results only when applied to symmetric systems. However, the fact that the symmetry considerations are shown to affect only one term permits the ternary van Laar equation to be extended to unsymmetric systems by considering B as an arbitrary constant. The most suitable value of this constant would have to be determined from ternary data and

theoretically may be evaluated from only one vapor-liquid equilibrium point. When Eq. (7) is used to predict ternary activity coefficients from binary data only, the constant B should be estimated from the relation

$$B_1 = A_{2\text{-}1}A_{3\text{-}1}\left(\frac{1}{A_{1\text{-}2}} + \frac{1}{A_{1\text{-}3}}\right) - \frac{1}{2}(\alpha_1 + \beta_1) \qquad (9)$$

Reference

1. Wohl, K., "Thermodynamic Evaluation of Binary and Ternary Liquid Systems," Trans. Am. Inst. Chem. Engrs., 42, 215-49 (1946).

## PROPOSITION III

When x-ray intensity measurements are made with a crystal monochromator, the correct polarization factor to be used depends upon the scattering geometry.

---

The x-ray polarization factor is a term occurring in the equation for the scattered intensity from a system of electrons. This factor is an angular dependent function which is used to correct experimentally observed intensities and is due to the inherent nature of radiation and scattering phenomena.

The usual case of polarization corrections is well treated in the literature and for unpolarized incident radiation, the polarization factor is given by the equation[1, 2]

$$P(\Theta) = \frac{1}{2}\left(1 + \cos^2 2\Theta\right) \tag{1}$$

where $2\Theta$ is the scattering angle. When crystal reflection is used to produce monochromatized radiation, the polarization factor is given as[2]

$$P(\Theta) = \frac{1 + \cos^2 2\Theta \cos^2 2\alpha}{1 + \cos^2 2\alpha} \tag{2}$$

where $2\alpha$ is the diffraction angle of the monochromator.

The purpose of this proposition is to point out that the polarization factor as given by Eq. (2) applies only when the crystal monochromator is placed between the x-ray target and the sample. When the monochromator is located between the sample and the radiation detector, the correct polarization factor is

$$P(\Theta) = \frac{1}{2}\left(1 + \cos^2 2\Theta \cos^2 2\alpha\right) \qquad (3)$$

The need for a different polarization factor depending upon the scattering geometry is not generally apparent, and the use of the wrong factor has been reported in the literature[3, 4, 5].

References


1. Compton, A. H., and Allison, S. K., "X-Rays in Theory and Experiment," D. Van Nostrand, Princeton, N. J., 1935.

2. Klug, H. P., and Alexander, L. E., "X-Ray Diffraction Procedures," John Wiley, New York, 1954, p. 594.

3. Katzoff, S., "X-Ray Studies of the Molecular Arrangement in Liquids," J. Chem. Phys., 2, 841-51, (1934).

4. Morgan, J., and Warren, B. E., "X-Ray Analysis of the Structure of Water," J. Chem. Phys., 6, 666-73, (1938).

5. Sharrah, P. C., and Gingrich, N. S., "The Diffraction of X-Rays by Liquid Oxygen," J. Chem. Phys., 10, 504, (1942).

## PROPOSITION IV

All existing x-ray diffraction studies of liquid structure should be critically examined for possible errors resulting from the improper correction for incoherent scattering.

---

The interaction of x-rays with matter results in the emission of several types of secondary radiation, e. g., fluorescent, coherent, and incoherent. Of these various types, the coherently scattered radiation is of special interest because it produces interference or diffraction effects that are useful in gaining information regarding the internal structure of the irradiated material. The other types of secondary radiation do not produce interference effects, but are always present to some degree in any diffraction experiment. While the fluorescent radiation may usually be eliminated through a suitable choice of experimental conditions, the incoherently scattered radiation is almost always present. Consequently, the total observed scattering must be corrected for the presence of this incoherent scattering before any structural analysis can be made. The purpose of this proposition is to point out that this correction is usually improperly made.

A fundamental assumption in the theory of x-ray scattering from fluids is that the observed scattering, suitably corrected for absorption and polarization, converges to the total independent

scattering of the isolated atom at large scattering angles. With values of the independent scattering factors available from the literature, this criterion provides a means of normalizing the observed intensities and subtracting the unwanted incoherent scattering. The validity of this analysis hinges on the condition that the experimentally observed scattering is properly corrected for all factors which can affect the intensity of the scattered radiation.

An examination of the existing x-ray diffraction studies of fluid structure indicates a strong possibility of an improper application of the incoherent scattering correction. This possibility originates from the commonly used assumption that incoherently scattered radiation is detected with the same efficiency as the coherently scattered radiation at all scattering angles. However, because of its angular dependent wavelength, the incoherent scattering will generally suffer additional or increased intensity losses. Although incoherent scattering is always present to some degree in the observed intensity, its effect will depend rather strongly on the nature of the experiment and on the fluid under investigation. However, the importance of this effect should not be overlooked, as is usually done in most diffraction studies of fluid structure.

Perhaps the most common occurrence of this improper treatment of the incoherent scattering is in the correction for absorption within the fluid sample. Because of its higher wavelength, the

incoherent scattering will be more strongly absorbed than the coherent scattering. If the assumption is made that the same absorption factor applies to both types of scattering, the resulting "fully corrected" intensity will contain an angular dependent error.

Unfortunately, most published studies of fluid structure do not clearly indicate the detailed nature of the absorption correction. However, this correction has been worked out for a variety of sample shapes and scattering geometries[1-6], and the appropriate reference is usually cited as a means of identifying the method of absorption correction that has been used. The important fact to be noted is that these standard references are strictly applicable only for coherently scattered radiation and none of them take into account the presence of incoherent scattering in the experimentally observed intensity. Moreover, no indication is ever given that these standard methods have been in any way modified to account for the incoherent scattering.

A typical example of the improper correction for incoherent scattering is provided by a recent study on the structure of liquid oxygen and nitrogen made by Furumoto[7]. In this instance, a critical examination of the type proposed is possible, since the experimental method is described in detail. To illustrate the nature of the possible errors, we will examine Furumoto's results for liquid oxygen ($T = 64^{\circ}K$, $\bar{\rho}_b = 1.27$ gm/cc) at $S = 12.5\ \text{Å}^{-1}$ using Mo K$\alpha$ radiation ($\Theta \approx 45$ degrees). The following equation may be derived, relating

the experimentally observed intensity, $I_s^E(\Theta)$, to the total absolute intensity of scattered radiation originating within the liquid, $I_s^t(\Theta)$.

$$I_s^E(\Theta) = P(\Theta)\, A(\Theta)\, F(\Theta)\, (C/N)^{-1} I_s^t(\Theta) \qquad (1)$$

In this equation $P(\Theta)$ is the polarization factor, $A(\Theta)$ is the absorption factor for coherent scattering, $F(\Theta)$ is the incoherent scattering correction factor, and $(C/N)$ is the normalization constant.

From Furumoto's discussion of his experimental method, the expression for the incoherent scattering correction should be

$$F(\Theta) = \gamma(\Theta) + [1 - \gamma(\Theta)]\, (1/B^2)\, e^{-\Delta\mu\langle\ell\rangle} \qquad (2)$$

where $\gamma(\Theta)$ is the fraction of the total radiation that is scattered coherently and $B$ is the Breit-Dirac factor, a relativistic correction applicable to the incoherent scattering. The exponential term in Eq. (2) represents the increased absorption of incoherently scattered radiation; $\Delta\mu$ is the increase in the linear absorption coefficient and $\langle\ell\rangle$ is the average path length of the scattered rays through the liquid sample. For the conditions of his experiment at $S = 12.5$, the parameters in Eq. (2) are $\gamma(\Theta) = 0.22$, $B = 1.0344$, $\Delta\mu = 0.185\ \text{cm}^{-1}$, and $\langle\ell\rangle = 0.292$ cm. The resulting correct value for $F(\Theta)$ is then 0.911.

If the assumption is made that the absorption factor for incoherent scattering is the same as that for coherent scattering, this is equivalent to setting $\Delta\mu$ equal to zero in Eq. (2). The corresponding value for $F(\Theta)$ would then be 0.949 and the desired value for $I_s^t(\Theta)$ would be too low by 4.2%. Although this assumption was in fact made by Furumoto, the resulting error in his intensity curves was reduced by an additional compensating error. He incorrectly used a value of $B^3$ in Eq. (2) instead of the proper $B^2$ (ref. 8). As a result, his incoherent scattering correction factor came out to be $F(\Theta) = 0.925$. This gave a maximum error in his intensity curve of only 1.5%; a value comparable to his over-all experimental accuracy and, therefore, unnoticed.

This example of a typical improper correction for incoherent scattering should amply illustrate the proposed need for a critical examination of the existing x-ray diffraction studies of fluid structure.

References

1. Ritter, H. L., Harris, R. L., and Wood, R. E., "On the X-Ray Absorption Correction for Encased Diffractors in the Debye-Scherrer Technique," J. Appl. Phys., 22, 169, (1951).

2. Milberg, M. E., "Transparency Factor for Weakly Absorbing Samples in X-Ray Diffractometry," J. Appl. Phys., 29, 64, (1958).

3. Sawada, M., and Shaw, C. H., "Calculation of the Transmission Factor in X-Ray Scattering," J. Appl. Phys., 29, 1344, (1958).

4. Levy, H. A., Agron, P. A., and Danford, M. D., "X-Ray Diffractometry with Slightly Absorbing Samples," J. Appl. Phys., 30, 2012, (1959).

5. Gingrich, N. S., "The Diffraction of X-Rays by Liquid Elements," Rev. Mod. Phys., 15, 90, (1943).

6. Paalman, H. H., and Pings, C. J., "Numerical Evaluation of X-Ray Absorption Factors for Cylindrical Samples and Annular Sample Cells," J. Appl. Phys., 33, 2635, (1962).

7. Furumoto, H. W., "Diffraction of X Rays by Liquids — Nitrogen, Oxygen, and Their Mixtures," doctoral thesis, Ohio State University, (1963).

8. Walker, C. B., "X-Ray Compton Scattering for Aluminum," Phys. Rev., 103, 558, (1956).

# PROPOSITION V

The generalized compressibility factors presented by Lydersen, Greenkorn, and Hougen[1] deviate significantly from the observed behavior of real fluids for reduced temperatures greater than 2. 0.

---

The utility of generalized compressibility factors in engineering practice is well recognized. Of the many correlations of this type, one that has gained fairly wide acceptance[2] is due to Lydersen, Greenkorn, and Hougen (hereafter referred to as LGH) who generalized the PVT properties of 82 different fluids by the relation

$$Z = PV/RT = Z\,(T/T_c,\ P/P_c,\ Z_c)\,. \qquad (1)$$

The purpose of this proposition is to point out that the LGH correlation is questionable in the high temperature region because their results do not agree with the observed general behavior of pure fluids.

Extensive experimentation has demonstrated that the PVT behavior of gases exhibits general features that are common to all fluids. One such feature is the behavior of the isotherms in a plot of PV (or Z) versus P. At low temperatures, these isotherms exhibit a minimum. As the temperature is increased, this minimum

shifts toward smaller values of P until, for one temperature, the point of zero slope occurs at P = 0. This temperature is called the Boyle temperature and may be defined by the equation

$$\left[ \frac{\partial (PV)}{\partial P} \right]_{T_{Boyle}} = 0 \quad \text{at} \quad P = 0 \tag{2}$$

From Eq. (1), the slope of the compressibility factor, $(\partial Z/\partial P)_T$, is also zero at this point.

The relationship of the compressibility factor to the Boyle temperature may be further examined by a consideration of the second virial coefficient, B(T). For gases that behave nearly ideally ($Z \approx 1$), the following expression is applicable.

$$Z = 1 + \frac{B(T)}{\bar{V}} \tag{3}$$

At low temperatures, B(T) is negative and at high temperatures, it is positive. The temperature at which the second virial coefficient becomes zero is the Boyle temperature. Therefore, from Eq. (3), Z is greater than unity for all isotherms above the Boyle temperature. Moreover, these isotherms have no point of zero slope[3], i.e., the compressibility factor is a monotonically increasing function of the pressure for all temperatures above the Boyle temperature.

Although the Boyle temperature has little practical value, it is a general feature of the PVT behavior for all real fluids. Its numerical value is different for all gases, but when expressed in reduced units, it becomes nearly constant[4]. In terms of $T/T_c$, this constant reduced Boyle temperature has been found to be approximately 2.5 (ref. 5).

Since the generalized compressibility factor represents an attempt to describe the PVT behavior of all gases with a universal equation of state, any such correlation must have a reduced Boyle temperature near the observed average value. On this basis, the generalized compressibility factors presented by LGH deviate significantly from the behavior of real fluids. The LGH correlation shows that $Z$ is still less than unity for $T_r = 4.0$ instead of the observed value of $T_r = 2.5$. In addition, their isotherms indicate a point of zero slope for reduced temperatures as great as $T_r = 10$. These conditions are contrary to the observed PVT behavior of any typical fluid. Consequently, it is proposed that the LGH correlation is in error for values of $T_r$ greater than 2.0 and should not be used in this region.

References

1. Lydersen, A. L., Greenkorn, R. A., and Hougen, O. A., "Generalized Thermodynamic Properties of Pure Fluids," Univ. Wisconsin Eng. Exp. Sta. Rept., 4, (Oct. 1955).

2. Hougen, O. A., Watson, K. M., and Ragatz, R. A., Chemical Process Principles, Part II, second edition, (John Wiley and Sons, New York, 1959), Chapter 14.

3. Hirschfelder, J. O., Curtiss, C. F., and Bird, R. B., Molecular Theory of Gases and Liquids, (John Wiley and Sons, 1954), p. 232.

4. Nelson, L. C., and Obert, E. F., "Generalized PVT Properties of Gases," Trans. ASME., 76, 1057, (1954).

5. Dodge, B. F., Chemical Engineering Thermodynamics, McGraw-Hill Book Company, New York, 1944), p. 163.